Nonequilibrium Statistical Mechanics
COLLECTIVE BEHAVIOR OF ACTIVE PARTICLES

Dissertation

for the award of the degree

"Doctor rerum naturalium"

within the doctoral program GGNB IMPRS

Physics of Biological and Complex Systems

of the Georg-August University School of Science (GAUSS)

submitted by

Jérémy Vachier

from France

Göttingen, 2020

Thesis Committee

Dr. Marco G. Mazza	Nonequilibrium soft matter MPIDS, Göttingen, Germany	(First Reviewer)
Prof. Dr. Jörg Enderlein	Third Institute of Physics – Biophysics Georg August University, Göttingen, Germany	(Second Reviewer)
Dr. Michael Wilczek	Wilczek group MPIDS, Göttingen, Germany	

Members of the Examination Board

Dr. Marco G. Mazza	Nonequilibrium soft matter MPIDS, Göttingen, Germany
Prof. Dr. Jörg Enderlein	Third Institute of Physics – Biophysics Georg August University, Göttingen, Germany
Dr. Michael Wilczek	Wilczek group MPIDS, Göttingen, Germany
Prof. Dr. Ramin Golestanian	Department of Living Matter Physics MPIDS, Göttingen, Germany
Prof. Dr. Marcus Müller	Institute for Theoretical Physics Georg August University, Göttingen, Germany
Dr. Aljaz Godec	Mathematical Biophysics MPIBPC, Germany

Date of the oral examination: March, 10 2020

2

Abstract

Active matter is everywhere, from macroscopic to microscopic scales, we find systems such as human crowd or flock of birds as well as bacterial colonies. These systems composed of particles are able to convert their surrounding energy into motion, and naturally exist out of thermodynamic equilibrium. At the microscopic scale, a specific class of active particles is particularly interesting: called microswimmers, these are biological or artificial micro-sized particles able to move in a fluid, such as bacteria or chemically driven Janus particles. In nature, these microswimmers rarely swim alone and can exhibit intriguing collective behavior at interfaces such as cluster formation, as well as swarming, swirling, raft and biofilm formation. The fundamental mechanisms of the emergence of collective behavior for living and inanimate active systems is not yet understood, especially because these systems are far from equilibrium, where our experimental and theoretical understanding is limited.

This thesis aims to elucidate the impact of the activity on the emergence of collective behavior in an active system, at a microscopic level, by using a stochastic approach, over three works, from active sedimenting particles to early biofilm formation in the case of the bacteria *Pseudomonas aereginosa*, via the aggregation formation for the micro-algae *Chlamydomonas reinhardtii*.

The first work describes the sedimentation profile of one active particle as a function of its activity, in three dimensions under the influence of the gravity. The system is described in terms of two overdamped Langevin equations for the position and the orientation of the particle. From these equations the associated Fokker-Planck equation is derived. In this work, we developed an analytical method to study the sedimentation profile and the analytical solution of the Fokker-Planck equation in 3D for an active particle under gravity and with a confining wall is derived. We recovered experimental results: first in the steady-state the sedimentation profile given by an exponential decay of the density profile; second, the change of the length of the sedimentation by increasing the activity. This analytical method gave a direct access to the transient dynamics and kept the coupling between the position and the orientation. In order to study many interacting particles, we developed active Brownian particles simulations. By comparing the analytical solution for one active particle to the one obtained from the simulations and experimental results (Janus colloids), we have shown that our analytical solution was also valid in the dilute case. In addition, the simulations show the emergence of collective behavior as function of the activity.

The second work characterizes the aggregation of active particles. By means of active Brownian particles simulations, we studied the aggregation phenomena of active particles, for different activities, under confinement. Moreover, recent experimental results (in the case

of the algae *C. reinhardtii*) have shown that the phenomenon could not be described by a Motility-Induced Phase Separation (MIPS) model and the need of a new model was required. By varying the activity as well as the diffusion coefficients as functions of the local cell density and in the case of many interacting active particles, we observed in the steady state regime the emergence of collective behavior such as an aggregation of particles at the center of the compartment or a ring pattern. We show that the use of active Brownian particles simulations designed to describe the effect of the local cell density and confinement on the dynamics re-create the patterns observed in the experiment.

Finally, we studied the early stage biofilm formation in the case of two canonical strains of the bacteria family *P. aereginosa*, PA01 and PA14. Before forming a bacterial biofilm community, it is commonly observed that free-swimming bacteria initially undergo a phase known as "reversible attachment", a random and variable lag period of transient cell attachment. The population dynamics was described with a 'birth and death' process with a temporal dependence of the rates. These rates describe the reversible attachment by a division rate and a detachment rate. The division rate was described in terms of lineage time, meaning the time that the lineage stay continually on the surface. As a conclusion, our results unified disparate findings in the literature regarding early events in biofilm formation for PA01 and PA14. Moreover, we have shown that our model gave a framework to characterize different surface colonization strategies which lead to biofilm formation.

"Il avait toujours cru que la théorie sortait de l'expérience. Il pensait que les contradictions entre la théorie et de nouvelles expériences menaient naturellement à l'élaboration d'une nouvelle théorie, plus large que la précédente.

[...]

La théorie, semblait-il, était née librement du libre jeu de l'intelligence et c'était ce libre jeu qui se serait comme détaché de l'expérience, et qui avait permis de trouver une explication à toute la richesse des résultats expérimentaux anciens et nouveaux.

[...]

Et curieusement, dans sa tête de physicien, les processus du monde matériel n'étaient le reflet de lois engendrées dans le désert mathématique. Dans l'esprit de Sturm, ce n'était pas la mathématique qui était le reflet du monde, mais le monde qui était une projection d'équations différentielles, le monde était le reflet de la mathématique".

— '*Vie et Destin: roman*'. L'age d'homme (2018) p.465-466, Vassili Grossman

"Nobody ever figures out what life is all about, and it doesn't matter. Explore the world. Nearly everything is really interesting if you go into it deeply enough."

— Richard P. Feynman

To my mentor Ricardo and my parents Florence and Franck.

Contents

List of Figures

List of Abbreviations

MIPS	Motility induced phase separation
FPE	Fokker-Planck equation
RTPs	Run-and-tumble particles
ABPs	Active Brownian particles
AOUPs	Active Ornstein-Uhlenbeck particles
PBPs	Passive Brownian particles
SDEs	Stochastic differential equations
ODEs	Ordinary differential equations
WCA	Week-Chandler-Anderson
cAMP	cyclic-AMP
c-di-GMP	cyclic diguanylate GMP
EPS	Exopolysaccharide
GPU	Graphics processing unit
CPU	Central processing unit
MPCD	Multi-particles collision dynamics

Chapter 1

Introduction

Active matter is everywhere. The most obvious examples are living matter, Fig. 1.1: animals, algae and bacteria, but also inanimate systems, such as vertically vibrated granular layers, are considered active, and there are many parallels between the behavior of active and driven matter. We can find active systems also at the mesoscopic scale, such as flocks of birds or schools of fishes. In the last decades, a significant effort has been made to push toward this fascinating field and develop its applications in a broad area of topics such as statistical physics [1, 2], biology [3], soft matter [4, 5], robotics [6]. Among these topics, active matter has been intensively studied, from many different approaches, such as the dynamics of microswimmers at low Reynolds numbers [7, 8, 4, 5], which measures quite generally the ratio between inertial and viscous forces, or the biological implications of collective motion like school of fishes and flocks of birds [9]. Both can be described by using a stochastic approach [10, 2, 11, 1]. An important characteristic of active matter systems is the effect of the random fluctuations, from the surrounding environment to internal mechanisms, on their individual motion. We can see these fluctuations as a result of abstract decisions, interactions with the surrounding media, or even between particles, like for instance in a human crowd. In the following, the general modelling approach is based on the theory of stochastic processes, especially the Master equation, the Langevin equations and the corresponding Fokker-Planck equations (FPE) for the evolution of the probability density distribution of finding a particle at time t in a position between x and $x + dx$, will be used.

Equilibirum - Nonequilibrium. Let us first take a step back and describe the motion of one passive particle as a simple random walk [12, 13]. The position of the particle $x(t)$ takes values at each time t over a set of N states, $S = \{1, ..., i, ..., N\}$, with periodic boundary conditions at the edges A and B. The particle can move to the right or to the left, by jumping in a unit time step from site i to site $i + 1$ with a rate P_r or to site $i - 1$ with
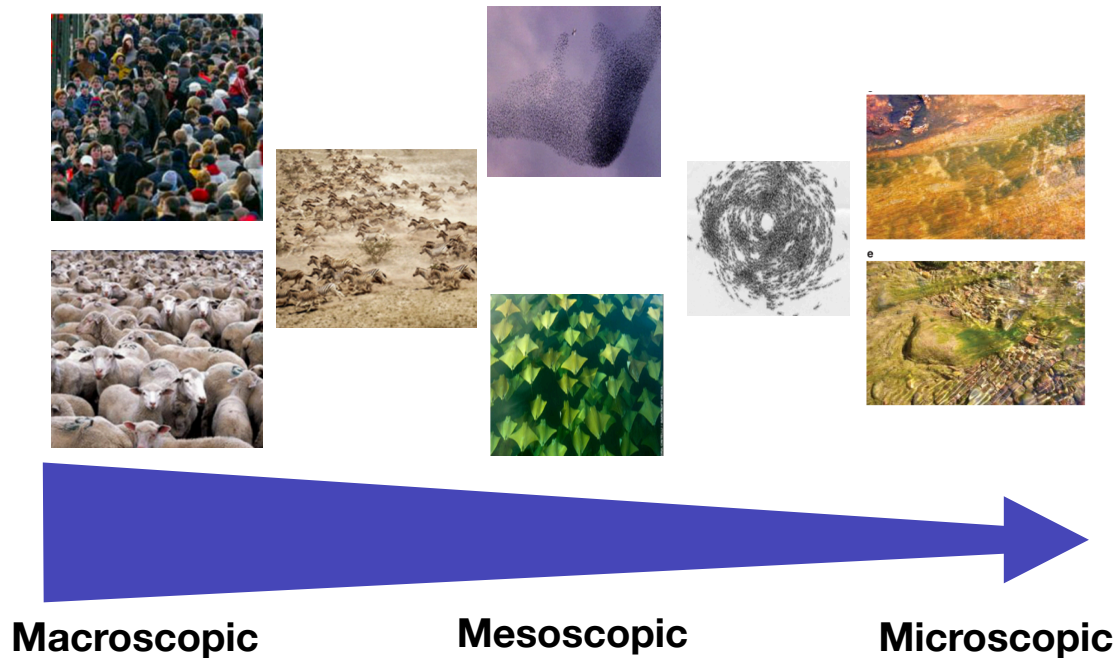
Figure 1.1 – Active matter is everywhere. From macroscopic to microscopic scales, we find systems such as human crowd or flock of birds as well as bacterial colonies, which are classical examples of active matter.[1]

a rate P_l, as shown in Fig. 1.2. The quantity that we want to look at is the probability distribution $\nu(x(t) = x_i)$, that $x(t)$ is in the state i at time t. When, there is no input from the surrounding environment, the rates are taken equal $P_l = P_r$ and the probability distribution is found constant over time or invariant, there is no net flux of probability in the system and the detailed balance is satisfied: the system is said to be at the equilibrium.

However, now let us assume that close to the edge B, the sun rises. The particle can take energy from the surrounding environment, convert it into motion and start to move toward this light source, as shown in Fig. 1.3. As a result, the probability distribution is found invariant but the rates P_l and P_r change and are not anymore equal, $P_l < P_r$. Therefore, there is a net flux of probability in the system and the detailed balance is not satisfied anymore: the system is said to be out of equilibrium. This system can be taken as a heuristic definition of active matter. These two simple examples illustrate firstly a difference between 'passive' and 'active' particle, and secondly their statistical description, either equilibrium or nonequilibrium.

Passive Particle

P_l P_r

A   B

$P_l = P_r$

No net flux

Periodic boundary conditions

Detailed Balance / Equilibrium
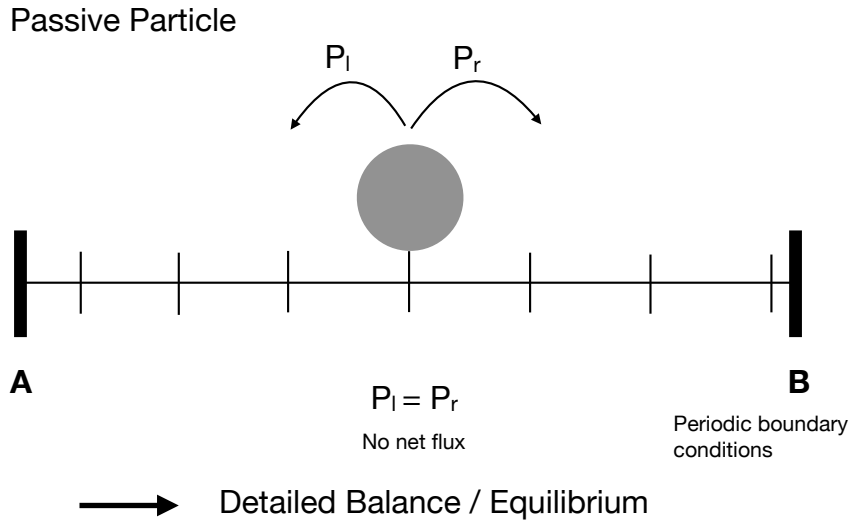
Figure 1.2 – Passive Particle - Equilibrium. Motion of one particle describing by a simple symmetric ($P_l = P_r$) random walk, with periodic boundary conditions at the edges A and B. There is no net flux of probability through the system, the detailed balance is satisfied: the system is said to be at the equilibirum.

Active matter a definition. More precisely, active matter can be specifically defined as [11, 1, 10, 9, 2] systems composed of particles able to convert their surrounding energy into motion, and naturally exist out of thermodynamic equilibrium by breaking the time-reversal symmetry and thus the detailed balance.

Different active particles. One specific class of active particles at the microscopic scale drew my attention. They are called microswimmers and we can distinguish two main classes: biological and artificial. Microswimmers have two main categories of propulsion mechanisms [14, 15]: they can be powered by local conversion of energy (e.g. catalytic processes) or they can be driven by external (e.g., electric, magnetic, acoustic) fields. There exist an important distinction between internally driven active matter and particles that are brought out of equilibirum by external fields: while microswimmers powered by these two mechanisms feature a motion that can be described with similar effective models, they present quite different microscopic details in their interaction with their environment. More specifically, my thesis will be focusing on the microswimmers propelled by local energy conversion.

Active Particle

P_l P_r

A   B

$P_l < P_r$

Net flux to the right

Periodic boundary
conditions

Detailed Balance / Out of Equilibrium
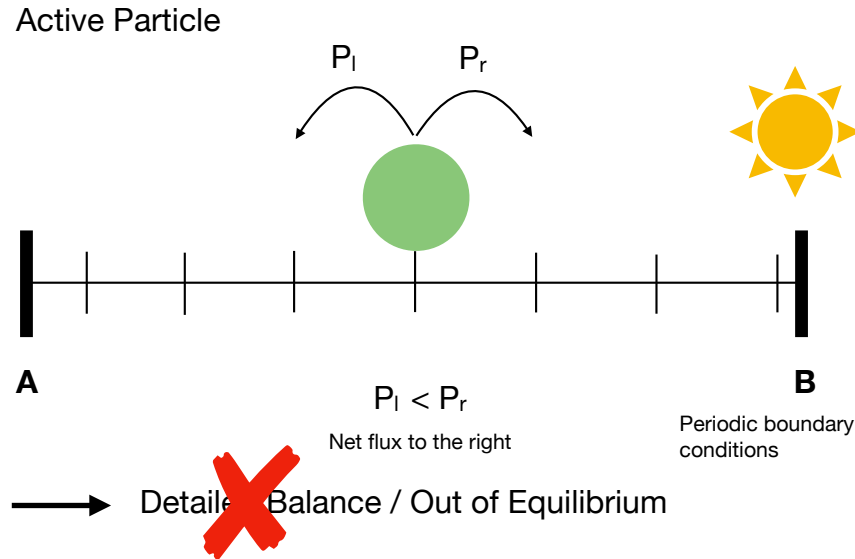
Figure 1.3 – Active Particle - Nonequilibrium. Motion of one particle describing by an asymmetric ($P_l \neq P_r$) random walk, with periodic boundary conditions at the edges A and B. However, the sun rises close to the edge B, that 'bias' the motion of the particle which is able to convert the surrounding energy into motion to move toward (in this case) the light source. Due to this 'bias', there is the emergence of a net flux of probability through the system, the detailed balance is not satisfied: the system is said to be out of equilibrium.

Biological active particles. There exist many kinds of biological microswimmers, e.g., bacteria [16, 17, 18, 19, 20, 21], unicellular protozoa [22, 23, 24], spermatoza [25, 26] and algae [27, 28, 29, 30]. The swimming motion in the planktonic state of these microswimmers is essentially powered by flagella or cilia controlled by molecular motors [31, 32, 33, 4]. More specifically, as shown in Fig. 1.4, two really interesting biological microswimmers draw my attention: the algae *Chlamydomonas reinhardtii* and the bacteria *Pseudomonas aeruginosa*. *C. reinhardtii* cells are a unicellular soil-dwelling microalgae of about $10\mu m$ in diameter, which swims with two flagella. This swimming mechanism can be described by a run-and-tumble particle [34]. However, in a crowded environment the swimming mechanism of a single *C. reinhardtii* is better approximated by an active Brownian particle, due to the competition between the mean free path and the tumbling rate. *P. aeruginosa* is a common bacterium that can cause disease in plants and animals, including humans [35]. It exhibits, in its planktonic state, a swimming behavior powered by flagella, however at surfaces and when its motility is suppressed *P. aeruginosa* can form surface colonies also called biolfim. As a results, *P. aeruginosa* is a multidrug resistant pathogen recognized for

its ubiquity, its intrinsically advanced antibiotic resistance mechanisms, and its association with serious illnesses. Especially, it plays an important role in hospital-acquired infections such as ventilator-associated pneumonia and various sepsis syndromes.

Artificial active particles. In order to reproduce the swimming behavior of biological microswimmers making use of diverse propulsion mechanisms, a broad range of methods have been used to realize artificial microswimmers. The motivation for these man-made self-propelling particles is to change the way in which we perform several tasks in, e.g, health care and environmental applications [36, 37, 38, 39, 40]. The key ingredient of the self-propulsion of these artificial microswimmers is to break their symmetry to lead to propulsion through various phoretic mechanisms. In the following, we will not discuss the passive colloidal particles which move under phoretic motion, but we will focus on the dielectric particles (e.g. made of silica, polystyrene, or melamine). This class of particles is based on so-called Janus particles (named after the two-faced Roman god), as shown in Fig. 1.4, where dielectric colloids are partially coated with thin layers of catalytic materials like platinum (Pt) or palladium (Pd) [41]. The mechanism is described as follow: by immersing such particles in an aqueous solution enriched with H_2O_2, they locally decompose it into H_2O and O_2, and thus create a local concentration gradient that eventually leads to self-diffusiophoresis. This concept was first successfully introduced by Howse *et al* 2007 and has been used and modified by many other groups worldwide. An other material than the Pt or Pd, the hematite has also been used with blue light [42]. The catalytic processes involved in the H_2O_2 decomposition are really complex and their details are still under investigation. For example, the propulsion strength and direction show a strong dependence on added salt and ionic surfactants [43].

Collective behavior. In nature, microswimmers rarely swim alone. For example, the competition between the sperm cells, released by the millions, for the egg; bacteria grow by dividing and invading their surroundings together; or in future the potential transport of pharmaceuticals treatment or the modification of material properties by a large numbers of artificial microswimmers [44]. Moreover, biological microswimmers like motile bacteria can exhibit intriguing collective behavior at interfaces such as cluster formation, observed for *Myxocoscus xanthus* [45] or *Thiovulum majus* [46], as well as swarming, swirling, raft formation, and the emergence of mesoscale turbulence [47], observed for *E. coli* [47] or *Bacillus subtilis* [48]. One common example of collective behavior is the biofilm. It is an accumulation of microorganisms, e.g. algae or bacteria, on surfaces where they can stick and form sedentary communities. Biofilms may form on a wide variety of surfaces, which include household and industrial pipes, biomaterials such as contact lenses, medical devices including implants and urinary catheters, as well as living tissues [49]. A similar kind of

behavior has been shown and studied experimentally in the case of self-phoretic artificial spherical microswimmers, such as Janus particles, self-propelled liquid droplets, and photo-activated colloids, exhibit cluster formation and phase separation despite their isotropic shape and purely repulsive interactions[50].
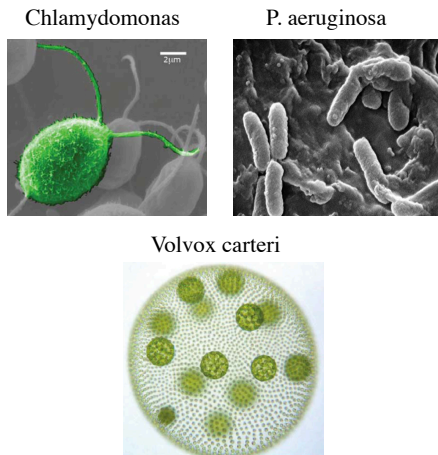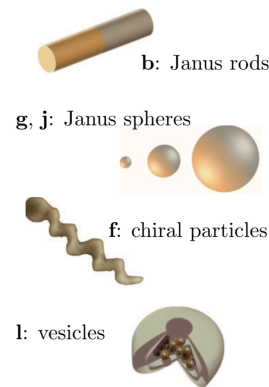
Figure 1.4 – Different active particles. We can distinguished two main classes of microswimmers, one is described as biocological active particles, such as the algae *Chlamydomonas reinhardtii* or *Volvox carteri*, the bacteria *P. aeruginosa* or *E. coli*. The other one is described as artificial active particles, such as the Janus rods or the Janus colloids. The dynamics of both can be approximated by active Brownian particles, especially the algae *C. reinhardtii* (in the case of collective motion or crowded environment, when the mean free path is shorter than the tumbling time) and the Janus colloids [51]. Moreover, the activity in the cellular division process e.g. in the case of the bacteria *P. aeruginosa* can be approximated by a 'birth and death' process.[1]

Gap in the field.   After almost two decades of study, active matter is still confronted with many open challenges which keep the research quite active. The fundamental mechanism of the emergence of collective behavior for living and inanimate active systems is not yet understood, especially because we are far from equilibrium. Moreover, describing the dynamics of such system in a real-life environment like porous soils or growing systems, where the light conditions, food sources vary in time, is challenging.

This thesis is focused on the central question: How can the activity affect the emergence of collective behaviors in an active system ?

Motivation.   Active matter can exhibit phases and phase transitions which are absent in equilibrium system [52, 53]. Active matter is also subject to strong instabilities and small fluctuations which lead to unusual mechanical properties. Moreover, a fascinating and challenging aspects of active matter is to be able to use and adapt the 'tools' for equilibrium statistical mechanics to intrinsic nonequilibrium systems. The motivation for it is that even with the inherent nonequilibirum properties of active systems, active matter appears to have striking similarities to equilibrium systems [54, 55, 56, 57]. As an example, the dynamics of individual active particles at large scales can be described by passive Brownian diffusion [58].

Many active systems play an important role on our daily life. Biofilms are encountered almost everywhere, and they can be beneficial (production of biofuel) or harmful (diseases). In human body, we generally associate biofilms with pathogenic form, e.g., the cystic fibrosis which is caused by the infections of the bacteria *P. aerugenosa*, but they can be beneficial such as the bacteria *Staphylococcus epidermidis*, which stop the colonization of potential bacteria via the stimulation of host-cell immune defenses and the prevention of adhesion in the biofilms [49, 59, 35]. In marine biology, biofilms have a strong impact, either advantageous or costly. For examples, due to ocean pollution by plastic one may use biofilms to facilitate the removal of microplastics from the surface layer of the oceans [60]; the development of various technics to prevent the biolfilm formation and to clean infected surfaces, lead to significative costs onto marine transport, aquaculture, oil and gas industries, desalination plants and other industries as it is well described in [61]. Recently, the production of biofuel from microalgae has received lot of attention, from the sunlight-driven cell factories, as a source of energy production. The advantages of using algae for the biomass sources are that they grow fast, under certain light and nutrition conditions, in a wide range of environments and only require sunlight and basic nutrients. By using photosynthesis the microalgae convert the sunlight energy into chemical energy to grow, and have a doubling times as short as half a day. In comparison to other agriculturally produced biodiesel feedstocks (e.g. corn, soybean, jatropha, palm oil), microalgae require much less land area and they seem more capable of displacing fossil fuels [62]. However, the microalgae are also known to form biolfilm, which

can at some extend reduce the production of energy due to the accumulation of cells at the surface of the bioreactors.

One key parameter on the formation of such collective behavior is the activity of the cells. Studying how the activity affects the emergence of collective behaviors can lead to a better understanding of the early stage biofilm formation and in future to develop better strategies to control their effects. For examples, due to the increase of antibiotic resistance, the focus of current research is to target bacterial growth/division that causes cell death or dormancy, from novel approaches. Moreover, the need of developing clean and renewable energy is one of the major challenges of the twenty first century to reduce the dependence on fossil fuels. By looking at the early stage of biofilm formation, we can prevent the maturation of the biofilm and find new treatment against infectious diseases as well as better energy source production.

Outline of the thesis.   This thesis aims to elucidate the impact of the activity on the emergence of collective behavior in an active system, at a microscopic level. Three different works are presented, which approach this problem from both analytical and numerical directions. The first one describes the sedimentation profile of one active particle as a function of its activity. The solution of the Fokker–Planck equation, in 3D, matched the results from the simulation and is in agreement with experimental results found for the Janus particles. This result showed that the solution is valid for one single active particle but can be extended to the dilute case. The other two focus on the emergence of collective behaviors. The second work studies aggregation of cells for the algae *Chlamydomonas reinhardtii* based on active Brownian simulations, in which the self-propulsion as well as the diffusion coefficients are dependent on the local cell density. The third work studies the early stage biofilm formation for the bacteria *Pseudomonas aeruginosa* by comparing the probability density distributions and its moments, obtained experimentally with the analytical solution of the modified 'birth and death' process used to describe the systems. The theoretical background and its numerical implementation necessary for these three works are introduced in Chapter 2. The results presented in Chapter 3 are ordered from the motion of one single active particle to the emergence of collective behaviors:

In the first work, I investigate the stochastic dynamics of one sedimenting active Brownian particle in three dimensions under the influence of gravity and passive fluctuations in the translational and rotational motion. I present an analytical solution of the Fokker–Planck equation for the stochastic process which allows us to describe the dynamics of the active Brownian particle in three dimensions. I address the time evolution of the monopole, the polarization, and the steady-state solution. I also perform Brownian dynamics simulations and study the effect of the activity of the particles on their collective motion. These results qualitatively agree with our model. Finally, I compare our results with experiments [51] and

find very good agreement.

In the second work, I studied the aggregation of active particles. A collection of self-propelled particles can undergo complex dynamics due to hydrodynamic and steric interactions. In highly concentrated suspensions, it is possible for such particles to form large-scale concentration patterns, where the active suspension separates into regions of high and low particle concentrations. This can be attributed to the interactions of the particles with boundaries, their specific particle-particle interactions, or other particle specific motility behavior. Since many biological microswimmers, such as the bacteria *E. coli* and the algae *C. reinhardtii*, are sensitive to a umber of external stimuli, we investigated if this phenomenon is related to phototactic, gravitactic or chemotactic mechanism. By performing active Brownian simulations of such active particles with the observed motility characteristics, we show that we can re-create the pattern observed in recent experiments. The observed pattern formation is switchable by lights and depends on the geometry of the confinement, both of which are not captured by current models and thus require a revision of the state-of-the-art theoretical approach.

In the third work, I studied the early stage biofilm formation in the case of two different strains of the bacteria *Pseudomonas aeruginosa*. Before forming a bacterial biofilm community, it is commonly observed that free-swimming bacteria initially undergo a phase known as "reversible attachment", a random and variable lag period of transient cell attachment. For example, PAO1 and PA14 are two canonical strains in distinct sub-groups of the *Pseudomonas aeruginosa* phylogeny with different surface sensing circuits. However, they both exhibit reversible attachment and apparently indistinguishable early biofilm behavior in bulk and single cell assays. Here, we show that stark differences between these strains are visible when their behaviors are considered at the lineage level with full family tree analysis. An exactly solvable "divide-detach" stochastic model provides a unified understanding and classification of surface colonization strategies. Results suggest two complementary but distinct strategies, illustrated by PAO1 Wsp-based and PA14 Pil-Chp-based surface sensing mechanisms, which differ in division and detachment behaviors and are roughly analogous to "immediate-" vs "deferred-gratification" in a prototypical cognitive-affective processing system.

Chapter 2

Methods

Contents

In this Chapter, we briefly recall some known models, results and methods in stochastic dynamics used during our work. Markov chains were first introduced by A. A. Markov in 1906 [63], and since then they have been applied to a huge number of situations in mathematics, physics, biology, financial analysis and computer science [64, 65, 66, 67, 68]. The mathematical foundations of stochastic processes goes back to A. Kolmogorov in 1931 [69], and pursued by W. Feller [70, 71], and J. L. Doob [72] and many others. Currently, in

modern natural sciences [73] as well as in statistical physics [74, 75, 76], stochastic processes play an indispensable role.

In the following, the necessary theoretical background for the derivation of the Master, Langevin and Fokker-Planck equations will be introduced. Following this fundamental theoretical framework, the specific model used in this thesis will be presented. Finally, a numerical integration scheme of the Langevin equations will be presented.

2.1 Random Walks

Let $X_1, X_2 \ldots X_t, \ldots$ be a sequence of independent identical distributed random variables, $X_t = +1$ with probability $1/2$ and $X_t = -1$ with probability $1/2$. We can imagine the result of a fair coin that is tossed repeatedly. The index t indicates (discrete) time and such sequence is called a discrete-time stochastic process[1]. It has mean $\mathbf{E}(X_t) = 0$ and variance $\mathbf{Var}(X_t) = 1$. For convenience, we define $S_0 = 0$ such that for each positive t

$$S_t = X_t + \cdots + X_1 \,. \tag{2.1}$$

It results that for each t, $\mathbf{E}(S_t) = 0$ and $\mathbf{Var}(S_t) = t$. The sequence of random variables $S_0, S_1, \ldots S_t, \ldots, t \in \mathbb{Z}_+$ is a discrete-time stochastic process known as the simple symmetric random walk on $\mathbb{Z}$. Notice that this discrete-time process is a stationary Markov chain on the infinite countable state space $\mathbb{Z}$ with probability transition matrix T

$$T_{xy} = \begin{cases} 1/2 & \text{, if } y = x - 1 \\ 1/2 & \text{, if } y = x + 1 \\ 0 & \text{, otherwise.} \end{cases} \tag{2.2}$$

A simple random walk models a walker starting at zero on the number line and making a unit step to the left or to the right with independent and equal probability at each time step. Variants of this model include the asymmetric random walk made with the sums corresponding to $X_t = +1$ with probability p and $X_t = -1$ with probability $(1 - p)$ and the lazy random walk where $X_t = +1$, $X_t = 0$ or $X_t = -1$. Another class of simple random walks, symmetric or asymmetric are defined in a finite interval of integers $[0, k]$ with periodic, reflecting or absorbing boundary conditions. Notice that in this case the corresponding Markov chain has a finite number of states and the boundary conditions may be implemented in the first and last row of the stochastic transition matrix T. As for any Markov chain the random walk may have two dual readings. In the first one, we may devise

---

[1]The readers are referred to the Appendix A for a definition of stochastic process.

the random trajectory of a single walker, e.g. an active particle, that can only jump to neighboring sites of a lattice at each time step. Such trajectory is known as a sample path or realization of the process, see Fig. 2.1.
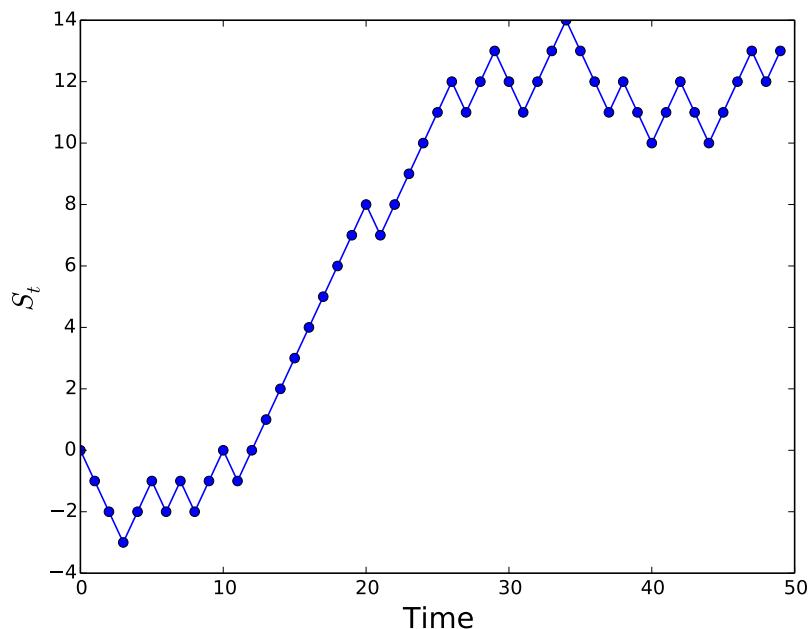
Figure 2.1 – A trajectory of a symmetric random walk, representing the time evolution of the random variable S_t.

In the second one, the dual notion consists of the time evolution of a distribution ν, for example a population of bacteria. In this case we fix, for each $x \in \mathbb{Z}$, the initial distribution $\nu(0)$, the fraction of the total population being in x at $t = 0$. The population distribution evolves then as

$$\nu(t) = \nu(0)T^t.$$

Under suitable conditions there is a unique time invariant distribution $\nu(\infty) = \nu(\infty)T$ and moreover for any initial distribution $\nu(0)$, $\lim_{t\to\infty} \nu(t) = \nu(\infty)$. To illustrate it, let us take the example of a Markov chain with four states, an initial distribution $\nu(0) = (1/4, 1/4, 1/4, 1/4)$ and transition matrix

$$T = \begin{pmatrix} 0.0 & 0.9 & 0.1 & 0.0 \\ 0.8 & 0.1 & 0.0 & 0.1 \\ 0.0 & 0.5 & 0.3 & 0.2 \\ 0.1 & 0.0 & 0.0 & 0.9 \end{pmatrix}. \tag{2.3}$$

The time evolution of the distribution ν is shown in Fig. 2.2. We remarque that for time higher than $t > 500$, the distribution does not change and we can find that $\nu(t > 500)$ satisfies $\nu(\infty) = \nu(\infty)T$.
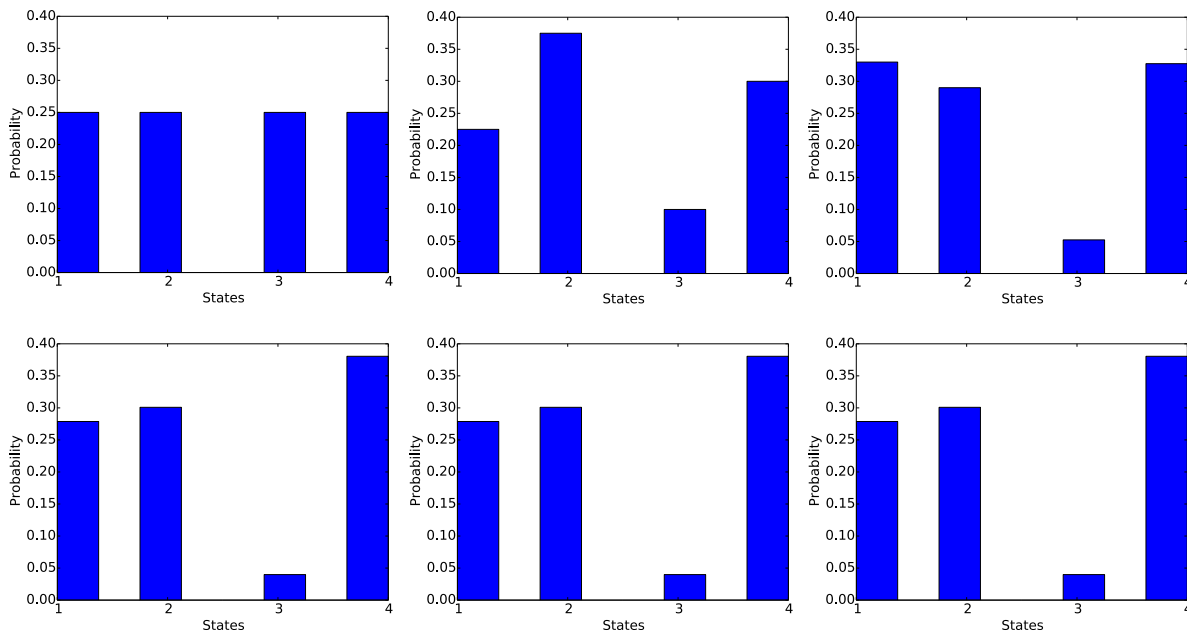
Figure 2.2 – Time evolution of the distribution ν computed with the transition matrix T, Eq. (2.3). Top: at time $t = 0, 1, 2$ (left to right). Bottom: at time $t = 500, 503$. The stationary distribution is shown at the bottom right.

Notice that in case of a chain with infinite number of states as the random walk on $\mathbb{Z}$ or $\mathbb{N}$ a distance in the set of the distributions is needed, the total variation distance, to properly define the limit. Moreover, in this case, the invariant distribution may not be normalizable. Under the invariant distribution, for any time step, the total input of the distribution arriving in a state is equal to the total output leaving the state. A more restrictive property verified by some specific Markov chains, the so-called detailed balance condition, tells that for each pair of connected states the invariant distribution moves as much in one direction as in the other at each time step. This condition reads

$$\nu_x T_{xy} = \nu_y T_{yx} , \tag{2.4}$$

for all pair of states and in fact implies the time invariance of ν. It can be interpreted as a time reversibility of the chain. Notice that a slight tailoring of this formula may be used to define a distribution flux per time step from any subset A of states to any other subset B, namely $\sum_{x \in A} \sum_{y \in B} \nu_x T_{xy}$. This flux stands for the fraction of the population moving from A

to B in one time step. For the invariant distribution this migration should be compensate by an equal incoming flux to A, not necessarily from B except if B is the complement of A.

2.1.1 Two useful Markov chains
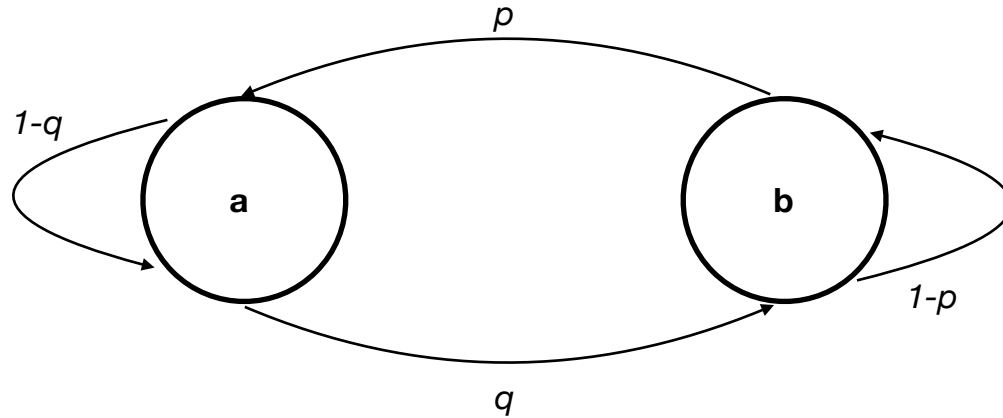
Figure 2.3 – Schematic representation of a two-states Markov chain.

The two-states model. Let us consider a Markov chain of two-states, $S = \{a, b\}$, see Fig. 2.3. The transition matrix has the form

$$T = \begin{pmatrix} 1 - q & q \\ p & 1 - p \end{pmatrix},$$

with $\sum_j T_{ij} = 1$, $\forall i$. The invariant distribution $\nu = (n_1, n_2)$ should satisfy

$$\nu = \nu T.$$

By using $1 = n_1 + n_2$, elementary computations yield to

$$n_1 = \frac{p}{p + q} \text{ and } n_2 = \frac{q}{p + q}.$$

The system is said to be at the equilibrium if it satisfies the detailed balance

$$\nu_i T_{ij} = \nu_j T_{ji}.$$

Because we only have two states

$$T_{12} = \frac{\nu_2}{\nu_1} T_{21} = q.$$

For any values of p and q the system satisfies the detailed balance and the system is said to be at the equilibrium.
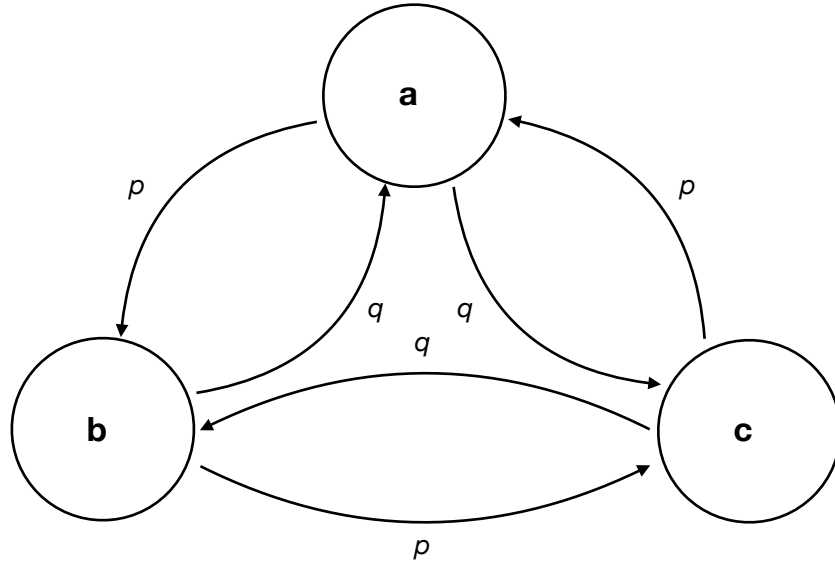
Figure 2.4 – Schematic representation of a three-states Markov chain.

The three-states model   Let us consider a Markov chain of three-states, $S = \{a, b, c\}$, Fig. 2.3. The transition matrix has the form

$$T = \begin{pmatrix} 0 & p & q \\ q & 0 & p \\ p & q & 0 \end{pmatrix} \, ,$$

with $\sum_j T_{ij} = 1$, $\forall i$. The invariant distribution $\nu = (n_1, n_2, n_3)$ should satisfy

$$\nu = \nu T \, .$$

By using $1 = n_1 + n_2 + n_3$, elementary computations yield to

$$n_1 = n_2 = n_3 = \frac{1}{3} \, .$$

The system is said to be at the equilibrium if it satisfies the detailed balance

$$\nu_i T_{ij} = \nu_j T_{ji} \, .$$

If only one of the three relations is not satisfied, the system does not satisfied the detailed. Because $n_1 = n_2 = n_3$, the detailed balance reads

$$T_{ij} = T_{ji} \, .$$

The only possibility to satisfy the detailed balance is $p = q$. Only in this situation, the system is said to be at the equilibrium, otherwise when $p \neq q$, the system is said to be out of equilibrium. The three states model is a special case of a random walk $S = \{0, 1, 2..., N\}$ with periodic boundary condition, for which $N = 2$. In the introduction, we motivated the difference between 'passive' (equilibrium) and 'active' (out of equilibrium) particle by using a random walk $S = \{0, 1, 2..., N\}$ with periodic boundary condition.

2.2 Jump Markov processes

We can use the continuous Markov chains or jump Markov process to represent population dynamics, epidemics, queueing models etc. In the jump Markov process, the time evolution is described by exponentially distributed holding times (to stay in one state before jumping to another) in each state while the succession of states visited is defined by a Markov chain.

More specifically, in order to define the time duration between two consecutive events, let us consider a discrete-time Markov chain $E_k, k \in \mathbb{N}$ on a countable state space S with transition matrix T. For convenience we suppose that $T_{nn} = 0$ for $\forall n \in S$. Furthermore for each $n \in S$, we define an exponential distributed random variable τ_n (a clock) with parameter λ_n

$$\mathbb{P}[\tau_n > t] = \exp(-\lambda_n t), \tag{2.5}$$

with $\mathbf{E}(\tau_n) = \frac{1}{\lambda_n}$ and $\mathbf{Var}(\tau) = \frac{1}{\lambda_n^2}$. Recall that the counting process associated to an exponential random variable is a homogeneous Poisson process. A continuous time stochastic process X_t, called Jump Markov process with state space S associated to the embedded Markov chain $E_k, k \in \mathbb{N}$ with transition matrix T and the collection of independent random variables τ_n is defined as follow:

Starting in an initial state X_0 suppose that the process is in $X_t = n$ at time t. At a random time τ_n (when the clock n expires) the chain moves to a new state m with probability T_{nm}. This process is a Markov process and, under suitable conditions on the embedded matrix T and on the collection of rates λ_n, the realizations of this process may always to be taken as step functions, see Fig. 2.5, continuous from the right such that the process stays for a random strictly positive time in each visited state, i.e for almost all realization of the process and all $t \geq 0$ there exists a $\delta(t) > 0$ depending of the realization such that $X_t + \tau = X_t$ for $\tau \in [0, \delta(t)[$, for an example see [77].

It is worth to notice that, from this point of view, a Markov jump process is completely defined by a stochastic matrix T with zero diagonal and the set of positive (time) rates

$\{\lambda_n\}, n \in S$. The exponential distributions with rates λ_n define the clocks of the events in the process.
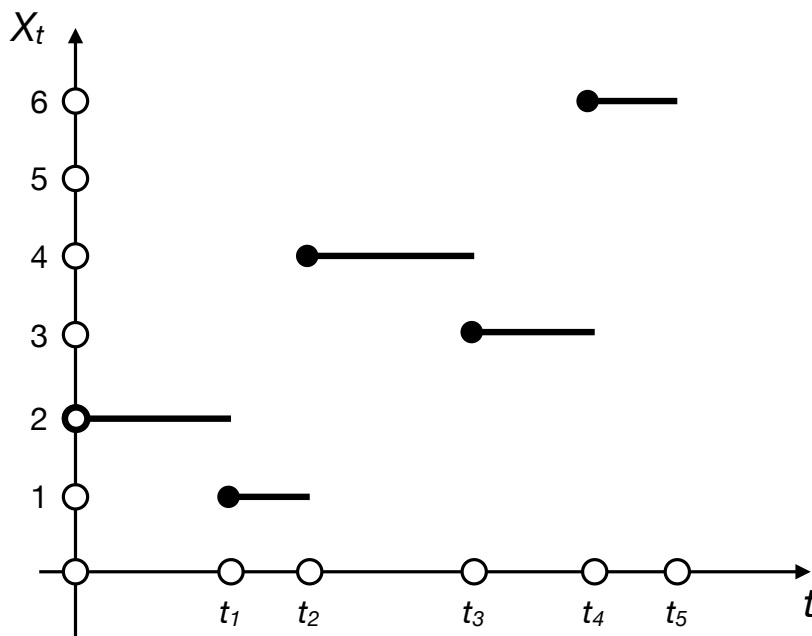
Figure 2.5 – Step function realization. Example of a trajectory of a jump Markov process with state space S associated to the embedded Markov Chain $E_k, k \in \mathbb{N}$.

Example 1 ***Uniform Markov jump process*** *with intensity $\lambda > 0$ refers to the case where all the time rates $\{\lambda_n\}$ are equal to λ.*

Example 2 ***Birth-death processes****. One important and fairly tractable example of Markov Jump process is a birth-death process. It combines some properties of a random walk on the non-negative integers $\mathbb{Z}_+$ with reflection on zero and continuous transition time. It aims to model the evolution of a population whose number of individuals changes at random times by one unit, either increasing by one, a birth, or decreasing by one, a death.*

Back to the general Markov jump process, it is well known that a jump Markov process can be characterized by the transition probability

$$P_{nm}(t) = \mathbb{P}[X(t + u) = m | X(u) = n],$$

and is independent for $u > 0$. Indeed, $\mathbb{P}[X(t) = m | X(0) = n]$ is a function of t and describes a time homogeneous Markov process[2].

---

[2]$\mathbb{P}[X(t + u) = m | X(u) = n] = \mathbb{P}[X(t) = m | X(0) = n]$.

By specifying all transition matrices $P_{nm}(t)$ in $0 < t < t_0$ for some $t_0 > 0$, all other transition probabilities can be constructed from these. These transition probability matrices should satisfy the Chapman-Kolmogorov equation

$$P_{nm}(t + s) = \sum_{k=0}^{\infty} P_{nk}(t) P_{km}(s) \, . \tag{2.6}$$

This equation can be rewritten in matrix notation by the following so-called semigroup property

$$\mathbf{P}(t + s) = \mathbf{P}(t)\mathbf{P}(s) \, . \tag{2.7}$$

In the matrix notation, we now synthesize the situation from this point of view:

1. $\lim_{t \to 0} \mathbf{P}(t) = \mathbb{I}$

2. The **infinitesimal generator Q** is defined as

$$\mathbf{Q} = \lim_{t \to 0} \frac{\mathbf{P}(t) - \mathbf{P}(0)}{t} = \lim_{t \to 0} \frac{\mathbf{P}(t) - \mathbb{I}}{t} \, , \tag{2.8}$$

   or in components

$$Q_{nm} = \lim_{t \to 0} \frac{P_{nm}(t) - P_{nm}(0)}{t}, \, \forall n, m \text{ and } Q_{nm} = \lim_{t \to 0} \frac{P_{nm}(t)}{t}, \, n \neq m \, . \tag{2.9}$$

3. $\mathbf{Q}$ is a matrix with elements Q_{nm} such that $Q_{nn} \leq 0 \leq Q_{nm}$ and the sum of the elements of any row is zero. Moreover $Q_{nn} = 0$ if and only if n is absorbing.

4. $\mathbf{P} = e^{(t\mathbf{Q})}$

$$\mathbf{P}(t) = \sum_{k=0}^{\infty} \frac{(t\mathbf{Q})^k}{k!} \, . \tag{2.10}$$

5. Under conditions allowing the existence of the product $\mathbf{QP}$ or $\mathbf{PQ}$ the following differential equations apply

$$\frac{d\mathbf{P}(t)}{dt} = \mathbf{QP}(t), \, t \geq 0 \, , \tag{2.11}$$

   known as the Kolmogorov backward equation and

$$\frac{d\mathbf{P}(t)}{dt} = \mathbf{P}(t)\mathbf{Q}, \, t \geq 0 \, , \tag{2.12}$$

   known as the Kolmogorov forward equation

According to Eq. (2.6), giving an initial distribution $\nu(0)$ on the state space S we have, at time t

$$\nu(t) = \nu(0)T^t. \tag{2.13}$$

A measure ν on S such that $\nu = \nu T$ for all $t \geq 0$ is called an invariant measure. If this measure is such that $\nu(S) < \infty$ the normalized corresponding measure is called by some authors stationary distribution. Instead to simplify we call it distribution even in the non normalizable case. Given an embedded Markov chain with transition matrix T and a collection of time rates $\{\lambda_n \geq 0\}$, $n \in S$ defining a jump Markov process, the corresponding infinitesimal generator $\mathbf{Q}$ reads

$$Q_{nm} = \begin{cases} -\lambda_n & , \text{if } n = m \\ \lambda_n T_{nm} & , \text{if } n \neq m \end{cases}, \tag{2.14}$$

Conversely given the infinitesimal generator $\mathbf{Q}$ of a jump Markov process the transition matrix T and the time rates $\{\lambda_n \geq 0\}$, $n \in S$ are known:

$$T_{nm} = \begin{cases} 0 & , \text{if } n = m \\ -(Q_{nn})^{-1}Q_{nm} & , \text{if } n \neq m \end{cases}, \tag{2.15}$$

and

$$\lambda_n = -Q_{nn}. \tag{2.16}$$

From the Chapman-Kolmogorov equation, it is possible to derive the Master equation. We can rewrite Eq. (2.6) as

$$P_{nm}(t+h) - P_{nm}(t) = \sum_{k=0}^{+\infty} P_{nk}(t)P_{km}(h) - P_{nm}(t)$$
$$= \sum_{k \neq n}^{+\infty} P_{nk}(t+h)P_{km}(h) + [P_{nn}(h) - 1] P_{nm}(t).$$

By taking the limit when $h \to 0$, we obtain

$$\lim_{h \to 0} \frac{P_{nm}(t+h) - P_{nm}(t)}{h} = \lim_{h \to 0} \frac{1}{h} \left[\sum_{k \neq n}^{+\infty} P_{nk}(t)P_{km}(h) + [P_{nn}(h) - 1] P_{nm}(t) \right].$$

By identifying $P_{nn}(h) - 1 = -\sum_{k \neq n}^{+\infty} P_{kn}(h)$ and by rewriting $\lim_{h \to 0} P_{nk}(h)/h = Q_{nk}$, we obtained the Master equation

$$\frac{d}{dt}P_{nm}(t) = \sum_{k \neq n}^{+\infty} [Q_{nk}P_{km}(t) - Q_{kn}P_{nm}(t)]. \tag{2.17}$$

Furthermore, by knowing the relation between the transition probability P and the probability distribution ν

$$\nu_n(t) = \sum_m P_{nm}^t \nu_m(0) \,,$$

we can rewrite the Master equation, Eq. (2.17), with the probability distribution

$$\frac{d}{dt}\nu_n = \sum_{k \neq n}^{+\infty} [Q_{nk}\nu_k - Q_{kn}\nu_n] \,. \tag{2.18}$$

2.2.1 'Birth and death' process: Bacterial population

Experimentally, we describe the successive bacteria generations in terms of family trees. A family tree represents all the successive generations of a mother cell, also called lineage. The time $t = 0$ is given when a bacterium lands onto a surface and starts to divide. We describe its lineage with a family tree as shown in Fig. 2.6. At any given time t, we can count/measure the number of bacteria in the system (family tree).
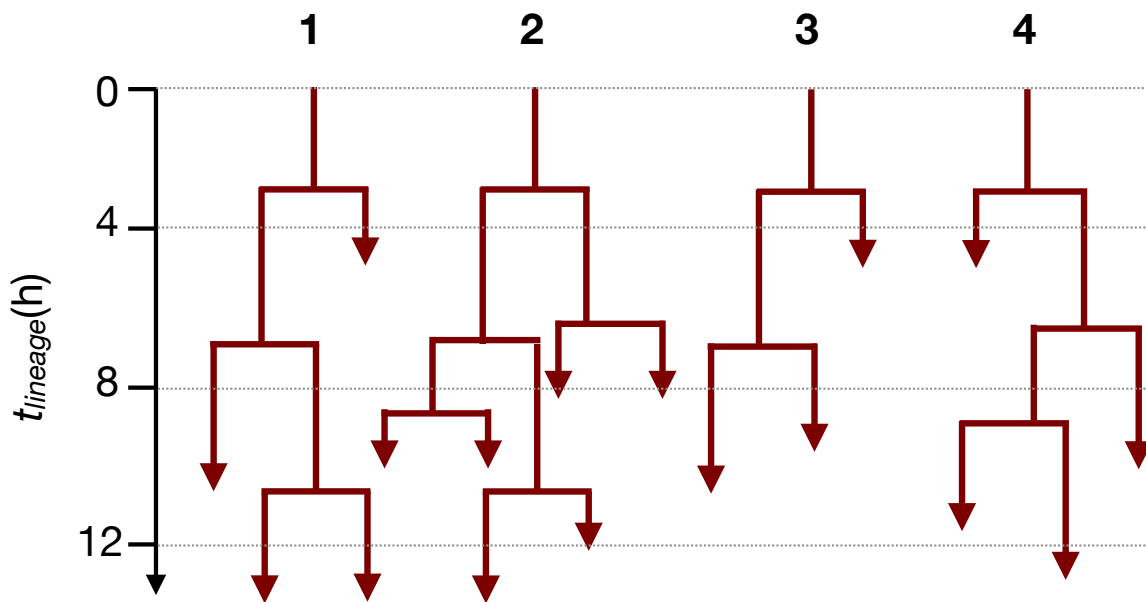
Figure 2.6 – Example of family trees. Each family start at $t_{\text{lineage}} = 0$ h when the founder cell attaches to the surface.

We can imagine the experimental situation described in Fig. 2.6 as a process with 'division' or 'detachment' at random time. Moreover, at any given time t, we count the number of

bacteria X_t in the system. Graphically, in Fig. 2.6, by drawing a straight horizontal line at a given time and counting the number of intersections between this line and the family tree, gives the number of bacteria in the system. For example, at $t = 4$, we have two intersections, we have two bacteria in the system. A family tree represents one independent experiment, by repeating the experiments N times, meaning having N independent family trees, we can build the probability distribution of the number of bacteria in a family tree.
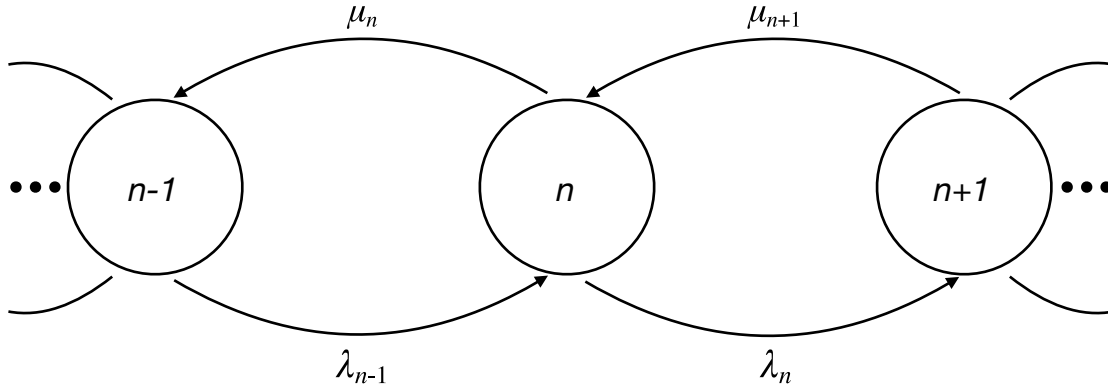
Figure 2.7 – 'Birth and death' process. The state $n \in \mathbb{N}$ represents the number of bacteria in a family tree. The states $n + 1$ and $n - 1$ are the neighboring states of n. Only transitions between neighboring states are possible. The number of bacteria (or population size) increases by $+1$ with a division rate λ_n and decreases by -1 with a detachment rate μ_n.

The question is now how to transcript this picture in terms of a model. We can describe the increase or decrease of the population size by ± 1 at each event with a 'birth and death' process, see Fig. 2.7. The assumption consist of considering the duration between two consecutive events as exponentially distributed. The 'birth and death' process is a special case of jump Markov process, in which the states can represent the current population size and the transitions are limited to birth and death. When a birth occurs, the process goes from state n to state $n + 1$, and when a death occurs, the process goes from state n to state $n - 1$. Moreover, this process is characterized by the birth rate $\{\lambda_n\}_{n=0,..,\infty}$ and death rate $\{\mu_n\}_{n=0,..,\infty}$, which depend on the state n of the system. The population increases by one if the birth occurs prior to death and decreases by one otherwise. These dynamics are analogous to a random walk with the difference that the transition occur at random times exponentially distributed. A jump Markov process is characterized by the transition probabilities $P_{nm}(t)$, which satisfy the forward and backward Kolmogorov equation.

Let us use the Kolmogorov backward equation

$$\frac{d}{dt}P_{nm}(t) = Q_{nk}P_{km}(t)\,,$$

where P is the transition probability matrix, and Q is the infinitesimal generator. From the Chapman-Kolmogorov equation

$$P_{nm}(t+h) = \sum_{k=0}^{\infty} P_{nk}(t+h)P_{km}(t) \,,$$

and by definition of the time derivative

$$\frac{d}{dt}P_{nm}(t) = \lim_{h\to 0} \frac{P_{nm}(t+h) - P_{nm}(t)}{h} \,,$$

the previous equation can be rewritten as

$$\frac{d}{dt}P_{nm}(t) = \lim_{h\to 0}\frac{1}{h}\left[\sum_{k=0}^{\infty} P_{nk}(t+h)P_{km}(t)) - P_{nm}(t)\right] \,. \tag{2.19}$$

Because $m \neq n-1, n, n+1$, we can rewrite the sum inside the Chapman-Kolmogorov equation as

$$\sum_{k=0}^{\infty} P_{nk}(t+h)P_{km}(t) = P_{nn-1}(t+h)P_{n-1m}(t) + P_{nn}(t+h)P_{nm}(t) + P_{nn+1}(t+h)P_{n+1m}(t)$$

$$+ \sum_{k\neq m}^{\infty} P_{nk}(t+h)P_{km}(t) \,.$$

If all cases are taking into account $\sum_k P_{nk}(t) = 1$, however $m \neq n-1, n, n+1$ and $\sum_k P_{nk}(t) = 1 - [P_{nn-1}(t) + P_{nn}(t) + P_{nn+1}(t)]$. Only neighboring transitions are possible, so every other elements of the corresponding line are zero. The sum should be equal to 1 and therefore

$$\sum_k P_{nk}(t) = 1 - [P_{nn-1}(t) + P_{nn}(t) + P_{nn+1}(t)]$$

$$= 1 - 1$$

$$= 0 \,,$$

and this lead to

$$\sum_{k\neq m}^{\infty} P_{nk}(t+h)P_{km}(t) = 0 \,.$$

Equation (2.19) reads

$$\frac{d}{dt}P_{nm}(t) = \lim_{h\to 0}\frac{1}{h}\left[P_{nn-1}(t+h)P_{n-1m}(t) + P_{nn}(t+h)P_{nm}(t) + P_{nn+1}(t+h)P_{n+1m}(t) - P_{nm}(t)\right] \,.$$

Moreover, $P_{nn-1}(t+h) = \mu$, $P_{nn+1}(t+h) = \lambda$ and $P_{nn}(t+h) = 0 = 1 - (\mu + \lambda)$. Therefore, the previous equation becomes

$$\frac{d}{dt}P_{nm}(t) = \mu P_{n-1m}(t) + (1 - (\mu + \lambda))P_{nm}(t) + \lambda P_{n+1m}(t) - P_{nm(t)}.$$

Finally, we obtain the Kolmogorov backward equation, so-called Master equation, for our process and it is given by

$$\frac{d}{dt}P_{nm}(t) = \mu P_{n-1m}(t) - (\mu + \lambda)P_{nm}(t) + \lambda P_{n+1m}(t),$$

or

$$\frac{dP_n}{dt} = \lambda P_{n+1} - (\mu + \lambda)P_n + \lambda(n - 1)P_{n-1}.$$

By using the Kolmogorov forward equation, we obtain a similar equation and the Master equation reads

$$\frac{dP_n}{dt} = \mu P_{n+1} - (\lambda + \mu)P_n + \lambda P_{n-1},$$

and when $\mu = \mu n$ and $\lambda = \lambda n$, the previous equation reads

$$\frac{dP_n}{dt} = \mu(n + 1)P_{n+1} - (\lambda + \mu)nP_n + \lambda(n - 1)P_{n-1}. \tag{2.20}$$

The solution of Eq. (2.20) can be found by using the so-called generating function $G(z, t) = \sum_{n=0}^{+\infty} z^n P_n$. By plugging the generating function into Eq. (2.20), we find

$$\partial_t G(z, t) = -(\lambda + \mu)\sum_n nz^n P_n(t) + \mu \sum_n (n + 1)z^n P_{n+1}(t) + \lambda \sum_n (n - 1)z^n P_{n-1}(t)$$

$$= \mu \left[\sum_n (n + 1)z^n P_{n+1}(t) - \sum_n nz^n P_n(t)\right] + \lambda \left[\sum_n (n - 1)z^n P_{n-1}(t) - \sum_n nz^n P_n(t)\right].$$

By using $z^n P_{n-1} = zz^{n-1}P_{n-1}$ and $z^n P_{n+1} = \frac{1}{z}z^{n+1}P_{n+1}$, then the previous reads

$$\partial_t G(z, t) = \mu \left[\sum_n (n + 1)\frac{1}{z}z^{n+1}P_{n+1}(t) - \sum_n nz^n P_n(t)\right]$$

$$+ \lambda \left[\sum_n (n - 1)zz^{n-1}P_{n-1}(t) - \sum_n nz^n P_n(t)\right].$$

By rewriting $n' = n + 1$ and $n'' = n - 1$

$$\partial_t G(z,t) = \mu \left[\frac{1}{z} \sum_{n'} n' z^{n'} P_{n'}(t) - \sum_n n z^n P_n(t) \right] + \lambda \left[z \sum_{n''} n'' z^{n''} P_{n''}(t) - \sum_n n z^n P_n(t) \right]$$

$$= \left[\mu(\frac{1}{z} - 1) + \lambda(z - 1) \right] \partial_z G(z,t),$$

we finally obtain

$$\partial_t G(z,t) = (1-z)(\mu - \lambda z)\partial_z G(z,t). \tag{2.21}$$

Equation (2.21) can be rewritten in a Ricatti's form [78] which reads

$$\frac{dz}{dt} = P + Qz + Rz^2,$$

where $P = -\mu$, $Q = (\lambda + \mu)$ and $R = -\lambda$. A particular solution is given by Y, and the previous equation can be solved by quadrature $z(t) = x(t) + Y(t)$

$$\frac{dx}{dt} = [P + 2YQ]x + Qz^2.$$

A change of variable, $u = \frac{1}{x} = \frac{1}{z-Y}$, yield to

$$\frac{du}{dt} = [P + 2YQ]u + Q.$$

Therefore, the solution of the Ricatti's equation [79] is a homographic function of an arbitrary constant C

$$u = Ce^{\int [P+2YQ]dt} + U,$$

where U is a particular solution. We can rewrite u as

$$u = C\psi + \phi,$$

and the solution for z reads

$$z = Y + \frac{1}{C\psi + \phi} = \frac{C\psi Y + \phi Y}{C\psi + \phi}$$

$$= \frac{C\alpha + \beta}{C\gamma + \delta}.$$

By using the Palm's formulae [80, 81, 82], it is possible to express P_0 and P_n as a function of η_t and ξ_t, two unknown functions, which read

$$P_0 = \xi_t, \ P_n = (1 - P_0)(1 - \eta_t)\eta_t^{n-1} \,.$$

We rewrite the previous equation as

$$
\begin{aligned}
(1 - \xi_t)(1 - \eta_t)\eta_t^{n-1} &= (1 - \eta_t - \xi_t + \eta_t\xi_t) \\
&= (1 - \eta_t - \xi_t)\eta_t^{n-1} + \eta_t^n \xi_t \,.
\end{aligned}
$$

By means of geometric series $\sum\limits_{n=0}^{+\infty} aq^n = \frac{a}{1-q}$ and $\sum\limits_{n=0}^{+\infty} (aq)^n = \frac{1}{1-aq}$ the generating function $G(z, t)$ reads

$$G(z, t) = \sum_{n=0}^{+\infty} z^n P_n(t) = \sum_{n=0}^{+\infty} (1 - \eta_t - \xi_t)\eta_t^{n-1} z^n + \sum_{n=0}^{+\infty} \eta_t^n \xi_t z^n \,,$$

where $\sum\limits_{n=0}^{+\infty} \eta_t^n \xi_t z^n = \frac{\xi_t}{1-\eta_t z}$ and $\sum\limits_{n=0}^{+\infty} \eta_t^{n-1} \xi_t z^n = \sum\limits_{n=-1}^{+\infty} \eta_t^n \xi_t z^{n+1}$. Moreover,

$$\sum_{n=0}^{+\infty} z^n P_n(t) = (1 - \eta_t - \xi_t)z \sum_{n=-1}^{+\infty} \eta_t^n z^n + \frac{\xi_t}{1 - \eta_t z} \,.$$

We can express the generating function in terms of ξ_t and η_t

$$G(z, t) = \frac{\xi_t + (1 - \xi_t - \eta_t)z}{1 - \eta_t z} \,.$$

By plugging back this equation into Eq. (2.21), and after some computations (see Appendix B), ξ_t and η_t read

$$\xi_t = 1 - \frac{e^{-\rho}}{W}, \ \eta_t = 1 - \frac{1}{W} \,.$$

Finally, the solution for $P_0(t)$ and $P_n(t)$ when the coefficients μ and λ are time dependent reads

$$P_n(t) = \frac{e^{-\rho}}{W^2} \left(1 - \frac{1}{W}\right)^{n-1}, \ P_0(t) = 1 - \frac{e^{-\rho}}{W} \,, \tag{2.22}$$

where

$$W = e^{-\rho(t)} \left(1 + \int_0^t \mu(\tau)e^{\rho(\tau)}d\tau\right) \,, \tag{2.23}$$

and

$$\rho(t) = \int_0^t (\mu(\tau) - \lambda(\tau))d\tau \,.$$

It is possible to find the probability distribution $P_n(t)$ and $P_0(t)$, when the rates are time independent, by using either the moment generating function, as shown in Appendix B or by using directly the first and second moments [67]. In order to compare the model with the experimental results we can use the moments defined as

$$\langle n(t)^k \rangle = \sum_{n=0}^{\infty} n^k P_n \, .$$

However, from the master equation, we can find

$$\frac{d}{dt}\langle n(t)^k \rangle = \sum_{n=0}^{\infty} n^k \frac{d}{dt} P_n$$

$$= \sum_{n=0}^{\infty} \left[((n+1)^k - n^k)\lambda(t) - (n^k - (n-1)^k)\mu(t) \right] n P_n \, .$$

The first moment reads

$$\frac{d\langle n \rangle}{dt} = \sum_n n \frac{dP_n}{dt}$$

$$= -(\lambda + \mu) \sum_n n^2 P_n + \mu \sum_n (n^2 + n) P_{n+1} + \lambda \sum_n (n^2 - n) P_{n-1}$$

$$= \lambda \sum_{n=1} \left[(n-1)^2 P_{n-1} + (n-1) P_{n-1} \right] + \mu \sum_{n=0} \left[(n+1)^2 P_{n+1} - (n+1) P_{n+1} \right]$$

$$- (\lambda + \mu) \sum_{n=0} n^2 P_n$$

$$\iff \frac{d\langle n \rangle}{dt} = \lambda \left[\langle n^2 \rangle + \langle n \rangle \right] + \mu \left[\langle n^2 \rangle - \langle n \rangle \right] - (\lambda + \mu)\langle n^2 \rangle$$

$$\implies \frac{d\langle n \rangle}{dt} = (\lambda - \mu)\langle n \rangle$$

$$\langle n \rangle = n(0)e^{-\rho} = e^{-\rho}, \ n(0) = 1 \, ,$$

where $\rho = \int_0^t (\mu - \lambda) dt$. The first moment reads

$$\langle n \rangle = \exp\left(- \int_0^t (\mu - \lambda) dt\right) . \tag{2.24}$$

The second moment reads

$$\frac{d}{dt}\langle n^2 \rangle = \sum_{n=0}^{\infty}[((n+1)^2 - n^2)\lambda - (n^2 - (n-1)^2)\mu]nP_n(t)$$
$$= \langle n \rangle(\lambda + \mu) + 2\langle n^2 \rangle(\lambda - \mu)\,.$$

Elementary computations yield

$$\langle n^2 \rangle = e^{2\int(\lambda-\mu)d\tau}\left[1 + \int(\lambda+\mu)e^{-\int_0^t(\mu-\lambda)d\tau}e^{2\int(\lambda-\mu)d\tau}dt\right]\,. \qquad (2.25)$$

The probability distribution with constant rates is plotted for different times in Fig. 2.8, for the case where $\lambda > \mu$. In this case, the probability distribution makes a transition from an initial exponential form to a flat form. The first form shows an exponential decay of the population, while the second one shows a constant size population. Figure 2.9 shows results
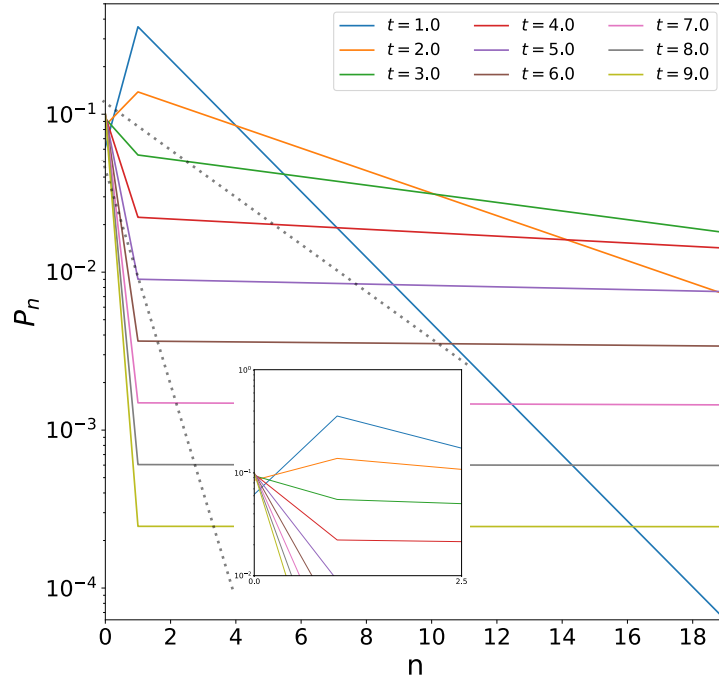
Figure 2.8 – The growth-dominated distribution, $\lambda = 1.0 > \mu = 0.1$ where both rates are constant. Dependence of the probability distribution P_n, in semi-log scale, of the size population at different times. We observe two slopes for the probability distribution: one flat, i.e at a time t the population is constant; the other one represent the exponential decay of the population.

when a time dependence in the death rate was added. When under some parameters we can recover the case where $\lambda > \mu$ and we recovered similar results obtained for constant rates.

In the Chapter 3.3 a Master equation with time-dependent rates will be used to describe the time evolution of the number of bacteria into a system to study different strategies of the early stage biofilm for different bacteria strains.

2.3 Stochastic differential equations

In the previous sections, we described processes with discrete state and time, or discrete state and continuous time. Now, we will look at processes continuous in state and time. In a small time interval such a process can only undergo a small displacement or change of state. Therefore, the realizations of such processes are given by continuous functions. A classical example of such processes is given by the motion of micro-sized particles suspended in a fluid, under the rapid, successive, random collision with neighboring fluid molecules. This motion is a realization of a stochastic process in continuous time with continuous state. This phenomenon is known as Brownian motion, first described experimentally by Robert Brown in 1827 [83] and then by Jean Perrin one hundred years ago [84]. A phenomenological description was proposed by Paul Langevin [85] and Norbert Wiener, in 1923, who gave a mathematical definition and developed a rigorous theory based on stochastic processes [86]. Markov processes are strongly connected to the theory of diffusion and the kinetic theory of matter, which describe the aggregate motion of collections of molecules. Therefore, Markov processes with continuous state are called diffusion processes. We can define the Brownian motion or Wiener process as a limit of a random walk. Let us subdivide a unit interval [0,1] into $N \in \mathbb{N}$ subintervals of equal length $\Delta t = 1/N$. In order to create continuous step intervals, we transform N into $\sqrt{N} \in \mathbb{R}$ [87]. The length between the subintervals becomes $\sqrt{\Delta t}$. We can imagine on this interval a sequence of random variable $\{X_N\}$ of probability distribution with a mean equal to 0 and a variance equal to Δt. It is possible from this sequence of random variable $\{X_N\}$ to create a random walk S_N

$$S_N = \frac{1}{\sqrt{N}} \sum_i X_i \,.$$

Its associated probability distribution has a mean equal to 0 and a variance equal to Δt. When the number of subintervals N goes to infinity the probability distribution associated to S_N converge to a normal distribution $N(0, \Delta t)$, by the central limit theorem. Finally, the random walk S_N is called a Wiener process.
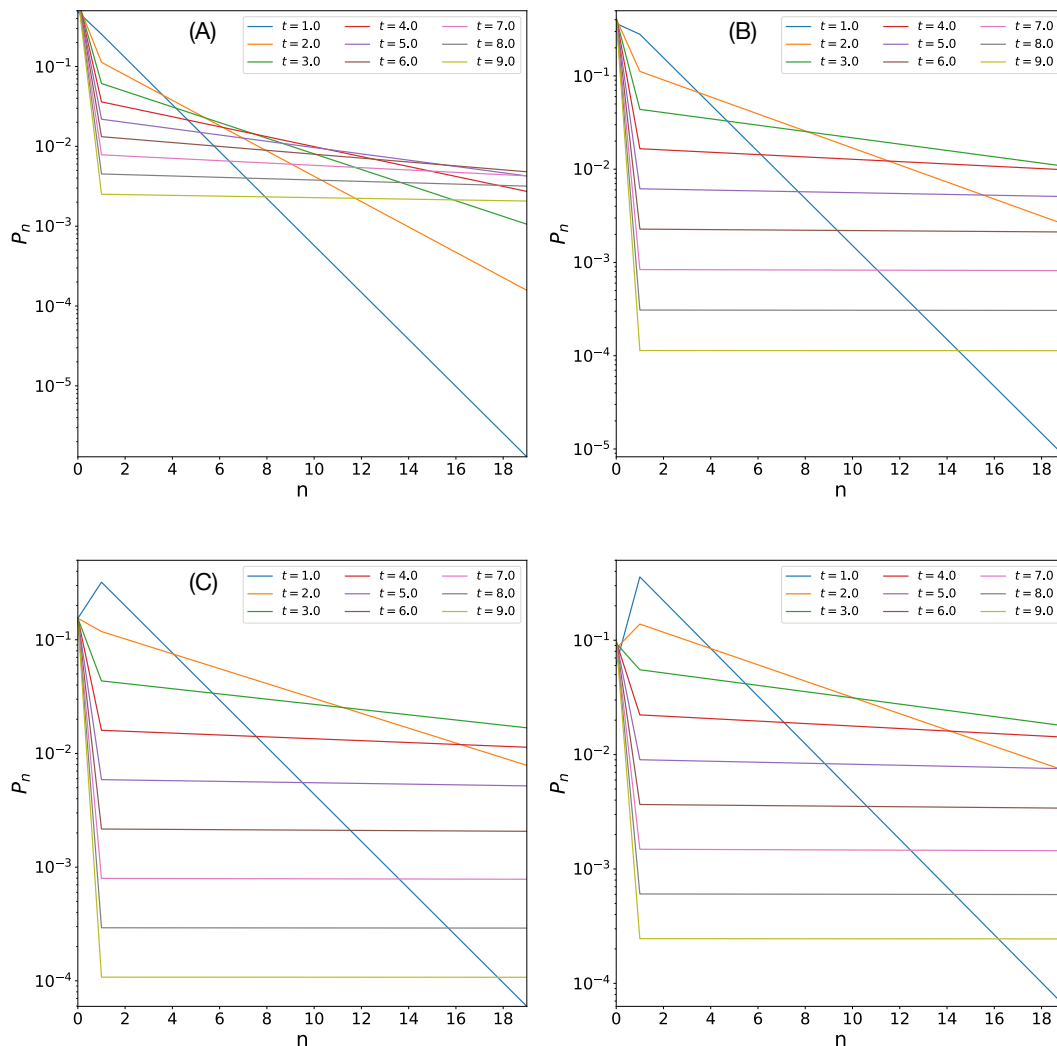
Figure 2.9 – The growth-dominated distribution - Exponential decay of the death rate. Dependence of the probability distribution P_n, in semi-log scale, of the size population at different times. The growth rate $\lambda = 1.0$ and the death rate $\mu = \exp(-ct)$, where $c = \{0.1, 1.0, 5.0\}$. (A) $c = 0.1$, (B) $c = 1.0$, (C) $c = 5.0$, and (D) Safety check: λ and μ are not time dependent. Figure (D) is identical to Fig. 2.8. We observe two slopes for the probability distribution: one flat, i.e at a time t the population is constant; the other one represent the exponential decay of the population.

We just saw that, from a Markov process, called random walk, it was possible to define a Wiener process. However, let us give a rigorous definition of it.

Definition 1 (Wiener process or Brownian motion) *There exist a probability distribution over the set of continuous functions* $B : \mathbb{R}^+ \to \mathbb{R}$ *such that:*

1. *Start from 0:* $\mathbb{P}(B(0) = 0) = 1$, $B(0) = 0$;

2. *Stationary:* $\forall \, 0 \leqslant s \leqslant t$: $B(t) - B(s) \sim N(0, t - s)$;

3. *Independent increment: If intervals* $[s_i, t_i]$ *and* $B(t_i) - B(s_i)$ *are independent.*

Its realizations are the Brownian trajectories. In the following, we will use $B = W$ and define $dW = \xi dt$, where ξ is a noise.

Before moving on to a mathematical description of the stochastic differential equations, let us start with an example. We can imagine an 'active' particle, e.g the alga *Chlamydomonas*, moving inside a tube in 1D. In order to find more light, the particle moves toward the surface, however due to gravity, the particle feels a force pushing it in the opposite direction of its motion. Moreover, due to its size, the particle is subject to random fluctuations due to the surrounding environment. It is possible to describe its dynamics by the following equation

$$dX_t = v_g dt + v_s dW_t, \ X_0 = 0 \,, \tag{2.26}$$

where v_g is the terminal velocity (effect of the gravity) and v_s the self-propulsion velocity. We now look at the time evolution of the particle's position given by the random variable X_t, while the surrounding fluctuations are described by a Wiener process W_t. When the particle has no activity, $v_s = 0$, the particle sediments due to the gravity, and when the activity of the particle is much larger than the effect of the gravity, $v_s \gg v_g$, the only external perturbations on the particle are random fluctuations. Because we consider the evolution of the random variable X_t, we can build its probability distribution. An easy way to get it, is by means of simulations. For different times t, one value of the 'activity', v_s, and a constant value of the terminal velocity, v_g, the probability distributions are shown in Fig. 2.10.

The distribution is shifted by a factor $v_g \Delta t$ and its variance increases as $v_s \sqrt{\Delta t}$. More precisely, by fixing v_g and varying v_s, we can obtain the mean and the variance, Fig. 2.11.

This example was used to give an intuition on the role of the factors v_g and v_s on the dynamics and the distribution. Now, let me give a more rigorous description of the stochastic differential equation.

(a) Distribution at time $t = 200 \times \Delta t$

(b) Standard deviation for a time $t = 600 \times \Delta t$

(c) Distribution at time $t = 800 \times \Delta t$

(d) Standard deviation for a time $t = 1000 \times \Delta t$
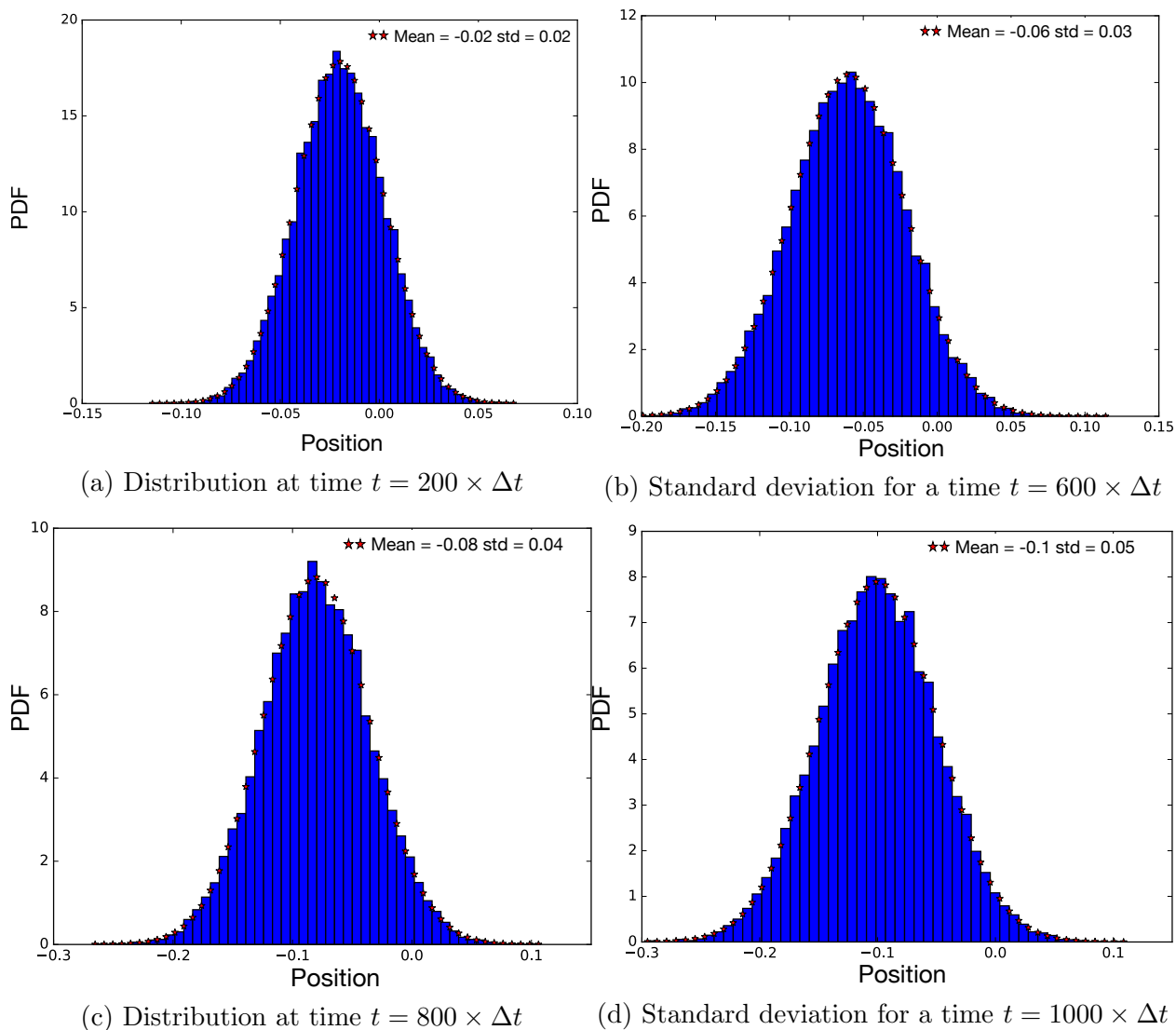
Figure 2.10 – Time evolution of the probability distribution. The mean distribution is shifted by a factor $v_g \Delta t$ and the variance increases by a factor $v_s \sqrt{\Delta t}$. For the simulations, the time step is given by $\Delta t = 10^{-5}$, the number of iterations is $N = 10^3$ and the initial condition is $X_0 = x = 0$.

Stochastic differential equation. We consider stochastic differential equations (SDEs) of the form

$$\frac{dX_t}{dt} = A(X_t, t) + C(X_t, t)\xi(t) \,, \tag{2.27}$$
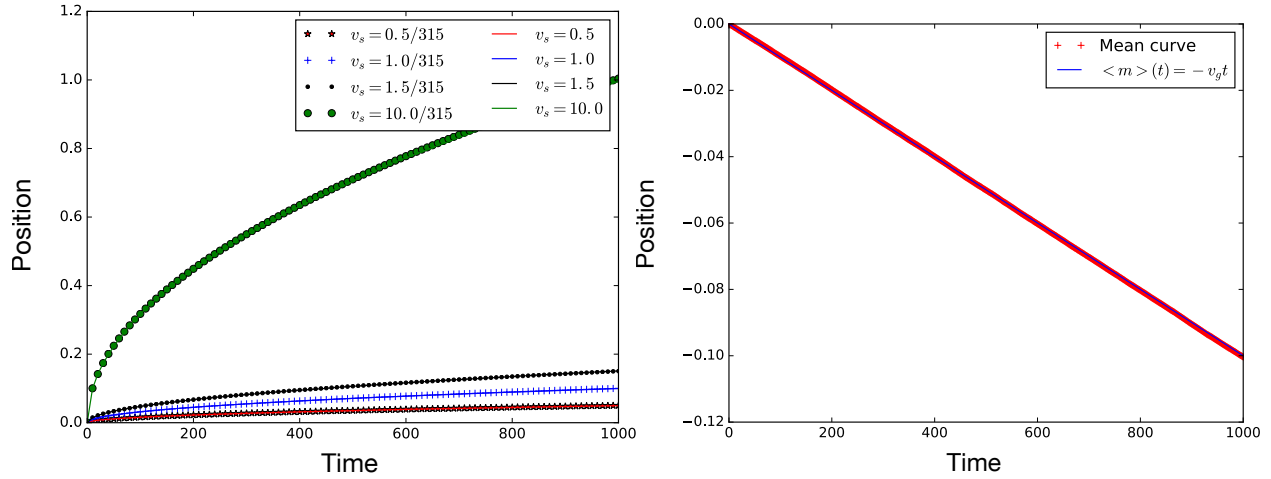
Figure 2.11 – Mean and standard deviation for different 'activity' v_s. The symbols are given by $\sqrt{\Delta t} \times v_s/315$ and the lines are given by the simulations; time step $\Delta t = 1 \times 10^{-5}$.

with initial condition $X(t = 0) = X_0$, and where $X_t \in \mathbb{R}^d$ is a stochastic process, $A :$ $[0, T] \times \mathbb{R}^d \to \mathbb{R}^d$, $C : [0, T] \times \mathbb{R}^d \to \mathbb{R}^d \times \mathbb{R}^m$ are the coefficients and $\xi(t)$ a noise.

If $\xi(t)$ is a white noise, then we can rewrite $\xi(t)$ as a Brownian motion in $\mathbb{R}^m$: $\xi(t) = \frac{dW}{dt}$. A white noise is a zero-mean Gaussian with variance $\langle \xi_i(t)\xi_j(s) \rangle = \delta_{ij}\delta(t - s)$. In the case of a white noise we rewrite Eq. (2.27) as

$$dX_t = A(X_t, t)dt + C(X_t, t)dW , \qquad (2.28)$$

and in terms of components, this equation reads

$$dX_i(t) = A_i(X_t, t)dt + \sum_{j=1}^{m} C_{ij}(X_t, t)dW_j, \qquad i = 1 \ldots, d .$$

The stochastic integration of Eq. (2.28) is given by

$$X_t = X_0 + \int_0^t A(X_t, t)dt + \int_0^t C(X_t, t)dW .$$

The difficulty is how to integrate the Brownian motion. We know that the Brownian motion is not differentiable and for this reason we cannot use the basic rules of calculus. Itô defined the rule of calculus for the Brownian motion (Itô's lemma) and used one of its properties the quadratic variation of the Brownian motion $(dW)^2 = dt$ [88, 87]. To evaluate the previous integral, two interpretations are commonly used in the literature: the Itô interpretation or the Stratonovich interpretation. Let start with the Itô interpretation. Firstly, we will

define the Itô's Lemma and secondly we will discuss the difference between additive and multiplicative noises.

Let $f(t, X)$ be a function depending on a Brownian motion. We want to differentiate the Brownian motion and by using a multivariable Taylor expansion, we obtain

$$
\begin{aligned}
f(t + \Delta t, X + \Delta X) = {} & f(t, X) + \partial_t f(t, X)\Delta t + \partial_X f(t, X)\Delta X \\
& + \frac{1}{2}[\partial_t^2 f(t, X)(\Delta t)^2 + 2\partial_t\partial_X f(t, X)\Delta t\Delta x + \partial_X^2 f(t, X)(\Delta X)^2] \\
& + o(\Delta t^2 + \Delta X^2) \,.
\end{aligned}
$$

The previous equation can be rewritten as

$$
\begin{aligned}
\Delta f(t, X) = {} & \partial_t f(t, X)\Delta t + \partial_X f(t, X)\Delta X \\
& + \frac{1}{2}[\partial_t^2 f(t, X)(\Delta t)^2 + 2\partial_t\partial_X f(t, X)\Delta t\Delta X + \partial_X^2 f(t, X)(\Delta X)^2] + o(\Delta t^2 + \Delta X^2) \,.
\end{aligned}
$$

Knowing that f depends of a Brownian motion, $f(t, X)$ reads $f(t, W)$ and by using $(dW)^2 = dt$ lead to

$$
df(t, W) = [\partial_t f(t, W) + \frac{1}{2}\partial_X^2 f(t, W)]dt + \partial_X f(t, W)dW \,,
$$

where the higher terms in dt are neglected.

Theorem 1 (Itô's lemma) . *Let $f(t, X)$ be a function of two variables, and let X_t be a stochastic process define by $dX_t = A(t)dt + C(t)dW$, where W is a Brownian motion. Then*

$$
df(t, X_t) = [\partial_t f(t, X_t) + A(t)\partial_X f(t, X_t) + \frac{1}{2}C^2(t)\partial_X^2 f(t, X_t)]dt + \partial_X f(t, X_t)dW \,. \quad (2.29)
$$

Additive and multiplicative noises.   Let a stochastic differential equation

$$
dX_t = A(X_t, t)dt + C(X_t, t)dW \,, \quad (2.30)
$$

- if C is a constant, then we say that in the Eq. (2.30) the noise is additive and corresponds to thermal fluctuations;

- if C depends on the state of the system, then we say that in the Eq. (2.30) the noise is multiplicative and can be seen as a control parameter.

A physical application for a multiplicative noise in three dimensions is the rotational diffusion of a rigid or linear molecule in an external potential [89].

After introducing the Itô interpretation, let us describe the difference between the Itô and Stratonovich interpretations.

Itô versus Stratonovich. Consider a stochastic integral of the form

$$I(t) = \int_0^t f(s)dW \, . \tag{2.31}$$

We want to compute this integral in terms of Riemann sum. The classical Riemann sum is defined by

$$\int_a^b f(t)dt = \lim_{n \to +\infty} \sum_{k=1}^n f(t_k)(x_{k+1} - x_k) \, , \tag{2.32}$$

where the subdivision is $\sigma = (a = x_0 < \cdots < x_n = b)$ and $t_k \in [x_{k-1}, x_k]$.
A way to evaluate a point taken in an interval $[0, T]$ for the integration is to chose: $\tau_k = (1 - \lambda)t_k + \lambda t_{k+1}$, $k = 0, \ldots, K - 1$. We can rewrite the Riemann sum for a Brownian motion as

$$I(t) = \lim_{k \to +\infty} \sum_{k=0}^{K-1} f(\tau_k)(W_{k+1} - W_k) \, . \tag{2.33}$$

Moreover, we can identify two cases:

- $\lambda = 0$, Itô integral $\int_0^t f(s)dW = \lim\limits_{k \to +\infty} \sum\limits_{k=0}^{K-1} f(t_k)(W_{k+1} - W_k)$

- $\lambda = 1/2$, Stratonovich integral $\int_0^t f(s) \circ dW = \lim\limits_{k \to +\infty} \sum\limits_{k=0}^{K-1} f(\frac{1}{2}(t_k + t_{k+1}))(W_{k+1} - W_k)$

We have just shown the difference for the integration for both Itô and Stratonovich interpretations. Let us move onto the difference in the interpretations from the SDEs and how to change from one to the other. First, we write a SDE by using Itô interpretation

$$dX_t = A(X_t)dt + C(X_t)dW \, . \tag{2.34}$$

From this interpretation, we want to move onto the Stratonovich interpretation

$$dX_t = A(X_t)dt + C(X_t) \circ dW \, . \tag{2.35}$$

From Eq. (2.34) and by using a Taylor series expansion, we find

$$dX_t = \left(\hat{A}(X_t) + \frac{1}{2}\frac{d\hat{C}(X_t)}{dx}\hat{C}(X_t) \right) dt + \hat{C}(X_t)dW \, , \tag{2.36}$$

where we can identify $\hat{A}(X_t) = A(X_t) - \frac{1}{2}\frac{dC(X_t)}{dx}C(X_t)$ and $\hat{C}(X_t) = C(X_t)$. The SDE from the Itô interpretation Eq. (2.34) is equivalent to the following SDE in the Stratonovich

interpretation and reads

$$dX_t = \left(A(X_t) - \frac{1}{2}\frac{dC(X_t)}{dX_t}C(X_t) \right) dt + C(X_t) \circ dW \,,$$

with a correction term $-\frac{1}{2}\frac{dC(X_t)}{dX_t}C(X_t)$. In the same way, we can start from Eq. (2.35)

$$dX_t = A(X_t)dt + C(X_t) \circ dW \,,$$

and by using a Taylor series expansion, we can rewrite it in terms of Itô interpretation

$$dX_t = \left(A(X_t) + \frac{1}{2}\frac{dC(X_t)}{dX_t}C(X_t) \right) dt + C(X_t)dW \,,$$

This correction term $\frac{1}{2}\frac{dC(X_t)}{dX_t}C(X_t)$ is called Itô-to-Stratonovich correction. In components, the Itô-to-Stratonovich correction reads

$$h_i(x) = \frac{1}{2}\sum_{j=1}^{d}\sum_{k=1}^{m} C_{jk}(x)\frac{\partial C_{ik}}{\partial x_j}(x), \quad i = 1,\dots,d\,. \tag{2.37}$$

When the noise is additive, the correction term vanishes. However, when the noise is multiplicative, the correction term plays an important role in the dynamics. As an example, let us consider a stochastic differential equation in the Stratonovich interpretation

$$\frac{de}{dt}(t) = \xi_e(t) \times e(t)\,. \tag{2.38}$$

We can rewrite this equation in components

$$de_i(t) = \sum_{j=1}^{d}\sum_{k=1}^{m}\epsilon_{ijk}dW^j e^k = -\sum_{j=1}^{d}\sum_{k=1}^{m}\epsilon_{ikj}e^k dW^j\,. \tag{2.39}$$

In order to express the previous equation in Itô interpretation, from Eq. (2.37), we identify the Itô-to-Stratonovich correction (using the Einstein convention of repeated indices)

$$C_{jk}(e) = -\epsilon_{jlk}e^l, \quad C_{ik}(e) = -\epsilon_{ilk}e^l, \quad \frac{dC_{ik}}{de_j} = -\epsilon_{ilk}\frac{de^l}{de_j} = -\epsilon_{ilk}\delta_j^l = -\epsilon_{ijk}\,.$$

The Itô-to-Stratonovich correction reads

$$h_i(e) = \frac{1}{2}(-)\epsilon_{jlk}e^l(-)\epsilon_{ijk} = \frac{1}{2}\epsilon_{jlk}\epsilon_{ijk}e^l = -\frac{1}{2}\epsilon_{ljk}\epsilon_{ijk}e^l = -\delta_i^l e^l = -e_i$$

Equation (2.38) in the Itô interpretation reads

$$\frac{de}{dt}(t) = \xi_e(t) \times e(t) - e(t)\,. \tag{2.40}$$

We obtained an extra term in the equation. As we saw, this correction term plays an important role in the dynamics and it is important to be careful in the interpretation we choose.

2.3.1 Langevin equation

Paul Langevin proposed a phenomenological description of the Brownian motion [85]. Since the emergence of active matter, three important minimal models, Fig. 2.12, have been studied and developed: run-and-tumble particles (RTPs), first modeled by Schnitzer in 1993 [90] and experimentally described by Berg and Brown in 1972 [16, 17, 19, 18, 91]; active Brownian particles (ABPs), first introduced by Schimansky-Geier *et al.* in 1995 [92]; and active Ornstein-Uhlenbeck particles (AOUPs) [93]. To understand and compare these models, we should first start with the classical passive Brownian particle (PBP).
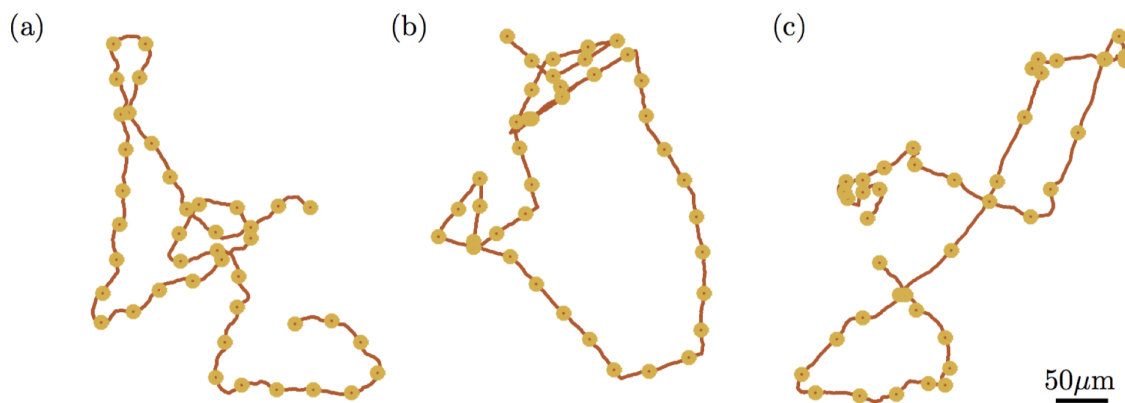
Figure 2.12 – Active particles in complex and crowded environments. (Color online) Sample trajectories of active Brownian particles corresponding to different mechanisms generating active motion: (a) rotational diffusion dynamics; (b) run-and-tumble dynamics; and (c) Gaussian noise dynamics. The dots correspond to the particle position sampled every 5 s [3].

Passive Brownian particles model. Brownian motion can be described by a Langevin equation which takes into account the effect of the solvent on the colloids with two contributions: the mean drag force opposed to the direction of motion, and a random force describing the collisions between the solvent and the colloids. This equation reads

$$m\dot{\boldsymbol{v}} = -\zeta\boldsymbol{v} + \xi\,, \tag{2.41}$$

where m is the colloid's mass, ζ the friction and ξ a Gaussian white noise $\langle \xi_\alpha(t)\xi_\beta(0)\rangle = \delta_{\alpha\beta}2D\delta(t)$. This is equivalent to look at the time evolution of the position, given by the

---

[3]Reprinted figure with permission from Clemens Bechinger et al., Reviews of Modern Physics, Active particles in complex and crowded environments, 88, 045006, 2016. Copyright 2019 by the American Physical Society.

random variable $X = r$, of a particle and the stochastic differential equation, Eq. (2.27), can be rewritten as

$$m\frac{d^2}{dt^2}r = -\zeta\frac{d}{dt}r + \xi\,,$$

where $A(X_t, t) = -\zeta\frac{d}{dt}r$ and $B(X_t, t) = 1$. In the overdamped limit, Eq. (2.41), reads

$$\dot{\boldsymbol{r}} = \frac{1}{\zeta}\xi\,. \tag{2.42}$$

Active Brownian particles model.   We can rewrite the previous equation for a self-propelled particle as

$$\dot{\boldsymbol{r}} = \boldsymbol{u} + \eta\,, \tag{2.43}$$

where $\boldsymbol{u}$ is the self-propulsion and $\langle\eta_\alpha(t)\eta_\beta(0)\rangle = \delta_{\alpha\beta}2D_t\delta(t)$ with $D_t = D/\zeta$. In order to take into account the fluctuations of the orientation, the correlation of the self-propulsion is defined by $\langle u_\alpha(t)u_\beta(0)\rangle = \delta_{\alpha\beta}\frac{v_0^2}{d}e^{-|t|/\tau}$, with τ is the persistence time.

By introducing a coupling between the self-propulsion term and the orientation of the particle, Eq. (2.43) reads

$$\begin{aligned} \dot{\boldsymbol{r}} &= v_0\boldsymbol{e} + \xi \\ \dot{\boldsymbol{e}} &= \boldsymbol{e} \times \xi_e\,, \end{aligned} \tag{2.44}$$

where $\langle\xi_\alpha(t)\xi_\beta(0)\rangle = \delta_{\alpha\beta}2D_t\delta(t)$ and $\langle\xi_{e_\alpha(t)}\xi_{e_\beta(0)}\rangle = \delta_{\alpha\beta}2D_r\delta(t)$.

Run-and-tumble particles model.   The run-and-tumble motion is inspired by the dynamics of bacteria [16]. The main feature of this model is the tumbling time of the particle, in other word, the reorientation of the particle given by a rate ν. The motion of the particle alternate between two states: when the particle moves in a specific direction at constant speed v_0, ('run'), and when the particle does not move and reorient with a given rate ν, ('tumble'). The particle reorients instantaneously and completely isotropically, occurring with a given rate ν, thus the typical trajectories are made of straight lines with random length of typical size v_0/ν. In two dimensions, we can rewrite the previous equation in a more compact way as

$$\begin{aligned} \dot{\boldsymbol{r}} &= \boldsymbol{u} + \xi \\ \dot{\theta} &= \gamma\,, \end{aligned} \tag{2.45}$$

where $\langle\gamma_\alpha(t)\gamma_\beta(0)\rangle = \delta_{\alpha\beta}2D_r\delta(t)$ and $\boldsymbol{u} = v_0(\cos(\theta), \sin(\theta))^T$. The correlation for the self-propulsion are given by $\langle u_\alpha(t)u_\beta(0)\rangle = \delta_{\alpha\beta}\frac{v_0^2}{d}e^{-|t|/\tau}$, where $\tau^{-1} = \nu + (d-1)D_r$ [94]. The main difference between RTPs and ABPs is the value of the persistence time τ, which differ from ν, the tumbling rate.

Active Ornstein-Uhlenbeck particles model.   The term active Ornstein-Uhlenbeck particles was recently introduced by Fodor *et al.* [93]. However, a similar concept was used to approximate the treatment of ABPs [54, 95]. The equation of motion for an overdamped active particle with an interaction potential reads

$$\dot{\boldsymbol{r}} = -\mu\nabla(\Phi) + \boldsymbol{v}\,.$$

The activity $\boldsymbol{v}$ has correlations taken as an Ornstein-Uhlenbeck process $\langle v_\alpha(t)v_\beta(0)\rangle = \delta_{\alpha\beta}\Gamma(t)$, and obeys the equation

$$\tau\dot{\boldsymbol{v}} = -\boldsymbol{v} + \eta\,,$$

where $\langle\eta_\alpha(t)\eta_\beta(0)\rangle = \delta_{\alpha\beta}2D\delta(t)$. Thus [93, 54]

$$\Gamma(t) = \frac{D_{ac}}{\tau}e^{\frac{-|t|}{\tau}}\,,$$

where $D_{ac} = v_0^2/d$ represents an active diffusion coefficient and τ the persistence time (to remind $\tau^{-1} = (d-1)D_r$). The limit for vanishing persistence time of AOUPs corresponds to a passive Brownian particle, since $\boldsymbol{v}$ reduces to a Gaussian white noise. The main difference between these three minimalist models resides in the interpretation of the orientational diffusion coefficient. In the rest of my thesis, my attention will be focused on the concept of 'Active Brownian Particles' to study the motion of active particles at the microscopic level under external force and confinement.

2.3.2   Fokker-Planck equation

We want to study the time evolution of the probability distribution associated to the continuous random variable X_t, in continuous time. Instead of having discrete states in the Kolmogorov backward equation, the state are now continuous, and the equation obtained from it, is called Fokker-Planck equation. This equation enables us to calculate the transition probability, useful to calculate the expectation value of observables of a diffusion process. It is possible to derive the Fokker-Planck equation from the Chapman-Kolmogorov equation, by employing a similar method used previously to compute the Master equation but in the following Itô's Lemma, Eq. (2.29), will be used. For further details on the Chapmann-Kolmogorov equation method, the readers are referred to [96]. Let us assume that a function $f(t)$ does not depend explicitly on t, i.e. $\partial_t f = 0$. By averaging over the Wiener process we obtain

$$\frac{d}{dt}\langle f(X_t)\rangle = \langle A\frac{\partial}{\partial X}f + \frac{1}{2}C^2\frac{\partial^2}{\partial X^2}f\rangle\,, \tag{2.46}$$

where $\langle dW\rangle = 0$. We can rewrite $\langle f(X_t)\rangle$ with the transition probability $P(X,t)$. This expectation value is given by

$$\langle f(X_t)\rangle = \int dX P(X,t)f(X_t)\,,$$

and Eq. (2.46) can be rewritten as

$$\frac{d}{dt}\langle f(X_t)\rangle = \int dX f(X_t)\frac{\partial}{\partial t}P(X,t)$$

$$= \int dX P(X,t)A\frac{\partial}{\partial X}f(X_t) + \int dX P(X,t)\frac{1}{2}C^2\frac{\partial^2}{\partial X^2}f(X_t)\,. \qquad (2.47)$$

By integrating by parts the last line [4] , we obtain

$$\int dX f(X_t)\frac{\partial}{\partial t}P(X,t) = -\int dX f(X_t)\partial_X(P(X,t)A) + \int dX \frac{1}{2}f(X_t)\partial_{X^2}(P(X,t)C^2)\,. \qquad (2.48)$$

This equation hold for any arbitrary function $f(X_t)$ and the Fokker-Planck equation for the transition probability $P(X,t)$ reads

$$\frac{\partial}{\partial t}P(X,t) = -\partial_X(P(X,t)A) + \frac{1}{2}f\partial_{X^2}(P(X,t)C^2)\,. \qquad (2.49)$$

The previous equation has been obtained from the SDE in Eq. (2.28), which describes the evolution of the random variable (e.g. coordinates) X_t. From a mathematical point of view, the explicit solution of the Fokker-Planck equation, Eq. (2.49), depends on the functional forms of the drift coefficient $A(X_t,t)$ and of the diffusion coefficient[5] $C^2(X_t,t)/2$.

2.3.3 From the Langevin equation to the Fokker-Planck equation

As we saw, it is possible to derive the Fokker-Planck equation by using Itô's Lemma in a general matter. However, it can be difficult to derive the Fokker-Planck equation with

---

[4]The first integral reads

$$\int dX P(X,t)a\partial_X f = [AP(X,t)f] - \int dX f\partial_X(P(X,t)A)\,,$$

and the second one reads

$$\int dX P(X,t)\frac{1}{2}C^2\partial_{X^2}f = \left[\frac{1}{2}C^2 P(X,t)f\right] - \int dX \frac{1}{2}\partial_X f\partial_X(P(X,t)C^2)$$

$$= \left[\frac{1}{2}C^2 P(X,t)f\right] - \left[\frac{1}{2}C^2 P(X,t)f\right] + \int dX \frac{1}{2}f\partial_{X^2}(P(X,t)C^2)\,.$$

By using $\int dA P(A) = 1$, we obtain Eq. (2.48).

[5]Problem of establishing the condition for the existence and the uniqueness of the solution of the FPE require specific assumption of space and time dependence of $A(X_t,t)$ and $C(X_t,t)$. For further details, the readers are referred to the Appendix A and [87].

this method from any Langevin equations, especially when the coefficients A and C are complicated. Let me present another method based on the variational derivation, which will be used in the Chapter 3.1.

It is possible to describe the motion of a particle subject to external force and random force with the Langevin equation

$$\frac{d\boldsymbol{x}}{dt} = f_{ext}\boldsymbol{x} + \boldsymbol{\xi}\,. \tag{2.50}$$

The probability distribution $P(\boldsymbol{x}, t) = \langle \delta(\boldsymbol{x}(t) - \boldsymbol{x}) \rangle$ and its temporal derivation reads

$$\begin{aligned}
\frac{d}{dt}P(\boldsymbol{x}, t) &= \frac{d}{dt}\langle \delta(\boldsymbol{x}(t) - \boldsymbol{x}) \rangle \\
&= -\nabla \cdot \langle \delta(\boldsymbol{x}(t) - \boldsymbol{x})\frac{d\boldsymbol{x}}{dt} \rangle \\
&= -f_{ext}\nabla P(\boldsymbol{x}, t) - \nabla \cdot \langle \delta(\boldsymbol{x}(t) - \boldsymbol{x})\boldsymbol{\xi} \rangle\,.
\end{aligned}$$

The last term can be found by using a variational derivation or also called Furutsu-Novikov-Donsker relation [97, 98, 99, 100, 101, 102, 103, 104, 105]

$$\langle \delta(\boldsymbol{x}(t) - \boldsymbol{x})\boldsymbol{\xi} \rangle = \int\limits_{-\infty}^{+\infty} dt' \langle \boldsymbol{\xi}(t)\boldsymbol{\xi}(t') \rangle \langle \frac{\delta\delta(\boldsymbol{x}(t) - \boldsymbol{x})}{\delta\boldsymbol{\xi}(t')} \rangle\,. \tag{2.51}$$

By using

$$\langle \frac{\delta\delta(\boldsymbol{x}(t) - \boldsymbol{x})}{\delta\boldsymbol{\xi}(t')} \rangle = -\nabla \cdot \delta(\boldsymbol{x}(t) - \boldsymbol{x})\,,$$

Equation (2.51) reads

$$\langle \delta(\boldsymbol{x}(t) - \boldsymbol{x})\boldsymbol{\xi} \rangle = -\nabla \cdot D\delta(\boldsymbol{x}(t) - \boldsymbol{x})\,,$$

where $D = \int\limits_{-\infty}^{+\infty} dt' \langle \boldsymbol{\xi}(t)\boldsymbol{\xi}(t') \rangle$ is the diffusion coefficient. The Fokker-Planck equation associated to the Langevin equation in 3D, Eq. (2.50), reads

$$\frac{d}{dt}P(\boldsymbol{x}, t) = -f_{ext}\nabla P(\boldsymbol{x}, t) + D\Delta P(\boldsymbol{x}, t)\,. \tag{2.52}$$

In the most simple case, where $f_{ext} = 0$, its solution can be found by moving to the Fourier space

$$\frac{d}{dt}P(\boldsymbol{k}, t) = D\boldsymbol{k^2}P(\boldsymbol{k}, t)\,,$$

and its solution reads

$$P(\boldsymbol{k}, t) = P(\boldsymbol{k}, 0)e^{-D\boldsymbol{k^2}t}\,,$$

with the initial condition $P(\boldsymbol{k}, 0) = e^{-i\boldsymbol{k}\boldsymbol{x}_0}$. Elementary computations lead to

$$P(\boldsymbol{x}, t) = \frac{1}{\sqrt{4\pi Dt}} e^{-\frac{(\boldsymbol{x}-\boldsymbol{x}_0)^2}{4Dt}} \,. \tag{2.53}$$

Let us imagine the motion a passive particle under the gravity force in 1D. The Fokker-Planck equation, Eq. (2.52), can be rewritten as

$$\frac{d}{dt} P(x, t) = v_g \frac{d}{dx} P(x, t) + D \frac{d^2}{dx^2} P(x, t) \,,$$

where $v_g = -f_{ext}\hat{x}$ represents the effect of the gravity, also called terminal velocity. The solution can be obtained by moving into the Fourier space

$$\frac{d}{dt} P(k, t) = v_g k P(k, t) - Dk^2 P(k, t) \,,$$

and its solution reads

$$P(k, t) = e^{-ikx_0} e^{v_g k - Dk^2 t} \,.$$

Elementary computations lead to

$$P(x, t) = \frac{1}{\sqrt{4\pi Dt}} e^{-\frac{(x - v_g t - x_0)^2}{4Dt}} \,. \tag{2.54}$$

2.3.4   Reflective boundary condition: Fokker-Planck equation

In order to include the boundary condition at $x = 0$, we use the reflective boundary condition. From the continuity equation

$$\frac{d}{dt} P(x, t) = -\frac{d}{dx} J \,,$$

where J is the probability current or flux of the system. The reflective boundary condition corresponds to no flux at the boundary, which reads

$$\left[D \frac{d}{dx} P_r(x, t) + v_g P_r(x, t) \right]_{x=0} = 0 \,.$$

By using the method of images, see Fig. 2.13, which consists of taking a mirror source at $x = -x_0$ to reproduce the boundary condition at the wall $x = 0$ at any time, for a diffusion process [106, 107, 108, 109, 105]

$$P_r(x, t) = P(x, t|x_0) + AP(x, t| - x_0) + \int_{-\infty}^{-x_0} k(\xi) P(x, t|\xi) d\xi \,. \tag{2.55}$$

After some computations, the readers are referred to Chapter 3.1.8 for the intermediate steps, the solution for Eq. (2.54) with reflective boundary condition reads

$$P_r(x,t) = \frac{1}{\sqrt{4\pi Dt}} \left[e^{-(x-x_0)^2/4Dt} + e^{-(x+x_0)^2/4Dt} \right] e^{\frac{-v_g(x-x_0)}{2D} - \frac{v_g^2 t}{4D}} + \frac{v_g}{D\sqrt{\pi}} e^{-v_g z/D} \int\limits_{\frac{x+x_0-v_g t}{2\sqrt{Dt}}}^{+\infty} e^{-\eta^2} d\eta \,.$$

This method will be use in the first work of the Chapter 3.1 to find the probability density
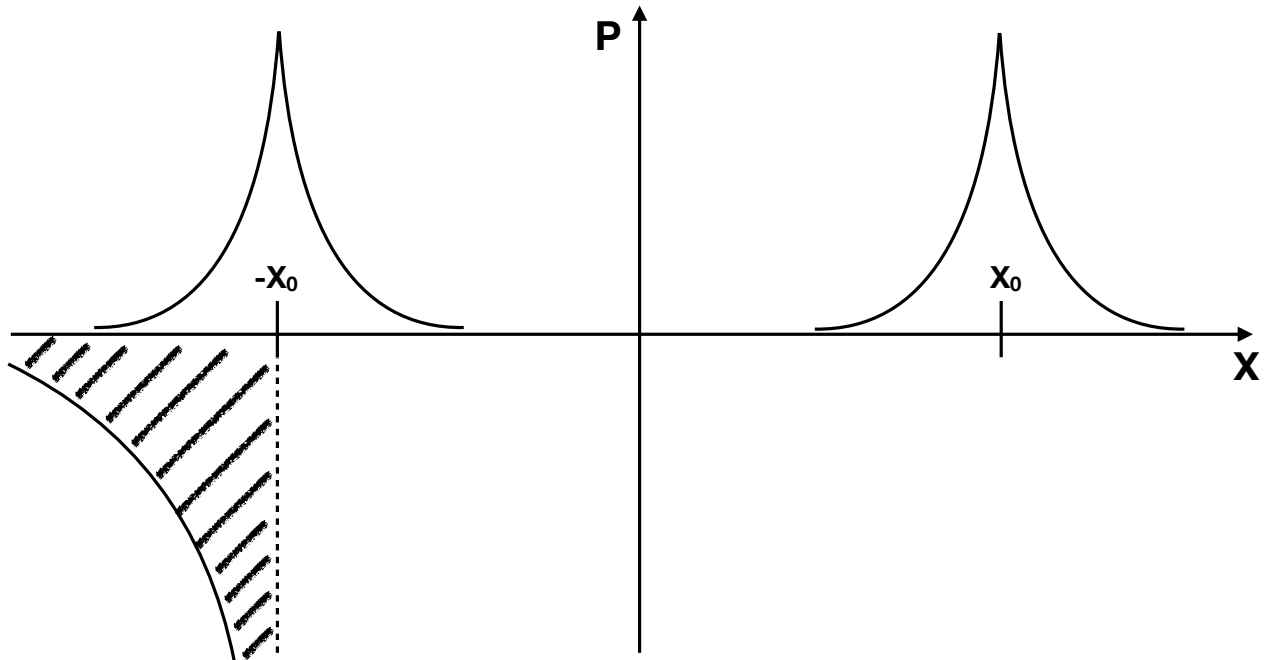
Figure 2.13 – Reflective boundary conditions. At time $t = 0$, the particle is at the position x_0 and its mirror image at $-x_0$, with an associated continuous sequence of images located at all points $\xi < -x_0$.

function in the case of one active particle in 3D.

2.4 Numerical solution

The numerical analysis of SDEs is different from the ordinary differential equation due to the stochastic calculus of the Wiener process. The stochastic Taylor expansion gives the foundation of the discrete time numerical methods for differential equations. The simplest numerical analysis method for the approximation of ordinary differential equation is given

by Euler's method [110]. Moreover, in 1955, Maruyama developed a method to approximate the stochastic differential equation based on Euler's method. This method is called Euler-Mayurama method. For more details, the readers are referred to [87, 110].

2.4.1 Discretization scheme

In the following, the Euler-Mayurama method will be used. Let a stochastic differential equation (in the Itô interpretation)

$$dX_t = a(X_t, t)dt + b(X_t, t)dW_t \,,$$

where $dW_t = \xi dt$. The discrete scheme reads

$$X_{n+1} = X_n + a(X_n, t_n)\Delta t + b(X_n, t_n)\Delta W_n \,,$$

we can express ΔW_n as $\sqrt{\Delta t} N(0,1)$[6], and then obtain

$$X_{n+1} = X_n + a(X_n, t_n)\Delta t + n \cdot b(X_n, t_n)\sqrt{\Delta t} \,,$$

where n is a number draw from a unit normal distribution $N(0,1)$.

2.4.2 Molecular Dynamics simulations

In order to investigate the emergence of collective behavior of many interacting active particles under external forces, we developed molecular dynamics simulations based on the Euler-Mayurama scheme. To this end, we study the behavior of N particles in two domains: a cubic box and a cylindrical box. We describe the particle by its position $\mathbf{r}$ and its orientation $\mathbf{e}$ with $\mathbf{e}^2 = 1$. The particle moves with a self-propulsion speed v_0 along its orientation.

---

[6]From the theorem of the strong convergence, see Appendix A, the Euler-Mayurama scheme gives

$$X(t + \Delta t) = x + v_g \Delta t + v_s n(t)\sqrt{\Delta t} \,.$$

Moreover, by knowing that a Wiener process $dW_t = W(t + \Delta t) - W(t) \sim N(0, \Delta t)$ and by using $N(0, \Delta t) \overset{d}{=} N(0,1)\sqrt{\Delta t}$, where $\overset{d}{=}$ indicates that the random processes follow the same distribution, the discretization for a Wiener process reads

$$\Delta W(\Delta t) = \sqrt{\Delta t} n(t), \, n(t) \in N(0,1) \,.$$

Two stochastic differential equations in three dimensions (in the Stratonovich interpretation) draw our attention and reads

$$\frac{d}{dt}\mathbf{r_i}(t) = v_0\mathbf{e_i}(t) + \mathbf{f_{ext_i}} - \nabla U_{WCA}(r) + \xi_{r_i}(t) \tag{2.56}$$

$$\frac{d}{dt}\mathbf{e_i}(t) = \xi_{e_i}(t) \times \mathbf{e_i}(t) \,. \tag{2.57}$$

The hard core repulsion between the particles is given by Weeks-Chandler-Anderson potential [111]

$$U_{WCA}(r) = \begin{cases} 4\epsilon \left[(\frac{\sigma}{r_{ij}})^{12} - (\frac{\sigma}{r_{ij}})^{6} \right] + \epsilon & \text{for } r \leq 2^{1/6}\sigma \\ 0 & \text{for } r > 2^{1/6}\sigma \end{cases} \tag{2.58}$$

where σ is the particle diameter and ϵ is the strength of the potential. This potential is a modified Lennard-Jones potential, shifted by ϵ and truncated at the minimum $2^{1/6}\sigma$. It is composed of repulsive r^{-12} and attractive r^{-6} terms. The Lennard-Jones pair potential is decomposed into two parts, one repulsive which correspond to the WCA potential and another one attractive. The term $\mathbf{f_{ext}}$ gives the external forces applied on the particles, for example it can represent the gravity.

The previous equation of motion are integrated by using Euler-Mayurama scheme, with parameters which satisfy the convergence criterion (see Appendix A), and read

$$r_i(t + \Delta t) = r_i(t) + (v_0 e_i + f_{ext_i} - \partial_i U_{WCA}(r))\Delta t + n(t)\sqrt{\Delta t} \tag{2.59}$$

$$e_i(t + \Delta t) = e_i(t) + \sqrt{\Delta t}(\sum_{l=1}^{3}\sum_{j=1}^{3}\sum_{k=1}^{3} \varepsilon_{ljk} n^j e^k)_i \,. \tag{2.60}$$

The norm of the orientation vector can be kept by means of a Lagrangian multiplier [112] or by changing the interpretation of the stochastic differential equation as in (2.40).

2.4.3 Boundary conditions

When a confined geometry is considered the Molecular Dynamics simulations require the definition of the collision dynamics at the boundary. By assuming that the translational velocity undergoes elastic reflection, two possibilities are considered for the orientation dynamics. One is to consider the orientation unchanged during the collision, called sliding boundary condition described in [113]. The other one is to fix the outside angle at a given value fixed by the experimental observations. In the following, firstly we discuss the dynamics for flat and curved boundaries. Secondly, the change in the orientation in the case of a curved boundary.

Flat boundary   The flat boundary condition was considered to study the sedimentation of active particles such as Janus colloids, in 3D. We considered the sliding boundary condition and under this assumption, the Janus colloids tend to slide along the boundaries for an average time of the order of τ_e, given by the orientational diffusion coefficient. At the boundary, the reflective implementation is made by modifying the positions computed from Eqs. (2.59)-(2.60). As shown in Fig. 2.14, the position at time t of the active particle is defined by $[r(t)]$, the position outside the boundary at $t + \Delta t$ by $[\tilde{r}(t + \Delta t)]$ and the reflected position by $[r(t + \Delta t)]$. The orientation stays unchanged over this reflecting process.

Particle outside $\tilde{r}(t + \Delta t)$

Boundary

Particle at time $r(t)$

Particle reflected $r(t + \Delta t)$
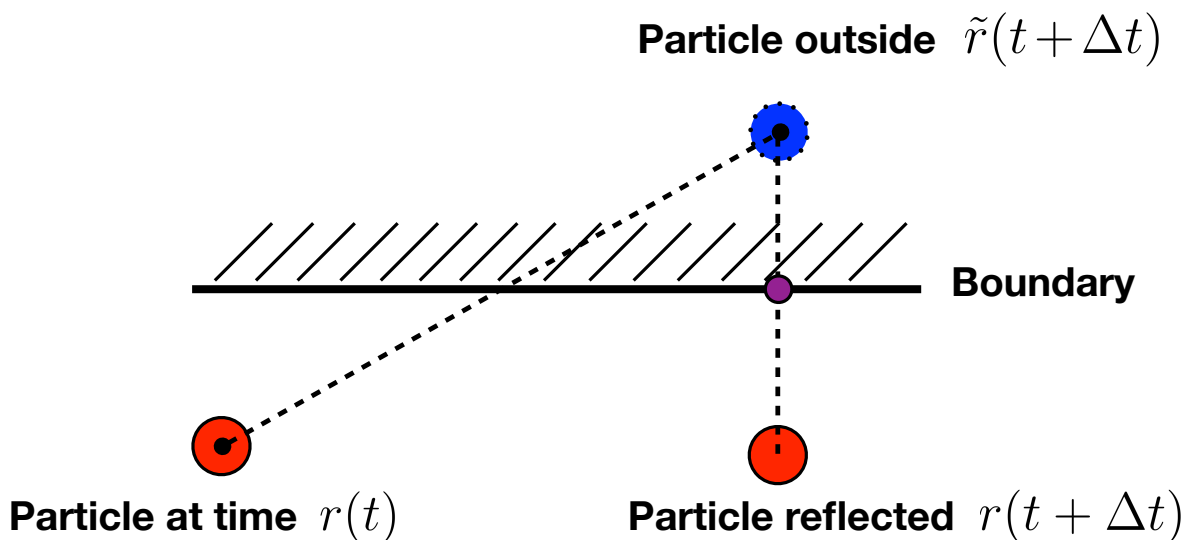
Figure 2.14 – Flat boundary. It simulates a reflection as it can be observed in billiards, when the balls collide with the border and the angle of reflection is the same as the angle of incidence. The reflection is realized by taking its image and reflect it by the perpendicular with the boundary.

Curved boundary   The curved boundary condition was considered to study the aggregation phenomena in the case of the algae *C. reinhardtii*, in a quasi-2D cylindrical domain. In that work, we have considered the reflective boundary condition, as shown in Fig. 2.15, with and without a change in the orientation.

The reflective process is structured as follows for the curved boundary.

1. Compute the position at $t + \Delta t$, $[\tilde{r}(t + \Delta t)]$ according to Eqs. (2.59)-(2.60).

2. If the new position is inside the boundary, then we assign $[\tilde{r}(t + \Delta t)] = [r(t + \Delta t)]$.

3. If the new position is outside the boundary, as illustrated in Fig. 2.14 - 2.15, then:
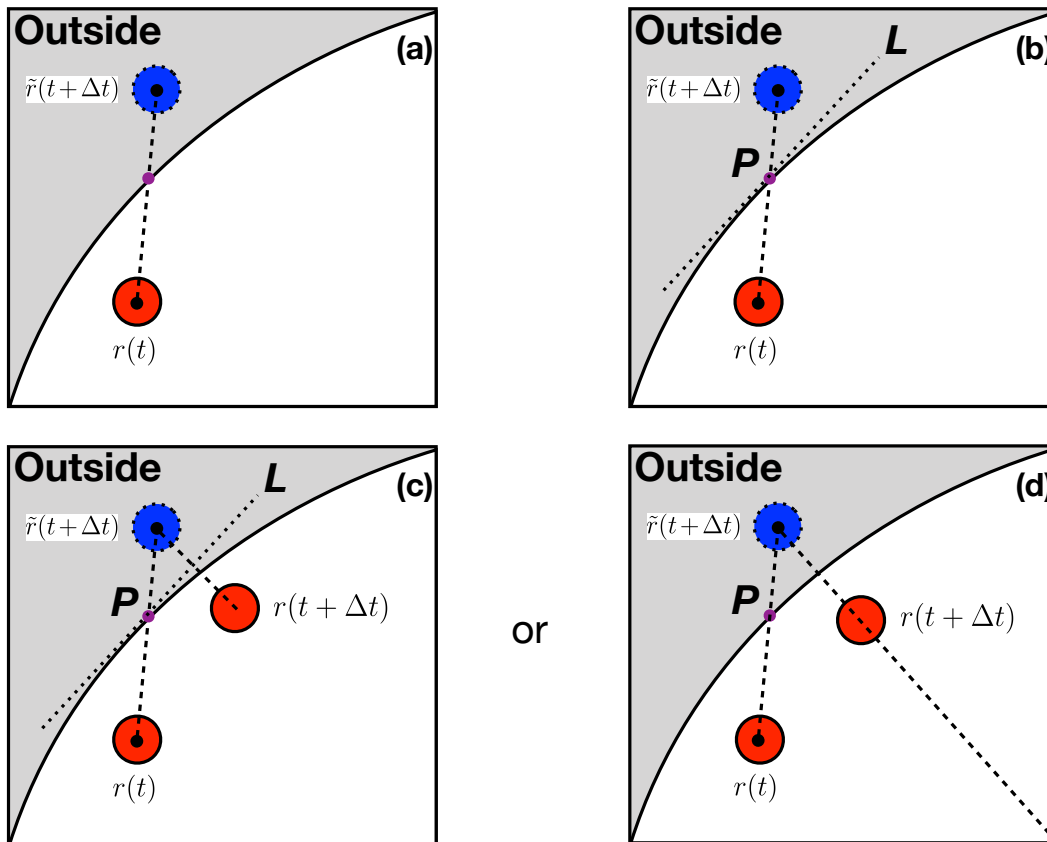
Figure 2.15 – Curved boundary. At each time step, (a) we check if the particle at $t + \Delta t$ is inside or outside of the boundary; (b) if outside, we perform the reflection process by computing the intersection point P and its associate tangent line L; and either (c) the particle is reflected via L or (d) the particle is reflected via the radius. Both (c)-(d) obtaining $r(t + \Delta t)$ after this reflection correction.

(a) Compute the intersection point P: $[r_p]$

(b) Derive the tangent line L

(c)   • Unchanged orientation. Take the mirror image from the tangent line of $[\tilde{r}(t + \Delta t)]$ to find the new position $[r(t + \Delta t)]$

     • Change orientation. Take the mirror image by using the radius. Due to the small time step $\Delta t = 10^{-5}$ (needed for the convergence criterion), there is not much difference between the tangent line and the radius. However, the advantage offered by using the radius is the adjustment of the position to get the desired outside angle. In the work with the algae *C. reinhardtii*, this

angle is found to be 16 degrees [114].

Let me describe in more details the computation for the quasi-2D cylindrical domain. The system is in quasi-2D, the curved boundary applies in the x, y directions and we have a flat boundary in the z direction.

- First, we need to compute the intersection point P: $[x_p, y_p]$.

  We start by deriving the line between $[x(t), y(t)]$ and $[\tilde{x}(t + \Delta t), \tilde{y}(t + \Delta t)]$. From the equation for a line $y(t) = ax(t) + b$, elementary computations lead to

  $$a = \frac{\tilde{y}(t + \Delta t) - y(t)}{\tilde{x}(t + \Delta t) - x(t)}$$

  $$b = y(t) - \left(\frac{\tilde{y}(t + \Delta t) - y(t)}{\tilde{x}(t + \Delta t) - x(t)} \right) x(t) \, .$$

  Then, we need to find the intersection between this line and the boundary, which is given by a circle. The following system of equation need to be solved

  $$(x(t) - x_c)^2 + (y(t) - y_c)^2 = R^2, \text{ with } (x_c, y_c) = (0, 0)$$
  $$y(t) = ax(t) + b \, .$$

  By subsitution, the equation for the line into the one for the circle

  $$x^2(t)(1 + a^2) + 2abx(t) + b^2 - R^2 = 0 \, .$$

  The solution of this equation read

  - $\Delta > 0$: $x_p = \frac{-B \pm \sqrt{\Delta}}{2A}$ and $y_p = ax_p + b$.
  - $\Delta = 0$: $x_p = \frac{-B}{2A}$ and $y_p = ax_y + b$.

  where $A = 1 + a^2$, $B = 2ab$, $C = b^2 - R^2$ and $\Delta = B^2 - 4AC$.

- Second, in order to use the mirror image by using the tangent line, we need to compute it. The product of the radius with the gradient of the tangent line gives -1 and reads

  $$m_R \cdot m_T = -1 \, ,$$

  where $m_R = y_p/x_p$ and $m_T = -1/m_R$. The tangent line is given by

  $$y = m_T x \, .$$

- Third, the reflection of $[\tilde{x}(t + \Delta t), \tilde{y}(t + \Delta t)]$ via the tangent line is given by

$$x(t + \Delta t) = \frac{(1 - m_T^2)\tilde{x}(t + \Delta t) + 2m_T\tilde{y}(t + \Delta t)}{m_T^2 + 1}$$

$$y(t + \Delta t) = \frac{(m_T^2 - 1)\tilde{y}(t + \Delta t) + 2m_T\tilde{x}(t + \Delta t)}{m_T^2 + 1}.$$

The computation of the mirror image by using the radius requires fewer steps. We compute the distance or radius from the center of the circle with the positions outside of the boundary and in order to find the distance from the boundary, we take the difference between this new radius and the one from the boundary. The reflective image $[x(t + \Delta t), y(t + \Delta t)]$ is found by the subtraction of this distance with the radius of the boundary.

Outside angle θ From the intersection point P, we compute the outside angle by using the polar coordinates, see Fig. 2.16, which read

$$e_r = e_x \cos(\phi) + e_y \sin(\phi)$$
$$e_\phi = -e_x \sin(\phi) + e_y \cos(\phi).$$
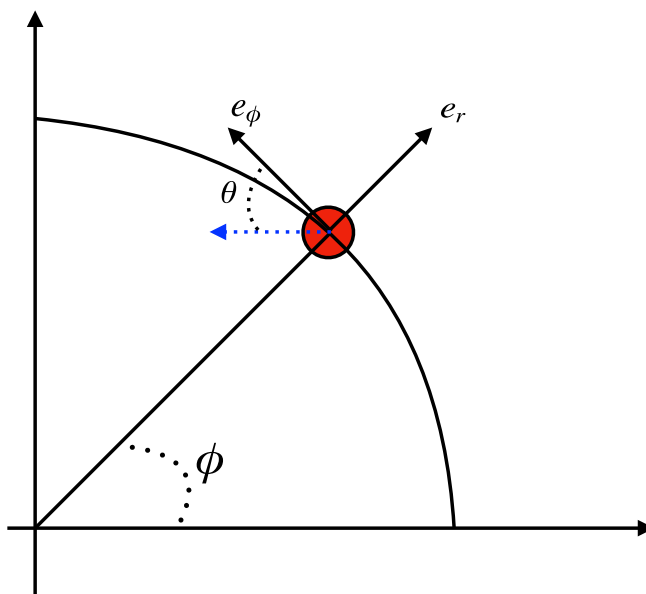
Figure 2.16 – Reflection angle. When the reflection process does not keep the angle of reflection equal to the incident angle, but it is instead fixed at $\theta = \theta_0$.

The direction of the orientation is either $+e_\phi$ or $-e_\phi$, and is given by the scalar product: $e(t) \cdot e_\phi$.

If $e(t) \cdot e_\phi > 0$, then

$$e(t + \Delta t) = \cos(\theta)e_\phi - \sin(\theta)e_r \ .$$

The new orientation for an outside angle θ read

$$e_x(t + \Delta t) = - \left[\cos(\theta)\sin(\phi) + \sin(\theta)\cos(\phi)\right]$$
$$e_y(t + \Delta t) = \left[\cos(\theta)\cos(\phi) - \sin(\theta)\sin(\phi)\right] \ .$$

If $e(t) \cdot e_\phi < 0$, then

$$e(t + \Delta t) = - \cos(\theta)e_\phi - \sin(\theta)e_r \ .$$

The new orientation for an outside angle θ read

$$e_x(t + \Delta t) = \left[\cos(\theta)\sin(\phi) - \sin(\theta)\cos(\phi)\right]$$
$$e_y(t + \Delta t) = - \left[\cos(\theta)\cos(\phi) + \sin(\theta)\sin(\phi)\right] \ .$$

Chapter 3

Results

Contents

3.1   Dynamics of sedimenting active Brownian particles

Summary

The motion of active particles under external field can lead to the emergence of collective behavior. Theoretical studies of active particles, based on the framework of active Brownian particles [10] and stochastic processes, have mostly focused on two-dimensional systems [103, 115, 102, 116, 117]. A complete description in three dimensions (3D) in terms of the Fokker–Planck equation is challenging [118, 104] and some recent progress in the theory of one active particle [119, 120, 121] highlights the fact that many questions are still open, especially in 3D. In this work, I focused my attention on a dilute suspension of active particles, *e.g.* Janus colloids, and characterized the transient sedimentation dynamics. I analytically characterized the sedimentation of one active Brownian particle in 3D and, by means of Brownian dynamics simulations for many weakly-interacting particles. Firstly, I developed a model to described the sedimentation of one active particle under gravity based on two overdamped Langevin equations and the associated Fokker–Planck equation to obtain the particles' density profile in the direction of gravity. The density profile is obtained from the probability density function $P(\boldsymbol{r}, \boldsymbol{e}, t|\boldsymbol{r}_0, \boldsymbol{e}_0, t_0)$ of finding an active particle at the position $\boldsymbol{r}$, with an orientation $\boldsymbol{e}$ at time t, given the initial state $(\boldsymbol{r}_0, \boldsymbol{e}_0, t_0)$. Due to the complexity of the problem, finding the general expression of $P(\boldsymbol{r}, \boldsymbol{e}, t|\boldsymbol{r}_0, \boldsymbol{e}_0, t_0)$ in 3D is challenging. This method allows us to maintain the coupling between the orientation and the position obtained in 3D, which I then specialize in one direction. Furthermore, in comparison with previous work [119, 122, 120, 118, 117] this method has the additional advantage of providing access to the full temporal dynamics, and is not limited to steady-state conditions, so that I can also investigate high Péclet numbers. Secondly, I performed Brownian dynamics simulations to describe the sedimentation of many particles, where fluid-mediated hydrodynamic interactions are approximated via a short-range potential with up-down symmetry. I did the computations and I wrote the paper with the support of Dr. Mazza.

EPJ E

FOUNDED BY PIERRE-GILLES DE GENNES

Recognized by European Physical Society

Soft Matter and Biological Physics

From: Dynamics of sedimenting active Brownian particles
by Jérémy Vachier and Marco G. Mazza
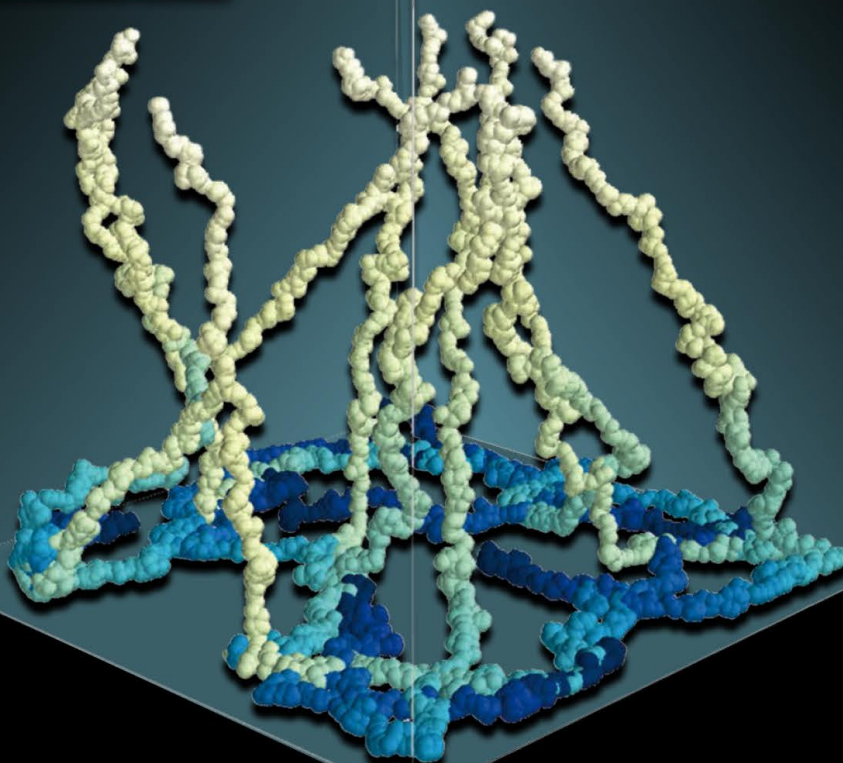
edp sciences

Società Italiana di Fisica

Springer

Dynamics of sedimenting active Brownian particles

Jérémy Vachier[1] and Marco G. Mazza[1,2]

[1] Max Planck Institute for Dynamics and Self-Organization, Am Faßberg 17, 37077 Göttingen, Germany

[2] Interdisciplinary Centre for Mathematical Modelling and Department of Mathematical Sciences, Loughborough University, Loughborough, Leicestershire LE11 3TU, UK

We investigate the stochastic dynamics of one sedimenting active Brownian particle in three dimensions under the influence of gravity and passive fluctuations in the translational and rotational motion. We present an analytical solution of the Fokker–Planck equation for the stochastic process which allows us to describe the dynamics of the active Brownian particle in three dimensions. We address the time evolution of the monopole, the polarization, and the steady-state solution. We also perform Brownian dynamics simulations and study the effect of the activity of the particles on their collective motion. These results qualitatively agree with our model. Finally, we compare our results with experiments [J. Palacci *et al.*, Phys. Rev. Lett. **105**, 088304 (2010)] and find very good agreement.

3.1.1 Introduction

Active particles convert energy from chemical, biological, or other processes into motion. The study of active particles, and especially their collective motion, has received much attention due to a renewed interest in the physical principles underlying the motion of, *e.g.*, plankton or bacteria, and also on account of technological applications involving both biological and artificial controllable active systems [4, 123, 124]. Active particles exhibit a fascinating multitude of interesting behaviors from the single particle to collective states [125, 126, 127], due to their nonequilibrium nature.

Typically, active particles move in an aqueous environment, where, because of their size, viscous forces dominate, and inertial forces are completely negligible. In fact, consideration of the Navier–Stokes equations identifies that the nature of the dynamics is dictated by the ratio of viscous to inertial forces, known as the Reynolds number $\mathcal{R} = \sigma v \rho / \eta$, where σ is the typical size of the microorganism, v its mean velocity, and ρ, η are the fluid's density and viscosity, respectively. For motile bacteria $\mathcal{R} \approx 10^{-5}$. As noted by Purcell [128], this means that if the propulsion of the active particle were to suddenly disappear, it would only coast

for 0.1 Å. Thus, the state of motion is only determined by the forces acting at that very moment, and inertia is negligible.

Even in dilute suspensions, where particle-particle interactions can largely be neglected, and the dynamics are dominated by the balance of active motion and gravity, interesting results are found [129, 120, 130, 131]. Palacci *et al.* [51] showed experimentally with active Janus colloids that activity increases the sedimentation length, by increasing the effective diffusivity. More recently, Ginot *et al.* [132] characterized the equation of state of sedimenting active colloids as a function of the activity.

Theoretical studies of active particles, based on the framework of active Brownian particles [10] and stochastic processes, have mostly focused on two-dimensional systems [103, 115, 102, 116, 117]. A complete description in three dimensions (3D) in terms of the Fokker–Planck equation is challenging [118, 104] and some recent progress in the theory of one active particle [119, 120, 121] highlights the fact that many questions are still open, especially in 3D. For example, in dilute suspensions, what is the transient sedimenting dynamics? the emergence of polarization (and possibly higher orders) is intriguing and currently under investigation [133]; what are the appropriate variables to construct an equation of state? In denser suspension, the important role of hydrodynamic interactions makes the situation even more complicated. For what physical conditions is the sedimenting steady state stable? What are the other possible steady states? Can we write an equation of state in this case? What are its relevant dynamical variables? In this work, we address the first question, that is, the transient state.

We aim to analytically characterize the sedimentation of one active Brownian particle in 3D and, by means of Brownian dynamics simulations for many weakly-interacting particles. First, we analytically describe the sedimentation of one active particle under gravity with two overdamped Langevin equations and the associated Fokker–Planck equation to obtain the particles' density profile in the direction of gravity. The density profile is obtained from the probability density function $P(\boldsymbol{r}, \boldsymbol{e}, t | \boldsymbol{r}_0, \boldsymbol{e}_0, t_0)$ of finding an active particle at the position $\boldsymbol{r}$, with an orientation $\boldsymbol{e}$ at time t, given the initial state $(\boldsymbol{r}_0, \boldsymbol{e}_0, t_0)$. Due to the complexity of the problem, finding the general expression of $P(\boldsymbol{r}, \boldsymbol{e}, t | \boldsymbol{r}_0, \boldsymbol{e}_0, t_0)$ in 3D is challenging. This method allows us to maintain coupling between the orientation and the position obtained in 3D, which we then specialize in one direction. Furthermore, in comparison with previous work [119, 122, 120, 118, 117] this method has the additional advantage of providing access to the full temporal dynamics, and is not limited to steady-state conditions, so that we can also investigate high Péclet numbers. We find an approximate solution for the time-dependent monopole, polarization and the steady-state solution. Secondly, we perform Brownian dynamics simulations to describe the sedimentation of many particles, where fluid-mediated hydrodynamic interactions are approximated via a short-range potential with up-down symmetry.

The remainder of this work is organized as follows. In section 3.1.2, we introduce the
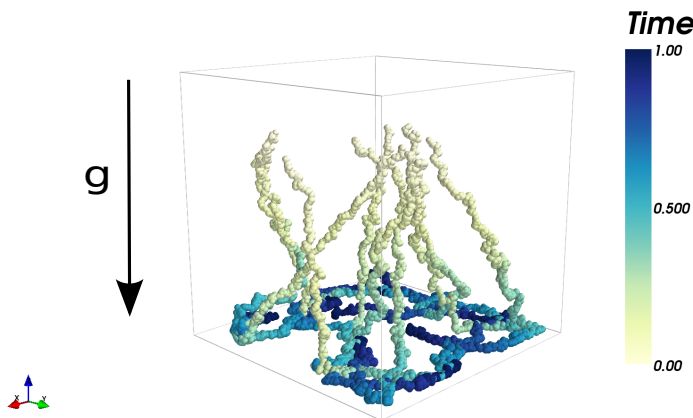
Figure 3.1 – Perspective view of the 3D motion of a few active Brownian particles under gravity in the presence of a reflective wall at the bottom. The trajectories are marked by showing the overlaid particles at subsequent times. The color code of each sphere indicates the time of that configuration.

stochastic process and solve the associated Fokker–Planck equation for a single, sedimenting active Brownian particle. In section 3.1.3, we show the results of Brownian dynamics simulations of dilute suspensions of active particles. Finally, in section 3.1.4 we discuss our conclusions.

3.1.2   Analytical solution for a single active Brownian particle

We study analytically the motion of one self-propelled microscopic particle (active particle), considered as a point particle, in 3D under an external force: gravity. An example of this motion is shown in the Fig. 3.1. The activity of the particle means that it is able to convert energy in order to move. We represent the self-propulsion with a constant speed v_s acting on the particle. Typically, an active particle moves inside a fluid and due to its microscopic size we cannot neglect the influence of thermal fluctuations caused by the surrounding fluid buffeting the particle. The interactions with the fluid are represented by stochastic terms as for a Brownian particle. Due to gravity, the suspended active particle approaches a stationary state where its position has an increased probability of being close to the confining interface. This phenomenon is called sedimentation. To describe this motion, we derive a Fokker–Planck equation [134, 135, 96, 136, 137].

We treat the motion of one active particle, described as a point particle, in 3D under gravity by considering a single active Brownian particle moving with a constant active speed v_s along

a direction represented by the orientation $\boldsymbol{e}$, subject to random fluctuations. The motion of the active particle is biased by a drift velocity $-v_g\boldsymbol{z}$ in the direction of gravity. Our system is then described by two overdamped Langevin equations

$$\frac{d}{dt}\boldsymbol{r}(t) = v_s\boldsymbol{e}(t) - v_g\boldsymbol{z} + \boldsymbol{\xi}(t)\,, \tag{3.1}$$

$$\frac{d}{dt}\boldsymbol{e}(t) = \boldsymbol{\xi}_\mathrm{e}(t) \times \boldsymbol{e}(t)\,. \tag{3.2}$$

The random fluctuations are modeled in terms of the vectors $\boldsymbol{\xi}$ and $\boldsymbol{\xi}_\mathrm{e}$, with zero-mean, Gaussian white noise components, and with variance $\langle \xi_i(t)\xi_j(t')\rangle = 2D_\mathrm{t}\delta_{ij}\delta(t-t')$, $\langle \xi_{\mathrm{e}i}(t)\xi_{\mathrm{e}j}(t')\rangle = 2D_\mathrm{e}\delta_{ij}\delta(t-t')$, where D_t and D_e are the translational and rotational diffusivities, respectively, δ_{ij} is the Kronecker delta, and $\delta(t)$ the Dirac distribution.

From Eqs. (3.1)-(3.2) we can derive a Fokker–Planck equation that accounts for the evolution in time of the one-particle probability density function, $P(\boldsymbol{r},\boldsymbol{e},t|\boldsymbol{z}a,\boldsymbol{e}_0,t_0)$, of finding an active particle under gravity diffusing in 3D, with the initial condition $P(\boldsymbol{r},\boldsymbol{e},t = t_0|\boldsymbol{z}a,\boldsymbol{e}_0,t_0) = \delta(\boldsymbol{r} - \boldsymbol{z}a)\delta(\boldsymbol{e} - \boldsymbol{e}_0)$. In the following, to lighten the notation we will use $P(\boldsymbol{r},\boldsymbol{e},t) = P(\boldsymbol{r},\boldsymbol{e},t|\boldsymbol{z}a,\boldsymbol{e}_0,t_0)$.

After some manipulation (see Appendix 3.1.5), we obtain the following Fokker–Planck equation

$$\frac{\partial}{\partial t}P(\boldsymbol{r},\boldsymbol{e},t) = -v_s\boldsymbol{e}\cdot\nabla P(\boldsymbol{r},\boldsymbol{e},t) + v_g\frac{\partial}{\partial z}P(\boldsymbol{r},\boldsymbol{e},t) + D_\mathrm{t}\nabla^2 P(\boldsymbol{r},\boldsymbol{e},t) + D_\mathrm{e}\mathsf{L}_\mathrm{e}P(\boldsymbol{r},\boldsymbol{e},t)\,, \tag{3.3}$$

with $\mathsf{L}_\mathrm{e} \equiv \left[\frac{1}{\sin\theta}\frac{\partial}{\partial\theta}\left(\sin\theta\frac{\partial}{\partial\theta}\right) + \frac{1}{\sin^2\theta}\frac{\partial^2}{\partial\phi^2}\right]$ the Laplace–Beltrami operator on the 2-sphere $\mathbb{S}^2$, and where we expressed $\boldsymbol{e} = (\sin\theta\cos\phi,\,\sin\theta\sin\phi,\,\cos\theta)^\mathsf{T}$ in spherical coordinates. Equation 3.3 can be written symbolically as a continuity equation

$$\frac{\partial}{\partial t}P(\boldsymbol{r},\boldsymbol{e},t) = -\nabla\cdot\boldsymbol{J}\,, \tag{3.4}$$

which defines the current $\boldsymbol{J}$. To solve Eq. (3.3), we proceed in the following way: (i) we will move to Fourier space; (ii) we will use an expansion in terms of eigenfunctions of the Fokker–Planck operator; (iii) we will perform a multipole expansion; (iv) we will focus on the dependence of the probability on the z-direction, along which gravity applies; and (v) we will perform the inverse-Fourier transform.

The Fourier transform of Eq. (3.3) then reads

$$\frac{\partial}{\partial t}\widehat{P}(\boldsymbol{k},\boldsymbol{e},t) = iv_s\boldsymbol{e}\cdot\boldsymbol{k}\widehat{P}(\boldsymbol{k},\boldsymbol{e},t) - iv_gk_z\widehat{P}(\boldsymbol{k},\boldsymbol{e},t) - D_\mathrm{t}k^2\widehat{P}(\boldsymbol{k},\boldsymbol{e},t) + D_\mathrm{e}\mathsf{L}_\mathrm{e}\widehat{P}(\boldsymbol{k},\boldsymbol{e},t)\,. \tag{3.5}$$

Let us for the moment consider the simple case $v_s = 0$ and $v_g = 0$ which corresponds to a simple Brownian particle. Because the operator $\mathsf{O}_{FP} = (\frac{\partial}{\partial t} + D_t k^2 - D_e \mathsf{L}_e)$ is Hermitian, its eigenfunctions $e^{-D_t k^2 t} e^{-\lambda_n D_e t} Y_n^m(\theta, \phi)$ form an orthonormal basis of the space of our solutions, where $\lambda_n = n(n+1)$, $Y_n^m(\theta, \phi) = (-1)^m \sqrt{\frac{2n+1}{4\pi} \frac{(n-m)!}{(n+m)!}} P_n^m(\cos(\theta)) e^{im\phi}$ are the spherical harmonics including the Condon–Shortley phase factor, and $n, m \in \mathbb{N}$, $-n \leq m \leq n$. Additionally, because $\mathsf{O}_g = iv_g k_z$ is simply a multiplicative scalar, an eigenfunction of $\mathsf{O}_{FP} + \mathsf{O}_g$ is $e^{-(iv_g k_z + D_t k^2)t} e^{-\lambda_n D_e t} Y_n^m(\theta, \phi)$.

Taking into account the initial condition

$$\widehat{P}(\boldsymbol{k}, \boldsymbol{e}, t = t_0) = \frac{1}{(2\pi)^{\frac{3}{2}}} \int d^3 \boldsymbol{r} e^{-i\boldsymbol{k} \cdot \boldsymbol{r}} P(\boldsymbol{r}, \boldsymbol{e}, t = t_0) = \frac{1}{(2\pi)^{\frac{3}{2}}} e^{-ik_z a}$$

and the linearity of Eq. (3.5), we will search for solutions of the form

$$\widehat{P}(\boldsymbol{k}, \boldsymbol{e}, t) = e^{-\left(iv_g k_z + D_t k^2\right)t} e^{-ik_z a} \sum_{n=0}^{+\infty} \sum_{m=-n}^{+n} \widehat{P}_n^m(\boldsymbol{k}, t) e^{-D_e n(n+1)t} Y_n^m(\boldsymbol{e}) , \tag{3.6}$$

where the coefficients $\widehat{P}_n^m(\boldsymbol{k}, t)$ are determined by using the expression in Eq. (3.6) in Eq. (3.5) (see Appendix 3.1.6). Physically, the infinite sums on the right-hand side of Eq. (3.6) represent the increasingly faster decay with time of higher-order spherical harmonics [104].

Because of the rotational dynamics in our problem, it is convenient to explicitly highlight the underlying physical symmetries by expanding the full probability $P(\boldsymbol{r}, \boldsymbol{e}, t)$ in terms of spherical tensors, that is, the irreducible representations of the rotation operator. Each spherical tensor transforms like the eigenfunctions of the angular momentum of corresponding rank $n = 0, 1, 2, \ldots$, where the first three tensors represent the density ρ (monopole, $n = 0$), the polarization $\boldsymbol{D}$ (dipole, $n = 1$), and the nematic tensor $\mathbf{Q}$ (quadrupole, $n = 2$), respectively. The probability can then be expanded as

$$P(\boldsymbol{r}, \boldsymbol{e}, t) = \rho(\boldsymbol{r}, t) + \boldsymbol{D}(\boldsymbol{r}, t) \cdot \boldsymbol{e} + \boldsymbol{e} \cdot \mathbf{Q}(\boldsymbol{r}, t) \cdot \boldsymbol{e} + \ldots \tag{3.7}$$

In the large time limit, the monopole term $\rho(\boldsymbol{r}, t)$ will dominate the sedimentation process (while higher order terms in Eq. (3.7) are relevant for observables with shorter characteristic time scales). Its Fourier transform can be found by truncating the sum in Eq. (3.6) at the $n = 0$ term, that is

$$\hat{\rho}(k_z, t) = \frac{1}{\sqrt{4\pi}} e^{-\left(iv_g k_z + D_t k_z^2\right)t} e^{-ik_z a} \widehat{P}_0^0 . \tag{3.8}$$

After some computations (see Appendix 3.1.7), we can work out the equation governing the dynamics of $\widehat{P}_0^0$

$$\frac{\partial^2}{\partial t^2} \widehat{P}_0^0 + 2D_e \frac{\partial}{\partial t} \widehat{P}_0^0 + \frac{v_s^2}{3} k_z^2 \widehat{P}_0^0 = 0 , \tag{3.9}$$

which is the telegrapher's equation [138], and accounts for processes with a finite speed of propagation.

A solution of Eq. (3.9) reads $\widehat{P}_0^0(k_z, t) = e^{-D_e t}[\widehat{F}(k_z)e^{-iw(k_z)t} + \widehat{G}(k_z)e^{iw(k_z)t}]$, where $w(k_z) = (k_z^2 \frac{v_s^2}{3} - D_e^2)^{1/2}$, with $\widehat{F}(k_z)$ and $\widehat{G}(k_z)$ arbitrary functions of the wavevector in the z-direction k_z. The expression for the monopole is found from the inverse Fourier transform, and reads

$$
\begin{aligned}
\rho(z,t) &= \int_{-\infty}^{+\infty} \frac{dk_z}{\sqrt{2\pi}} \hat{\rho}(k_z, t) e^{ik_z z} \\
&= \frac{e^{-D_e t}}{\pi\sqrt{8}} \int_{-\infty}^{+\infty} dk_z e^{-iv_g k_z t - D_t k_z^2 t} e^{-ik_z a} e^{ik_z z} [\widehat{F}(k_z)e^{-iw(k_z)t} + \widehat{G}(k_z)e^{iw(k_z)t}].
\end{aligned}
$$

The term $w(k_z) = (k_z^2 v_s^2/3 - D_e^2)^{1/2}$ in the exponential makes it difficult to perform the inverse Fourier transform. However, because we are interested in the long-wavelength limit of the sedimentation profile, it is natural to consider a Taylor expansion of $w(k_z)$ around $k_z = 0$

$$
\rho(z,t) = \frac{e^{-D_e t}}{\pi\sqrt{8}} \int_{-\infty}^{+\infty} dk_z e^{-D_t k_z^2 t - iv_g k_z t} e^{ik_z z} e^{-ik_z a} \left[\widetilde{F} e^{-D_e t + \frac{v_s^2 k_z^2 t}{6D_e}} + \widetilde{G} e^{D_e t - \frac{v_s^2 k_z^2 t}{6D_e}} \right].
$$

where $\widetilde{F}$ and $\widetilde{G}$ are defined as follow

$$
\begin{aligned}
\widehat{F}(k_z)e^{-iw(k_z)t} &= \widehat{F}(k_z)e^{-D_e t + \frac{v_s^2 k_z^2 t}{6D_e} - iO((w(k_z)t)^2)} \\
&= e^{-D_e t + \frac{v_s^2 k_z^2 t}{6D_e}} \widehat{F}(k_z)e^{-iO((w(k_z)t)^2)} \\
&= e^{-D_e t + \frac{v_s^2 k_z^2 t}{6D_e}} \widetilde{F}
\end{aligned}
$$

and similarly for $\widetilde{G}$. Elementary integration yields

$$
\rho(z,t) = \frac{1}{\sqrt{8\pi}} \left[e^{-2D_e t} \frac{\widetilde{F}}{\sqrt{D_{\text{eff}}^- t}} e^{-(z-a-v_g t)^2/(4D_{\text{eff}}^- t)} + \frac{\widetilde{G}}{\sqrt{D_{\text{eff}}^+ t}} e^{-(z-a-v_g t)^2/(4D_{\text{eff}}^+ t)} \right], \qquad (3.10)
$$

where we have defined the effective diffusivities $D_{\text{eff}}^\pm \equiv D_t \pm \frac{v_s^2}{6D_e}$. That active motion enhances diffusion has been repeatedly observed in experimental [51] and theoretical works [121, 139]. By imposing that mass is conserved during the sedimentation process

$$
\frac{d}{dt} \int dz \rho(z,t) = 0,
$$

we can determine the functions $\widetilde{F} = \exp(2D_e t)$ and $\widetilde{G} = 1$.

In order to describe the sedimentation phenomena, we need to impose a reflective boundary condition at the confining wall located at $z = 0$. By integrating (3.3) over the orientation, we find

$$\frac{\partial}{\partial t}\rho(z,t) = -\frac{1}{2}v_s\frac{\partial}{\partial z}D(z,t) + v_g\frac{\partial}{\partial z}\rho(z,t) + D_t\frac{\partial^2}{\partial z^2}\rho(z,t)\,.$$

The associated continuity equation reads

$$\frac{\partial}{\partial t}\rho(z,t) = -\frac{\partial}{\partial z}J_z\,,$$

and by imposing no flux $J_z = 0$ at the wall, the boundary condition, of the Robin type, reads [**?**]

$$\left[D_t\frac{\partial}{\partial z}\rho(z,t) + v_g\rho(z,t) - \frac{1}{2}v_sD(z,t)\right]_{z=0} = 0\,. \tag{3.11}$$

Moreover, in large time limit, the monopole $\rho(z,t)$ dominate the sedimentation process and therefore the dipole $D(z,t)$ is negligible. Hence,

$$\left[D_t\frac{\partial}{\partial z}\rho(z,t) + v_g\rho(z,t)\right]_{z=0} = 0\,. \tag{3.12}$$

We rewrite eq.(3.10) as

$$\rho(z,t) = \rho_1(z,t) + \rho_2(z,t)\,,$$

where

$$\rho_1(z,t) = \frac{1}{\sqrt{8\pi}}\frac{e^{-(z-a-v_gt)^2/4D_{\text{eff}}^-t}}{\sqrt{D_{\text{eff}}^-t}}\,,$$

and

$$\rho_2(z,t) = \frac{1}{\sqrt{8\pi}}\frac{e^{-(z-a-v_gt)^2/4D_{\text{eff}}^+t}}{\sqrt{D_{\text{eff}}^+t}}\,.$$

In order to impose no net flux across the reflective wall, we use the method of images, but as known in the theory of partial differential equation [Sommerfeld] the appropriate image system consists of replacing the wall at $z = 0$ with a mirror source placed at $z = -a$ (in addition to the real source at $z = a$) and a continuous sequence of images which take place at all points $\xi < -a$ [140, 106, 107, 108, 109]. We can rewrite the probability density as

$$\rho_{\text{r}}(z,t) = \rho(z,t|a) + A\rho(z,t|-a) + \int_{-\infty}^{-a} k(\xi)\rho(z,t|\xi)d\xi\,, \tag{3.13}$$

By applying eq.(3.13) to our system, $\rho_r(z,t)$ reads

$$\rho_r(z,t) = \rho_{r1}(z,t|a) + \rho_{r2}(z,t|a) + A_1\rho_{r1}(z,t|-a) + A_2\rho_{r2}(z,t|-a) + \int\limits_{-\infty}^{-a} k_1(\xi)\rho_{r1}(z,t|\xi)d\xi$$

$$+ \int\limits_{-\infty}^{-a} k_2(\xi)\rho_{r2}(z,t|\xi)d\xi\,, \tag{3.14}$$

where the coefficients A_1, A_2, $k_1(\xi)$, and $k_2(\xi)$ are also found via the Robin boundary condition (see appendix 3.1.8) the solution yields

$$\rho_r(z,t) = \frac{v_g}{D_{\text{eff}}^-\sqrt{2}}\text{erfc}\left(\frac{z+a-v_gt}{2\sqrt{D_{\text{eff}}^-t}}\right)e^{-v_gz/D_{\text{eff}}^-} + \frac{1}{\sqrt{8\pi}\sqrt{2D_{\text{eff}}^-t}}\left[e^{\frac{-(z-a)^2}{4D_{\text{eff}}^-t}} + e^{\frac{-(z+a)^2}{4D_{\text{eff}}^-t}}\right]e^{\frac{-v_g(z-a)}{2D_{\text{eff}}^-} - \frac{v_g^2t}{4D_{\text{eff}}^-}}$$

$$+ \frac{v_g}{D_{\text{eff}}^+\sqrt{2}}\text{erfc}\left(\frac{z+a-v_gt}{2\sqrt{D_{\text{eff}}^+t}}\right)e^{-v_gz/D_{\text{eff}}^+} + \frac{1}{\sqrt{8\pi}\sqrt{2D_{\text{eff}}^+t}}\left[e^{\frac{-(z-a)^2}{4D_{\text{eff}}^+t}} + e^{\frac{-(z+a)^2}{4D_{\text{eff}}^+t}}\right]e^{\frac{-v_g(z-a)}{2D_{\text{eff}}^+} - \frac{v_g^2t}{4D_{\text{eff}}^+}}\,. \tag{3.15}$$

The steady state regime is given by taking the limit $t \to \infty$ of eq.(3.15) and reads

$$\lim_{t\to\infty}\rho_r(z,t) = \frac{2v_g}{D_{\text{eff}}^-\sqrt{2}}e^{-v_gz/D_{\text{eff}}^-} + \frac{2v_g}{D_{\text{eff}}^+\sqrt{2}}e^{-v_gz/D_{\text{eff}}^+} \tag{3.16}$$

We note that the correct boundary condition is given by eq.(11), but in the large time limit the dipole term vanishes; additionally, by matching our parameters with the experimental values in [51], for which D_{eff}^- is positive, it follows that $D_t > v_s^2/6D_e$ and $D_t^2 >> v_s^4/36D_e^2$, and that the Robin condition is satisfied in the large time limit.

In the following, we take the active particle's diameter σ, mass m and its translational diffusion coefficient D_t as the units of length, mass and diffusivity. Thus, we can measure rotational diffusivity in terms of $\widetilde{D}_e = D_t/\sigma^2$. A dimensionless measure of the relative strength of the self-propulsion to the diffusive behavior, that is, the relative persistence of the active motion, is given by the Péclet number $\mathcal{P} = v_s\sigma/D_t$.

Figure 3.2 shows the evolution of the density profile $\rho_r(z,t)$ found from our solution to the sedimentation process in Eq. (3.15). The initial position of the active particle is chosen at $z/\sigma = 40$. The corresponding initial density $\rho_r(z,t=0)$ is a Dirac delta distribution. As time progresses, we observe the shifting and flattening of the density profile. The steady state regime, given by Eq. (3.16) is characterized by an exponential decay, which match the sedimentation profile. We match our parameters with the experimental values given in

[51], where the Péclet number $0.5 \lesssim \mathcal{P} \lesssim 5$, and we find a near-quantitative agreement with the experiments. As predicted in theoretical works [118, 119], $\rho_r(z,t)$ decays exponentially away from the confining surface. Upon increasing the self-propulsion v_s, and therefore the effective diffusivity D_{eff}, the density profile tends to spread away from the wall as observed in the experiment [51]. This behavior is shown in Fig. 3.3.
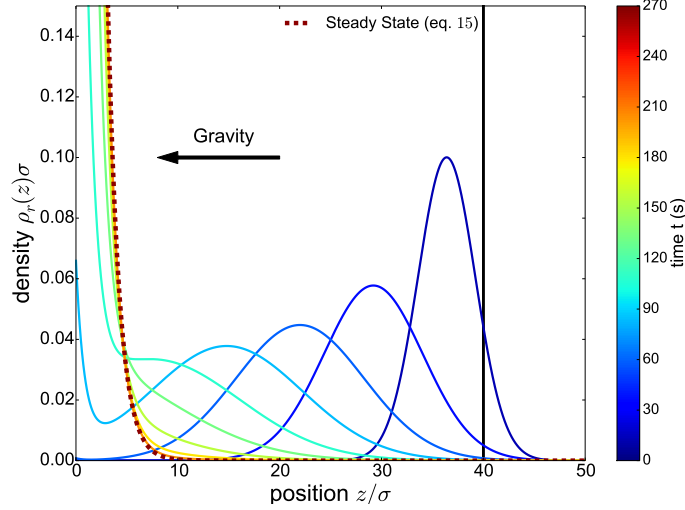
Figure 3.2 – Analytical sedimentation profile. Dependence of the density $\rho_r(z,t)$ on the position z, computed from Eq. (3.15), at different times for a system with one active Brownian particle under gravity in a cubic box of linear size $L = 50\sigma$ with wall on bottom ($z = 0$) and with gravity pointing in negative z-direction. At $t = 0$, the initial position of the active particle is at $z/\sigma = 40$, and the corresponding probability density is a Dirac delta distribution. With time we observe a spreading of the density profile and a shift in the direction of gravity. In the steady state regime, Eq. (3.16), we obtain a sedimentation profile characterized by an exponential decay with distance. Different curves correspond to different moments during the time evolution. The model parameters are $v_s/v_g = 1.1$, and $D_e\sigma^2/D_t = 1.8$.

The sedimentation length δ_{eff} is the characteristic length scale of the decay of $\rho_r(z,t)$ with z. It was found to depend strongly on the activity of the self-propelling particle [51, 118]. In general, we find a linear relationship governing the growth of δ_{eff} with D_{eff}/v_g, $\delta_{\mathrm{eff}} = c_0 + D_{\mathrm{eff}}/v_g$. The constant $c_0 \equiv c_0(v_g)$, and can be chosen to be zero, which is the value consistent with the experiments in [51]. The relationship between δ_{eff} and D_{eff} provides a connection between the microscopic behavior of the active particle and the long-time emergent dynamics [51]. The precise nature of the density profile in proximity of the confining surface will be affected by a number of effects such as: electrostatics, and hydrodynamic interactions of the active particles with the walls. For example, in a recent work [141], the authors show that

boundaries can steer Janus colloids, which, as a result, move above the boundary at a fixed distance. These effects are not taken into account here.
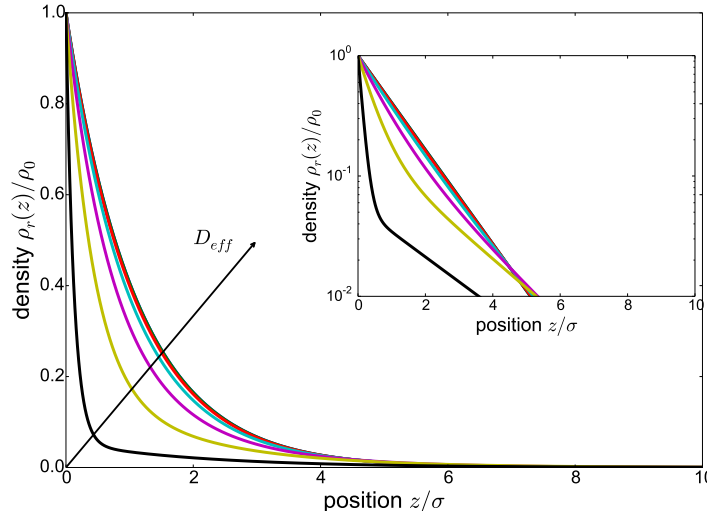
Figure 3.3 – Normalized sedimentation profile in the steady state regime for a reflective barrier. Dependence of the normalized density $\rho_{\mathrm{r}}(z)/\rho_0$ on the position z, in the steady state regime given by Eq. (3.16). Different curves correspond to the long time behavior of the sedimentation process for different values of the effective diffusion coefficient $D_{\mathrm{eff}}^{\pm} = D_{\mathrm{t}} \pm \frac{v_s^2}{6D_{\mathrm{e}}}$. We observe a good match with the experimental results in [51]. The model parameters are $D_{\mathrm{e}}\sigma^2/D_{\mathrm{t}} = 1.8$, and $v_s/v_g \in [1.2, 6.6]$.

Additional information about the active sedimentation process can be gained by considering the next term in the expansion Eq. (3.7), *i.e.* the polarization. The probability density function becomes

$$P(z, \cos(\theta), t) \simeq \rho(z, t) + D(z, t)\cos(\theta).$$

We can express the polarization D by means of the Legendre polynomials. Again, we are only interested in the z-direction. In Fourier space we find

$$D(k_z, t) = \sqrt{\frac{3}{4\pi}} e^{-(iv_g k_z - D_t k_z^2)t} e^{-ik_z a} \widehat{P}_1^0. \tag{3.17}$$

After some computations and applications of the boundary conditions (at $z = 0$, $J = 0$ and
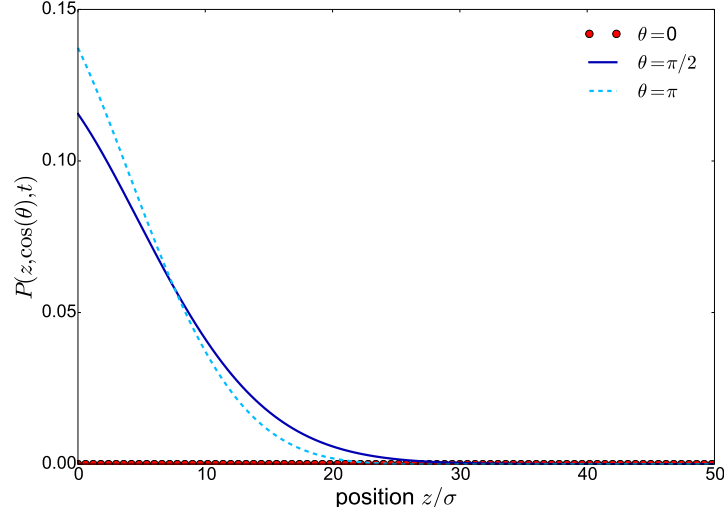
Figure 3.4 – Polarization. Dependence of the probability density function $P(z, \cos(\theta), t)$ on the position z, computed at large t for three values of the orientation $\theta \in \{0, \pi/2, \pi\}$. The model parameters are $v_s/v_g = 1.1$, and $D_e\sigma^2/D_t = 1.8$.

$\theta = \pi$), the probability density function reads

$$
\begin{aligned}
P(z, \cos(\theta), t) &= \frac{1}{\sqrt{8\pi}} \left[\frac{1}{\sqrt{D_{\text{eff}}^- t}} e^{-(z-a-v_g t)^2/(4D_{\text{eff}}^- t)} + \frac{1}{\sqrt{D_{\text{eff}}^+ t}} e^{-(z-a-v_g t)^2/(4D_{\text{eff}}^+ t)} \right] \\
&+ \sqrt{\frac{3}{4\pi}} \frac{\cos(\theta)}{\sqrt{2tD_t}} \left(\frac{B_1 + B_2}{C} + 1 \right) \cos(\alpha) \\
&\times e^{-(a^2 - 2az + z^2 + 2atv_g - 2tzv_g + t^2 v_g^2 - ft^2 D_e^2 v_s^2)/(4D_t t)} .
\end{aligned} \tag{3.18}
$$

We refer the readers to Appendix 3.1.9 for further details, and for the definition of the constants B_1, B_2, C, α and f.

After imposing the condition $P(z, \cos(\theta), t) \geq 0$, we show in Fig. 3.4 $P(z, \cos(\theta), t)$, at large t and for three values of the orientation $\theta \in \{0, \pi/2, \pi\}$. As predicted in [120], we observe an accumulation of active particles with a net polarization at the bottom wall, moving againts the wall ($\theta = \pi$). The qualitative picture is in agreement with [120].

3.1.3   Simulations of the collective motion

We next investigate a many-particle system composed of active Brownian particles under the effect of gravity. An analytical approach is a formidable task; thus we turn to numerical sim-

ulations. Even in the simpler case of passive Brownian particles, sedimentation is a complex process on account of velocity correlations and hydrodynamic interactions [142, 143, 144]. Because we are interested in the impact of active motion on the sedimentation, we can reduce the nonlinearities associated to hydrodynamic interactions by working in the dilute limit, similarly to [51, 120, 119, 118]. We do however consider weak hydrodynamic interactions via a short-ranged effective potential (see below). We perform Brownian dynamics simulations in 3D.

We consider again a typical Reynolds number $\mathcal{R} \ll 1$. An example of such particles in a biological setting is the microalga *Chlamydomonas reinhardtii*, which has a typical length $\sigma = 10$ μm and self-propulsion speed $v_s = 60$ μm s^{-1}. In colloidal physics active Janus particles have a typical linear size $\sigma = 1$ μm and self-propulsion speed which can vary as a function of the chemical gradient. As a reference, we can take the results found in experiment [51], where the self-propulsion $v_s = (0.3 - 4)$μm s^{-1}.

We describe the system by using two first-order stochastic differential equations, for N active particles

$$\frac{d}{dt}\boldsymbol{r}_i = v_s \boldsymbol{e}_i - \nabla\phi_{WCA} - v_g \widehat{\boldsymbol{z}} + \boldsymbol{\xi}_i \,, \tag{3.19}$$

$$\frac{d}{dt}\boldsymbol{e}_i = \boldsymbol{\xi}_{e_i} \times \boldsymbol{e}_i - \gamma\frac{\partial U}{\partial \boldsymbol{e}_i} \,, \tag{3.20}$$

where $i = 1, \ldots, N$, $\|\boldsymbol{e}_i\| = 1$ (implemented by means of a Lagrangian multiplier), v_g is the limiting velocity of a particle in the fluid under gravitational acceleration. In Eq. (3.19), $\phi_{WCA} = 4\epsilon[(\sigma/r_{ij})^{12} - (\sigma/r_{ij})^6] + \epsilon$ is the Weeks–Chandler–Anderson potential [111], $r_{ij} = |\boldsymbol{r_i} - \boldsymbol{r_j}|$, representing a hard-core repulsion between active particles, where σ is the linear size of the active particles, and ϵ is the energy scale of the repulsive interaction. In Eq. (3.20), $U = \sum_{i \neq j} \cos^2(\theta_{ij})$ is the Lebwohl–Lasher potential, which we use to model to first approximation the up-down symmetric interaction due to hydrodynamics that tends to align neighboring particles (see *e.g.* [145]).

We integrate Eqs. (3.19)-(3.20) with a discretization scheme based on the Euler–Maruyama algorithm in which we take into account the issue of multiplicative noise. We solve Eqs. (3.19)-(3.20) in a domain of volume $V = L^3$, with $L = 50\sigma$, with a reflective wall at the bottom at $z = 0$, and gravity pointing in negative z-direction. The filling fraction of our system is $\phi = N\frac{\pi}{6}\sigma^3/V = 10^{-3}$. Our results shown below are averaged over 10^4 independent simulations. Figure 3.5 shows the dependence of the density profile $\rho_{\rm r}(z,t)$ on the position z at different times. At $t = 0$, the active particles are randomly placed on a plane located at $z/\sigma = 40$. After some time, all the active particles sediment on the bottom wall. We observe a qualitative agreement of our simulation with our theory. We conclude that, as long as hydrodynamic interactions are weak, or the system is diluted enough, the theory derived for a single active particle is also applicable to a many-particle system.
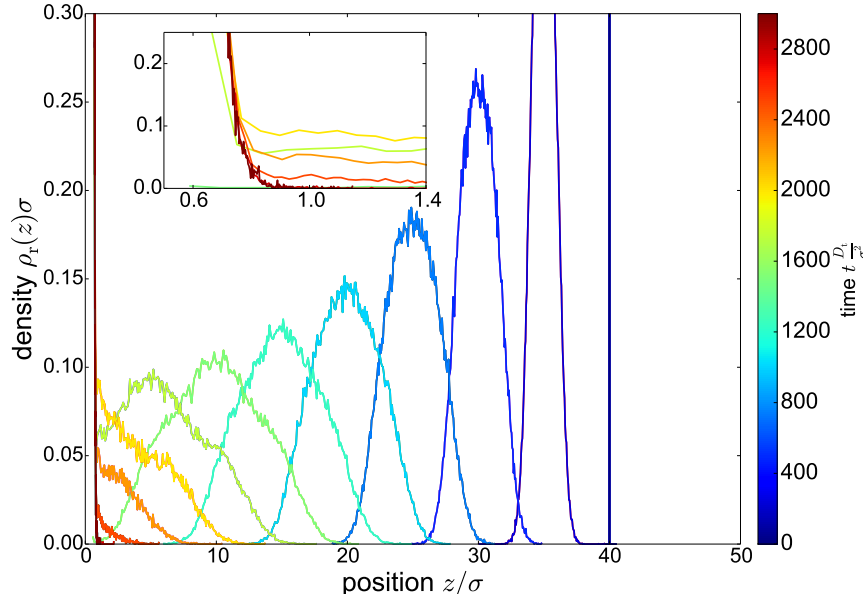
Figure 3.5 – Sedimentation profile from simulations. Dependence of the density $\rho_{\mathrm{r}}(z)$ on the position z at different times from simulations of $N = 1000$ active particles in a cubic box of linear size $L = 50\sigma$ with a wall on bottom $(z = 0)$ and with gravity pointing in negative z-direction. Results are averaged over 10^4 independent simulations. At $t = 0$, the active particles are randomly placed on a plane located at $z/\sigma = 40$. Different curves correspond to different moments during the time evolution. The model parameters are $v_s/v_g = 0.2$.

To measure the importance of the active motion with respect to the diffusion, we vary the Péclet number $\mathcal{P}$ by changing the self-propulsion v_s. Figure 3.6 shows the results of our simulations for the density profile at large t, and at different values of self-propulsion v_s.

When the activity is lower than the sedimentation velocity, $v_s/v_g = 0.2$, we observe a clear sedimentation profile. If $v_s/v_g = 1.0$, we observe a weaker sedimentation profile and a peak appears close to the upper part of the simulated domain. This peak is due to balance of the weak, effective hydrodynamic interactions introduced in our simulations with the self-propulsion and the effect of gravity. This is a consequence of the emerging polar order in sedimenting active particles as discussed in sec. 3.1.2.

Finally, as soon as $v_s > v_g$, we observe an accumulation of particles both on the bottom and top end, which differs from the classical sedimentation profile. We clearly highlight the importance of the activity of the particles, which allows them to move against an external force, in our case the gravity. From a biological point of view, this capacity play an important
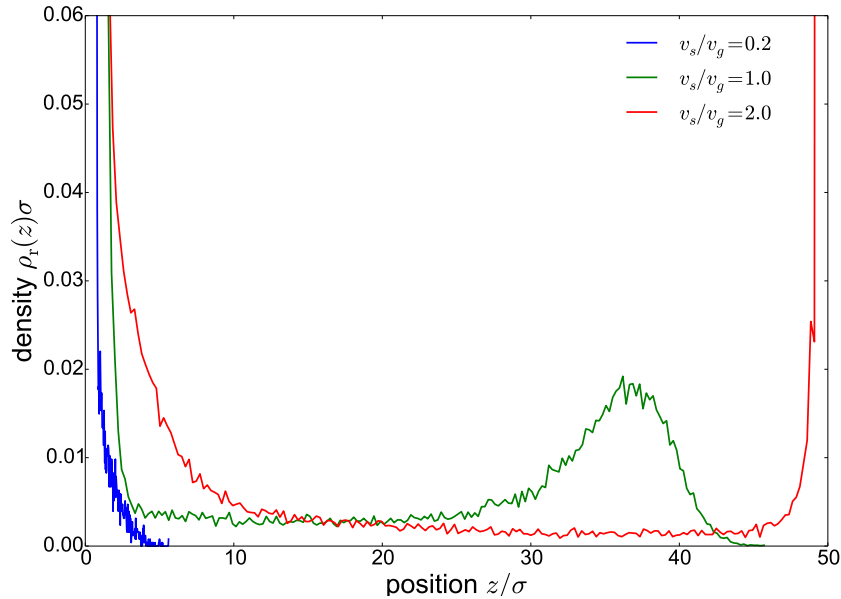
Figure 3.6 – Variation of the activity of the particles. Dependence of the density $\rho_{\mathrm{r}}(z)$ on the position z for a system with $N = 1000$ active particles, for large t. Different curves correspond to different values of v_s/v_g.

role, *e.g.* the algae need light to survive and they need to move against gravity to reach the surface.

3.1.4   Conclusion

The dynamics of sedimenting active particles prove to be an interesting arena where different nonequilibrium effects are at play, providing a testbed for our understanding of far-from-equilibrium phenomena. Including a self-propulsion to the motion of sedimenting colloidal particles ushers in a wealth of intriguing effects unimaginable from the classical results of Perrin [84]. This is in fact reflected in the considerable interested elicited by this problem [51, 132, 119, 120, 118, 117]. We study the sedimentation process of active Brownian particles in three dimensions. Firstly, we develop an analytical method describing the sedimentation profile of one active particle. We solve analytically the Fokker–Planck equation for an active particle in the presence of gravity and a confining wall at the bottom. We address the time evolution of the monopole, and find a solution which matches the late-time density profile in [51, 132]. Furthermore, we calculate the the dipolar term, and find the emergence of polar order at the bottom wall, with an accumulation of particles moving against the wall,

and a depletion of particles moving away from it. Imposing the no-flux condition at the confining bottom wall produces the steady-state solution. This solution is consistent with a number of previous results (most recently [117], for example). We recover the following experimental results found in [51, 132]: (i) the exponentially decaying density profile for the long-time regime and the steady state (ii) the increasing sedimentation length upon increase of the effective diffusivity. Importantly, our method retains the temporal dynamics of the sedimentation process, and therefore in addition to the steady state we also have access to the intermediate states. Our method also allows us to keep the coupling between the rotational and the positional degrees of freedom. In order to characterize more realistic conditions for the sedimentation process, we also consider many particles with weak, effective hydrodynamic interactions and we carry out Brownian dynamics simulations. We are able to measure the importance of the active motion at large times by varying the Péclet number $\mathcal{P}$. We recover the density profile, shown in Fig. 3.6, found experimentally in [132] and in numerical simulations [118] of active bottom-heavy particles. However, our model allows us to characterize more in details the richness of the sedimentation process of active particles as function of the activity. Furthermore, the sedimentation profile predicted by our analytical method for one active particle (see Fig. 3.3) matches our simulations for many particles (see Fig. 3.5).

3.1.5   Furutsu–Novikov–Donsker relation

To derive the Fokker–Planck equation, we consider the derivative of $P(\boldsymbol{r}, \boldsymbol{e}, t) = \langle \delta(\boldsymbol{r}(t) - \boldsymbol{r}) \delta(\boldsymbol{e}(t) - \boldsymbol{e}) \rangle$ with respect to time

$$
\frac{\partial}{\partial t} P(\boldsymbol{r}, \boldsymbol{e}, t) = - (v_s \boldsymbol{e} - v_g \boldsymbol{z}) \cdot \nabla P(\boldsymbol{r}, \boldsymbol{e}, t) - \nabla \cdot \langle \boldsymbol{\xi}(t) \delta(\boldsymbol{r}(t) - \boldsymbol{r}) \delta(\boldsymbol{e}(t) - \boldsymbol{e}) \rangle
$$
$$
- \nabla_{\boldsymbol{e}} \cdot \langle [\boldsymbol{\xi}_{\mathrm{e}}(t) \times \boldsymbol{e}] \delta(\boldsymbol{r}(t) - \boldsymbol{r}) \delta(\boldsymbol{e}(t) - \boldsymbol{e}) \rangle \,, \tag{3.21}
$$

where $\nabla_{\boldsymbol{e}} \equiv (\frac{\partial}{\partial e_x}, \frac{\partial}{\partial e_y}, \frac{\partial}{\partial e_z})^{\mathsf{T}}$, where the superscript T indicates transposition. To calculate the ensemble averages involving the noise ξ and ξ_e, we use the Furutsu–Novikov–Donsker relation [97, 98, 99, 100, 101, 102, 103, 104]

$$
\langle \xi(t) R[\xi] \rangle = \int_{-\infty}^{+\infty} dt' \langle \xi(t) \xi(t') \rangle \langle \frac{\delta R[\xi]}{\delta \xi(t')} \rangle \,, \tag{3.22}
$$

where $R[\xi]$ is an arbitrary functional of ξ. Physically, relation (3.22) helps obtain the dependence of a stochastic observable (e.g. the position of a colloidal particle) on the properties of the noise term.

3.1.6 Eigenfunction expansion

Inserting Eq. (3.6) into Eq. (3.5), and then multiplying by the complex conjugate of the spherical harmonics $Y_{n'}^{*m'}$ and integrating over the solid angle $d\Omega = \sin\theta d\theta d\phi$, we find

$$\frac{\partial}{\partial t}\widehat{P}_n^m(\boldsymbol{k},t) = -\sum_{n'=0}^{\infty}\sum_{m'=-n'}^{+n'}\widehat{P}_{n'}^{m'}(\boldsymbol{k},t)e^{-D_e(\lambda_{n'}-\lambda_n)t}\int d\Omega\, Y_{n'}^{m'}(\boldsymbol{e})\,(iv_s\boldsymbol{e}\cdot\boldsymbol{k})\,Y_n^{*m}(\boldsymbol{e})\,. \quad (3.23)$$

To proceed we define the following integrals

$$\mathcal{J}_{xn,n'}^{m,m'} = \int d\Omega\, Y_{n'}^{m'}(\theta,\phi)\sin\theta\cos\phi\, Y_n^{*m}(\theta,\phi)\,, \quad (3.24)$$

$$\mathcal{J}_{yn,n'}^{m,m'} = \int d\Omega\, Y_{n'}^{m'}(\theta,\phi)\sin\theta\sin\phi\, Y_n^{*m}(\theta,\phi)\,, \quad (3.25)$$

$$\mathcal{J}_{zn,n'}^{m,m'} = \int d\Omega\, Y_{n'}^{m'}(\theta,\phi)\cos\theta\, Y_n^{*m}(\theta,\phi)\,. \quad (3.26)$$

Equation (3.23) can then be written as

$$\frac{\partial}{\partial t}\widehat{P}_n^m(\boldsymbol{k},t) = -iv_s\sum_{n'=0}^{\infty}\sum_{m'=-n'}^{+n'}\widehat{P}_{n'}^{m'}e^{-D_e(\lambda_{n'}-\lambda_n)t}\left[k_x\mathcal{J}_{xn,n'}^{m,m'} + k_y\mathcal{J}_{yn,n'}^{m,m'} + k_z\mathcal{J}_{zn,n'}^{m,m'}\right]\,. \quad (3.27)$$

The calculation of the integrals $\mathcal{J}_{in,n'}^{m,m'}$ is straightforward [104, 89]. Equation (3.23) becomes

$$\begin{aligned}
\frac{\partial}{\partial t}\widehat{P}_n^m &= \frac{v_s}{2}e^{-2D_e(n+1)t}\left\{(k_y - ik_x)\widehat{P}_{n+1}^{m+1}\left[\frac{(n+m+2)(n+m+1)}{(2n+3)(2n+1)}\right]^{\frac{1}{2}}\right.\\
&\quad - 2ik_z\widehat{P}_{n+1}^m\left[\frac{(n+m+1)(n-m+1)}{(2n+3)(2n+1)}\right]^{\frac{1}{2}} + \widehat{P}_{n+1}^{m-1}\left[\frac{(n-m+2)(n-m+1)}{(2n+3)(2n+1)}\right]^{\frac{1}{2}}(k_y + ik_x)\right\}\\
&\quad - \frac{v_s}{2}e^{2D_ent}\left\{(k_y - ik_x)\widehat{P}_{n-1}^{m+1}\left[\frac{(n-m)(n-m-1)}{(2n+1)(2n-1)}\right]^{\frac{1}{2}} + 2ik_z\widehat{P}_{n-1}^m\left[\frac{(n+m)(n-m)}{(2n+1)(2n-1)}\right]^{\frac{1}{2}}\right.\\
&\quad \left. + (k_y + ik_x)\widehat{P}_{n-1}^{m-1}\left[\frac{(n+m)(n+m-1)}{(2n+1)(2n-1)}\right]^{\frac{1}{2}}\right\}\,. \quad (3.28)
\end{aligned}$$

We are interested in the dynamics along the direction of gravity, the z-direction; hence we specialize the previous equation to this case. The equation for the coefficients $\widehat{P}_n^m$ specialized to the z-direction reads

$$\frac{\partial}{\partial t}\widehat{P}_n^m = -v_s i k_z \left\{ e^{-2D_e(n+1)t}\widehat{P}_{n+1}^m \left[\frac{(n+m+1)(n-m+1)}{(2n+3)(2n+1)}\right]^{\frac{1}{2}} + e^{2D_e nt}\widehat{P}_{n-1}^m \left[\frac{(n+m)(n-m)}{(2n+1)(2n-1)}\right]^{\frac{1}{2}} \right\}.$$
(3.29)

3.1.7   Telegrapher's equation

Here we provide details of the computation of the telegrapher's Eq. (3.9). We start by considering the equations for the two coefficients $\widehat{P}_0^0$ and $\widehat{P}_1^0$

$$\frac{\partial}{\partial t}\widehat{P}_0^0 = -\frac{v_s}{\sqrt{3}}e^{-2D_e t}i k_z \widehat{P}_1^0\,,$$
(3.30)

$$\frac{\partial}{\partial t}\widehat{P}_1^0 = -v_s e^{-4D_e t}\sqrt{\frac{4}{15}}i k_z \widehat{P}_2^0 - \frac{v_s}{\sqrt{3}}e^{2D_e t}i k_z \widehat{P}_0^0\,,$$
(3.31)

combining these two Eqs. yields

$$\frac{\partial^2}{\partial t^2}\widehat{P}_0^0 = 2D_e\frac{v_s}{\sqrt{3}}e^{-2D_e t}i k_z \widehat{P}_1^0 - \frac{v_s}{\sqrt{3}}e^{-2D_e t}i k_z \frac{\partial}{\partial t}\widehat{P}_1^0\,,$$
(3.32)

and after replacing the last term on the right hand side with Eq. (3.31) we find

$$\frac{\partial^2}{\partial t^2}\widehat{P}_0^0 + 2D_e\frac{\partial}{\partial t}\widehat{P}_0^0 + \frac{v_s^2}{3}k_z^2\widehat{P}_0^0 = -v_s^2\sqrt{\frac{4}{45}}k_z^2\widehat{P}_2^0 e^{-6D_e t}\,.$$

Finally, neglecting the higher order yields

$$\frac{\partial^2}{\partial t^2}\widehat{P}_0^0 + 2D_e\frac{\partial}{\partial t}\widehat{P}_0^0 + \frac{v_s^2}{3}k_z^2\widehat{P}_0^0 = 0\,,$$

which is the telegrapher's Eq. (3.9).

3.1.8   Monopole reflective boundary

Let's start from the solution of a diffusion process

$$\rho(z,t) = \frac{e^{-(z-a-v_g t)^2/4Dt}}{\sqrt{4\pi Dt}}\,.$$

It is convenient to introduce a change in the independent variable [109]

$$\rho(z,t) = U e^{\frac{v_g(z-a)}{2D} - \frac{v_g^2 t}{4D}},$$

where

$$U = \frac{1}{\sqrt{4\pi D t}} e^{-(z-a)^2/4Dt}.$$

Finally

$$\rho(z,t) = U e^{\frac{v_g(z-a)}{2D} - \frac{v_g^2 t}{4D}} = \frac{1}{\sqrt{4\pi D t}} e^{-(z-a-v_g t)^2/4Dt}$$

In order to take into of the reflecting barrier, $\rho(r,t)$ becomes [106, 107, 108, 109]

$$\rho_{\mathrm{r}}(z,t) = \rho(z,t|a) + A\rho(z,t|-a) + \int_{-\infty}^{-a} k(\xi)\rho(z,t|\xi)d\xi, \qquad (3.33)$$

which tells you that an isolated point (image) $z = -a$ is not sufficient, but we need a continuous sequence of images which take place at all points $\xi < -a$. The Robin boundary condition for our system reads

$$\left[D_t \frac{\partial}{\partial z}\rho_{\mathrm{r}}(z,t) + v_g\rho_{\mathrm{r}}(z,t) \right]_{z=0} = 0 \iff \left[D_t \frac{\partial}{\partial z}U_{\mathrm{r}} + \frac{1}{2}v_g U_{\mathrm{r}} \right]_{z=0} = 0,$$

then

$$\sqrt{4\pi D_t t}\, U_r = e^{-(z-a)^2/4D_t t} + A e^{-(z+a)^2/4D_t t} + \int_{-\infty}^{-a} k(\xi)e^{-(z-\xi)^2/4D_t t}d\xi.$$

By applying the Robin boundary condition (3.33) reads

$$\frac{a}{2t}e^{-a^2/4D_t t}(1-A) - D_t k(-a)e^{-a^2/4D_t t} + D_t \int_{\infty}^{-a} \frac{\partial}{\partial \xi}k(\xi)e^{-\xi^2/4D_t t}d\xi - \frac{1}{2}v_g e^{-a^2/4D_t t}(1+A)$$

$$- \frac{1}{2}v_g \int_{\infty}^{-a} k(\xi)e^{-\xi^2/4D_t t}d\xi = 0 \qquad (3.34)$$

By setting the terms of different time dependance individually equal to zero, the coefficients A and $k(\xi)$ read

- $A = 1$

- $k(-a) = -\frac{v_g}{D_t}$

- $k(\xi) = -\frac{v_g}{D_t}e^{\frac{2v_g(\xi+a)}{D_t}}$

By replacing the function and coefficient inside the equation, the solution for U_r is given by

$$\sqrt{4\pi D_t t}U_r = e^{-(z-a)^2/4D_t t} + e^{-(z+a)^2/4D_t t} - \int\limits_{-\infty}^{-a} \frac{v_g}{D_t}e^{\frac{2v_g(\xi+a)}{D_t}}e^{-(z-\xi)^2/4D_t t}d\xi \,,$$

and by rewriting the integral term

$$-\int\limits_{-\infty}^{-a} \frac{2v_g}{D_t}e^{\frac{v_g(\xi+a)}{D_t}}e^{-(z-a)^2/4D_t t}d\xi = \frac{2v_g}{D_t}\int\limits_{a}^{\infty} e^{\frac{v_g(\xi-a)}{D_t}}e^{-(z+\xi)^2/4D_t t}d\xi = \frac{v_g}{D_t}\int\limits_{a}^{+\infty} e^{\frac{v_g(\xi-a)}{2D_t}}e^{-(\xi-a)^2/4D_t t}d\xi$$

and by doing a change of variable [109] for the limits of the integral U_r reads

$$U_r = \frac{1}{\sqrt{4\pi D_t t}}\left[e^{-(z-a)^2/4D_t t} + e^{-(z+a)^2/4D_t t}\right] + \frac{v_g}{D_t\sqrt{\pi}}e^{(\frac{v_g^2 t}{4D_t} - \frac{v_g(z+a)}{2D_t})}\int\limits_{\frac{z+a-v_g t}{2\sqrt{D_t t}}}^{+\infty} e^{-\eta^2}d\eta \,.$$

Finally, the complete solution reads

$$\rho_r(z,t) = U_r e^{\frac{v_g(z-a)}{2D_t} - \frac{v_g^2 t}{4D_t}}$$

$$= \frac{1}{\sqrt{4\pi D_t t}}\left[e^{-(z-a)^2/4Dt} + e^{-(z+a)^2/4D_t t}\right]e^{(\frac{v_g(z-a)}{2D_t} - \frac{v_g^2 t}{4D_t})} + \frac{v_g}{D_t\sqrt{\pi}}e^{-v_g z/D_t}\int\limits_{\frac{z+a-v_g t}{2\sqrt{D_t t}}}^{+\infty} e^{-\eta^2}d\eta \,.$$

$$(3.35)$$

3.1.9   Probability density function

We want to take into account the polarization $D(z,t)$, in the probability density function $P(z, \cos(\theta), t)$, defined in Fourier space as

$$D(k_z, t) = \sqrt{\frac{3}{4\pi}}e^{-(iv_g k_z - D_t k_z^2)t}e^{-iak_z}\widehat{P}_1^0 \,.$$

We can find $\widehat{P}_1^0$ by using Eq. (3.29). From there, we can work out the associated telegrapher's equation and by neglecting the higher orders, we find

$$\frac{\partial^2}{\partial_t^2}\widehat{P}_1^0 - (4\sqrt{\frac{4}{15}} - \frac{2}{3})v_s^2 k_z^2 D_e \widehat{P}_1^0 = 0\,.$$

Simple computations yield

$$\widehat{P}_1^0 = C_1 e^{f v_s k_z D_e t} + C_2 e^{-f v_s k_z D_e t}\,,$$

where $f = \sqrt{4\sqrt{\frac{4}{15}} - \frac{2}{3}}$. By applying the inverse Fourier transform

$$D(z,t) = \sqrt{\frac{3}{8\pi^2}} \left[\frac{C_1}{\sqrt{2tD_e}} e^{-(a-z+v_g t + f it D_e v_s)^2/4tD_t} + \frac{C_2}{\sqrt{2tD_e}} e^{-(a-z+v_g t - f it D_e v_s)^2/4tD_t} \right]\,.$$

We only consider the two first terms of the probability density function

$$P(z,\cos(\theta),t) \simeq \rho(z,t) + D(z,t)\cos(\theta)$$

and by plugging in the polarization, and focusing only on the real part of the exponentials, the probability density function reads

$$P(z,\cos(\theta),t) = \frac{1}{\sqrt{8\pi}} \left[e^{-2D_e t} \frac{\widetilde{F}}{\sqrt{D_{\text{eff}}^- t}} e^{-(z-a-v_g t)^2/(4D_{\text{eff}}^- t)} + \frac{\widetilde{G}}{\sqrt{D_{\text{eff}}^+ t}} e^{-(z-a-v_g t)^2/(4D_{\text{eff}}^+ t)} \right]$$

$$+ \sqrt{\frac{3}{8\pi^2}} \frac{\cos(\theta)}{\sqrt{2tD_t}} e^{-(a^2 - 2az + z^2 + 2atv_g - 2tzv_g + t^2 v_g^2 - f^2 t^2 D_e^2 v_s^2)/2D_t} \left[C_1 + C_2 \right] \cos(\alpha)\,, \tag{3.36}$$

where

$$\alpha = \frac{-af D_e v_s + fz D_e v_s - ft D_e v_g v_s}{2D_t}\,.$$

In order to find the coefficients C_1 and C_2, we apply the Robin boundary conditions at $z = 0$, $J_z = 0$, to eq.(3.4). Moreover, $\widetilde{F} = e^{2D_e t}$ and $\widetilde{G} = 1$ to keep the mass constant over time. After some computations we find

$$C_1 = \frac{C_2 B_1 + B_2}{C}\,, \tag{3.37}$$

where

$$B_1 = -(-v_s + v_g)\frac{-1}{4\sqrt{tD_t}}\sqrt{\frac{3}{\pi}}e^\Lambda \cos(\Omega) - D_t\sqrt{\frac{3}{\pi}}\frac{\cos(\pi)}{8tD_t\sqrt{tD_t}}e^\Lambda \cos(\Omega)$$

$$- \frac{-1}{4\sqrt{tD_t}}\sqrt{\frac{3}{\pi}}e^\Lambda fD_e v_s \sin(\Omega)\,, \tag{3.38}$$

$$\Omega = \frac{faD_e v_s + ftD_e v_g v_s}{2D_t}\,, \tag{3.39}$$

$$\Lambda = \frac{-a^2 - 2atv_g - t^2 v_g^2 + f^2 t^2 D_e^2 v_s^2}{4tD_t}\,, \tag{3.40}$$

and

$$B_2 = -(-v_s + v_g)\frac{1}{\sqrt{8\pi}}\left[\frac{1}{\sqrt{D_{\text{eff}}^- t}}e^{-(z-a-v_g t)^2/(4D_{\text{eff}}^- t)} + \frac{1}{\sqrt{D_{\text{eff}}^+ t}}e^{-(z-a-v_g t)^2/(4D_{\text{eff}}^+ t)}\right]$$

$$- D_t\frac{(a+v_g t)}{2\sqrt{2\pi}}\left[\frac{e^{(a+v_g t)^2/(4D_{\text{eff}}^- t)}}{2tD_{\text{eff}}^- \sqrt{tD_{\text{eff}}^-}} + \frac{e^{(a+v_g t)^2/(4D_{\text{eff}}^+ t)}}{2tD_{\text{eff}}^+ \sqrt{tD_{\text{eff}}^+}}\right]\,, \tag{3.41}$$

and

$$C = (-v_s + v_g)\frac{-1}{4\sqrt{tD_t}}\sqrt{\frac{3}{\pi}}e^\Lambda \cos(\varphi) + D_t\left[-\sqrt{\frac{3}{\pi}}\frac{(a+v_g t)}{8tD_t\sqrt{tD_t}}e^\Lambda \cos(\varphi)\right.$$

$$\left. - \sqrt{\frac{3}{\pi}}\frac{-1}{4t\sqrt{tD_t}}e^\Lambda fD_e v_s \sin(\varphi)\right]\,, \tag{3.42}$$

$$\varphi = \frac{-faD_e v_s - ftD_e v_g v_s}{2D_t}\,. \tag{3.43}$$

Finally, the probability density function is given by

$$P(z, \cos(\theta), t) = \frac{1}{\sqrt{8\pi}}\left[\frac{1}{\sqrt{D_{\text{eff}}^- t}}e^{-(z-a-v_g t)^2/(4D_{\text{eff}}^- t)} + \frac{1}{\sqrt{D_{\text{eff}}^+ t}}e^{-(z-a-v_g t)^2/(4D_{\text{eff}}^+ t)}\right]$$

$$+ \sqrt{\frac{3}{4\pi}}\frac{\cos(\theta)}{\sqrt{2tD_t}}\left[C_2\cos(\alpha)\left(\frac{B_1}{C} + 1\right) + \frac{B_2}{C}\cos(\alpha)\right]$$

$$\times e^{-(a^2 - 2az + z^2 + 2atv_g - 2tzv_g + t^2 v_g^2 - ft^2 D_e^2 v_s^2)/(4D_t t)}\,. \tag{3.44}$$

For the sake of simplicity we set $C_2 = 1$.

3.2 Light dependent motility of microalgae induces pattern formation in confinement

This work is in collaboration with Dr. Bäumchen, Dr. Mazza, Dr. Wilczek and Dr. Fragkopoulos. The results presented in this section are mainly from the simulations and were presented during conferences. Regarding the paragraph 'Being closer to reality', the results are preliminary and soon an arXiv version with the experimental results will be submitted.
Dr. Fragkopoulos built the experimental set-up and performed the experiments. I developed and performed the simulations. Dr. Fragkopoulos and I are writing the paper with the support of Dr. Bäumchen, Dr. Mazza and Dr. Wilczek.

A collection of self-propelled particles can undergo complex dynamics due to hydrodynamic and steric interactions. In highly concentrated suspensions, it is possible for such particles to form large-scale concentration patterns, where the suspension separates into regions of high and low particle concentrations. This can be attributed to the interactions of the particles with boundaries, their specific particle-particle interactions, or other particle specific motility behavior. Since many biological microswimmers, such as the bacteria *E. coli* and the algae *C. reinhardtii*, are sensitive to a umber of external stimuli, we investigated if this phenomenon is related to phototactic, gravitactic or chemotactic mechanism. We found that these properties are not the principal origin of the emergence of collective behavior, such as a localized aggregation of particles, and another mechanism is involved: the motility of the particles. The observed pattern formation is switchable by lights and depends on the geometry of the confinement, both of which are not captured by current models and thus require a revision of the state-of-the-art theoretical approach. Moreover, we show that the use of active Brownian particles simulations designed to describe the effect of the local cell density and confinement on the dynamics re-create the pattern observed in the experiment. We represent the alga as an active Brownian particle, which moves with a self-propulsion function of the local cell density along a direction represented by an orientation subject to random fluctuation. The dynamics is described by two overdamped Langevin equations for the position and the orientation. These equations are integrated with a discretization scheme based on the Euler-Mayurama algorithm.

3.2.1 Introduction

A collection of self-propelled particles can undergo complex dynamics due to hydrodynamic and steric interactions. Typically, self-propelled particles move in an aqueous medium. Due to their size, viscous forces dominate, and inertial forces are negligible. We can characterize

this effect with the so-called Reynolds number, R, which gives the ratio of inertial to viscous forces. In highly concentrated particle suspensions, it is possible for such particles to form large-scale concentration patterns, where the active suspension is separated into regions of high and low particle concentrations [146, 147, 148, 149]. This can be attributed to the interactions of the particles with boundaries, their specific particle-particle interactions, or other particle specific motility behavior. It was shown that a suspension of the unicellular microalgae *C. reinhardtii*, a biflagellated puller-type miscroswimmer, confined in a quasi-2D box, may form pattern of high and low particle density regions under certain light and global particle density. In order to quantify and characterize the relation between the self-propulsion, tunable by light and the local particle density, we describe the system by means of active Brownian particles simulations. These simulations are designed to describe the effect of the local particle density and confinement on the dynamics to characterize the underlying mechanism of the aggregation pattern formation. We represent, e.g. the algae *C. reinhardtii*, as an active Brownian particle, which moves with a self-propulsion speed depending on the local particle density along a direction represented by an orientation subject to random fluctuation. The dynamics is described by two overdamped Langevin equations for the position and the orientation of the particle. These equations are integrated with a discretization scheme based on the Euler-Mayurama algorithm. The reminder of this work is organized as follows. Firstly, we introduce the model. Secondly, in the case of a quasi-2D rectangular box, we show the effects of the velocity and diffusion coefficient on the pattern formation. Thirdly, the effects of the geometry of the confinement, from quasi-2D rectangular box to quasi-2D cylindrical box are shown. Finally, as an example, we match our parameters with recent experimental results for the algae *C. reinhardtii*.

3.2.2   Minimalist model

We investigate a many-particle system composed of active Brownian particles under confinement in quasi-2D and 3D. We consider a typical Reynolds number $R \ll 1$, which tells that due to the micro-size of the particles the viscous force dominate and inertial forces are negligible. The microalgae *C. reinhardtii* is an example of such particles, which has typical length $\sigma = 10\mu m$ and self-propulsion speed $v_s = 60\mu m.s^{-1}$. The system is described by two overdamped Langevin equation for N active particles

$$\frac{d\boldsymbol{r}_i}{dt} = v_s \boldsymbol{e}_i - \nabla \Phi_{WCA} + \boldsymbol{\xi}_i \tag{3.45}$$

$$\frac{d\boldsymbol{e}_i}{dt} = \boldsymbol{\xi}_{\boldsymbol{e_i}} \times \boldsymbol{e}_i \,, \tag{3.46}$$

where v_s is the self-propulsion depending of the local particle density, $\langle \xi_i \xi_j \rangle = 2D\delta_{ij}\delta(t - t')$ and $\langle \xi_{e_i} \xi_{e_j} \rangle = 2D_e\delta_{ij}\delta(t - t')$ modelled the random fluctuations. The particle-particle interaction is given by the Week-Chandler-Anderson potential [111] $\Phi_{WCA} = 4\epsilon[(\sigma/r_{ij})^12 - (\sigma/r_{ij})^6] + \epsilon$, where σ is the particle diameter, ϵ is the energy scale of the repulsive interaction and $r_{ij} = |\boldsymbol{r_i} - \boldsymbol{r_j}|$. In the following, the term velocity is used for the measured speed, v_s, and the term self-propulsion is used for the natural speed, v_0, which is a speed of a single particle without interaction. We consider two kind of fluctuations: one called passive, given by the translational diffusion coefficient D, and the other one called active, given by the orientational diffusion coefficient D_e. The passive fluctuations represent the surrounding medium, the thermal fluctuation as well as the interactions with the others active particles [150, 151, 152]. By assuming the shape of the passive fluctuation [150], the translational diffusion coefficient reads

$$D = \sqrt{\frac{2c_0}{\rho_{loc}^p}} , \tag{3.47}$$

where c_0 is a positive constant and $p \in \{1, 2\}$ determines the dependence on the local particle density [146], and ρ_{loc} gives the number of neighboring particles in a given volume matched with experimental results. The active fluctuations are obtained from the effective diffusion coefficient [51, 105]

$$D_{eff} = D + \frac{v_s^2}{d(d-1)D_e} , \tag{3.48}$$

where d gives the dimension of the system. From this equation, the active fluctuation reads

$$D_e = \frac{v_s^2}{d(d-1)(D_{eff} - D)} . \tag{3.49}$$

In the following, three approaches will be used. Firstly, in order to describe the effect of the velocity and diffusion coefficients in a quai-2D rectangular box, we fixed the active fluctuation to a constant and we use two velocity shapes

- A step function

$$v_s = \begin{cases} v_0 & , \text{if } \rho_{loc} < \rho_{cri} \\ \frac{v_0}{b} & , \text{otherwise} \end{cases} , \tag{3.50}$$

  where ρ_{loc} is the local particle density, ρ_{cri} a critical density and b a multiplicative factor.

- An inverse function

$$v_s = \frac{k_0}{\rho_{loc}^2} , \tag{3.51}$$

where k_0 is a positive constant.

In order to characterize the pattern formation, we use the so-called clustering coefficient [150], C_M, based on the Shannon entropy, S. The Shannon entropy gives us the 'level' of information that we have on a process onto the system. Let us imagine that we divide our system into N states. If a process visit all the states with equal probability, we do not know in which state the process is. This corresponds to have a 'low' information on the process, the entropy is maximum. However, if a process only visits one specific state, we do know precisely in which state it is. This corresponds to have a 'high' information on the process, the entropy is minimum.

In order to obtain these states, we divide our system into M boxes and count the number of particle in each boxes. It is possible to associate a probability to each boxes and compute the Shannon entropy S

$$S = -\sum_{i=0}^{M} p_i \log(p_i) \,,$$

with $p_i = m_i/N$, N the total number of particles, m_i the number of particles inside the box i and M the total number of boxes. The clustering coefficient reads

$$C_M = \frac{\exp(S)}{M} \,. \tag{3.52}$$

From this coefficient we can compute a typical time scale for the pattern formation.

Secondly, in order to describe the effect of the boundary, we move from a quasi-2D rectangular box fo a quasi-2D cylindrical box, by using the same parameters. Finally, in order to compare our simulations with a more realistic system, we modify the shape of the velocity as well as the diffusion coefficients. The velocity reads

$$v_s = \frac{k_0}{\sqrt{\rho_{loc}}} \,. \tag{3.53}$$

The effective diffusion coefficient is found

$$D_{eff} = \frac{1}{\rho_{loc}^{3/2}} \,, \tag{3.54}$$

and the passive fluctuation

$$D = \frac{\sqrt{2c_0}}{\rho_{loc}} \,. \tag{3.55}$$

3.2.3 Results

3.2.3.1 Quasi-2D rectangular box
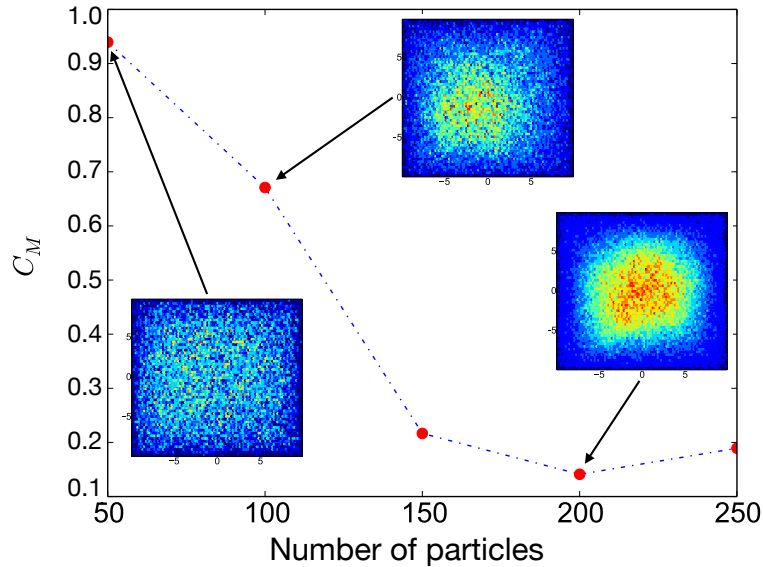
Figure 3.7 – Critical particle density. Clustering coefficient as a function of the number of particles.

In order to characterize the critical particle density, for which below a threshold the pattern cannot emerge, we use the clustering coefficient in Eq. (3.52) and shown in Fig. 3.7. The inset figures are the top view of the density map, which gives the density of particles in the system (red: high particle density, blue: low particle density). When the number of particle is below $N = 100$, a pattern cannot emerge, independently of the shape of the velocity and diffusion coefficients.

Velocity as a step function, Eq. (3.50). For the low-light intensity parameter space, we observe the emergence of a dense region at the center of the compartment, Fig. 3.8, left figure. By changing the parameters between low ($p = 2$) to high ($p = 1$) light intensity, we observe the emergence and annihilation of the pattern, Fig. 3.9, which is quantified by the clustering coefficient, C_M.

From this figure, we can find a time scale for the dynamics, which for the pattern formation is around $30s$ and $50s$ for the simulations. In comparison to experimental results obtained for the algae *C. reinhardtii*, a similar time scale was found, showing that the model can
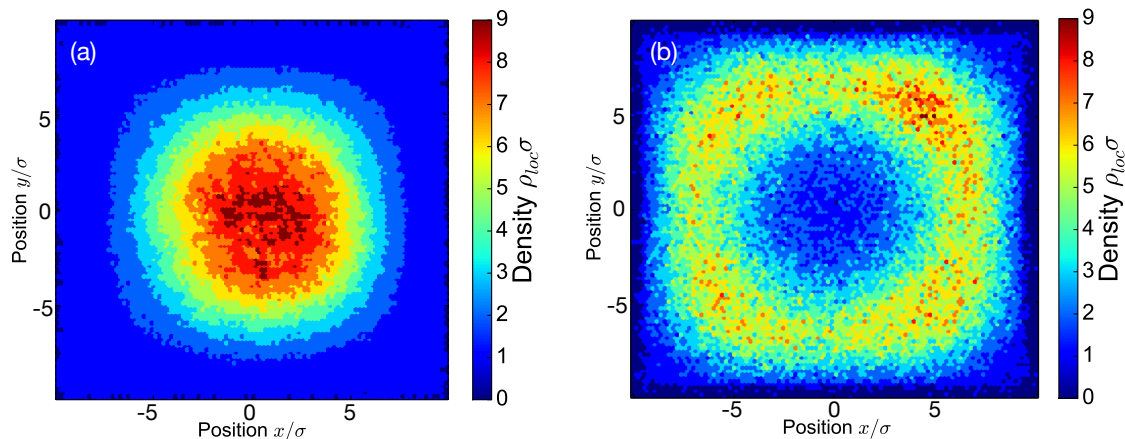
Figure 3.8 – Density map of the pattern formation: rectangle. Top view of a quasi-2D rectangular box with 500 particles, in the steady state regime. (a) Velocity as a step function. (b) Velocity as an inverse function.
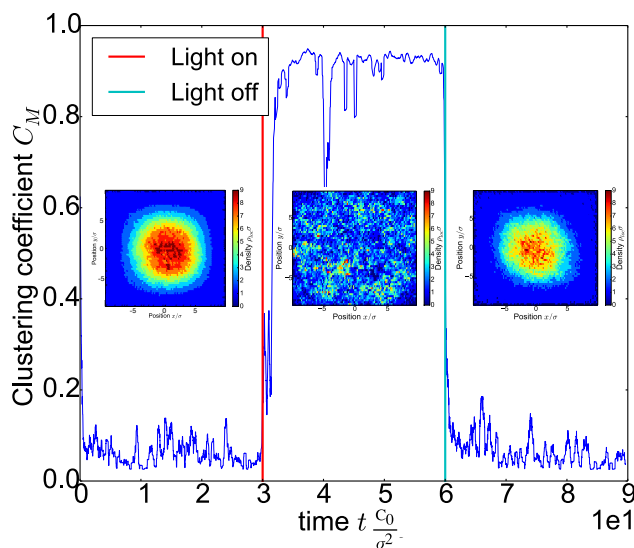
Figure 3.9 – Clustering coefficient as a function of time and light switchability.

capture multiple aspects of the aggregation phenomenon. As a first conclusion, these observations support the hypothesis that the interplay between the local particle density and the velocity as well as the diffusion coefficients is a key mechanism of the aggregation pattern formation.

In order to explore how the functional dependence of the velocity on density can modify the shape of the pattern, the velocity is now taken as an inverse function of the local particle

density.

Velocity as an inverse function of the local particle density, Eq. (3.51)**.** By changing the shape of the velocity, it is possible to modify the pattern formation. This result is shown in Fig. 3.8, right panel, and we observe the emergence of a ring.

In this section, we saw the effect of the light intensity, including in the passive fluctuation, on the emergence and the annihilation of the pattern. Moreover, by changing the shape of the velocity, the pattern can be modified and we observe the emergence of a ring.

3.2.3.2 Quasi-2D cylindrical box

In order to study the effect of the geometry of the compartment on the pattern formation, we move from a rectangular box to a cylindrical one. By using a step function for the velocity, we find a similar behavior to the rectangular box, Fig. 3.10, left panel.
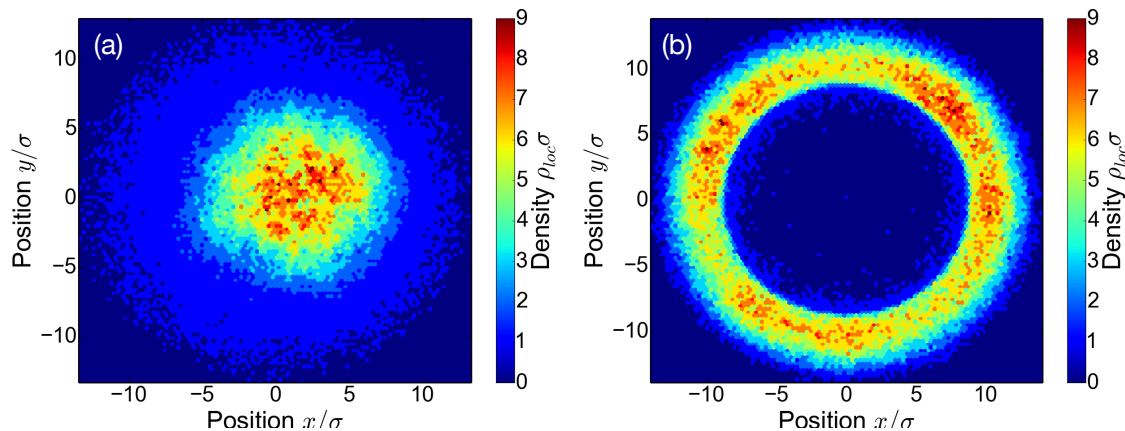
Figure 3.10 – Density map of the pattern formation: cylinder. Top of view a quasi-2D cylindrical boy with 500 particles, in the steady state regime. (a) Velocity as a step function. (b) Velocity as an inverse function.

However, the behavior change when the velocity is taken as an inverse function. We observe a huge accumulation at the boundary and not any more the emergence of a ring, Fig. 3.10, right panel.

3.2.3.3   Being closer to reality

From the previous section, we modify the shape of the velocity by using Eq. (3.53), according to experimental results $v_s \propto \rho_{loc}^{-0.5}$. Moreover, we fix v_0 with the self-propulsion speed measured for the algae *C. reinhardtii* in the dilute case $v_s = 60\mu\text{m.s}^{-1}$. Experimentally, the light condition modifies the minimum velocity but not the maximum velocity. As a first approach, and in order to keep the model as simple as possible, by minimizing the number of free parameters, we looked at the ratio between the maximum and minimum velocity. The result in quasi-2D is shown on Fig. 3.11, left figure. We have matched the global particle density with the experimental results. We observed a strong accumulation at the center of the compartment.
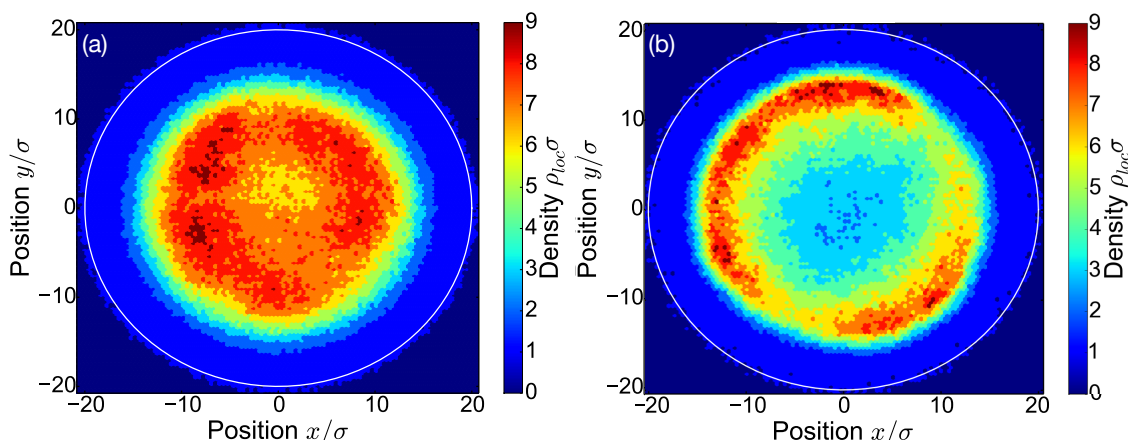
Figure 3.11 – Density map of the pattern formation: realistic model. (a) Top view of a quasi-2D cylindrical box with 300 particles, in the steady state regime. (b) Top view of a 3D cylindrical box with 2000 particles, in the steady state regime.

In order to study the effect of the global particle density on the pattern formation, we performed simulations with different densities. We show the distribution of the local particle density in Fig. 3.12. We observe two regions, characterize by two peaks, one at low density and the other one at high density. These two regions are characteristic of the pattern formation, with an aggregation at the center of the compartment.

So far, we only modified the geometry in the xy-plane, moving from a rectangular to a cylindrical box. Experimentally, it was also observed that the pattern is modified by the height of the compartment. In order to verify if our model capture this effect, we move from quasi-2D to 3D, Fig. 3.11, right figure.

For the same parameters used in quasi-2D, we observe the emergence of a ring pattern. Moreover, one can look at the radial distribution of the ring formation, Fig. 3.13, to explore
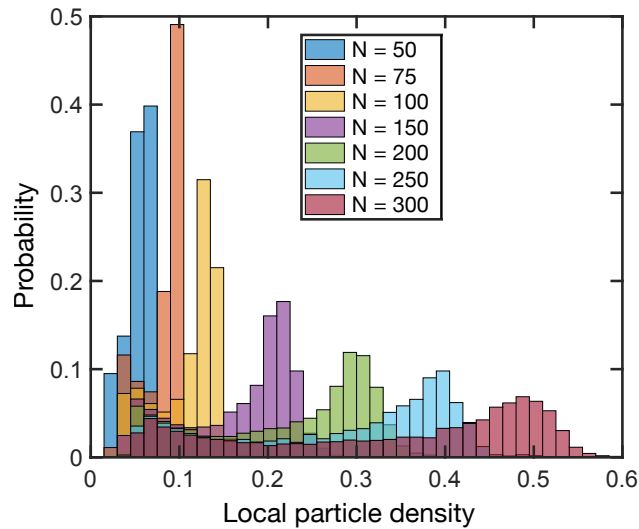
Figure 3.12 – Distribution of the local particle density. For different global particle densities (from 50 to 300 particles), we observe the emergence of two regions of low and high particle densities, characteristic of the pattern formation.

and compare with the experimental results the distance between the region of maximum particle density and the boundary.
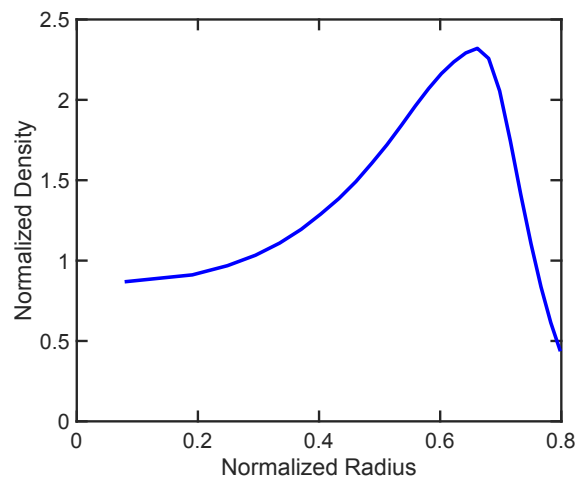
Figure 3.13 – Radial distribution of a 3D cylindrical box. We observe a pic of high particle density, characteristic of a ring formation.

Again, the model can capture another aspect of the pattern formation. In order to refine even more the model, the particles are now reflected with an outside angle of 16 degrees found experimentally in [114], the maximum velocity is fixed and the minimum velocity vary

accordingly to the light conditions, Fig. 3.14.
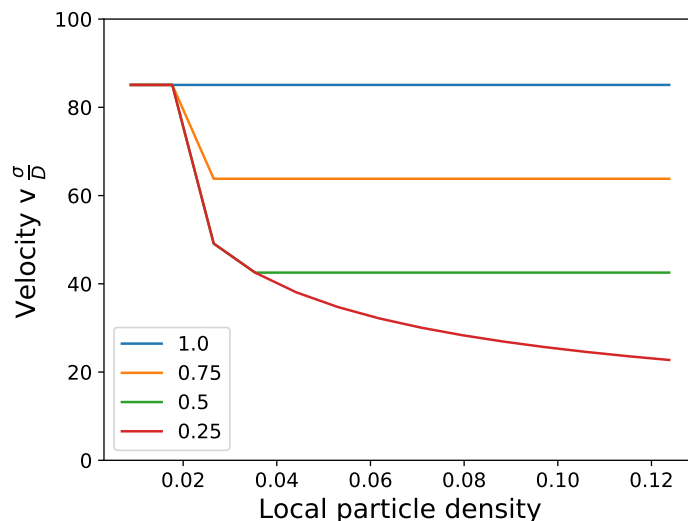
Figure 3.14 – Velocity as a function of the local particle density. After a plateau, fixed by a critical particle density matched with experimental results, the velocity decay accordingly to Eq. (3.53) and finally reach a minimum value.

With these new parameters, we can build a phase diagram describing the evolution of the pattern, from homogeneous to a ring via aggregation as shown in Fig. 3.15. In this figure, we observe the effects of the global particle density and velocity on the pattern formation. When the particle density is too low the pattern cannot be formed. However, when the particle density reaches a critical value, we observe a transition from a large to a small aggregation, to finally reaches for really high velocity a ring pattern formation.

This phase diagram catches the global picture but some work is still needed to find a better agreement with the experimental observations.

3.2.4 Conclusion

By means of active Brownian particles simulations, we studied the aggregation phenomena of active particles, for different activities, under confinement. By varying the activity as well as the diffusion coefficients as functions of the local cell density and in the case of many interacting active particles, we observed in the steady state regime the emergence of collective behaviors such as an aggregation of particles at the center of the compartment or a ring pattern. Moreover, by identifying the shape of the activity and the effective diffusion coefficient with the experimental results (in the case of the algae *C. reinhardtii*) and by using reflective boundary conditions with an outside angle of 16 degrees found experimentally [114],
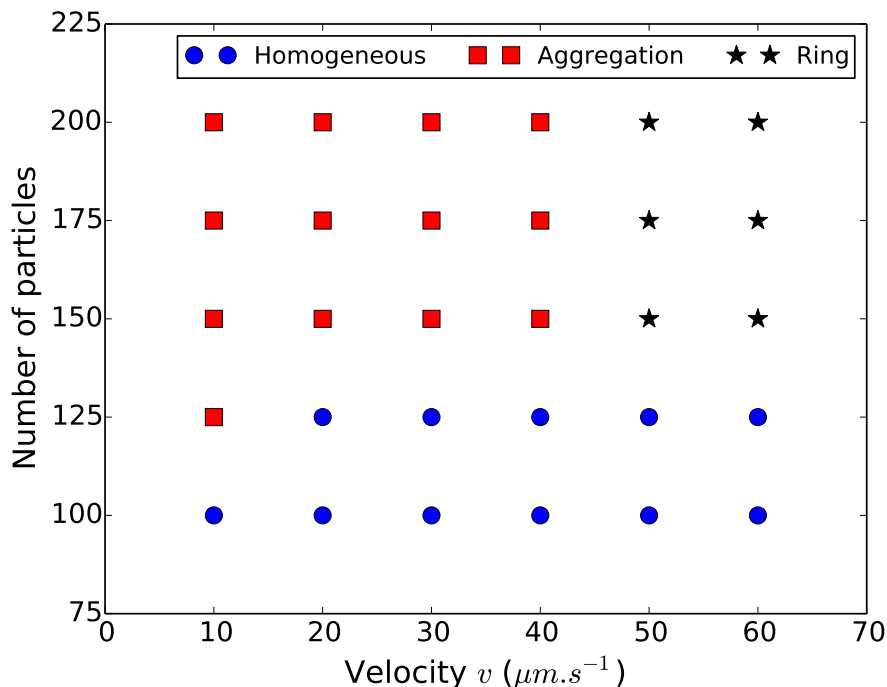
Figure 3.15 – Phase diagram. Global particle density as a function of the velocity for a quasi-2D cylindrical box.

it made possible to find some underlying mechanisms of the aggregation phenomena. The key ingredient is the relation between the self-propulsion and diffusion coefficients with the local cell density. We showed that the use of active Brownian particles simulations designed to describe the effect of the local cell density and confinement on the dynamics re-create the patterns observed in the experiment. In comparison to previous work [153, 154], having a direct access to the shape of the self-propulsion and the effective diffusion coefficient allows our simulation to be faithful to the experimental observations. Importantly, it was possible to match the global cell density used experimentally with the one used in the simulations, while other models need to reach a higher global cell density to describe similar collective behaviors.

3.3   Phenotypic differences in reversible attachment behavior reveal distinct *P. aeruginosa* surface colonization strategies

Summary

Biofilms are surface-adhered communities or suspended aggregates of bacteria that have increased tolerance to environmental stresses and antibiotics, and impact human health and the environment in complex ways. These biofilms can be harmful by causing diseases [155, 59], and can be beneficial by serving as commensals in various hosts as well as having application in bioremediation and energy production[156]. A critical step in forming a bacterial biofilm is surface sensing [157], where free-swimming planktonic cells detect, attach to, and physiologically respond to a surface. Moreover, before forming a bacterial biofilm, planktonic bacteria exhibit a random period of transient surface attachment known as 'reversible attachment'. For the case of the bacteria *P. aeruginosa*, there are at least two well-studied but distinct surface sensing circuits, the Wsp and Pil-Chp systems, that can contribute to initiating biofilm formation. Different strains of *P. aeruginosa*, such as PA01 and PA14, use these surface sensing mechanisms to varying extents. The PA01 strain uses the Wsp systems [158] leading to the surface deposition of the exopolysaccharide (EPS) Psl [159, 160] while PA14 uses the Pil-Chp system leading to the suppression of surface motility [161] and production of a Pel-dominant biofilm matrix [162]. Both strains PA01 and PA14 exhibit similar exponential trends of surface cell population increase and show different behavior for the early stage, when the cell are considered at the lineage level. By using community tracking methods at single-cell resolution, we examine how reversible attachment progresses during initial stages of surface sensing.

Moreover, we show that the use of an exactly solvable 'divide-detach' stochastic model, designed to examine the reversible attachment behaviors of *P. aeruginosa* PA01 and PA14 lineages in the form of family trees, reveal differences in their biofilm formation behavior during reversible attachment. Within this model, reversible attachment is described by two parameters: the division rate and the detachment rate. The attachment can be understood in terms of lineage time, meaning the time that lineage stays continually on the surface, and the detachment rate with the EPS production. Our model provides a framework to characterize different surface colonization strategies which lead to biofilm formation.

Our results suggest that PA01 and PA14 use two different surface colonization strategies. For PA01, the result is a steady progressive increase of a surface cell population that is irreversibly attached, meaning that it will commit to form a biofilm. For PA14, due to the

high rates of cell detachment, the result is to leave the surface for the early stage. Finally, our results unify disparate findings in the literature regarding early events in biofilm formation for PA01 and PA14.

Prof. Golestanian and Prof. Wong conceived the research topic as well as the project. Prof. Wong designed the experiment, Calvin built the experimental set-up and performed the experiments with the help of Prof. Wong. Prof. Golestanian designed the models, I developed and built the stochastic model under his supervision. Prof. Golestanian, Prof. Wong, Calvin and I interpreted the data and we wrote the paper together with the support of Prof. O'Toole, Prof. Parsek as well as Prof. Hogan.

Phenotypic differences in reversible attachment behavior reveal distinct *P. aeruginosa* surface colonization strategies

Calvin Kai-man Lee[*1], Jérémy Vachier[*2] , Jaime de Anda[1], Kun Zhao[3], Amy Baker[4], Rachel R Bennett[5], Catherine R Armbruster[6,9], Kimberley A Lewis[4], Rebecca L Tarnopol[7], Charles J Lomba[1], Deborah A Hogan[4], Matthew R Parsek[6], George A O'Toole[4], Ramin Golestanian[2,8†], Gerard CL Wong[1†]

[1]Department of Bioengineering, Department of Chemistry and Biochemistry, and California NanoSystems Institute, University of California Los Angeles, Los Angeles, CA 90095-1600, USA.
[2] Max Planck Institute for Dynamics and Self-Organization, Am Faßberg 17, 37077 Göttingen, Germany
[3] Key Laboratory of Systems Bioengineering (Ministry of Education), School of Chemical Engineering and Technology, Collaborative Innovation Center of Chemical Science and Engineering, Tianjin University, Tianjin 300072, People's Republic of China.
[4] Department of Microbiology and Immunology, Geisel School of Medicine at Dartmouth, Hanover, NH 03755, USA.
[5] School of Mathematics, University of Bristol, Bristol BS8 1TW, UK.
[6] Department of Microbiology, University of Washington, Seattle, Washington 98195, USA.
[7] Department of Plant and Microbial Biology, University of California Berkeley, Berkeley, CA 94720-3102, USA.
[8] Rudolf Peierls Centre for Theoretical Physics, University of Oxford, Oxford OX1 3PU, United Kingdom.
[9] Department of Microbiology and Molecular Genetics, University of Pittsburgh School of Medicine, Pittsburgh, PA, 15219.

[†] Corresponding authors: gclwong@seas.ucla.edu and ramin.golestanian@ds.mpg.de
[*] These authors contributed equally to this work.

1 Title

2 Phenotypic differences in reversible attachment behavior reveal distinct *P. aeruginosa* surface
3 colonization strategies

4 Authors

5 Calvin K. Lee*1, Jérémy Vachier*2, Jaime de Anda 1, Kun Zhao 3, Amy E. Baker 4, Rachel R. Bennett 5, Catherine R.
6 Armbruster 6,9, Kimberley A. Lewis 4, Rebecca L. Tarnopol 7, Charles J. Lomba 1, Deborah A. Hogan 4, Matthew R.
7 Parsek 6, George A. O'Toole 4, Ramin Golestanian 2,8†, and Gerard C. L. Wong 1†

8 Affiliations

9 1 Department of Bioengineering, Department of Chemistry and Biochemistry, and California NanoSystems Institute,
10 University of California Los Angeles, Los Angeles, CA 90095-1600, USA.

11 2 Max Planck Institute for Dynamics and Self-Organization (MPIDS), Am Fassberg 17, D-37077 Göttingen, Germany.

12 3 Key Laboratory of Systems Bioengineering (Ministry of Education), School of Chemical Engineering and Technology,
13 Collaborative Innovation Center of Chemical Science and Engineering, Tianjin University, Tianjin 300072, People's
14 Republic of China.

15 4 Department of Microbiology and Immunology, Geisel School of Medicine at Dartmouth, Hanover, NH 03755, USA.

16 5 School of Mathematics, University of Bristol, Bristol BS8 1TW, UK.

17 6 Department of Microbiology, University of Washington, Seattle, Washington 98195, USA.

18 7 Department of Plant and Microbial Biology, University of California Berkeley, Berkeley, CA 94720-3102, USA.

19 8 Rudolf Peierls Centre for Theoretical Physics, University of Oxford, Oxford OX1 3PU, United Kingdom.

20 9 Department of Microbiology and Molecular Genetics, University of Pittsburgh School of Medicine, Pittsburgh, PA,
21 15219.

22

23 † Corresponding authors:

24 gclwong@seas.ucla.edu

25 ramin.golestanian@ds.mpg.de

26 * These authors contributed equally to this work.

27 Abstract

28 Despite possessing the machinery to sense, adhere to, and proliferate on surfaces, it is commonly observed that bacteria
29 initially have a difficult time attaching to a surface. Before forming a bacterial biofilm, planktonic bacteria exhibit a
30 random period of transient surface attachment known as "reversible attachment" which is poorly understood. Using
31 community tracking methods at single-cell resolution, we examine how reversible attachment progresses during initial
32 stages of surface sensing. *Pseudomonas aeruginosa* strains PAO1 and PA14, which exhibit similar exponential trends of
33 surface cell population increase, show unanticipated differences when the behavior of each cell was considered at the
34 full lineage level and interpreted using the unifying quantitative framework of an exactly solvable stochastic model.
35 Reversible attachment comprises two regimes of behavior, processive and nonprocessive, corresponding to whether
36 cells of the lineage stay on the surface long enough to divide, or not, before detaching. Stark differences between PAO1
37 and PA14 in the processive regime of reversible attachment suggest the existence of two complementary surface

1

38 colonization strategies, which are roughly analogous to "immediate-" vs "deferred-gratification" in a prototypical
39 cognitive-affective processing system. PAO1 lineages commit relatively quickly to a surface compared to PA14 lineages.
40 PA14 lineages allow detaching cells to retain memory of the surface so that they are primed for improved subsequent
41 surface attachment. In fact, it is possible to identify motility suppression events in PA14 lineages in the process of
42 surface commitment. We hypothesize that these contrasting strategies are rooted in downstream differences between
43 Wsp-based and Pil-Chp-based surface sensing systems.

Keywords

45 Bacteria biofilms | *Pseudomonas aeruginosa* | Reversible attachment | Stochastic model | Surface sensing

Importance

47 The initial pivotal phase of bacterial biofilm formation known as "reversible attachment," where cells undergo a period
48 of transient surface attachment, is at once universal and poorly understood. What is more, although we know that
49 reversible attachment culminates ultimately in irreversible attachment, it is not clear how reversible attachment
50 progresses phenotypically as bacterial surface sensing circuits fundamentally alters cellular behavior. We analyze diverse
51 observed bacterial behavior one family at a time (defined as a full lineage of cells related to one another by division)
52 using a unifying stochastic model and show that it leads to new insights on the time evolution of reversible attachment.
53 Our results unify apparently disparate findings in the literature regarding early events in biofilm formation by PAO1 and
54 PA14 strains.

Introduction

56 Biofilms are surface-adhered communities or suspended aggregates of bacteria that have increased tolerance to
57 environmental stresses and antibiotics, and impact human health and the environment in complex ways. These biofilms
58 can be harmful by causing diseases (1, 2), and can be beneficial by serving as commensals in various hosts as well as
59 having applications in bioremediation and energy production (3). A critical step in forming a bacterial biofilm is surface
60 sensing (4), where free-swimming planktonic cells detect, attach to, and physiologically respond to a surface. Recent
61 work has shown that different appendages or extracellular structures, such as flagella (5, 6) or type IV pili (TFP) (7, 8) are
62 involved in activating cellular responses (e.g., protein production, motility, and biofilm formation) during surface
63 sensing. In many bacterial species, these responses are primarily controlled by intracellular secondary messenger
64 molecules, such as cyclic diguanylate (c-di-GMP) (9-16) and cyclic AMP (cAMP) (8, 17, 18). For the case of *Pseudomonas*
65 *aeruginosa*, a clinically relevant model system (19), there are at least two well-studied but distinct surface sensing
66 circuits, the Wsp and the Pil-Chp systems, that can contribute to initiating biofilm formation. In our current
67 understanding, the Wsp system senses through the membrane-bound, chemosensory-like Wsp protein complex which
68 localizes laterally along the cell body (10), activating the diguanylate cyclases WspR and c-di-GMP synthesis via a
69 mechanism that requires clustering of (20). On the other hand, the Pil-Chp system senses a surface through polarly-
70 localized TFP, which activates the adenylate cyclases CyaB and results in cAMP synthesis. Increased cAMP levels then
71 induces the production and secretion of PilY1, which in turn activate the diguanylate cyclases SadC and results in c-di-
72 GMP synthesis (17). Downstream consequences of c-di-GMP synthesis include exopolysaccharide (EPS) production and
73 motility suppression. Different strains of *P. aeruginosa*, such as PAO1 and PA14, utilize these surface sensing
74 mechanisms to varying extents. The PAO1 strain predominantly uses the Wsp system (21) leading to the surface
75 deposition of the EPS Psl (22, 23), while PA14 predominantly uses the Pil-Chp system leading to the suppression of
76 surface motility (17) and production of a Pel-dominant biofilm matrix (24).

77 Despite the existence of diverse machinery to sense, adhere to, and proliferate on surfaces, it is commonly observed
78 that bacteria initially seem to have a difficult time attaching to a surface, as indicated by typical flow cell studies where
79 *P. aeruginosa* often takes >20 h before attaching to the surface in large numbers (25, 26). This phenomenon was first
80 reports in the 1930s (27, 28). Using high speed microscopy to measure the distribution of surface residence times, it was
81 previously observed that the overwhelming majority of cells that land on the surface eventually detach, and it is only
82 after a prolonged and variable time lag that cells begin to rapidly cover the surface (8). Reversible attachment is

2

83 counterintuitive and difficult to understand for a number of reasons. We stress that the low apparent probability of
84 successful attachment is not simply a matter of cells "bouncing" off the surface. (During reversible attachment, it is not
85 uncommon for cells to attach and stay long enough to divide but then subsequently detach.) Moreover, the
86 unpredictability of reversible attachment cannot be circumvented with better measurement statistics: the duration of
87 reversible attachment always appears random and do not converge to a specific duration for the same initial conditions.
88 This combination of characteristics in reversible attachment, low probability of success, intrinsic time dependence, and
89 structurally random outcomes, suggests that use of a stochastic model may lead to new understanding. From a
90 foundational perspective of surface sensing, although we know that reversible attachment can culminate in irreversible
91 attachment, it is not clear how reversible attachment progresses phenotypically as bacterial surface sensing circuits
92 fundamentally alters cellular behavior, and ultimately improve on an initial attachment probability of effectively zero.

93 Here, we show that the use of an exactly solvable "divide-detach" stochastic model, designed to examine the reversible
94 attachment behaviors of *P. aeruginosa* PAO1 and PA14 lineages in the form of family trees, reveals differences in their
95 biofilm formation behavior during reversible attachment. Within this model, reversible attachment is described by two
96 parameters: effective division rate and effective detachment rate. We find that reversible attachment can be
97 understood if we analyze behavior using lineage time (the time a lineage stays continually on the surface) rather than an
98 experiment time, defined by time from inoculation. Specifically, reversible attachment comprises two regimes of
99 behavior, defined by whether cells of the lineage stay on the surface long enough to divide, or not, before detaching. For
100 lineages that detach before dividing at all, both PAO1 and PA14 behave similarly with near certain lineage "extinction,"
101 wherein the entire lineage detaches. For lineages that stay long enough to divide, PAO1 and PA14 show surprisingly
102 different behaviors. Our theoretical model provides a framework wherein time-dependent division and detachment
103 rates and distributions of lineages can be extracted from our experiments. Our results suggest that PAO1 and PA14
104 utilize two fundamentally different surface colonization strategies. For PAO1, individual lineages commit relatively
105 quickly to a surface compared to PA14, resulting in a steady progressive increase of a surface cell population that is
106 irreversibly attached (i.e., committed to forming a biofilm). In contrast, PA14 lineages have high rates of cell detachment
107 from surfaces. However, these detaching cells retain a memory of the surface (8), and ultimately form a planktonic
108 population that is primed for attachment, so that sudden increases in irreversibly attached surface cell populations can
109 occur. Our model provides a framework for categorizing different surface colonization strategies that lead to biofilm
110 formation, and it is conceivable that in principle each approach has its own advantages under different circumstances.

Results

Two regimes of reversible attachment in PAO1 and PA14 are revealed through lineage analysis

113 When monitoring the number of cells on the surface as a function of the time from inoculation of the flow cell (denoted
114 as experiment time), both strains follow a similar pattern (Figure 1). At early times, widespread detachment behavior is
115 observed. Despite both division and additional attachment, the surface population essentially remains constant for a
116 long and variable lag period (~10-20 h), after which the surface population will then begin to rise steeply, in a manner
117 that can be fit to an exponential growth curve. However, further distinguishing their behaviors in a finer pitch of detail is
118 difficult due to the random nature of reversible attachment. When comparing the surface population increases between
119 PAO1 and PA14, we observe nearly all possibilities: we either observe that PAO1 has a steeper and earlier rise in the
120 surface population compared to PA14, that PAO1 and PA14 have similar rises, or that PA14 has an earlier and steeper
121 rise than PAO1 (Figure S1). Furthermore, it is difficult to correlate these observations with macroscopic crystal violet
122 biofilm assays, where PAO1 has statistically significantly higher OD_{550nm} values compared to PA14 (Figure S2), which
123 suggests that PAO1 is capable of forming early biofilms faster than PA14. PAO1 has a mean $OD_{550nm} = 0.23$ with a 95%
124 confidence interval of (0.19, 0.26), while PA14 has a mean $OD_{550nm} = 0.14$ with a 95% confidence interval of (0.099,
125 0.18). Comparing the bootstrap sampling distributions of the mean OD_{550nm} values (which also generate the 95%
126 confidence intervals) show that PAO1 has a higher mean OD_{550nm} value than PA14 (p-value of 0.0002).Using the median
127 instead of the mean gives similar results. PAO1 has a median $OD_{550nm} = 0.22$ with a 95% confidence interval of (0.17,
128 0.29), while PA14 has a median $OD_{550nm} = 0.12$ with a 95% confidence interval of (0.094, 0.21). Comparing the
129 bootstrap sampling distributions of the median OD_{550nm} values (which also generate the 95% confidence intervals)

3

130   show that PAO1 has a higher median $\text{OD}_{550\text{nm}}$ value than PA14 (p-value of 0.003). These apparently conflicting

131   observations are not easily resolved with increased data collection since they arise from the intrinsic randomness of the

132   process and not from incurring measurement errors. This instrinsic randomness, which is not uncommon in different

133   aspects of biofilm formation, is usually neglected in analyses. In the present context, these effects complicate any

134   analysis of the reversible attachment behaviors in PAO1 and PA14, that depend on traditional methods to monitor the

135   number of surface cells as a function of experiment time or by macroscopic assays.

136   To account for the random nature of reversible attachment and the large fluctuations in the observations, we

137   investigate the evolution of bacterial behavior as a function of surface sensing progression using lineage analysis. We

138   monitor the time that a given isolated family, consisting of an attached cell (founder cell) and its progeny (daughter

139   cells) via division, stays continually on the surface, which we designate as lineage time $\left(t = t_{\text{lineage}}\right)$. For each family,

140   we begin tracking at the frame that an individual, founder bacterium attaches and assign this time as $t_{\text{lineage}} = 0$ h. We

141   continue tracking until either the entire family detaches, or until we lose track of that family (where we can no longer

142   distinguish individual cells, or the cells move out of the recording boundaries). This final time point is recorded as the

143   family's residence time. During reversible attachment regimes, families are categorized by whether a division event

144   occurs or not before detaching. We denote families that detach before dividing at all as the "nonprocessive" regime of

145   reversible attachment, and families that divide one or more times before detaching as the "processive" regime of

146   reversible attachment, using language from enzyme kinetics. It is important to note that these regimes are distinct from

147   irreversible attachment because during both regimes of reversible attachment, detachment is still prominent, while

148   during irreversible attachment, detachment is much less common. All families analyzed here are shown in Figure 2 and

149   Figure S3.

150   Cells in both nonprocessive and processive regimes are present throughout the entire biofilm formation process.

151   However, during the initial variable lag period, where the total surface population is not increasing, almost all cells are in

152   the nonprocessive regime, while very few cells are in the processive regime. As experiment time elapses, the general

153   observed trend is that cells in the processive regime become more common, while cells in the nonprocessive regime

154   become less common, especially during period of surface population exponential increase. However, it is difficult to

155   quantify such cellular behavior in this system because both regimes coexist with fluctuating proportions due to the

156   inherent randomness in single cell behavior, thereby complicating any analysis of biofilm behavior as a function of

157   experiment time. Thus, we utilize an analysis of lineage time to quantify the behavior of individual families in each

158   regime.

159   When comparing the two regimes for either PAO1 or PA14, we find that the residence times are drastically different. In

160   the nonprocessive regime, ~99% of cells stay on the surface for less than 30s for both strains. Furthermore, of the

161   ~20,000 tracked families in the nonprocessive regime (both PAO1 and PA14), we observe less than 10 families (~0.05%)

162   that have residence times comparable to the average doubling time of 1-2 h (Figure S4), which is the minimum residence

163   time for families in the processive regime. Detachment dominates attachment and division in the nonprocessive regime,

164   and essentially the surface population does not increase over the first 10-20 h of experiment time. In contrast, cells in

165   the processive regime are in continuous contact with the surface for longer periods of time. Moreover, virtually all of the

166   cells that remain surface engaged in the processive regime do so longer than cells in the nonprocessive regime. Finally,

167   cells in the processive regime grow and divide on the surface and have clearly altered their behavior compared to

168   "surface-naïve" planktonic cells, presumably as a consequence of activating surface sensing pathways.

169   Interesting trends emerge when comparing PAO1 and PA14 lineages in each regime. In the nonprocessive regime, we

170   find that PAO1 and PA14 exhibit similar behaviors, where cells experience the surface transiently. However, in the

171   processive regime, we see stark differences between PAO1 (44 families with 622 total descendants analyzed) and PA14

172   (31 families with 381 total descendants analyzed) (Figure S3). PAO1 families have more progeny retained on the surface,

173   while PA14 families have more progeny detaching, which can be seen in a broad range of metrics. For example, we can

174   compare single cell detachment behavior via the proportion of detachment vs division events. PAO1 has a statistically

175   significantly lower proportion, with 143 (33%) detachment vs 289 (67%) division events, compared to PA14, with 130

176   (43%) detachment vs 175 (57%) division events, according to the χ^2 test (p-value of 0.008). We can compare family-

4

177 averaged detachment behavior with family tree asymmetry parameter Λ (8). Λ values closer to zero indicate a more
178 symmetric family tree where more progeny are retained (more "two-legged" division nodes in the family tree, where
179 both post-division daughter cells stay on the surface), while Λ values closer to one indicate a more asymmetric family
180 tree where more progeny detach (more "one-legged" division nodes in the family tree, where one of the post-division
181 daughter cells detach from the surface). PAO1 family trees have a median $\Lambda = 0.33$ with a 95% confidence interval of
182 (0.25, 0.39), while PA14 family trees have a median $\Lambda = 0.42$ with a 95% confidence interval of (0.37, 0.52). Comparing
183 the bootstrap sampling distributions of the median tree asymmetry values (which also generate the 95% confidence
184 intervals) show that PAO1 family trees have a lower median Λ than PA14 family trees (p-value of 0.015). Overall, our
185 data show that PAO1 and PA14 display similar behaviors during the nonprocessive regime, but during the processive
186 regime, PAO1 shows a significantly higher likelihood of remaining surface-associated.

"Divide-detach" stochastic model highlights differences between PAO1 and PA14 in the processive regime of reversible attachment

189 Our observations suggest that PAO1 is less prone to detachment than PA14. However, these metrics do not properly
190 consider the collective time-dependent effects of division and detachment. For example, having more detachment
191 events earlier in lineage time would have a much greater effect on the resulting family architecture compared to the
192 same detachment events occurring several generations later. Even at the single cell level, gene expression is stochastic
193 and can occur in a burst-like, intermittent manner (29), which contributes additional randomness to that cell's behavior.
194 Consequently, the behavior of an individual bacterium (in terms of whether or not in every instance they stay on the
195 surface or detach after a division event) may be completely random and can only be described using statistical metrics.
196 Since biofilm formation can be seen as an evolution of a population of random individual bacteria, it can be described as
197 a stochastic process that depends on a number of control parameters as well as random environment variables.
198 Consistent with that contention, large fluctuations are often observed in measured parameters (e.g., family trees), and
199 these fluctuations are not easily mitigated with increased data collection since they arise from the intrinsic randomness
200 of the process and not from incurring measurement errors. In general, although it is acknowledged that the
201 unpredictability of single cell behavior can be important to surface sensing and biofilm development, this randomness is
202 rarely accounted for in traditional microbiological studies.

203 To obtain more time-dependent comparisons that incorporate division and detachment effects, and to help account for
204 the inherent randomness in observed family trees, we develop a "divide-detach" stochastic model. We use this model to
205 study the temporal evolution of the expected number of surface cells in a family tree, or population size (30-35). In this
206 model, the population size can increase or decrease by one bacterium as time evolves, and the population size can be
207 infinite or null. The corresponding sample space Ω is given by $\Omega = \{0, 1, 2, \dots, N, \dots\}^m$, where m is the number of
208 independent family trees, or different populations of bacteria. As time evolves, the population size can change and
209 result in a sequence $\omega \in \Omega$, where ω is the set of family trees that are in the experiment. For example, if there is $m = 1$
210 family tree, then $\omega = \{\omega_1\}$, and if there are m family trees, then $\omega = \{\omega_1, \dots, \omega_m\}$. However, because this is a
211 stochastic process, we cannot predict ahead of time what ω will be. Instead, what we know for ω are the set of possible
212 observations (states) Σ and the actual observations X_t from experiments. The set of states is given by $\Sigma =$
213 $\{0, 1, \dots, N, \dots\}$, where N represents the number of surface cells in a family and is infinite. Σ tells us what observations
214 (number of surface cells) are possible for any family tree during an experiment. The actual observations of ω are given
215 by $X_t(\omega) = \{X_t^1(\omega_1), X_t^2(\omega_2), \dots, X_t^m(\omega_m)\}$, which is how many surface cells are observed in each of the m family trees
216 at time point t during an experiment, and $X_t(\omega)$ is a random variable $X_t: \omega \to \Sigma$ that defines this stochastic process.
217 Having a random variable means that for the family trees ω and each time point t, we observe $X_t(\omega)$ taken from the set
218 of states Σ according to a certain (not necessarily known) probability distribution; but when we repeat the experiment,
219 we will not necessarily observe the same $X_t(\omega)$ for the same time point t and family trees ω. Figure 3 shows examples
220 of this process for $m = 1$ family tree (Figure 3a) and for $m = 3$ family trees (Figure 3b).

221 The dynamics of such a stochastic process are given by the evolution of the probability distribution $P(j, s + t | i, s)$, which
222 gives the probability of transitions between all states for all $t \geq 0$ and can be rewritten as $P_t(j|i)$. For a family tree, the
223 only possible transitions are the neighboring transitions, $n \to n + 1 = (n + 1|n) = \lambda_n$ and $n \to n - 1 = (n - 1|n) =$

224 μ_n. As a result, the dynamics of this process can be described by looking only at the evolution of the probability
225 distribution $P_t(n|n)$ for state $n \in \Sigma$. The rates λ_n and μ_n determine the intensity of increase (i.e., division) or decrease
226 (i.e., detachment), respectively, for state n. In a family tree, each cell can divide (with a division rate λ) or detach (with a
227 detachment rate μ), so the rates become $\lambda_n = \lambda n$ and $\mu_n = \mu n$. Figure 3c shows a schematic of the dynamics described
228 here (i.e., how the population size can increase or decrease).

229 The equation describing the evolution of this process is given by the Kolmogorov backward equation, also called the
230 master equation, which reads

$$\frac{dP_0}{dt} = \mu P_1, \qquad n = 0$$

and   1

$$\frac{dP_n}{dt} = (\mu)(n+1)P_{n+1} - (\lambda+\mu)(n)P_n + (\lambda)(n-1)P_{n-1}, \qquad n > 0,$$

231 where $P_n = P_n(t) = P_t(n|n)$, $P_{n+1} = P_{n+1}(t) = P_t(n+1|n)$, and $P_{n-1} = P_{n-1}(t) = P_t(n-1|n)$. We refer the readers
232 to the methods to find the details of the solution to this equation.

233 Experimentally, by having access to m independent family trees, it is possible to build the probability distribution by
234 counting the number of families that have zero cells, one cell, two cells, and so on, at a given lineage time t. In other
235 words, for each time point t, we plot the actual observations $X_t(\omega)$ on a histogram to derive the probability of each of
236 the states n occurring. For families in the processive regime of reversible attachment, we avoid potential problems
237 arising from tracking limitations by selecting $m = 11$ families for PAO1 (out of 44 families) and $m = 12$ families for PA14
238 (out of 31 families), with a t_{lineage} range of 0-12 h for PAO1 and 0-10 h for PA14 (see Figure S3 caption for family
239 selection criteria).

240 Comparing the experimental data with the model is not straightforward when using the probability distributions
241 directly. In the experimental data, there are a finite number of families and a finite number of cells in a family, which
242 means that it is difficult to generate distributions that are well populated for quantitative comparisons. To overcome this
243 limitation, we employ the method of moments, which provides information about the distributions, to fit the model to
244 experimental data and obtain the rates. Instead of comparing the experimental and model probability distributions
245 $P_n(t)$, we compare the experimental and model moments, $\langle n(t)^k \rangle$, where k is the k-th moment. We can calculate the
246 experimental moments directly from the experimental probability distribution, and we can obtain the model moments
247 from the model probability distribution (eq. 2) given by the master equation (eq. 1). The equations for the model
248 moments are shown in the methods (eq. 3-4). To compare experiment with model, we use the first two moments. The
249 first moment is the mean, and the second moment is related to the variance, since the variance equals the second
250 moment minus the first moment squared.

251 When we plot the moments calculated from the experimental data for families in the processive regime of reversible
252 attachment (Figure 4), striking differences between PAO1 and PA14 are revealed. PAO1 follows an exponential growth
253 curve, while PA14 follows a Gaussian curve. These curves are consistent with what we see in the family trees. For PAO1,
254 many of the families have increasing number of cells, while for PA14, fewer of these families are present, and most
255 families end in detachment. However, as we have previously shown, PA14 cells that detach have already initiated the
256 surface sensing process, and they retain memory of the surface based on their prior surface residence, which primes
257 them for subsequent irreversible attachment (8). Also, from our data, the variances for both PAO1 and PA14 can be as
258 large as the mean population size, indicating that extinction in an individual lineage can happen at any time, even in a
259 population that is exponentially growing on average. Therefore, it is important to note that individual lineage
260 "extinction" events (where the entire family detaches) do not indicate a failure to form a biofilm.

261 With our model, the temporal evolution of a family tree can be described by the single cell division (λ) and detachment
262 (μ) rates. λ is likely related to cellular events that contribute to surface growth, which can be affected by complex
263 factors such as changes in cellular metabolism or the local availability of nutrients. Likewise, μ is likely to be related to

6

264 cellular events that contribute to detachment, such as the production of EPS and the activities of motility appendages.
265 Both rates can be time-dependent in principle, so $\lambda = \lambda(t)$ and $\mu = \mu(t)$. For example, as bacteria continue
266 proliferating on the surface, they can spend more of their metabolic energy towards EPS production rather than for
267 division, and they can start detaching less. However, finding the exact functional form of time dependence to use in the
268 model is difficult. We first start with the simplest form of time-dependence (linear, or first order polynomial), where
269 $\lambda(t) = L_0 + L_1 t$, $\mu(t) = C_0 + C_1 t$, and $\{L_0, L_1, C_0, C_1\}$ are the coefficients that we obtain by fitting the experimental
270 data to the model. $\lambda(t)$ and $\mu(t)$ are rates that represent probabilities per time unit, which means they are positive and
271 have dimensions of inverse time, $[\lambda] = [\mu] = [\text{time}]^{-1}$. Therefore, the coefficients L_0 and C_0 also have dimensions
272 $[L_0] = [C_0] = [\text{time}]^{-1}$, and the coefficients L_1 and C_1 have dimensions $[L_1] = [C_1] = [\text{time}]^{-2}$. By dimensional
273 analysis, we can extract time scales for lineage-level growth (via division) and death (via detachment) behaviors from
274 either the rates (λ^{-1} and μ^{-1}) and the coefficients (L_0/L_1 and C_0/C_1). If the experimental data and model do not show
275 good agreement, then we can reiterate this process with progressively more complicated functions. Additionally, the
276 shape of the experimental moments can guide us in choosing the correct function for the rates.

277 With linear time dependence, we already obtain good agreement when fitting using nonlinear least-squares, as shown
278 by the results of the model fits to the experimental moments in Figure 4. To ensure the fit results give meaningful
279 coefficient values, we set the following constraints based on experimental data. The rates are positive, so $\lambda(t) > 0$ and
280 $\mu(t) > 0$. As seen in the family trees in Figure 2 and Figure S3, division events are roughly evenly spaced out in time, and
281 cells are not nutrient-limited inside the experimental system, so $\lambda(t)$ should be constant. Thus, we set $L_1 = 0$, and
282 $\lambda(t) = L_0$. We consider any coefficient $< 10^{-5}$ as zero for subsequent analysis based on the precision of the
283 experimental data. The resulting coefficients from the fits are as follows: for PAO1, $L_0 = 0.136 \text{ h}^{-1}$, $L_1 = 0 \text{ h}^{-2}$, $C_0 =$
284 0.0242 h^{-1}, $C_1 = 0.00147 \text{ h}^{-2}$, and for PA14, $L_0 = 0.256 \text{ h}^{-1}$, $L_1 = 0 \text{ h}^{-2}$, $C_0 = 0 \text{ h}^{-1}$, $C_1 = 0.107 \text{ h}^{-2}$.

285 We find that $\mu(t)$ is time-dependent for both strains (i.e., C_1 is non-zero). For PAO1, we find that μ is slowly increasing,
286 since C_1 is ~1 order of magnitude smaller than C_0, and both coefficients are positive and smaller than L_0. For PA14, μ is
287 increasing quite rapidly, since C_1 is positive and is much greater than C_0. Because $\mu(t)$ is time-dependent, the relevant
288 time scale τ_μ to extract for time-dependent lineage-level detachment behavior for both PAO1 and PA14 is $\tau_\mu = C_0/C_1$
289 (≈16 h for PAO1, and 0 h for PA14). Also, because $\lambda(t)$ is constant, the relevant time scale τ_λ to extract for time-
290 independent lineage-level division behavior for both PAO1 and PA14 is $\tau_\lambda = L_0^{-1}$ (≈7 h for PAO1, and ≈4 h for PA14).
291 These values are consistent with the experimental data. Interestingly, for both strains, we find that τ_λ is bigger than the
292 average division time by a factor of ~3, which means that τ_λ corresponds to ~3 generations of division. The value of τ_λ
293 corresponds closely to the time that a given lineage persists on the surface before ultimately going extinct and detaching
294 (i.e., residence time). To calculate the mean residence times of the experimental lineages in Figure 2, we only include
295 lineages that ultimately detach before the cutoff time (12 h for PAO1, 10 h for PA14). This results in ≈6 h for PAO1 and
296 ≈5 h for PA14, which are very close to the τ_λ values obtained from the coefficients (≈7 h for PAO1, and ≈4 h for PA14,
297 see above). For PAO1, having a larger τ_λ and a slowly increasing and relatively small μ mean that lineages are division-
298 dominant ($\lambda > \mu$) as they spend more time on the surface. Rather than ultimately detaching, we see many lineages
299 persist on the surface and increase their number of cells despite having detachment events. At $t_{\text{lineage}} = 12$ h, 7 of the
300 11 families still exist on the surface (Figure 2c, #1-7). For PA14, having a smaller τ_λ and a rapidly increasing μ means that
301 lineages are initially division-dominant ($\lambda > \mu$), but then become detachment-dominant ($\mu > \lambda$) after a certain amount
302 of time on the surface, which is also the time scale described by τ_λ. We see that many lineages grow to at least 2-3
303 generations, which corresponds to the lineage time where $\lambda > \mu$. Once $\mu > \lambda$, then many families begin to detach until,
304 at $t_{\text{lineage}} = 10$ h, only 1 of the 12 families still exists on the surface (Figure 2d, #1). Clearly, unlike PAO1, PA14 cells that
305 have started the surface sensing process do not necessarily stay on the surface. Rather, as we have shown previously (8),
306 they rejoin the planktonic population as "surface-sentient" cells that are primed for longer surface residence times
307 during subsequent attachment. Similarly, the value of τ_μ corresponds closely to cellular activities that affect
308 detachment, such as, for example, the competition between EPS production and motility appendage activity. EPS is
309 likely to affect detachment more for PAO1 than for PA14, since PAO1 is known to produce the Psl EPS, while PA14
310 cannot. On the other hand, presumably because of the Pil-Chp system, motility appendage activity is likely to affect

7

311   detachment more for PA14 than for PAO1. Consistent with this hypothesis, PAO1 has a much larger τ_μ compared to
312   PA14 (which is zero).

313   With these model parameters, we can evaluate the model probability distribution $P_n(t)$ to then compare with the
314   experimental probability distribution $P_n(t)$. We show the comparisons of the probability distributions with two different
315   visual representations in Figure 5. The first is plotting $P_n(t)$ vs n for specific lineage times $t = \{2.5, 5, 7.5, 10\}$ h, and the
316   second is plotting the entire $P_n(t)$ vs n and t as a contour plot. The plots of the probability distributions also show good
317   agreement. For the probability contour plots, agreement between experiment and model are assessed as follows. The
318   regions of high $(P_n(t) \sim 1)$ and low $(P_n(t) \le 10^{-2})$ probability contours are similar in shape and location (in the n, t
319   plot space) between experiment and model. The shapes of the probability contours are consistent with the plots of the
320   moments in Figure 4. For PAO1, as t progresses, the probability of having more cells per family (higher n) increases. For
321   PA14, the probability of having higher n increases and then decreases as t progresses. However, further direct
322   comparisons of the probability distributions are difficult. As previously mentioned, the experimental probability
323   distributions will invariably be sparser than the model probability distributions, which can be seen in the plots as either
324   jagged lines or holes in the contours. This sparseness comes from having finite experimental data and is not
325   straightforward to remove (e.g., via interpolation). Nevertheless, the model probability distribution can be used to
326   describe what family tree architectures we expect to observe during similar experiments.

327   The model can also be applied for cells in the nonprocessive regime of reversible attachment. We find that for both
328   PAO1 and PA14, the moments fit to an exponential decay function (Figure 6). This is what the model predicts if there is
329   only detachment and no division, and it correctly describes the data, because cells in the nonprocessive regime detach
330   before dividing on the surface. Furthermore, the variances are of the same order of magnitude as the mean population,
331   which means that lineages can become extinct at any time. Thus, for both processive and nonprocessive regimes of
332   reversible attachment, the stochastic model described here accurately describes the behaviors of PAO1 and PA14,
333   including their differential paths to irreversible attachment.

PAO1 and PA14 have distinct progressions of surface colonization, which suggest contrasting surface engagement strategies

336   Our observations and results imply that both PAO1 and PA14 start their initial surface engagement with similar behavior
337   (in terms of surface residence times) in the nonprocessive regime of reversible attachment, but then they diverge
338   strongly in the processive regime of reversible attachment. PAO1 shows an increase in the number of families that
339   commit relatively quickly to surface growth, and this is likely a factor that contributes to the trend of PAO1 forming
340   faster biofilms compared to PA14 as seen in the crystal violet assays (Figure S2). For PAO1, this early attachment
341   behavior can be more intuitive when correlating with the general progression of biofilm formation. PA14, in contrast,
342   shows a larger number of detachment-dominated families even though the entire population eventually forms a biofilm,
343   which can be a counterintuitive result. Compared to PAO1, where production of sticky EPS appears to be the dominant
344   mechanism driving irreversible attachment (22, 23), PA14 appears to utilize a different surface colonization strategy
345   dependent on progressive suppression of surface motility appendage activity (8), but it is not obvious is how this motility
346   suppression strategy can lead to rapid changes in bacteria detachment rates from surfaces, as shown by the model.

347   We investigated how detachment events occur for PA14 to gain insight into this alternate surface colonization strategy
348   and why appendages and their activities can give rise to a time-dependent detachment rate μ. Consistent with previous
349   results where flagellum-mediated surface spinning generally results in a detachment event (36), we find that ~90% of
350   detachment events occur when a cell has the mature flagellum inherited from its ancestor, as opposed to that cell
351   having to form a new flagellum post-division (Figure 7a,c). Interestingly, deleting the *pilA* gene (Δ*pilA*, missing the major
352   subunit of the TFP filament) results in significantly fewer detachment events (χ^2 test p-value$\ll 10^{-4}$) for cells that have
353   a mature flagellum. Compared to WT, only roughly half of detachment events occur when the cell has a mature
354   flagellum in the Δ*pilA* mutant (Figure 7b,c), an observation that suggests that TFP are important to the detachment
355   process. For the Δ*pilA* mutant (and to a much lesser extent in WT), we also observe detachment events with cells that
356   did not have a labeled flagellum, which suggests that non-flagellum-mediated detachment events can also occur.

8

357 To study how TFP can influence flagellum-mediated spinning and detachment, we adapt a previously developed
358 hydrodynamic model (37). Simulations show that TFP activity (i.e., extension or retraction) can lead to changes in the
359 cell body tilt angle relative to the surface. In the case where the non-flagellated pole is attached to the surface, TFP
360 extension during flagellum-mediated spinning results in the cell tilting to near vertical orientations, while retraction
361 results in a smaller tilt angle (Figure 7d). During flagellum-mediated spinning, near vertical orientations correlate with
362 higher rates of detachment, while orientations closer to the surface correlate with a decreased likelihood of detachment
363 (36, 38). Consistent with previous results, the cell without TFP is more likely to assume an orientation closer to the
364 surface (i.e., horizontal), while the cell with TFP extended the entire time is more likely to assume a near vertical
365 orientation (8).

366 These results suggest that detachment rates are higher when TFP activity and flagellum activity are high and/or coincide,
367 and that detachment rates are lower when the activities are reduced and/or do not coincide. Given that PA14 has small
368 average family size, small surface residence times, and large surface detachment rates, observations of suppression of
369 both appendage activity and detachment are expected to be extremely rare during reversible attachment (i.e., while
370 cells are transiently on the surface). Nevertheless, in our family tree data, we can find examples where we can compare
371 cells from the same generation but on different branches of the family tree. In these cases, we observe detachment in
372 branches where appendage activities are high (and/or coincide), and no detachment in branches where appendage
373 activities are reduced and/or do not coincide (Figure 8). In example (i), we see that appendage activity is reduced around
374 $t_{\mathrm{lineage}} \sim 6$ h, which coincides with the presence of a division event where no daughter cells detach. In examples (ii) and
375 (iii), appendage activity does not become quiescent and detachment continues to occur for subsequent division events.
376 This appendage activity analysis was repeated with $\Delta pilA$ for validation and was consistent with previous results (Figure
377 S5).

Discussion

379 Clearly, the application of stochastic models can be quite powerful in understanding microbiological systems that involve
380 strong fluctuations. The behavior of each lineage is a record of how a specific cell and its progeny managed to stay and
381 proliferate on the surface during cellular changes induced by surface sensing, which has multigenerational
382 consequences. Even though the probability of a specific cell attaching to a surface and proliferating successfully is
383 initially vanishingly small, surface sensing can modify outcomes by changing the structure of family trees, as we can see
384 from the evolution of reversible attachment from the nonprocessive to processive regimes, for example. Interestingly,
385 that the process of reversible attachment can be described by a stochastic model is telling: whether a bacterium
386 encountering a surface makes it to irreversible attachment and eventually participates in biofilm formation may be
387 quantitatively cognate to the description of whether patient zero's disease will die out after a few infections, or take
388 hold and become an epidemic. The fact that biofilm formation seems to inevitably happen is due to factors such as the
389 large number of lineages that encounter the surface, and the existence of multigenerational memory, which can
390 mitigate against initial failure to attach by conditioning a planktonic population primed for improved subsequent
391 attachment.

392 Indeed, a recent study applied a variation of our approach to antibiotic treatment of bacteria (39). In fact, the
393 quantitative evolution of bacterial populations in early biofilm formation is analogous to a time-reversed version of
394 antibiotic treatment: the nonprocessive regime of reversible attachment behaves like bacterial population dynamics for
395 antibiotic treatment well above the minimum inhibitory concentration (MIC). In the present study, however, we are able
396 to perform an unprecedented level of longitudinal comparison between theory and experiment. Because we have
397 information on the fates for every cell in a large number of bacterial lineages that occur during early biofilm formation,
398 we can directly measure and analyze the time evolution of the system. This analysis provides a conceptual framework
399 for understanding the taxonomy of surface colonization strategies and reveals an unanticipated difference between
400 PAO1 and PA14 behavior.

401 One of the old questions about biofilm formation is whether it is the newly landed cells or the dividing cells on the
402 surface that contribute more to the biomass increase in the biofilm. Our results suggest that not only is the answer

9

403   species and strain dependent, the question is misleading because of the assumed either-or format of the answer.
404   Surface sensing can evolve progenitor cells which land on a surface and commit almost its entire division lineage to the
405   surface, thereby drastically increase biomass.

Complementary surface colonization strategies: immediate vs deferred gratification

407   The "divide-detach" stochastic model highlights two distinct but complementary strategies for surface colonization that
408   are illustrated by PAO1 and PA14. For PAO1, surface population increase takes the form of the few families that are
409   more successful in retaining surface progeny. PAO1 families generally stay on the surface during biofilm formation, likely
410   due to the Wsp surface sensing system and Psl EPS secretion. Previous work has shown that early surface attachment
411   behavior depends on EPS production via the Wsp system (9, 23). In contrast, for PA14, surface population increase takes
412   the form of many families that are less successful in retaining surface progeny due to surface detachment. However,
413   PA14 cells can "remember" the surface due to the Pil-Chp system and multigenerational cAMP-TFP memory (8), which
414   primes them for biofilm formation whether they are currently on the surface or not and eventually leads to progressive
415   suppression of motility appendage activity. Both strategies are viable for surface colonization. PAO1 cells tend to attach,
416   increase their surface population more quickly, and persist longer on a surface compared to PA14, which suggests that
417   PAO1 can potentially attach to surfaces even in ecologically crowded environments or successfully form biofilms by
418   outgrowing competing species. Indeed, this has been experimentally observed: EPS-producing *P. aeruginosa* strains tend
419   to persist on surfaces better than EPS nonproducers, despite possible exploitation by "cheaters" that can potentially use
420   the communal good of EPS (40). In contrast, PA14 exposed to a surface do not initially stay on the surface, and slowly
421   increase surface coverage. Rather, they form a surface-sentient planktonic population that can quickly attach and
422   colonize the surface later in time, which may be better adapted for overwhelming host defense (i.e., a naïve surface)
423   rather than microbial competition. Moreover, it is interesting to note that EPS secretion is extracellular and can be
424   shared spatially and temporally with both neighbors from different lineages and descendants in close proximity (41),
425   whereas memory is intracellular and can be only passed down temporally through division.

426   It is possible that our observations and results with PAO1 and PA14 may be generalizable to other *P. aeruginosa* strains.
427   The majority of strains in the International *Pseudomonas* Consortium Database (IPCD) can be identified as either PAO1-
428   like or PA14-like based on their phylogeny (i.e., same phylogenetic sub-group as either PAO1 or PA14) (42-45).
429   Consistent with our results, crystal violet biofilm assays show that the PAO1-like strains seem to produce early biofilms
430   faster than the PA14-like strains (Figure S6). Although it is clear from the data spread that there is more to
431   *Pseudomonad* phylogenetic diversity than biofilm behavior, this observation suggests that the phylogenetic distance
432   from either PAO1 or PA14 could be incorporated into a metric for categorizing a *P. aeruginosa* strain's biofilm formation
433   behavior as either PAO1-like or PA14-like. It is tempting to draw an analogy between differences in these strategies to
434   differences in "immediate-" vs "deferred-gratification" behavior in a prototypical cognitive-affective processing system,
435   with the latter correlating to successful outcomes in complex competitions (46). For *P. aeruginosa*, there is no cognition
436   of course, but the existence of a specific sensing cascade for PA14 effectively encodes the analog of "deferred-
437   gratification" behavior at a molecular level. Indeed, PA14 is usually considered to be more virulent than PAO1 (47).
438   However, it is likely that these bacterial strategies have their own advantages under different circumstances.
439   Furthermore, our model can be applied to other bacterial systems to understand how they utilize their cellular
440   machinery for various surface colonization strategies.

Materials and Methods

Strains and growth conditions

443   *Pseudomonas aeruginosa* PAO1 and PA14 wild type (WT) strains were used in this study. For the flagellum localization
444   data, PA14 WT and Δ*pilA* (deleting the major subunit of the TFP filament) (48) with FliC (the major subunit of the
445   flagellum filament) modified to FliC(T394C) (49) were used. PAO1 was cultured as previously described (21, 23), and
446   PA14 was cultured as previously described (8). Culturing protocols are summarized as follows. Bacteria were plated on
447   LB agar plates and incubated at 37 °C overnight. Individual colonies were swabbed from the plate and grown overnight
448   for ~18 h in an incubator at 37 °C shaking at 220 rpm. Overnight cultures were regrown in the same overnight growth

449 conditions to an OD_{600nm} ~ 0.4-0.6. Regrowth cultures were then diluted in flow cell conditions to an OD_{600nm} ~ 0.01-
450 0.03. These final diluted cultures were used for injection into the flow chamber.

451 Different medium conditions were chosen for PAO1 and PA14 based on the medium optimized for flow cell early biofilm
452 formation experiments for each individual strain in prior work. For PAO1, overnight and regrowth media consisted of
453 FAB medium with 30 mM glutamate, while flow cell media consisted of FAB medium with 0.6 mM glutamate (21, 23).
454 For PA14, overnight and regrowth media consisted of M63 medium with 1 mM magnesium sulfate, 0.2% glucose, and
455 0.5% casamino acids (CAA), while flow cell media consisted of M63 medium with 1 mM magnesium sulfate, 0.05%
456 glucose, and 0.125% CAA (8, 48). For flagellum staining experiments, the flow cell media also contained 0.375 µg/mL
457 Alexa Fluor 488 C5 maleimide dye (Molecular Probes). For more details on the culturing procedures, please refer to the
458 corresponding references. PAO1 experiments were repeated with the PA14 medium conditions, and the same basic
459 trends discussed in this paper still hold.

Crystal violet biofilm assays

461 Biofilm assays were performed as previously described with minor modifications (50, 51). Briefly, culture inocula were
462 grown in 100 µL of LB medium at 37 °C in a 96-well microtiter plate for ~16 h. Cultures were normalized and diluted
463 ~1:100 in M63 medium with 1 mM magnesium sulfate and 0.4% arginine (instead of glucose and CAA). To a 96-well
464 microtiter plate, 100 µL of the diluted culture was added to each well. Microtiter plates were then incubated at 37 °C for
465 24 h in a humidified environment to prevent culture evaporation. To remove unattached bacteria and spent medium,
466 the microtiter dishes were inverted, then washed twice by gently immersing the plate in tap water followed by removing
467 the liquid by briskly inverting the plate. Microtiter dish biofilms were stained by addition of 125 µL of 0.1% (w/v) crystal
468 violet to each well, and incubation for 15 min at room temperature. After the crystal violet solution was removed, the
469 plates were washed three times, as described above, with tap water. Plates were allowed to airdry overnight. The
470 amount of crystal violet retained by each biofilm was measured by adding 150 µL of 30% (v/v) glacial acetic acid,
471 incubating for 15 min at room temperature, and mixing by pipetting. Transfer of 100 µL of this mixture to a 96-well clear
472 flat-bottom plate enabled spectrophotometric analysis at 550 nm. Each assay included 4 measurements (technical
473 replicates), which were averaged, and the experiment was performed 5 times (biological replicates). The strains used in
474 these assays are shown in Table S1. *P. aeruginosa* strains PAO1 and PA14 were initially described in (52) and (47),
475 respectively. All clinical and environmental *P. aeruginosa* isolates were from the International *Pseudomonas* Consortium
476 Database (IPCD) (43). These strains have both been phenotypically and genotypically characterized (44, 45).

Flow cell experiments and data acquisition

478 Flow cells were prepared and inoculated as previously described (8) with the following modifications. Flow cells were
479 purchased from two sources: Department of Systems Biology, Technical University of Denmark, and Ibidi (sticky-Slide
480 $VI^{0.4}$ with a glass coverslip). An in-line injection port (Ibidi) was used at the inlet for inoculating bacteria into the flow
481 cell. For Ibidi flow cells, elbow connectors (Ibidi) were used to connect the chamber with tubing. The diluted bacteria
482 culture was injected into the flow cell and allowed to incubate for 10-20 min without flow on the heating stage at 30 °C.
483 Flow was then started at 3 mL/h for the entire acquisition time.

484 Images were taken using either an Andor iXon EMCCD camera with Andor IQ software on an Olympus IX81 microscope
485 equipped with a Zero Drift Correction autofocus system or an Andor Neo sCMOS camera with Andor IQ software on an
486 Olympus IX83 microscope equipped with a Zero Drift Correction 2 continuous autofocus system. Bright-field images
487 were taken every 3 s (30 ms exposure time) on the IX81 system and every 100 ms (30 ms exposure time) on the IX83
488 system. For flagellum staining experiments, bright-field images were taken every 3 s (30 ms exposure time) on the IX81
489 system, and two fluorescence images (+0 and +1 µm above the imaging focal plane) were taken every 15 min (100 ms
490 exposure time) using a Lambda LS (Sutter Instrument) xenon arc lamp and a GFP filter. On the IX81 system, total
491 acquisition time was ~40 h, resulting in ~48000 images. On the IX83 system, total acquisition time was ~20 h, resulting in
492 720000 images. Image size was 67 µm × 67 µm (1024 × 1024 pixels).

11

Multigenerational family tracking analysis

Image analysis, family tracking and manual validation, family tree plotting, and tree asymmetry calculations were performed in MATLAB as previously described (8) without modification. Fluorescence images were processed as follows to reduce noise and background signals and enhance flagella signals. Bandpass filtering, gamma correction, intensity percentile normalization, and then a green colormap were applied to the images. Fluorescence images were then overlaid on top of bright-field images using the lighten opacity setting. Probability distributions were obtained from the family trees as follows. The experimental probability distribution $P_n(t)$ is a 2D matrix, where the columns represent n, the number of cells present in one family, and each row is a time step t, the experimental image data acquisition interval (either every 3 s or 100 ms, depending on the data). For each time step t (in terms of lineage time, with each family starting at $t_{\text{lineage}} = 0$), we keep track of how many families have $n = 0$ cells, $n = 1$ cell, $n = 2$ cells, and so on. The proportion of families with $n = 0, 1, 2, \ldots$ cells then become one row in the matrix. This is equivalent to generating a histogram for $X_t(\omega)$ using the states Σ as the bins. The full matrix is generated by repeating this for all time steps in the experimental data. Experimental moments were calculated by the formula $\langle n(t)^k \rangle = \sum_{n=0}^{\infty} n^k P_n(t)$, where $P_n(t)$ is the experimental probability distribution. MATLAB functions from the base installation of MATLAB R2015a, Statistics and Machine Learning Toolbox, Curve Fitting Toolbox, Image Processing Toolbox, Signal Processing Toolbox, and custom MATLAB functions were used for all analyses. In particular, the MATLAB functions "fit", "fmincon", and "ode45" were used for function fitting, nonlinear least-squares minimization with constraints, and numerical integration.

Divide-detach stochastic model equations

Explanation of the model is given in the main text. The solution for the master equation (eq. 1), which is the model probability distribution $P_n(t)$, is given by

$$
P_n(t) = \begin{cases} 1 - \dfrac{\exp(-\rho(t))}{W(t)}, & n = 0 \\[2ex] \dfrac{\exp(-\rho(t))}{W(t)^2}\left(1 - \dfrac{1}{W(t)}\right)^{n-1}, & n > 1 \end{cases},
$$

$$
W(t) = \exp(-\rho(t))\left(1 + \int_0^t \mu(\tau)\exp(\rho(\tau))\,d\tau\right),
$$

$$
\rho(t) = \int_0^t (\mu(\tau) - \lambda(\tau))d\tau,
$$

2

and $\lambda(t)$ and $\mu(t)$ are the single cell division and detachment rates, respectively. Both rates are functions of time and positive (i.e., $\lambda(t) > 0$ and $\mu(t) > 0$).

The first and second model moments are given by the following equations and the linear form of the rates, $\lambda(t) = L_0 + L_1 t$ and $\mu(t) = C_0 + C_1 t$, which are used for fitting the experimental moments

$$
\langle n(t) \rangle = \exp\left[(L_0 - C_0)t - \frac{1}{2}(C_1 - L_1)t^2\right],
$$

3

$$
\langle n(t)^2 \rangle = \exp[2(L_0 - C_0)t - (C_1 - L_1)t^2]\left[1 + (L_0 + C_0)\int_0^t \exp\left[-(L_0 - C_0)\tau + \frac{1}{2}(C_1 - L_1)\tau^2\right]d\tau \right.
$$
$$
\left. + (C_1 + L_1)\int_0^t \tau\exp\left[-(L_0 - C_0)\tau + \frac{1}{2}(C_1 - L_1)\tau^2\right]d\tau\right].
$$

4

Evaluating the integral analytically in eq. 4 depends on the relative signs of $\{L_0, L_1, C_0, C_1\}$.

Analytical solutions to the equations in the stochastic model

The solution for the master equation (eq. 1), which is the model probability distribution $P_n(t)$, can be found by using the so-called generating function

12

521
$$G(z,t) = \sum_{n=0}^{+\infty} z^n P_n(t).$$

522 By plugging in the generating function into eq. 1, we obtain

$$\partial_t G(z,t) = (1-z)(\lambda z + \mu)\partial_z G(z,t). \qquad 5$$

523 We can rewrite the previous equation in a Ricatti's form, which reads

524
$$\frac{dz}{dt} = S + Qz + Rz^2,$$

525 where $S = -\mu$, $Q = (\lambda + \mu)$, and $R = -\lambda$. A particular solution of the previous equation is given by Y. Then the
526 previous equation can be solved by quadrature $z(t) = x(t) + Y(t)$ and

527
$$\frac{dx}{dt} = [S + 2YQ]x + Qz^2.$$

528 A change of variables $u = \frac{1}{x} = \frac{1}{z-Y}$ yields

529
$$\frac{du}{dt} = [S + 2YQ]u + Q.$$

530 The solution of the Ricatti's equation (53) is a homographic function

531
$$u = C \exp\left(\int [S + 2YQ]dt\right) + U,$$

532 where C is an arbitrary constant and U is a particular solution. We can rewrite u as

533
$$u = C\psi + \phi,$$

534 and the solution for z reads

535
$$z = Y + \frac{1}{C\psi + \phi} = \frac{C\psi Y + \phi Y}{C\psi + \phi} = \frac{C\alpha + \beta}{C\gamma + \delta}.$$

536 By using the Palm's formulae (31-33, 35, 54), it is possible to find $P_0(t)$ and $P_n(t)$ as a function of η_t and ξ_t, two
537 unknown functions, which reads

538
$$P_0(t) = \xi_t, \text{ and } P_n(t) = \left(1 - P_0(t)\right)(1 - \eta_t)\eta_t^{n-1}.$$

539 By means of geometric series, the generating function $G(z,t)$ reads

540
$$G(z,t) = \frac{\xi_t + (1 - \xi_t - \eta_t)z}{1 - \eta_t z}.$$

541 By plugging back this equation into eq. 5, we can find ξ_t and η_t and finally the solution (eq. 2).

542 To compare the model with the experimental results, we use the model moments defined as

543
$$\langle n(t)^k \rangle = \sum_{n=0}^{\infty} n^k P_n(t).$$

544 From the master equation (eq. 1), we can find

545
$$\frac{d}{dt}\langle n(t)^k \rangle = \sum_{n=0}^{\infty} n^k \frac{d}{dt} P_n(t) = \sum_{n=0}^{\infty} [((n+1)^k - n^k)\lambda(t) - (n^k - (n-1)^k)\mu(t)]n P_n(t).$$

546 The first moment reads

$$\frac{d}{dt}\langle n(t)\rangle = \sum_n n \frac{d}{dt} P_n(t)$$

548

$$= -(\lambda + \mu)\sum_n n^2 P_n(t) + \mu \sum_n (n^2 + n)P_{n+1}(t) + \lambda \sum_n (n^2 - n)P_{n-1}(t)$$

549

$$= \lambda \sum_{n=1}[(n-1)^2 P_{n-1}(t) + (n-1)P_{n-1}(t)] + \mu \sum_{n=0}[(n+1)^2 P_{n+1}(t) - (n+1)P_{n+1}(t)] - (\lambda + \mu)\sum_{n=0} n^2 P_n(t)$$

550

$$\Leftrightarrow \frac{d}{dt}\langle n(t)\rangle = \lambda[\langle n(t)^2\rangle + \langle n(t)\rangle] + \mu[\langle n(t)^2\rangle - \langle n(t)\rangle] - (\lambda + \mu)\langle n(t)^2\rangle$$

551

$$\Rightarrow \frac{d}{dt}\langle n(t)\rangle = (\lambda - \mu)\langle n(t)\rangle.$$

552 The solution to this differential equation is

553

$$\langle n(t)\rangle = n(0)\exp(-\rho), \qquad n(0) = 1, \qquad \rho(t) = \int_0^t \big(\mu(\tau) - \lambda(\tau)\big)d\tau.$$

554 Plugging in the linear form of the rates, $\lambda(t) = L_0 + L_1 t$ and $\mu(t) = C_0 + C_1 t$, yields eq. 3.

555 The second moment (again, using the linear form of the rates, $\lambda(t) = L_0 + L_1 t$ and $\mu(t) = C_0 + C_1 t$) reads

556

$$\frac{d}{dt}\langle n(t)^2\rangle = \sum_{n=0}^{\infty}[((n+1)^2 - n^2)(L_0 + L_1 t) - (n^2 - (n-1)^2)(C_0 + C_1 t)]nP_n(t)$$

557

$$= \langle n(t)\rangle(L_0 + L_1 t + C_0 + C_1 t) + 2\langle n(t)^2\rangle(L_0 + L_1 t - C_0 - C_1 t).$$

558 Elementary computations yield eq. 4.

Hydrodynamic model of TFP retraction during flagellum-mediated spinning

560 We adapt the hydrodynamic model that we developed previously (37) to investigate the effects of TFP on flagellum-
561 mediated spinning. Here, we consider a bacterium consisting of a cylindrical body attached to the surface at the pole
562 opposite the flagellum, a helical filament for the flagellum of equal length to the body, and a straight filament 2/3 of the
563 body length for a pilus protruding from the body. We use resistive force theory (55) to relate the angular velocities of
564 each component of the bacterium to the torques from the flagellar motor, the viscous resistance from the fluid, and the
565 flagellar hook which resists bending between the head and the flagellum. The resultant model is used to consider how
566 TFP affect the angle that the bacterium makes with the surface during flagellum-mediated spinning and thereby "stand
567 up" to a near vertical orientation commonly observed before detachment.

568 We use the example where the ratio of hook stiffness to motor torque is 0.5 to show the effects of TFP (see (37) for
569 details of the stiffness/motor torque ratio). We show time using units of seconds and a torque value of 2 pN μm. We
570 observe two significant effects on the surface angle when TFP retract during spinning: (i) the bacterium decreases its
571 surface angle after retraction, (ii) the amplitude of oscillations in surface angle decreases after retraction. The opposite
572 occurs when TFP extend during spinning: (i) the bacterium increases its surface angle after extension, (ii) the amplitude
573 of oscillations in surface angle increases after extension. The strength of these effects depends on the choice of value of
574 the flagellar motor torque and hook stiffness in the hydrodynamic model.

TFP and flagellum activity metrics

576 To characterize appendage activity during family tree tracking, we use the algorithms previously described (8) for TFP
577 activity and adapt them for flagellum activity. As previously described, TFP activity is inferred by recognizing surface
578 translational motion, which is the predominant behavior for TFP-driven motion for *P. aeruginosa* cells that attach to the

14

579 surface during early biofilm development. Analogous to this, the most common mode of flagellum activity is surface-
580 attached "spinning," where cells attach via one pole on the surface, and spin at angular velocities consistent with typical
581 flagellum motor output (~5 rad/s) (36, 37). So, flagellum activity is inferred by recognizing surface rotational motion.
582 Based on the majority of flagellum-mediated surface spinning behavior producing trajectories that are tightly clustered
583 together and have strongly subdiffusive MSDs, the multi-parameter metric for flagellum activity is defined as follows. A
584 bacterium has flagellum activity during a given time point when it is "spinning" and has non-zero displacement over a w
585 frame moving window every $w/10$ frames. A cell that is "spinning" is defined as having the following characteristics
586 during the w frame window: a Mean Squared Displacement (MSD) slope of less than 0.9 and having the maximum 2
587 point distance of its trajectory being greater than or equal to 15% of its maximum cell body length and less than its cell
588 body length. As previously described, a value of $w = 100$ was used (8).

Acknowledgements

595 Competing interests: none

Figure Legends
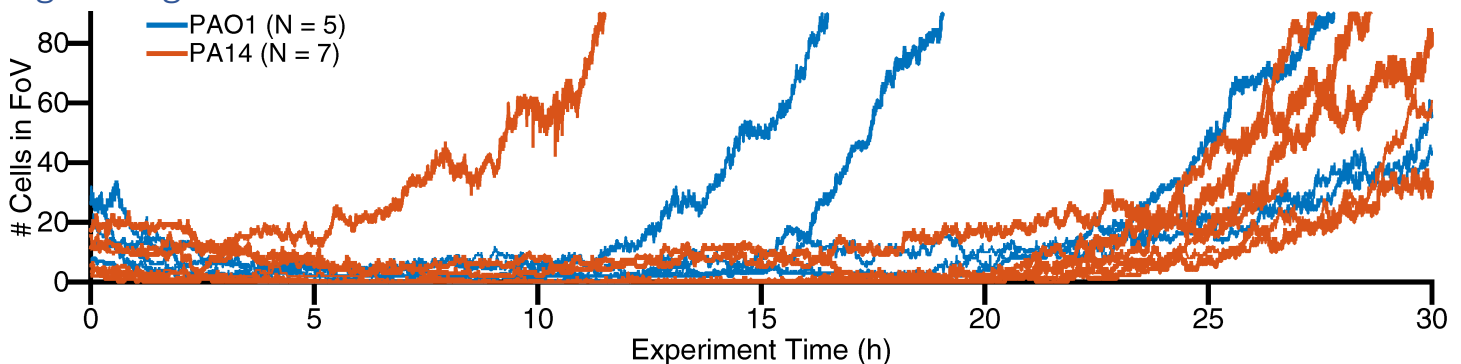
598 Figure 1. PAO1 and PA14 can both form biofilms and have similar trends of exponential surface population increase.
599 Each line reprsents one experiment where we count how many cells are in a single field of view (FoV) for WT PAO1 and
600 PA14 as experiment time progresses (5 and 7 independent experiments for PAO1 and PA14, respectively). Experiment
601 time = 0 h corresponds to when imaging commenced after cells were inoculated into the flow cell chamber. Both PAO1
602 and PA14 have the variable lag period and the exponential increase, which is consistent with the fact that both strains
603 initially undergo reversible attachment, and then subsequently form biofilms.
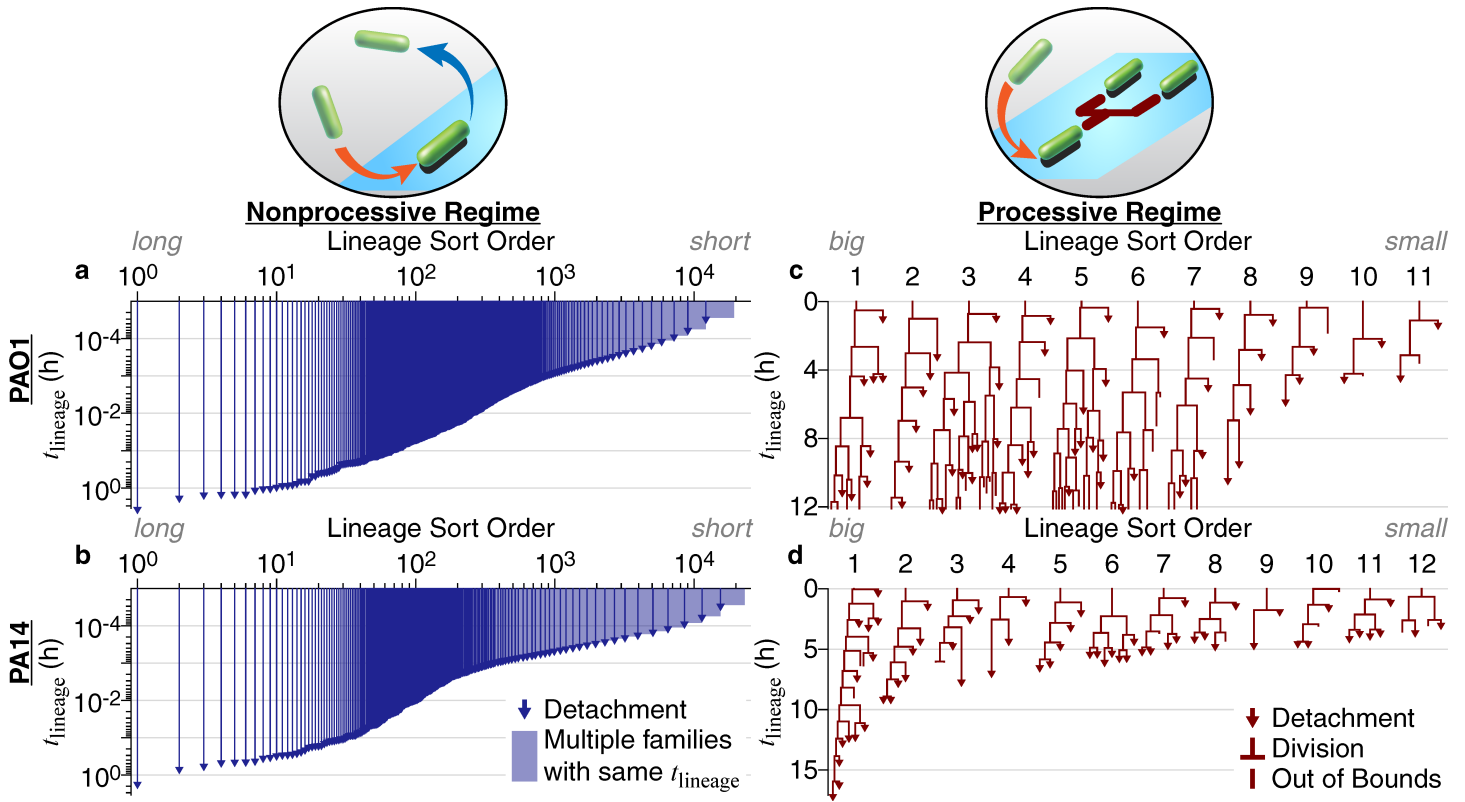
Figure 2. PAO1 and PA14 family trees in different regimes of reversible attachment. (a,b) Families in the nonprocessive regime of reversible attachment, which is when cells detach before dividing. Both axes are on a log scale. In this nonprocessive regime, PAO1 has $m = 19353$ tracked families, and PA14 has $m = 23104$ tracked families. Note the similarities between PAO1 and PA14. (c,d) Families in the processive regime of reversible attachment, which is when cells divide at least once before detaching. Both axes are on a linear scale. Each family start at $t_{\text{lineage}} = 0$ h when the founder cell attaches to the surface. Tracking continues for that family until either all members detach, or we lose track of the family (where we can no longer distinguish individual cells, or the cells move out of the recording boundaries). We then record this time as the family's residence time. For each regime and strain, we sort families by residence times in descending order, which sorts them by the amount of time that they have continuously contacted the surface. In this processive regime, families here are used for the model and are a subset of the full tracked families shown in Figure S3.

615
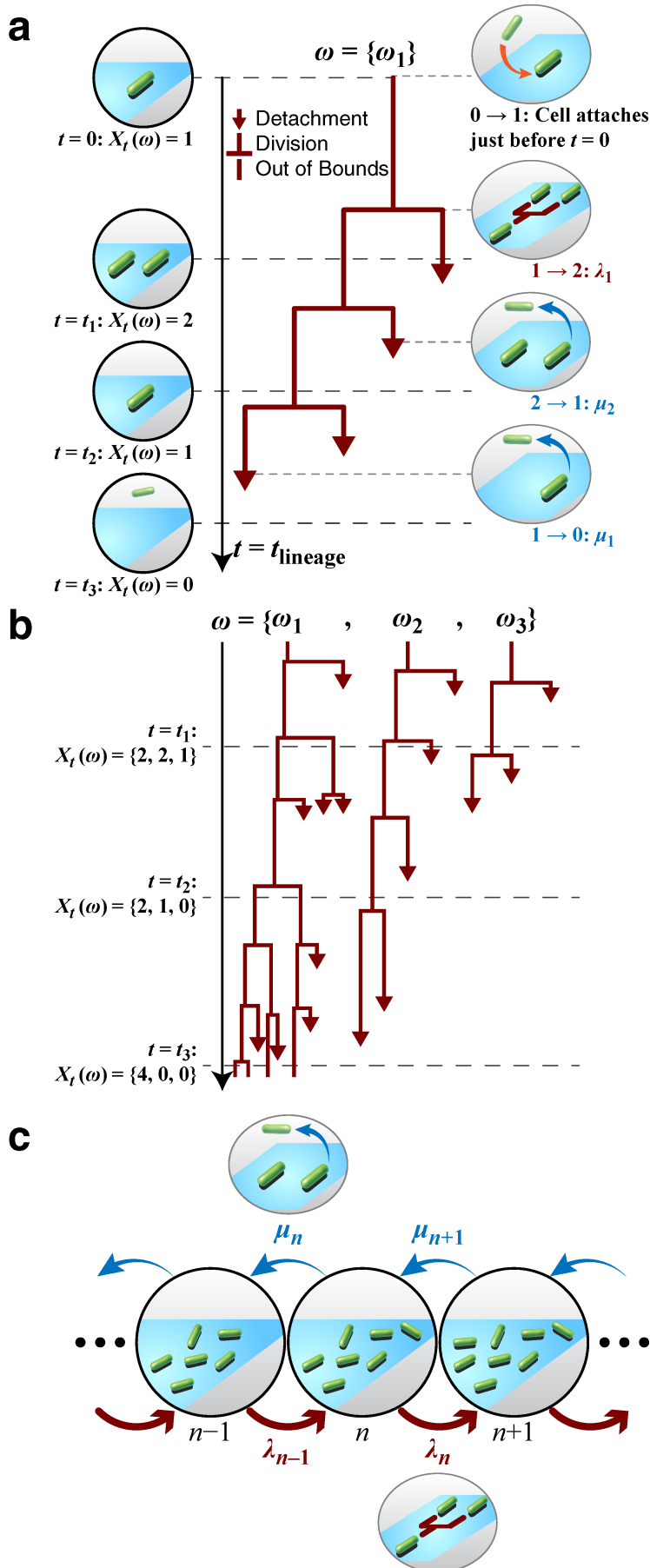
616 Figure 3. Family trees are a stochastic process. (a) Example illustrating the stochastic process with $m = 1$ family tree. In
617 this case, at time t, $X_t(\omega)$ is the number of observed cells in the family tree $\omega = \{\omega_1\}$ at time t. Attachment of the

618 founder cell happens just before time $t = t_{\text{lineage}} = 0$, so it is not explicitly captured by this process. When a cell
619 divides, it undergoes a transition $n \to n + 1 = \lambda_n$, and when it detaches, it undergoes a transition $n \to n - 1 = \mu_n$,
620 where n is the state (i.e., number of observed cells) before the transition. (b) Example illustrating the stochastic process
621 with $m = 3$ family trees. At time t, $X_t(\omega) = \{X_t^1(\omega_1), X_t^2(\omega_2), X_t^3(\omega_3)\}$ are the number of observed cells for each of the
622 family trees $\omega = \{\omega_1, \omega_2, \omega_3\}$. (c) Dynamics of the stochastic process for state n. As shown in part (a), a transition $n \to$
623 $n + 1 = \lambda_n$ occurs when a cell divides, and a transition $n \to n - 1 = \mu_n$ occurs when a cell detaches.
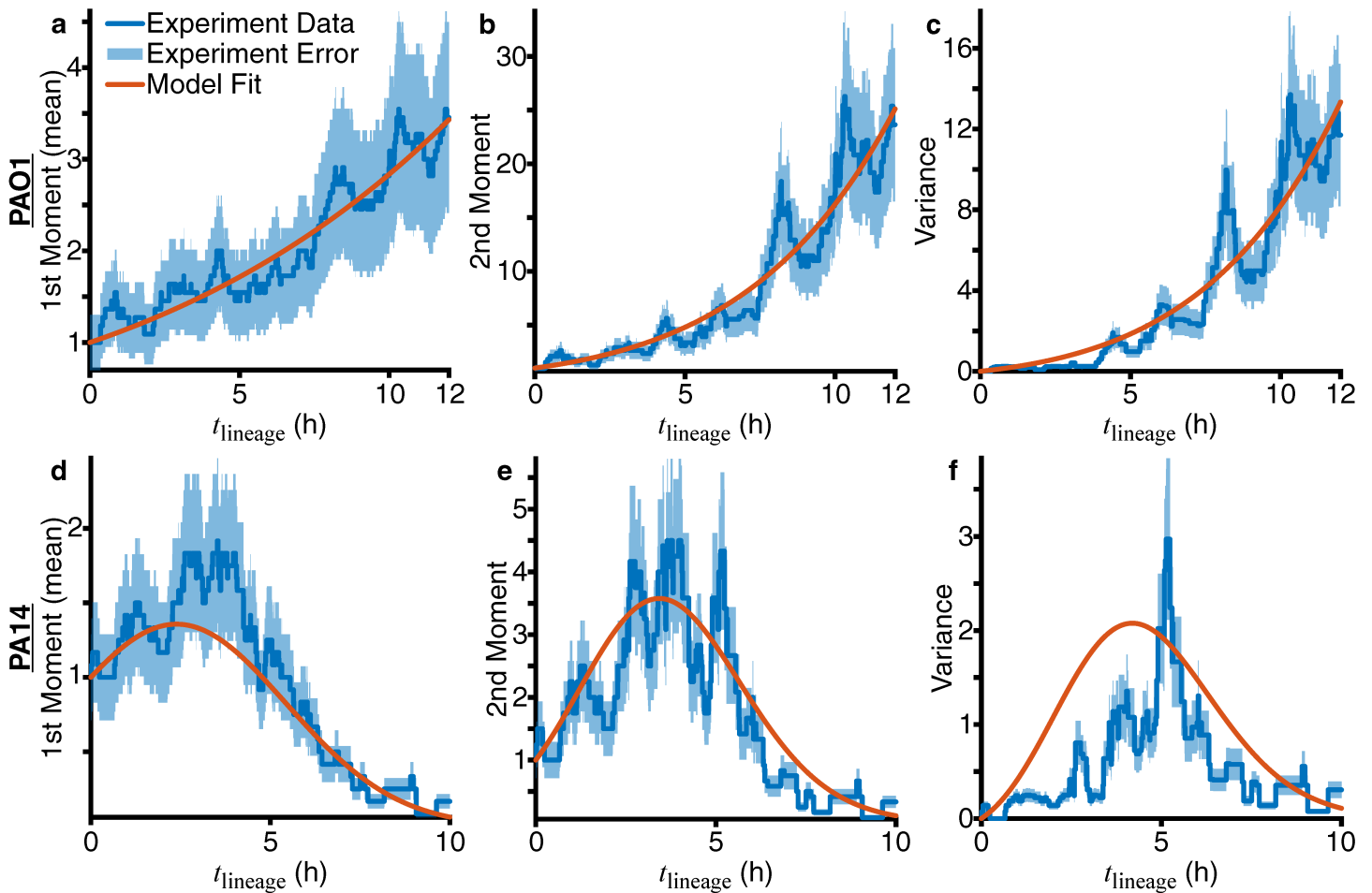
624

625 Figure 4. Obtaining division (λ) and detachment (μ) rates by fitting experimental and model moments of the number of
626 cells in a family for families in the processive regime of reversible attachment. Moments and variance calculated from
627 experimental data are plotted as blue lines, with the relative error (calculated as $1/\sqrt{m}$, where m is the number of
628 families used) shown as the light blue shaded area. Variance is defined as the second moment minus the first moment
629 squared. Red lines show the fits to the first and second moments (eq. 3-4) using nonlinear least-squares. For the model,
630 we use the linear functional form of the rates, $\lambda(t) = L_0 + L_1 t$ and $\mu(t) = C_0 + C_1 t$. The resulting coefficients from the
631 fits are as follows: for PAO1, $L_0 = 0.136 \text{ h}^{-1}$, $L_1 = 0 \text{ h}^{-2}$, $C_0 = 0.0242 \text{ h}^{-1}$, $C_1 = 0.00147 \text{ h}^{-2}$, and for PA14, $L_0 =$
632 0.256 h^{-1}, $L_1 = 0 \text{ h}^{-2}$, $C_0 = 0 \text{ h}^{-1}$, $C_1 = 0.107 \text{ h}^{-2}$.
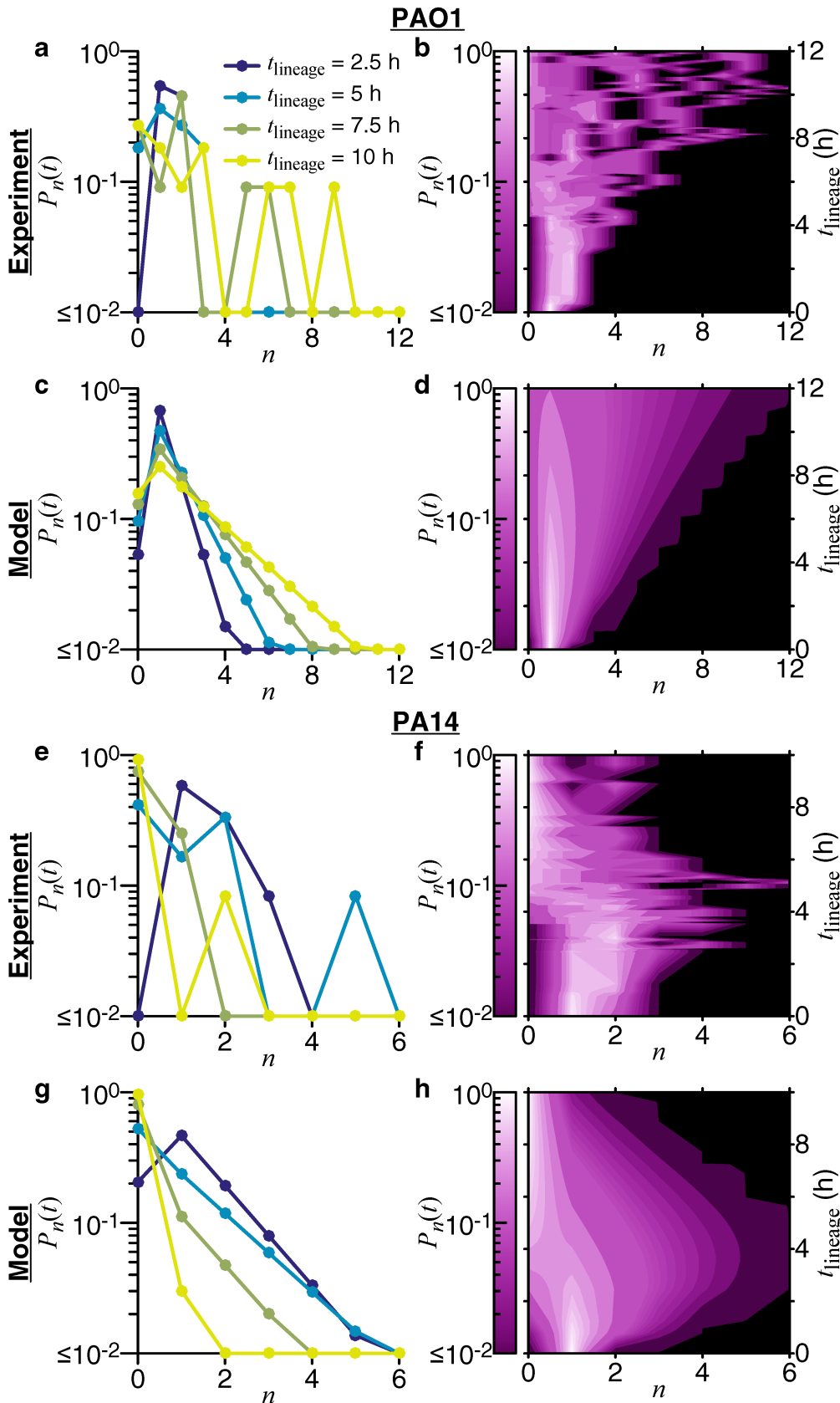
Figure 5. Comparing experimental and model probability distributions for the number of cells in a family for families in the processive regime of reversible attachment. Experimental probability distributions are built directly from the data, as described in the methods (section "Multigenerational family tracking analysis"). For the model probability distribution $P_n(t)$, we use eq. 2 and the linear functional form of the rates, $\lambda(t) = L_0 + L_1 t$ and $\mu(t) = C_0 + C_1 t$. The model rate coefficients used are shown in Figure 4. Probability distributions are compared in two different ways. The left column shows plots of $P_n(t)$ vs n for specific lineage times $t = \{2.5, 5, 7.5, 10\}$ h, and the right column shows plots of the entire

640    $P_n(t)$ vs n and t, where the probability is represented by the shades of color in the contour plots. Probabilities are
641   shown on a log scale.

642
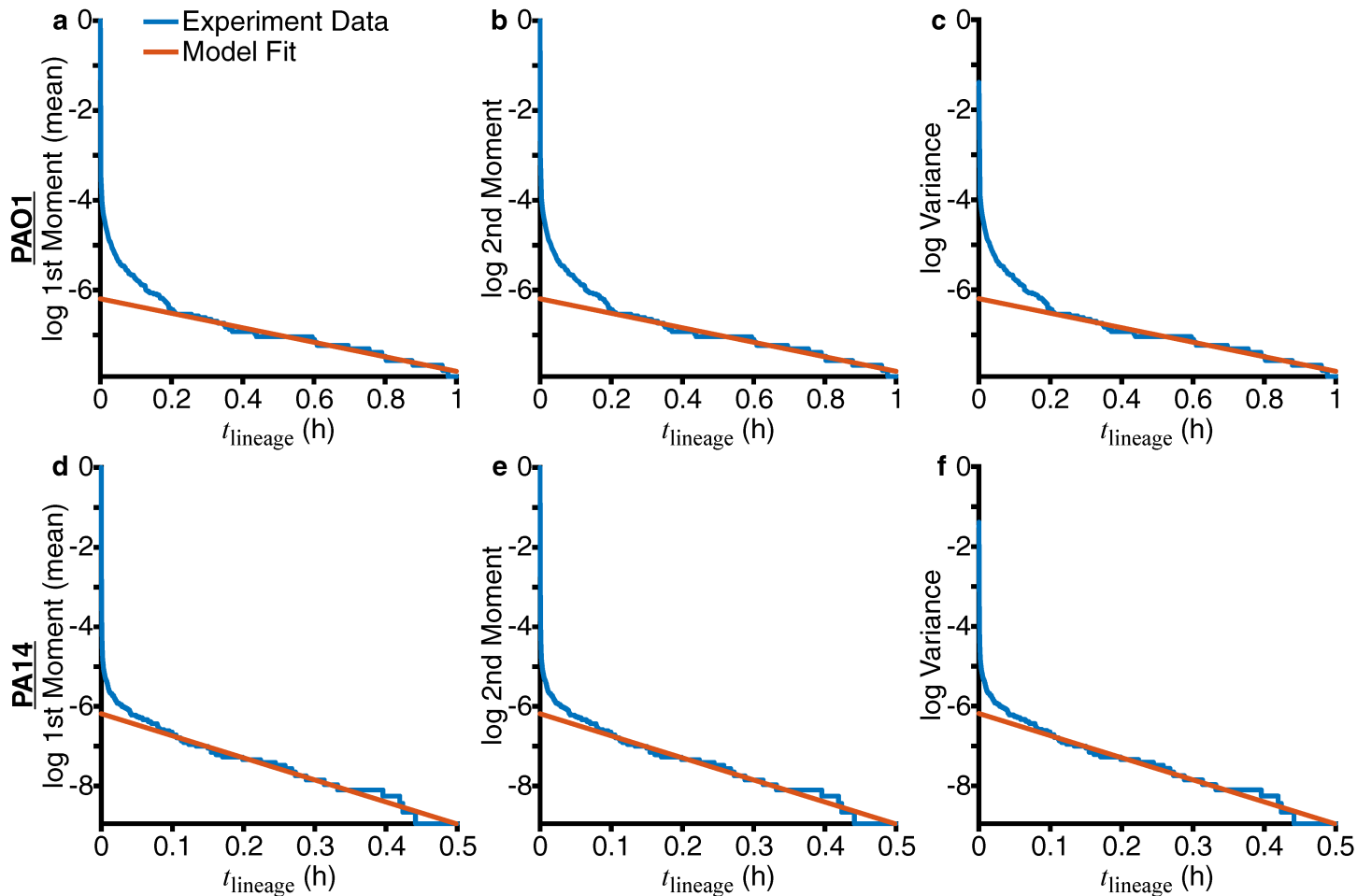
643   Figure 6. Fitting experimental moments show that families in the nonprocessive regime of reversible attachment have
644   only detachment events. The natural logarithm (log) of the moments and variance calculated from experimental data
645   are plotted as blue lines. Relative errors (calculated as $1/\sqrt{m}$, where m is the number of families used) are not plotted
646   here, as $m \sim 20000$ for both PAO1 and PA14, and the values are very small. Red lines show the fits of the experimental
647   data to the function $\log(y(t)) = a_1 t + a_0$. For PAO1, fits were performed for $0.2\,\text{h} \leq t \leq 1\,\text{h}$, with the resulting fit
648   coefficients as $a_1 = -1.61\,\text{h}^{-1}$, $a_0 = -6.19$. For PA14, fits were performed for $0.1\,\text{h} \leq t \leq 0.5\,\text{h}$, with the resulting fit
649   coefficients as $a_1 = -5.55\,\text{h}^{-1}$, $a_0 = -6.19$.

650
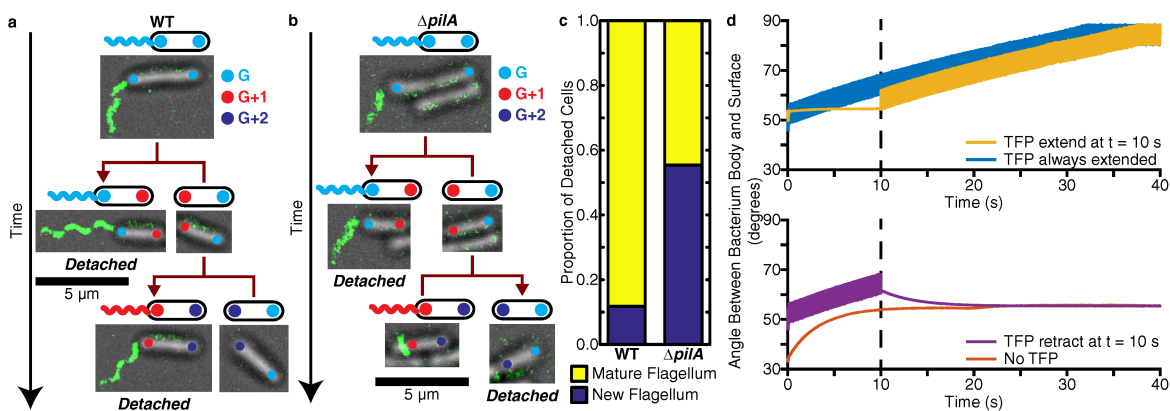
651   Figure 7. TFP and flagella are both important for the detachment process in PA14. (a,b) The location of the flagellum and
652   the age of poles (measured in generations) can be tracked across multiple generations. The fluorescence image of the
653   labeled flagellum is overlaid on top of the bright field image, and the poles are overlaid as colored circles (color

654 representing the pole generation G). Scale bars for the pictures are 5 µm. (a) Example tracking for WT, where cells with
655 mature flagella detach. (b) Example tracking for the Δ*pilA* mutant (deletion of the major subunit for the TFP filament),
656 where one cell with a mature flagellum and one cell without a flagellum detach. (c) Proportion of detached cells with a
657 mature flagellum vs a new flagellum (which includes no flagellum), calculated from 154 events for WT and 74 events for
658 Δ*pilA*. The proportions are statistically significantly different between the strains according to the χ^2 test (p-value$\ll$
659 10^{-4}). (d) Angle that the bacterium's body makes with the surface for different TFP conditions in the hydrodynamic
660 model: TFP extension at t = 10 s (top plot, yellow-orange), TFP retraction at t = 10 s (bottom plot, purple), TFP extended
661 throughout (top plot, blue), and no TFP (bottom plot, red). If the bacterium does not spin, then the angle between the
662 body and surface will stay at the (arbitrary) initial condition we have chosen in the model. We show time using units of
663 seconds and a torque value of 2 pN µm (37).
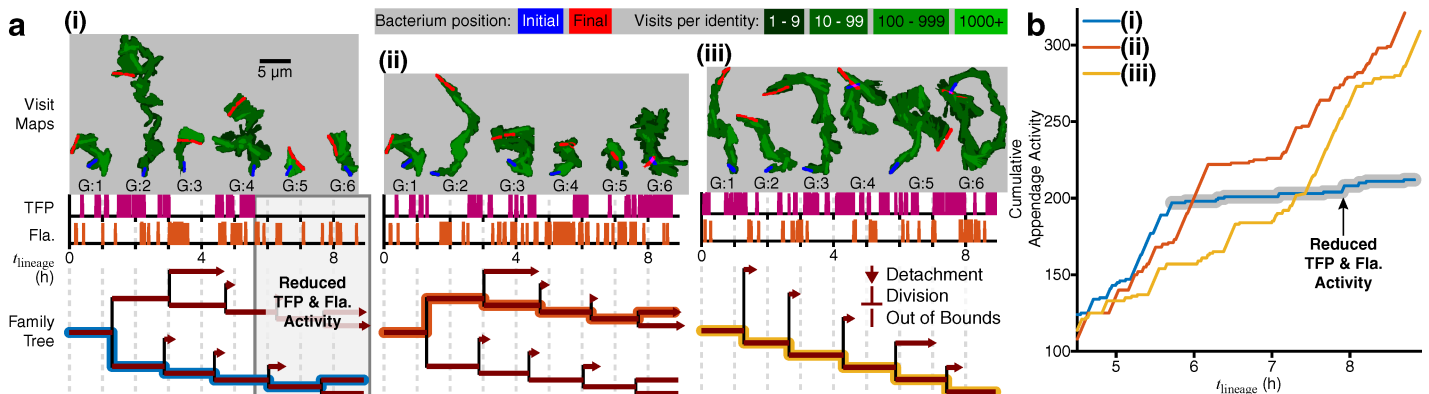
664

665 Figure 8. Family tree architecture controlled by generation-dependent motility activity. (a) TFP and flagellum activities
666 are plotted for single branches of a family as magenta and red spike plots, with each spike representing one instance of
667 activity. The colored line on the family tree plot traces the analyzed branch. We plot the corresponding visit map of each
668 single cell (top, gray boxes), shown as shades of green in a logarithmic color scale with initial (final) positions shown in
669 blue (red), to show the trajectory history and visual representation of TFP and flagellum activity. The size of each visit
670 map is roughly proportional to the level of activity: cells with high TFP activity have elongated visit maps, while cells with
671 high flagellum activity have circular visit maps. For WT, we see one example where TFP and flagellum activity are
672 reduced and do not coincide, resulting in a division event where no daughter cells detach (i). The other examples show
673 either higher activities or activities that coincide, resulting in a continuation of division events with detachment
674 occurring (ii, iii). (b) Plot of the cumulative appendage activity (i.e., the cumulative number of instances of either TFP or
675 flagellum activity) for the 3 examples in (a). For example (i), the curve plateaus out at $t_{\text{lineage}} \sim 6$ h, which is when the
676 reduction in appendage activity occurs. For examples (ii) and (iii), the curves continue to rise, which shows that the
677 appendages are continuing to be active.

678 # References

679 1.   Singh PK, Schaefer AL, Parsek MR, Moninger TO, Welsh MJ, Greenberg EP. 2000. Quorum-sensing signals
680   indicate that cystic fibrosis lungs are infected with bacterial biofilms. Nature 407:762-764.
681 2.   Hall-Stoodley L, Costerton JW, Stoodley P. 2004. Bacterial biofilms: from the Natural environment to infectious
682   diseases. Nature Reviews Microbiology 2:95.
683 3.   Biteen JS, Blainey PC, Cardon ZG, Chun M, Church GM, Dorrestein PC, Fraser SE, Gilbert JA, Jansson JK, Knight R,
684   Miller JF, Ozcan A, Prather KA, Quake SR, Ruby EG, Silver PA, Taha S, van den Engh G, Weiss PS, Wong GCL,
685   Wright AT, Young TD. 2016. Tools for the Microbiome: Nano and Beyond. ACS Nano 10:6-37.
686 4.   O'Toole GA, Wong GCL. 2016. Sensational Biofilms: Surface Sensing in Bacteria. Curr Opin Microbiol 30:139-146.
687 5.   Hug I, Deshpande S, Sprecher KS, Pfohl T, Jenal U. 2017. Second messenger–mediated tactile response by a
688   bacterial rotary motor. Science 358:531-534.
689 6.   McCarter L, Hilmen M, Silverman M. 1988. Flagellar Dynamometer Controls Swarmer Cell Differentiation of *V.*
690   *parahaemolyticus*. Cell 54:345-351.
691 7.   Ellison CK, Dalia TN, Vidal Ceballos A, Wang JC-Y, Biais N, Brun YV, Dalia AB. 2018. Retraction of DNA-bound type
692   IV competence pili initiates DNA uptake during natural transformation in *Vibrio cholerae*. Nature Microbiology
693   3:773-780.

694 8.   Lee CK, de Anda J, Baker AE, Bennett RR, Luo Y, Lee EY, Keefe JA, Helali JS, Ma J, Zhao K, Golestanian R, O'Toole
695   GA, Wong GCL. 2018. Multigenerational memory and adaptive adhesion in early bacterial biofilm communities.
696   Proceedings of the National Academy of Sciences 115:4471-4476.
697 9.   Guvener ZT, Harwood CS. 2007. Subcellular Location Characteristics of the *Pseudomonas aeruginosa* GGDEF
698   Protein, WspR, Indicate that It Produces Cyclic-di-GMP in Response to Growth on Surfaces. Mol Microbiol
699   66:1459-1473.
700 10. O'Connor JR, Kuwada NJ, Huangyutitham V, Wiggins PA, Harwood CS. 2012. Surface Sensing and Lateral
701   Subcellular Localization of WspA, the Receptor in a Chemosensory-like System Leading to C-di-GMP Production.
702   Mol Microbiol 86:720-729.
703 11. Chen Y, Chai Y, Guo JH, Losick R. 2012. Evidence for cyclic Di-GMP-mediated signaling in *Bacillus subtilis*. Journal
704   of bacteriology 194:5080-5090.
705 12. Ferreira RB, Chodur DM, Antunes LC, Trimble MJ, McCarter LL. 2012. Output Targets and Transcriptional
706   Regulation by a Cyclic Dimeric GMP-Responsive Circuit in the *Vibrio parahaemolyticus* Scr Network. J Bacteriol
707   194:914-924.
708 13. Gomelsky M, Galperin MY. 2013. Bacterial second messengers, cGMP and c-di-GMP, in a quest for regulatory
709   dominance. The EMBO journal 32:2421-2423.
710 14. Romling U, Galperin MY, Gomelsky M. 2013. Cyclic di-GMP: the first 25 years of a universal bacterial second
711   messenger. Microbiology and molecular biology reviews : MMBR 77:1-52.
712 15. Jones CJ, Utada A, Davis KR, Thongsomboon W, Zamorano Sanchez D, Banakar V, Cegelski L, Wong GCL, Yildiz FH.
713   2015. C-di-GMP Regulates Motile to Sessile Transition by Modulating MshA Pili Biogenesis and Near-Surface
714   Motility Behavior in Vibrio cholerae. PLOS Pathogens 11:e1005068.
715 16. Zamorano-Sánchez D, Xian W, Lee CK, Salinas M, Thongsomboon W, Cegelski L, Wong GCL, Yildiz FH. 2019.
716   Functional Specialization in *Vibrio cholerae* Diguanylate Cyclases: Distinct Modes of Motility Suppression and c-
717   di-GMP Production. mBio 10:e00670-19.
718 17. Luo Y, Zhao K, Baker AE, Kuchma SL, Coggan KA, Wolfgang MC, Wong GCL, O'Toole GA. 2015. A Hierarchical
719   Cascade of Second Messengers Regulates *Pseudomonas aeruginosa* Surface Behaviors. mBio 6:1-11.
720 18. Persat A, Inclan YF, Engel JN, Stone HA, Gitai Z. 2015. Type IV Pili Mechanochemically Regulate Virulence Factors
721   in *Pseudomonas aeruginosa*. Proc Natl Acad Sci U S A 112:7563-7568.
722 19. Costerton JW, Stewart PS, Greenberg EP. 1999. Bacterial biofilms: a common cause of persistent infections.
723   Science 284:1318-22.
724 20. Huangyutitham V, Güvener ZT, Harwood CS. 2013. Subcellular Clustering of the Phosphorylated WspR Response
725   Regulator Protein Stimulates Its Diguanylate Cyclase Activity. mBio 4:e00242-13.
726 21. Armbruster CR, Lee CK, Parker-Gilham J, de Anda J, Xia A, Zhao K, Tseng BS, Hoffman LR, Jin F, Harwood CS,
727   Wong GCL, Parsek MR. 2019. Heterogeneity in surface sensing suggests a division of labor in *Pseudomonas*
728   *aeruginosa* populations. eLife 8:e45084.
729 22. Irie Y, Borlee BR, O'Connor JR, Hill PJ, Harwood CS, Wozniak DJ, Parsek MR. 2012. Self-produced
730   exopolysaccharide is a signal that stimulates biofilm formation in *Pseudomonas aeruginosa*. Proc Natl Acad Sci U
731   S A 109:20632-20636.
732 23. Zhao K, Tseng BS, Beckerman B, Jin F, Gibiansky ML, Harrison JJ, Luijten E, Parsek MR, Wong GCL. 2013. Psl Trails
733   Guide Exploration and Microcolony Formation in *Pseudomonas aeruginosa* Biofilms. Nature (London, U K)
734   497:388-391.
735 24. Colvin KM, Gordon VD, Murakami K, Borlee BR, Wozniak DJ, Wong GC, Parsek MR. 2011. The pel polysaccharide
736   can serve a structural and protective role in the biofilm matrix of *Pseudomonas aeruginosa*. PLoS Pathog
737   7:e1001264.
738 25. Sauer K, Camper AK, Ehrlich GD, Costerton JW, Davies DG. 2002. *Pseudomonas aeruginosa* Displays Multiple
739   Phenotypes during Development as a Biofilm. Journal of Bacteriology 184:1140-1154.
740 26. Davey ME, Caiazza NC, O'Toole GA. 2003. Rhamnolipid Surfactant Production Affects Biofilm Architecture in
741   *Pseudomonas aeruginosa* PAO1. Journal of Bacteriology 185:1027-1036.
742 27. Henrici AT. 1933. Studies of Freshwater Bacteria: I. A Direct Microscopic Technique. J Bacteriol 25:277-87.
743 28. Zobell CE, Allen EC. 1935. The Significance of Marine Bacteria in the Fouling of Submerged Surfaces. Journal of
744   Bacteriology 29:239-251.
745 29. Sanchez A, Golding I. 2013. Genetic Determinants and Cellular Constraints in Noisy Gene Expression. Science
746   342:1188-1193.

30. Shiryayev AN. 2012. Selected Works of AN Kolmogorov: Volume II Probability Theory and Mathematical Statistics, vol 26. Springer Science & Business Media.

31. Arley N. 1949. On the "birth-and-death" process. Scandinavian Actuarial Journal 1949:21-26.

32. Kendall DG. 1949. Stochastic Processes and Population Growth. Journal of the Royal Statistical Society Series B (Methodological) 11:230-282.

33. Kendall DG. 1948. On the Generalized "Birth-and-Death" Process. Ann Math Statist 19:1-15.

34. Novozhilov AS, Karev GP, Koonin EV. 2006. Biological applications of the theory of birth-and-death processes. Briefings in Bioinformatics 7:70-85.

35. Feller W. On the Theory of Stochastic Processes, with Particular Reference to Applications, p 403-432. *In* (ed), University of California Press,

36. Conrad JC, Gibiansky ML, Jin F, Gordon VD, Motto Da, Mathewson Ma, Stopka WG, Zelasko DC, Shrout JD, Wong GCL. 2011. Flagella and Pili-Mediated Near-Surface Single-Cell Motility Mechanisms in *P. aeruginosa*. Biophys J 100:1608-1616.

37. Bennett RR, Lee CK, De Anda J, Nealson KH, Yildiz FH, O'Toole GA, Wong GCL, Golestanian R. 2016. Species-Dependent Hydrodynamics of Flagellum-Tethered Bacteria in Early Biofilm Development. J R Soc, Interface 13:20150966.

38. Gibiansky ML, Conrad JC, Jin F, Gordon VD, Motto DA, Mathewson MA, Stopka WG, Zelasko DC, Shrout JD, Wong GCL. 2010. Bacteria Use Type IV Pili to Walk Upright and Detach from Surfaces. Science (Washington, DC, U S) 330:197.

39. Coates J, Park BR, Le D, Şimşek E, Chaudhry W, Kim M. 2018. Antibiotic-induced population fluctuations and stochastic clearance of bacteria. eLife 7:e32976.

40. Irie Y, Roberts AEL, Kragh KN, Gordon VD, Hutchison J, Allen RJ, Melaugh G, Bjarnsholt T, West SA, Diggle SP. 2017. The *Pseudomonas aeruginosa* PSL Polysaccharide Is a Social but Noncheatable Trait in Biofilms. mBio 8:e00374-17.

41. Nadell CD, Drescher K, Foster KR. 2016. Spatial structure, cooperation and competition in biofilms. Nature Reviews Microbiology 14:589-600.

42. Freschi L, Jeukens J, Kukavica-Ibrulj I, Boyle B, Dupont M-J, Laroche J, Larose S, Maaroufi H, Fothergill JL, Moore M, Winsor GL, Aaron SD, Barbeau J, Bell SC, Burns JL, Camara M, Cantin A, Charette SJ, Dewar K, Déziel É, Grimwood K, Hancock REW, Harrison JJ, Heeb S, Jelsbak L, Jia B, Kenna DT, Kidd TJ, Klockgether J, Lam JS, Lamont IL, Lewenza S, Loman N, Malouin F, Manos J, McArthur AG, McKeown J, Milot J, Naghra H, Nguyen D, Pereira SK, Perron GG, Pirnay J-P, Rainey PB, Rousseau S, Santos PM, Stephenson A, Taylor V, Turton JF, Waglechner N, et al. 2015. Clinical utilization of genomics data produced by the international *Pseudomonas aeruginosa* consortium. Frontiers in Microbiology 6:1036.

43. De Soyza A, Hall AJ, Mahenthiralingam E, Drevinek P, Kaca W, Drulis-Kawa Z, Stoitsova SR, Toth V, Coenye T, Zlosnik JEA, Burns JL, Sá-Correia I, De Vos D, Pirnay J-P, J. Kidd T, Reid D, Manos J, Klockgether J, Wiehlmann L, Tümmler B, McClean S, Winstanley C, pathogens" EFfCABCsvdocf. 2013. Developing an international *Pseudomonas aeruginosa* reference panel. MicrobiologyOpen 2:1010-1023.

44. Cullen L, Weiser R, Olszak T, Maldonado RF, Moreira AS, Slachmuylders L, Brackman G, Paunova-Krasteva TS, Zarnowiec P, Czerwonka G, Reilly J, Drevinek P, Kaca W, Melter O, De Soyza A, Perry A, Winstanley C, Stoitsova SR, Lavigne R, Mahenthiralingam E, Sá-Correia I, Coenye T, Drulis-Kawa Z, Augustyniak D, Valvano MA, McClean S. 2015. Phenotypic characterization of an international *Pseudomonas aeruginosa* reference panel: strains of cystic fibrosis (CF) origin show less in vivo virulence than non-CF strains. Microbiology 161:1961-1977.

45. Freschi L, Bertelli C, Jeukens J, Moore MP, Kukavica-Ibrulj I, Emond-Rheault J-G, Hamel J, Fothergill JL, Tucker NP, McClean S, Klockgether J, de Soyza A, Brinkman FSL, Levesque RC, Winstanley C. 2018. Genomic characterisation of an international *Pseudomonas aeruginosa* reference panel indicates that the two major groups draw upon distinct mobile gene pools. FEMS Microbiology Letters 365.

46. Mischel W, Ebbesen EB, Raskoff Zeiss A. 1972. Cognitive and attentional mechanisms in delay of gratification. Journal of Personality and Social Psychology 21:204-218.

47. Rahme LG, Stevens EJ, Wolfort SF, Shao J, Tompkins RG, Ausubel FM. 1995. Common virulence factors for bacterial pathogenicity in plants and animals. Science 268:1899-1902.

48. Kuchma SL, Ballok AE, Merritt JH, Hammond JH, Lu W, Rabinowitz JD, O'Toole GA. 2010. Cyclic-di-GMP-mediated repression of swarming motility by *Pseudomonas aeruginosa*: the *pilY1* gene and its impact on surface-associated behaviors. J Bacteriol 192:2950-64.

23

800   49.   de Anda J, Lee EY, Lee CK, Bennett RR, Ji X, Soltani S, Harrison MC, Baker AE, Luo Y, Chou T, O'Toole GA, Armani
801   AM, Golestanian R, Wong GCL. 2017. High-Speed "4D" Computational Microscopy of Bacterial Surface Motility.
802   ACS Nano 11:9340-9351.
803   50.   O'Toole GA, Kolter R. 1998. Initiation of biofilm formation in *Pseudomonas fluorescens* WCS365 proceeds via
804   multiple, convergent signalling pathways: a genetic analysis. Molecular Microbiology 28:449-461.
805   51.   O'Toole GA. 2011. Microtiter dish biofilm formation assay. J Vis Exp doi:10.3791/2437:e2437.
806   52.   Holloway BW. 1955. Genetic Recombination in *Pseudomonas aeruginosa*. Microbiology 13:572-581.
807   53.   Soare MV, Teodorescu PP, Toma I. 2007. Ordinary differential equations with applications to mechanics, vol 585.
808   Springer.
809   54.   Khinchin AY, Andrews D, Quenouille MH. 2013. Mathematical methods in the theory of queuing. Courier
810   Corporation.
811   55.   Gray J, Hancock GJ. 1955. The Propulsion of Sea-Urchin Spermatozoa. J Exp Biol 32:802-814.

812

813 ## Supplementary Materials

814 ## Supplementary Figures
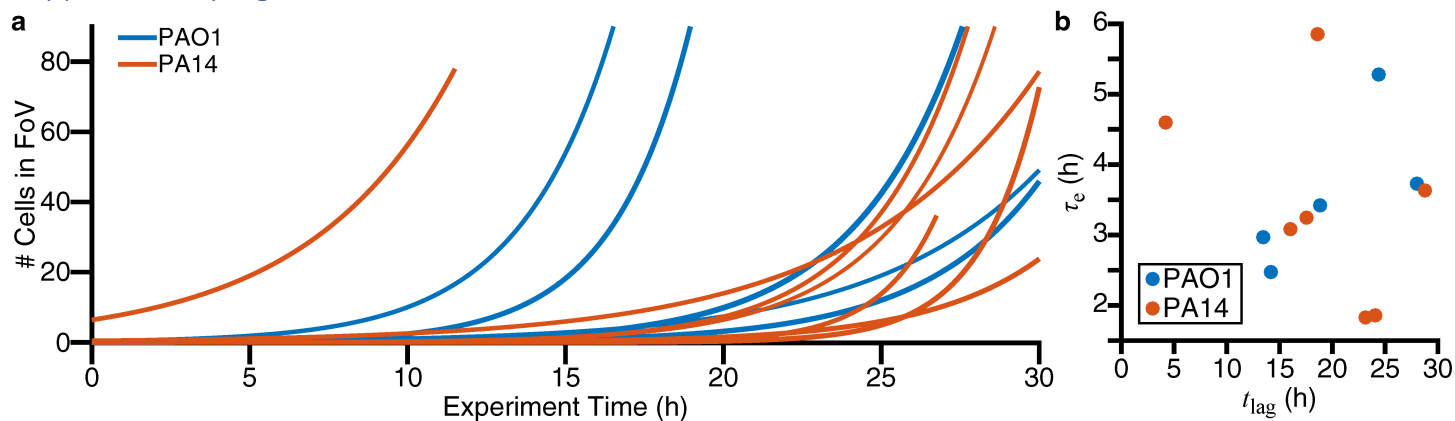
815

816 Figure S1. Exponential fits of bacteria count as a function of experiment time. (a) Each line is a fit to the function $N(t) =$
817 $N(0)\exp\big((t - t_{\text{lag}})/\tau_e\big)$ for data shown in Figure 1. $N(0)$ is the number of cells at time 0, t_{lag} characterizes the time
818 scale of the lag period where N is roughly constant, and τ_e characterizes the time scale of exponential increase ($1/\tau_e$
819 characterizes the rate of exponential increase). (b) Plots of τ_e vs. t_{lag} for the fits in part (a).
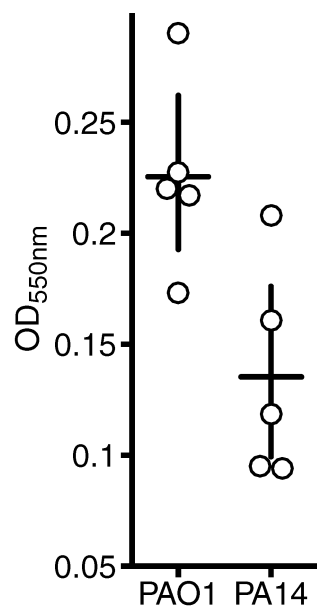
820

821 Figure S2. Monitoring biofilm formation via crystal violet assays. The $\text{OD}_{550\text{nm}}$ values are proportional to the amount of
822 biofilm stained by crystal violet. Circles represent individual biological replicates, each of which is the mean of 4
823 technical replicates. Horizontal lines represent the mean $\text{OD}_{550\text{nm}}$ values. Vertical lines indicate the 95% confidence
824 interval calculated from the bootstrap sampling distribution of the mean $\text{OD}_{550\text{nm}}$ values.

25
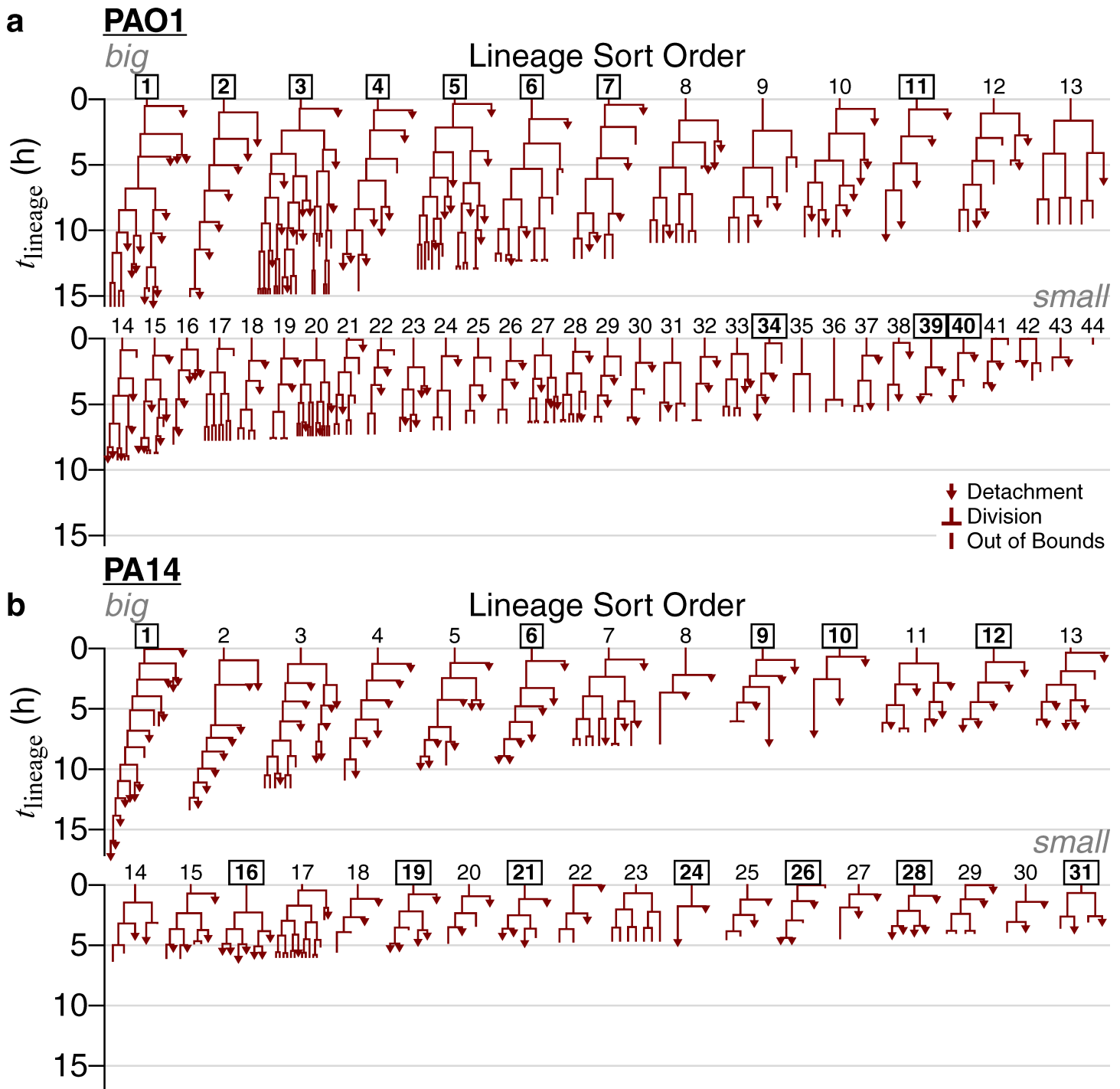
Figure S3. All families in the processive regime of reversible attachment, which is when cells divide at least once before detaching. We monitor the time that a given isolated family, consisting of an attached cell (founder cell) and its progeny (daughter cells), stays continually on the surface, which we designate as lineage time $(t = t_{lineage})$. For each family, we begin tracking at the frame individual, founder bacteria attach and assign this as $t_{lineage} = 0$ h. We continue tracking until either the entire family detaches, or until we lose track of that family (where we can no longer distinguish individual cells, or the cells move out of the recording boundaries). This final time point is recorded as the family's residence time. For families that we lose track of, their true residence times can be greater than or equal to these recorded values, while for families that end in detachment, their recorded and true residence times are equal. Only families that end in detachment are used for calculating the average residence time to avoid the uncertainty in actual residence times for families that we lose track of. For each regime and strain, we sort families by residence times in descending order, which sorts them by the amount of time that they have continuously contacted the surface. Lineage indices that are boxed and bolded are the families selected for use in the model. The criteria used to select families for the model are described as follows. We set the minimum number of families required for the model at ≈10 families.

839 First, we select all families that result in lineage "extinction" events (where we observe the family ending in a
840 detachment event), because these families all have defined outcomes (recorded and true residence times are equal).
841 Conversely, families that we lose track of (where we can no longer distinguish individual cells, or the cells move out of
842 the recording boundaries) have undefined outcomes (true residence times are greater than or equal to the recorded
843 residence times). For PA14, this results in 12 selected families (#1, 6, 9, 10, 12, 16, 19, 21, 24, 26, 28, and 31), which
844 meets the minimum family number requirement. For PAO1, this results in 4 selected families (#11, 34,39, and 40), which
845 is not enough. To increase the number of selected families for PAO1, we apply a residence time cutoff on the families
846 with undefined outcomes, so that all selected families have defined outcomes at least in the lineage time window the
847 analysis is performed on. A residence time cutoff of $t_{\text{lineage}} = 12$ h results in an additional 7 families (#1-7) for a total of
848 11 selected families for PAO1, which meets the minimum family number requirement.
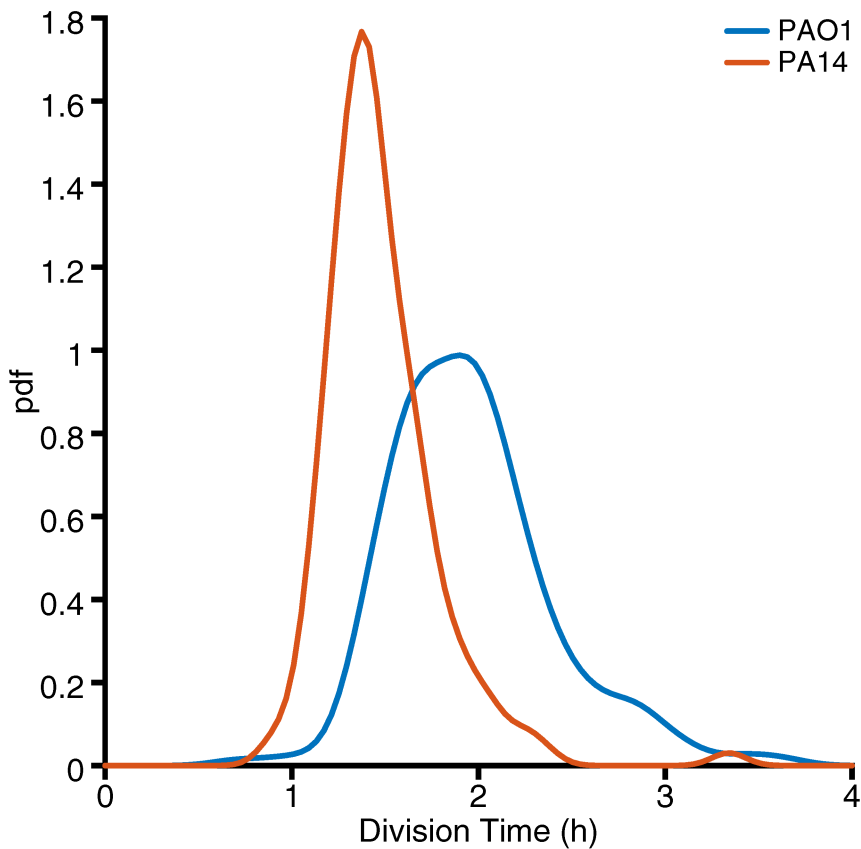
849
850 Figure S4. Distribution of division times for PAO1 and PA14. Division time is calculated as the time between
851 consecutively observed division events in a family. Distributions are plotted as pdf (probability density function)
852 calculated via kernel density estimation. PAO1 has a median division time of 1.92 h with a 95% confidence interval of
853 (1.87 h, 1.96 h), and PA14 has a median division time of 1.42 h with a 95% confidence interval of (1.38 h, 1.45 h). PAO1
854 has a mean ± standard deviation division time of 1.96 ± 0.44 h, and PA14 has a mean ± standard deviation division time
855 of 1.48 ± 0.30 h.

27
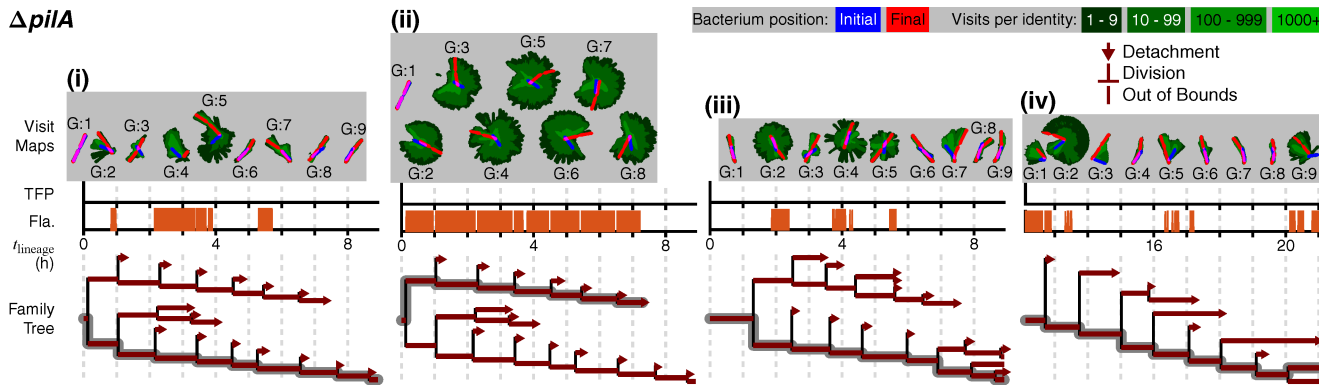
Figure S5. Appendage activity tracking for the ΔpilA mutant. We repeat the analysis in Figure 8 for the ΔpilA mutant and find one predominant behavior up the 9 generations shown here, consistent with this strain having predominantly one-legged division branching (8). We observe no TFP activity, which is consistent with this strain having no TFP; we observe sporadic, but prolonged, flagellum activity, which is consistent with observations of this strain spinning on the surface for prolonged periods of time; and we observe detachment events without flagellum activity, which is consistent with observations of detachment events where cells did not have a labeled flagellum. Beyond generation 9, the ΔpilA mutant continues to have mainly one-legged division-branching for multiple subsequent generations.
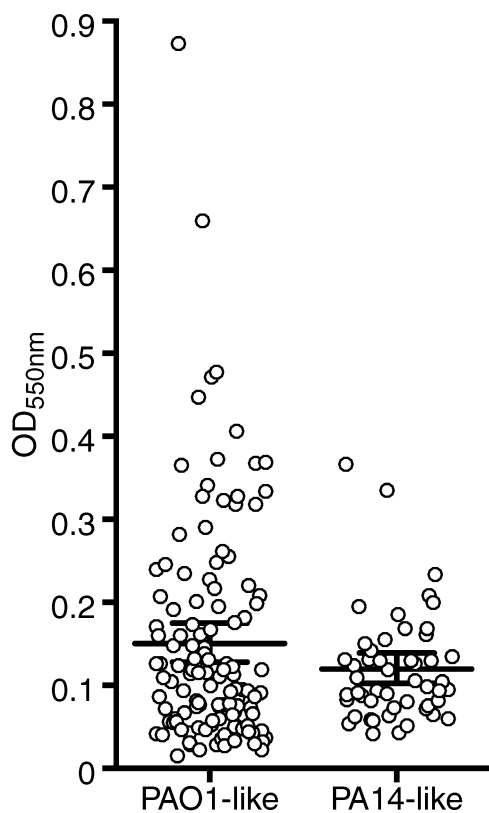
Figure S6. Crystal violet biofilm assay results for 35 *P. aeruginosa* strains (25 PAO1-like and 10 PA14-like strains, including PAO1 and PA14 strains) in the International *P. aeruginosa* Consortium Database (IPCD). These strains are identified as either PAO1-like or PA14-like based on their phylogeny (i.e., same phylogenetic sub-group as either PAO1 or PA14) (42-45). The OD_{550nm} values are proportional to the amount of biofilm stained by crystal violet. Circles represent individual biological replicates, each of which is the mean of 4 technical replicates. Longer horizontal lines represent the mean OD_{550nm} values. Vertical lines and error bars indicate the 95% confidence interval calculated from the bootstrap sampling distribution of the mean OD_{550nm} values. Comparing these distributions shows that the mean OD_{550nm} value for the PAO1-like strains are higher than the mean OD_{550nm} value for PA14-like strains (p-value of 0.02).

28

874   Tables

875   Table S1. Strains used in the crystal violet biofilm assays. The collection of isolates was described in (43). (CF = cystic
876   fibrosis)

Strain ID	Source ID	Local Strain collection #	Origin and source	Original reference
PA14 WT		DH123	PA14 *P. aeruginosa* wild type	(47)
PAO1 WT		DH1467	PAO1 *P. aeruginosa* wild type	(56)
1268	15108-1	DH3446	ICU (acute infection), Spain	(57)
87	679	DH3418	Non CF Urine sample, male, Wroclaw Poland, 2011	(43)
95	CPHL9433	DH3425	Tobacco plant, Philippines	(58)
1103	AUS23	DH3436	Adult CF (2007), Brisbane, Australia	(59)
80	AMT0060-1	DH3411	Pediatric CF, Seattle, WA	(60)
1273	TBCF10839	DH3451	CF, Germany	(61)
1260	AMT0023-30	DH3441	Pediatric CF, Seattle, WA	(60)
94	U018A	DH3424	Hobart, Australia, CF patient	(58)
92	LMG14084	DH3422	Bucharest, Romania, Water, 1960-1964	(58)
85	IST27N	DH3416	Lisbon Portugal, CF patient	(62)
1259	AA2	DH3440		
93	Pr335	DH3423	Prague, Czech Republic, Hospital environment 1997	(58)
91	Jpn1563	DH3421	Lake Tamaco, Japan, Lake water, 2003	(58)
84	IST27	DH3415	Lisbon Portugal, CF patient	(62)
1258	AUS52	DH3439	Adult CF (2008), Hobart, Australia	(63, 64)
1266	Mi162-2	DH3445	Non CF burn, Ann Arbor, MI, 1997	(58)
89	1709-12	DH3420	Leuven Belgium Non CF clinical 2004	(58)
2495	LES400	DH3459	CF, U.K.	(65)
1272	A5803	DH3450	Community-acquired pneumonia	(66)
1264	39016	DH3444	Keratitis eye isolate, U.K.	(67)
88	NH57388A	DH3419	CF, Denmark	(68)
2496	LES431	DH3460	Non CF parent of CF patient, U.K.	(67)
1271	KKI	DH3449	CF, Germany	(69)
1262	CHA	DH3443	CF	(70)
83	PAK	DH3414	Clinical non CF	(71)
2617	LESB58	DH3461	CF, U.K., 1988	(72)
1270	39177	DH3448	Keratitis, Manchester U.K.	(67)
1261	AMT0023-34	DH3442	Pediatric CF, Seattle, WA	(60)

29

Strain ID	Source ID	Local Strain collection #	Origin and source	Original reference
82	AMT0060-3	DH3413	Pediatric CF, Seattle, WA	(60)
2045	UCBPP-PA14	DH3458	Human Burn isolate	(47)
1269	13121-1	DH3447	ICU (acute infection), France	(66)
1256	C3719	DH3437	CF, Manchester, U.K.	(73)
81	AMT0060-2	DH3412	Pediatric CF, Seattle, WA	(60)

877

Supplementary References

878   8.   Lee CK, de Anda J, Baker AE, Bennett RR, Luo Y, Lee EY, Keefe JA, Helali JS, Ma J, Zhao K, Golestanian R, O'Toole
879   GA, Wong GCL. 2018. Multigenerational memory and adaptive adhesion in early bacterial biofilm communities.
880   Proceedings of the National Academy of Sciences 115:4471-4476.

881   42.   Freschi L, Jeukens J, Kukavica-Ibrulj I, Boyle B, Dupont M-J, Laroche J, Larose S, Maaroufi H, Fothergill JL, Moore
882   M, Winsor GL, Aaron SD, Barbeau J, Bell SC, Burns JL, Camara M, Cantin A, Charette SJ, Dewar K, Déziel É,
883   Grimwood K, Hancock REW, Harrison JJ, Heeb S, Jelsbak L, Jia B, Kenna DT, Kidd TJ, Klockgether J, Lam JS, Lamont
884   IL, Lewenza S, Loman N, Malouin F, Manos J, McArthur AG, McKeown J, Milot J, Naghra H, Nguyen D, Pereira SK,
885   Perron GG, Pirnay J-P, Rainey PB, Rousseau S, Santos PM, Stephenson A, Taylor V, Turton JF, Waglechner N, et al.
886   2015. Clinical utilization of genomics data produced by the international *Pseudomonas aeruginosa* consortium.
888   Frontiers in Microbiology 6:1036.

889   43.   De Soyza A, Hall AJ, Mahenthiralingam E, Drevinek P, Kaca W, Drulis-Kawa Z, Stoitsova SR, Toth V, Coenye T,
890   Zlosnik JEA, Burns JL, Sá-Correia I, De Vos D, Pirnay J-P, J. Kidd T, Reid D, Manos J, Klockgether J, Wiehlmann L,
891   Tümmler B, McClean S, Winstanley C, pathogens" EFfCABCsvdocf. 2013. Developing an international
892   *Pseudomonas aeruginosa* reference panel. MicrobiologyOpen 2:1010-1023.

893   44.   Cullen L, Weiser R, Olszak T, Maldonado RF, Moreira AS, Slachmuylders L, Brackman G, Paunova-Krasteva TS,
894   Zarnowiec P, Czerwonka G, Reilly J, Drevinek P, Kaca W, Melter O, De Soyza A, Perry A, Winstanley C, Stoitsova
895   SR, Lavigne R, Mahenthiralingam E, Sá-Correia I, Coenye T, Drulis-Kawa Z, Augustyniak D, Valvano MA, McClean
896   S. 2015. Phenotypic characterization of an international *Pseudomonas aeruginosa* reference panel: strains of
897   cystic fibrosis (CF) origin show less in vivo virulence than non-CF strains. Microbiology 161:1961-1977.

898   45.   Freschi L, Bertelli C, Jeukens J, Moore MP, Kukavica-Ibrulj I, Emond-Rheault J-G, Hamel J, Fothergill JL, Tucker NP,
899   McClean S, Klockgether J, de Soyza A, Brinkman FSL, Levesque RC, Winstanley C. 2018. Genomic characterisation
900   of an international *Pseudomonas aeruginosa* reference panel indicates that the two major groups draw upon
901   distinct mobile gene pools. FEMS Microbiology Letters 365.

902   47.   Rahme LG, Stevens EJ, Wolfort SF, Shao J, Tompkins RG, Ausubel FM. 1995. Common virulence factors for
903   bacterial pathogenicity in plants and animals. Science 268:1899-1902.

904   56.   Stover CK, Pham XQ, Erwin AL, Mizoguchi SD, Warrener P, Hickey MJ, Brinkman FS, Hufnagle WO, Kowalik DJ,
905   Lagrou M, Garber RL, Goltry L, Tolentino E, Westbrock-Wadman S, Yuan Y, Brody LL, Coulter SN, Folger KR, Kas A,
906   Larbig K, Lim R, Smith K, Spencer D, Wong GK, Wu Z, Paulsen IT, Reizer J, Saier MH, Hancock RE, Lory S, Olson
907   MV. 2000. Complete genome sequence of *Pseudomonas aeruginosa* PAO1, an opportunistic pathogen. Nature
908   406:959-964.

909   57.   Köhler T, Buckling A, van Delden C. 2009. Cooperation and virulence of clinical *Pseudomonas aeruginosa*
910   populations. Proceedings of the National Academy of Sciences 106:6339-6344.

911   58.   Pirnay J-P, Bilocq F, Pot B, Cornelis P, Zizi M, Van Eldere J, Deschaght P, Vaneechoutte M, Jennes S, Pitt T, De Vos
912   D. 2009. *Pseudomonas aeruginosa* Population Structure Revisited. PLOS ONE 4:e7740.

913   59.   O'Carroll MR, Syrmis MW, Wainwright CE, Greer RM, Mitchell P, Coulter C, Sloots TP, Nissen MD, Bell SC. 2004.
914   Clonal strains of *Pseudomonas aeruginosa* in paediatric and adult cystic fibrosis units. European Respiratory
915   Journal 24:101-106.

916   60.   Mulcahy LR, Burns JL, Lory S, Lewis K. 2010. Emergence of *Pseudomonas aeruginosa* Strains Producing High
917   Levels of Persister Cells in Patients with Cystic Fibrosis. Journal of Bacteriology 192:6191-6199.

918   61.   Bezuidt OK, Klockgether J, Elsen S, Attree I, Davenport CF, Tümmler B. 2013. Intraclonal genome diversity of
919   *Pseudomonas aeruginosa* clones CHA and TB. BMC Genomics 14:416.

920   62.   Leitão JH, Alvim T, Sá-Correia I. 1996. Ribotyping of *Pseudomonas aeruginosa* isolates from patients and water
921   springs and genome fingerprinting of variants concerning mucoidy. Pathogens and Disease 13:287-292.

922   63.   Bradbury R, Champion A, Reid DW. 2008. Poor clinical outcomes associated with a multi-drug resistant clonal
923   strain of *Pseudomonas aeruginosa* in the Tasmanian cystic fibrosis population. Respirology 13:886-892.

924   64.   Kidd TJ, Ramsay KA, Hu H, Marks GB, Wainwright CE, Bye PT, Elkins MR, Robinson PJ, Rose BR, Wilson JW,
925   Grimwood K, Bell SC. 2013. Shared *Pseudomonas aeruginosa* genotypes are common in Australian cystic fibrosis
926   centres. European Respiratory Journal 41:1091-1100.

927   65.   Salunkhe P, Smart CHM, Morgan JAW, Panagea S, Walshaw MJ, Hart CA, Geffers R, Tümmler B, Winstanley C.
928   2005. A Cystic Fibrosis Epidemic Strain of *Pseudomonas aeruginosa* Displays Enhanced Virulence and
929   Antimicrobial Resistance. Journal of Bacteriology 187:4908-4920.

930   66.   Wiehlmann L, Wagner G, Cramer N, Siebert B, Gudowius P, Morales G, Köhler T, van Delden C, Weinel C, Slickers
931   P, Tümmler B. 2007. Population structure of *Pseudomonas aeruginosa*. Proceedings of the National Academy of
932   Sciences 104:8101-8106.
933   67.   Stewart RMK, Wiehlmann L, Ashelford KE, Preston SJ, Frimmersdorf E, Campbell BJ, Neal TJ, Hall N, Tuft S, Kaye
934   SB, Winstanley C. 2011. Genetic Characterization Indicates that a Specific Subpopulation of *Pseudomonas*
935   *aeruginosa* Is Associated with Keratitis Infections. Journal of Clinical Microbiology 49:993-1003.
936   68.   Hoffmann N, Rasmussen TB, Jensen P, Stub C, Hentzer M, Molin S, Ciofu O, Givskov M, Johansen HK, Høiby N.
937   2005. Novel Mouse Model of Chronic *Pseudomonas aeruginosa* Lung Infection Mimicking Cystic Fibrosis.
938   Infection and Immunity 73:2504-2514.
939   69.   Cramer N, Wiehlmann L, Ciofu O, Tamm S, Høiby N, Tümmler B. 2012. Molecular Epidemiology of Chronic
940   *Pseudomonas aeruginosa* Airway Infections in Cystic Fibrosis. PLOS ONE 7:e50731.
941   70.   Toussaint B, Delicattree I, Vignais PM. 1993. *Pseudomonas aeruginosa* Contains an IHF-like Protein That Binds to
942   the *algD* Promoter. Biochemical and Biophysical Research Communications 196:416-421.
943   71.   Totten PA, Lory S. 1990. Characterization of the type a flagellin gene from *Pseudomonas aeruginosa* PAK. Journal
944   of Bacteriology 172:7188-7199.
945   72.   Kukavica-Ibrulj I, Bragonzi A, Paroni M, Winstanley C, Sanschagrin F, O'Toole GA, Levesque RC. 2008. In Vivo
946   Growth of *Pseudomonas aeruginosa* Strains PAO1 and PA14 and the Hypervirulent Strain LESB58 in a Rat Model
947   of Chronic Lung Infection. Journal of Bacteriology 190:2804-2813.
948   73.   Jones AM, Dodd ME, Doherty CJ, Govan JR, Webb AK. 2002. Increased treatment requirements of patients with
949   cystic fibrosis who harbour a highly transmissible strain of *Pseudomonas aeruginosa*. Thorax 57:924-925.

950

Chapter 4

Conclusion & Outlook

This thesis was focused on the effects of the activity on the emergence of collective behavior in an active system, at a microscopic level. Over three works, from active sedimenting particles to early biofilm formation in the case of the bacteria *P. aereginosa*, via the aggregation formation for the micro-algae *C. reinhardtii*, I studied how the activity at a microscopic level affects the emergence of collective behaviors.

These results showed that the activity is a critical and decisive parameter in the emergence of macroscopic structure, characteristic of collective behaviors. The activity triggers some survival mechanisms for living system such as micro-algae, *e.g.* moving against the gravity to reach the surface Chapter 3.1, protection mechanism for the aggregation pattern Chapter 3.2, and the formation of a sustainable biofilm to protect the bacterial colony from the surrounding environment Chapter 3.3.

The methods used and developed in these three works were based on the theory of stochastic processes. In Chapters 3.1 and 3.2 the dynamics was described by two overdamped Langevin equations for the position and orientation of the active particles. Moreover, in Chapter 3.1, the associated Fokker-Planck equation was derived and solved analytically. In Chapter 3.3, the population size of bacteria colony was described by a 'birth and death' process based on a master equation. These three works followed a bottom-up approach, from a microscopic description, at the particle's level, it was possible to describe macroscopic behaviors, such as the emergence of polar order, aggregation of particles and formation of biofilm.

In the first work, Chapter 3.1, we described an active sedimentation, in which the activity was understood as the magnitude of the self-propulsion of the particle. The active particle is considered as a point particle and moves at a constant speed along a direction given by the orientation of the particle. Moreover, due to the gravity, the motion of the particle is biased by a drift velocity pointing in the direction of gravity. The system was described

in terms of two overdamped Langevin equations for the position and the orientation of the particle. From these equations the associated Fokker-Planck equation was derived. By varying the activity, from low to high, the results have shown the emergence of a polar order and wall accumulation. In this work, we developed an analytical method to study the sedimentation profile of one active particle and the analytical solution of the Fokker-Planck equation in 3D for one active particle under gravity and a confining wall was derived. With this solution, we recovered experimental results observed in [51, 133]: first, in the steady-state (long time limit) the sedimentation profile given by an exponential decay of the density profile; second, the change of the length of the sedimentation by increasing the activity. Moreover, in comparison to previous works [163, 118], this analytical method gave a direct access to the transient dynamics and kept the coupling between the position and the orientation. In order to study many interacting particles, we developed active Brownian particles simulations. By comparing the analytical solution for one active particle to the one obtained from the simulations and experimental results (Janus colloids), we have shown that our analytical solution was also valid in the dilute case. In addition, the simulations did show the emergence of collective behavior as function of the activity. For living organisms, the activity has different functions. As an example, in the case of the micro-algae *C. reinhardtii*, which can be described as an active particle, the algae need light to get energy. By increasing its activity, the algae can move 'against' the gravity and reach the surface to get more light and thus more energy to survive.

Our simulations were limited to low particle density due to the nonlinearities associated to hydrodynamics interactions, and the local approximation of the hydrodynamics can be criticized. However, we showed that the results from the simulations were valid in the dilute case and gave good quantitative and qualitative agreement with the analytical solution and experimental results. To overcome the limitation to the local hydrodynamics effect, one would have to implement a full hydrodynamics model or a hybrid model with steric and hydrodynamics interactions.
An interesting extension of this work, for the analytical method, would be to incorporate an anisotropic diffusion behavior at the boundary and compare its results with previous work done for passive particles [164]. Moreover, in order to study the confinement effect of an active particle under an external field, it would be good to incorporate a second reflective boundary condition. From the simulations point of view, in order to study the effect of the wall on the dynamics of the active particles, it would be interesting to incorporate a coupling with the hydrodynamics interactions by using Blake's tensor. However, it might be really costly in computation time, due to the number of active particles and the number of boundaries in the systems. To overcome this problem, one could use the GPU (Graphics Processing Unit) computations instead of the classical CPU (Central Processing Unit) computations used in this work. Finally, it would also be really interesting to study in more details the effect of the activity on one species like the micro-algae *C. reinhardtii* to under-

stand the underlying mechanisms of the emergence of collective behavior such as particle's aggregation.

In the second work, Chapter 3.2, we characterized the aggregation of active particles, where the activity was understood in the same way as in Chapter 3.1. However, the magnitude of the self-propulsion varies as function of the light condition and the local cell density. By means of active Brownian particles simulations, we studied the aggregation phenomena of active particles, for different activities, under confinement. Moreover, recent experimental results (in the case of the algae *C. reinhardtii*) obtained by Dr. Fragkopoulos and Dr. Bäumchen, have shown that the phenomenon could not be described by a Motility-Induced Phase Separation (MIPS) model and the need of a new model was required. By varying the activity as well as the diffusion coefficients as functions of the local cell density and in the case of many interacting active particles, we observed in the steady state regime the emergence of collective behaviors such as an aggregation of particles at the center of the compartment or a ring pattern. Moreover, by identifying the shape of the activity and the effective diffusion coefficient with the experimental results and by using reflective boundary conditions with an outside angle of 16 degrees found experimentally [114], it made possible to find the underlying mechanisms of the aggregation phenomena. The key ingredient is the dependence of the self-propulsion and diffusion coefficients on the local cell density. We showed that the use of active Brownian particles simulations designed to describe the effect of the local cell density and confinement on the dynamics re-creates the patterns observed in the experiment. In comparison to previous work [153, 154], having a direct access to the shape of the self-propulsion and the effective diffusion coefficient allows our simulation to be faithful to the experimental observations. Importantly, it was possible to match the global cell density used experimentally with the one used in the simulations, while other models need to reach a higher global cell density to describe similar collective behaviors.

We have approximated the algae as interacting spherical active Brownian particles where the steric interactions are taken as dominant, which could be criticized. The advantages of our model were a minimum of free parameters, which led to identify the fundamental underlying mechanism, and the low computation time cost. However, the interaction with the boundary conditions as well as the long range interaction are idealized. In order to better describe the interaction with the boundary and the long-range interaction between the particles, it would be interesting either to implement a coupling with hydrodynamics or a complete hydrodynamics description by means of MPCD (Multi-Particles Collision Dynamics)[165], for example. Moreover, it would be interesting to explore the effect of different boundary conditions on the collective patterns as well as the shape of the particles, for example, to identify the key parameters which lead to the position at the center of the compartment of the aggregation pattern. Already, preliminary results from the simulations showed a picture similar to the one observed experimentally and started to give some answer to this effect. It

would be nice to use other species, for example *E. coli*, to try to identify a common biological mechanism which lead to an aggregation pattern.

Finally, we studied the early stage biofilm formation in the case of two canonical strains of the bacteria family *P. aereginosa*, PA01 and PA14. They use different surface sensing circuits and a 'reversible attachment' phase is commonly observed before forming a bacterial biofilm community. However, both of these strains exhibit reversible attachment and apparently indistinguishable early biofilm behavior in bulk and single cell assays. The population dynamics were described with a 'birth and death' process with a temporal time dependence of the rates. These rates describe the reversible attachment by a division rate and a detachment rate. The division rate was described in terms of lineage time, meaning the time that the lineage stays continually on the surface. The detachment rate was connected to the EPS production. In this work, the activity was seen as detachment events. When the activity, or motility of a bacterium is suppressed, the bacterium stays at the surface. However, when the activity is not suppressed, the bacteria can detach from the surface. Previous work have used either no time dependence for the rates [67, 78, 68] or a linear time dependence only for one of the rate [80, 81]. The method showed in this work allows a general time dependence, not only linear, for the rates and it was possible to derive the associated distribution probability as well as the first moments analytically. Moreover, by including a temporal dependence to the rates, we have then included an implicit effective 'age' dependence, given by the time spent at the surface. This effect has been shown in recent works, for example [166]. Our results have suggested that both strains PA01 and PA14 used two different strategies in the surface colonization. In the case of PA01, the result was in a steady progressive increase of cell population that was irreversibly attached. In other words as soon as a bacteria attach to a surface, its lineage will form a biofilm. However, in the case of PA14, due to the high rates of cell detachment, the result was to leave the surface for the early stage. As a conclusion, our results unified disparate findings in the literature regarding early events in biofilm formation for PA01 and PA14. Moreover, we have shown that our model gave a framework to characterize different surface colonization strategies which lead to biofilm formation.

We have reduced the internal machinery for the bacteria division to only two rates, and we have neglected the possible interactions between individuals as well as a spatial dependence. Experimentally the duration between two consecutive events follows a distribution which might not be exponential, while in the model this distribution was taken as an exponential. One can criticize these approximations, but this model enabled us to connect fundamental biology to only two parameters, the rates, and it was possible to directly compare the results obtained experimentally with the one from the model.

It would be interesting to extend this work to other bacteria species, for example *Vibrio cholerae*. Already, the first results are promising, but one difficulty resides into the connection between the rates and the 'different' biology of *V. cholerae*. Moreover it might be interesting

to couple this model, if possible, with other circuits such as the cyclic AMP (cAMP) or the c-di-GMP. For example, in order to compare within the same species, the difference in the two phases: stationary or exponential. From a more mathematical approach, one can try to derive a thermodynamic description of the early biofilm formation by extending a fluctuation theorem [167, 168].

Appendix A

A Methods

A.1 Stochastic processes

The term random experiments is used in experiments for which we cannot surely predict the output in advance. However, by repeating the same experiment N times, we can observe a regularity in the average output. An example is when we toss a coin N times ($N \to \infty$) and obtain 50% of 'heads'.

Probability theory describes such phenomena based on a mathematical theory. For it, we need four ingredients: 1) a set of all possible outcomes or sample space, 2) events, 3) probability or measure and 4) random variable.

1. The sample space Ω is the set of all possible outcomes of the experiment. For example, for the toss of a coin $\Omega = \{h, t\}$, or for the number of particles in a system $\Omega = \{0, \cdots, N\}$. A trajectory in Ω is noted ω and is defined by $\omega = \{\omega_t\} = \{\omega_{t_1}, \cdots, \omega_{t_m}, \cdots\}$, Fig. A.1.

2. An event is a property which can be observed either to hold or not to hold after the experiment is done. An event is a subset of Ω. The set of all the events form a family $\mathcal{A}$, under some properties [169, 170], called σ-algebra. For example, for a coin, whose sample space is $\Omega = \{h, t\}$, $\mathcal{A} = \{\{\emptyset\}, \{h\}, \{t\}, \{h, t\}, \{t, h\}, \{h, h, t\}\}$ can be an example of σ-algebra[1].

---

[1]Before moving onto the probability or measure of the trajectories in the sample space Ω, it is important to identify the 'events' to be measured. These 'events' are given by the so-called cylinder set, which is a sequence $\epsilon = \epsilon_1, \epsilon_2, ..., \epsilon_m$ to be the set of all trajectories (sequences) $\omega \in \Omega$ that correspond with ϵ in the first m blocks. In other words, the cylinder set is the set of all trajectories which coincide with a given block of length m, in a given time window. For more details, the readers are referred to [171, 172].
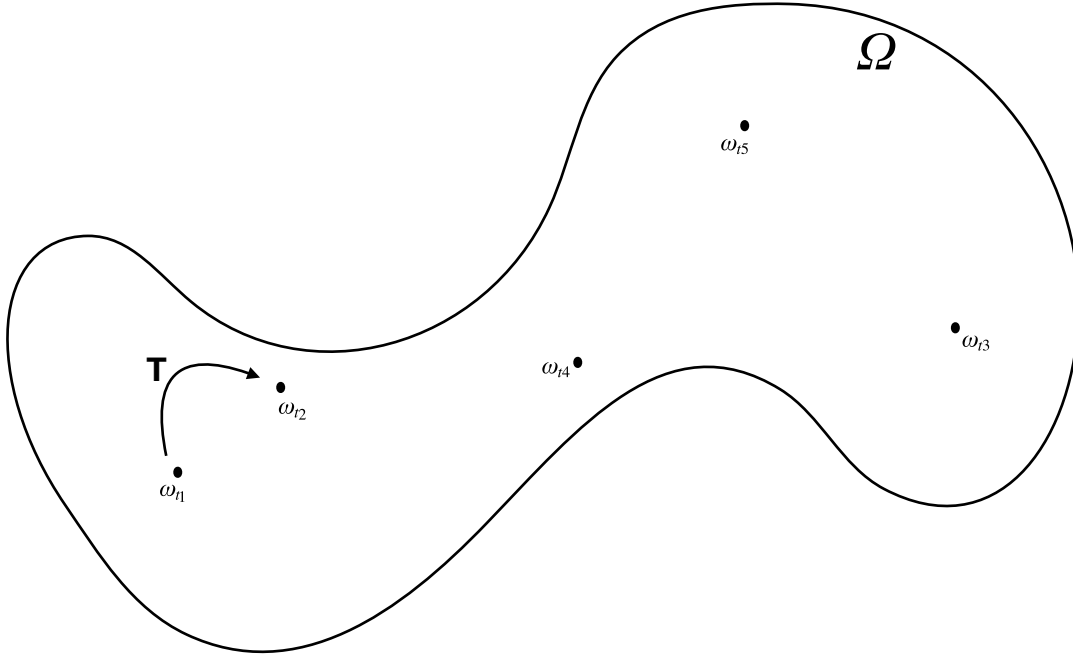
Figure A.1 – Time evolution in the sample space Ω. The time evolution is given by the application $T : \Omega \to \Omega$ and $T : \omega_t \to \omega_{t+1}$.

3. The probability (or measure) $\mathbb{P}(A)$ associates to each A ($A \in \mathcal{A}$) a number in $[0,1]$, and measures the likelihood of the event A to be realized before performing the experiment. We can built the probability $\mathbb{P}(A)$ by repeating the experiment n times. The n outcomes might be different. However, if we denote by $f_n(A)$, the number of times that the event A occurs, divided by n, also called the frequency, then we have

$$\mathbb{P}(A) = \lim_{n \to +\infty} f_n(A) \,.$$

Some properties

   (a) $0 \leqslant \mathbb{P}(A) \leqslant 1$

   (b) $\mathbb{P}(\Omega) = 1$

   (c) $\mathbb{P}(A_1 \cup A_2) = \mathbb{P}(A_1) + \mathbb{P}(A_2)$ if $A_1 \cap A_2 = \emptyset$.

   The triple $(\Omega, \mathcal{A}, \mathbb{P})$ is called a probability space, Fig. A.2.

4. A random variable X is an application from Ω into a state space E, where $E = \{\mathbb{R}, \mathbb{R}^d, \cdots\}$. Let X be a random variable $X : \Omega \to E$. It is then possible to 'transport' the probabilistic structure onto E

$$\mu_X(B) = \mathbb{P}_X(B) = \mathbb{P}(X^{-1}(B)),\ B \subset E \,.$$
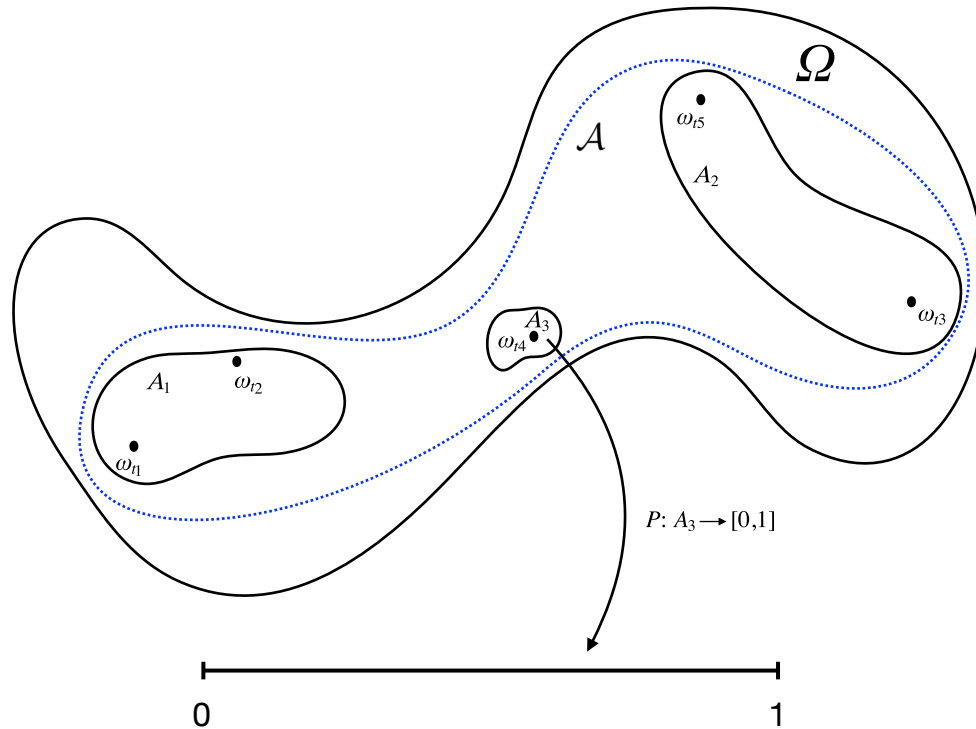
Figure A.2 – Probability or measure. The probability is an application $\mathbb{P} : A_3 \to [0, 1]$, where $A_3 \in \mathcal{A}$, which measure the likelihood of the event A_3 to be realized.

Every random variable induces a probability measure μ_X or also called the distribution (law) of X. Fig. A.3.

With these four ingredients, we can define a stochastic process.

Definition 2 (Stochastic process) *A stochastic process is a collection of random variables*

$$\{X_t\}_{t \in T},$$

defined on a probability space $\{\Omega, \mathcal{A}, \mathbb{P}\}$ and assuming values in $\mathbb{R}^d$.

Let me give a simple example of stochastic process, encountered in our daily life: tossing a coin.

Example 3 (Coin: head and tail) *Let $\Omega = \{h, t\}$ be the sample sspace and $\omega = \{\omega_{t=n}\}_{n \in \mathbb{N}} = \{h, h, t, h, h\}$ be a trajectory in the sample space. Let $E = \{0, 1\}$ be the state space and $X : \omega \to E$ a random variable, which project the trajectory ω into the state space E, $h \to 0$ and $t \to 1$. The resulting sequence for the trajectory ω reads $\{X_{t=n}\}_{n \in \mathbb{N}} = \{X_0 = 0, X_1 = 0, X_2 = 1, X_3 = 0, X_4 = 1\}$. A graphical representation is illustrated in the Fig. A.4.*

Figure A.3 – Probability distribution associated to the random variable X.

More generally, we can describe the stochastic dynamics of such process by using the Markov chains.

Figure A.4 – Toss a Coin. Time evolution of the random variable X.

Markov chains are stochastic processes discrete in time and state, which described the evolution of a random variable X_t. Before giving a mathematical defini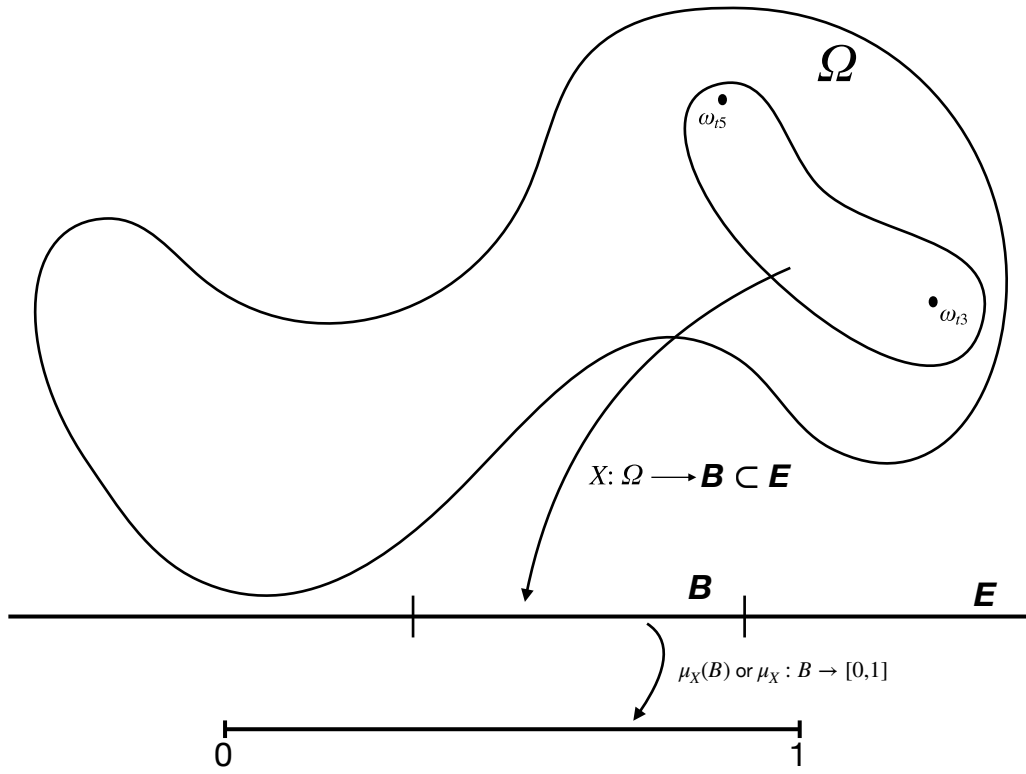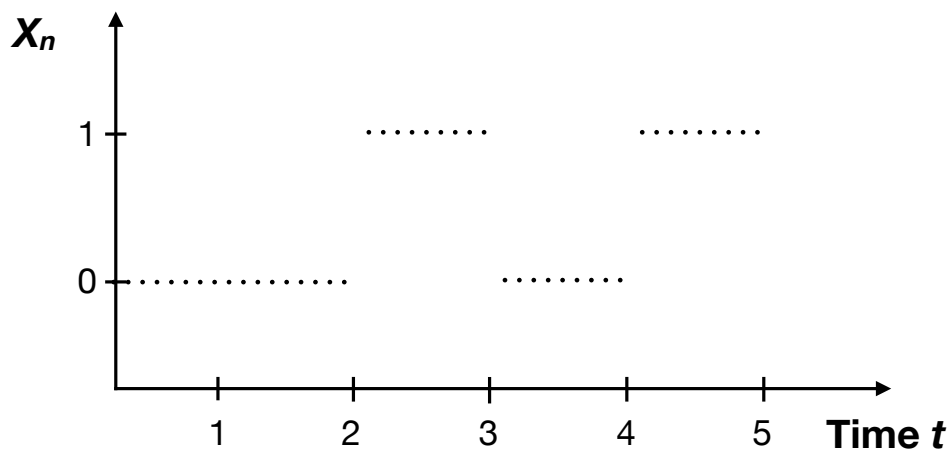tion, it is important to first give an example. In the introduction, we used a random walk to show the difference in the statistical descriptions of passive and active systems: either equilibrium or nonequilibrium.

This picture is similar to one for the coin, Fig. A.4, except that the state space E have more than two states. We can move to one state to the other according to a transition matrix P. Its elements $P(X_n = j | X_{n-1} = i)$ give the probability to move from a state i to a state j. The duration between two consecutive events, either going to the right or to the left, is taken constant. In the case of a Markov process, continuous time and discrete state, the duration between two consecutive events is exponentially distributed. A Markov chain is defined as

Definition 3 (Markov chain) *Let $E = \{1, ..., N\}$ be a state space and P a transition matrix of size N. A Markov chain on E of transition matrix P is a sequence $(X_0, X_1, X_2, ...)$ of random variables with values in E, satisfying the Markov properties*

$$P(X_n = j | X_{n-1} = i_{n-1}, X_{n-2} = i_{n-2}, ..., X_0 = i_0) = P(X_n = j | X_{n-1} = i_{n-1})$$
$$= P_{i_{n-1}j}, \qquad (A.1)$$

for all time $n \geqslant 1$ and all $(i_0, i_1, ..., i_{n-1}, ..., j)$ of E. The law or probability distribution associate to X_0, ν, is called the initial probability distribution of the chain.

In other words, if $P_{i_{n-1}j}$ does not depend on the previous history of the stochastic process, we are dealing with the simple case of a sequence of independent events, like tossing a coin. It is possible to characterize a Markov chain in terms of its trajectories, properties which can be easier to proof than the Markov property, and both relations are equivalent.

Theorem 2 *Let $\{X_n\}_{n \in \mathbb{N}}$ a sequence of random variables with values in E, ν a probability distribution on E and P a transition matrix. Then $\{X_n\}_{n \in \mathbb{N}}$ is a Markov chain of transition matrix P and of initial probability distribution ν if and only if for all $n \geqslant 0$, and for all $(i_0, i_1, ..., i_{n-1}, ..., j)$ of E, we have*

$$\mu(X_0 = i_0, X_1 = i_1 ..., X_n = i_n) = \nu_{i_0} P_{i_0 i_1} P_{i_1 i_2} ... P_{i_{n-1} i_n}. \qquad (A.2)$$

A.2 The existence and uniqueness of strong solutions

For the ordinary differential equations, we have properties on the coefficients. We use the Lipschitz condition which tell us if we have a unique solution or not. We will use the same logic for the stochastic differential equations (SDEs). In the next section we will distinguish two kind of solutions: strong and weak. We will focus more on the strong solution.

Let a general SDE

$$dX_t = a(t, X_t)dt + b(t, X_t)dW_t, \; X_{t_0} = x \tag{A.3}$$

To get the solution we should integrate

$$X_t = x + \int_0^t a(s, X_s)ds + \int_0^t b(s, X_s)dW_s \tag{A.4}$$

The first integral is just a Lebesgue integral, the second one is more tricky because we know that W_t is not differentiable. In the following, we use the Itô approach and then the Itô calculus.

For fixed a and b any solution X will depend on the particular initial value x and Wiener process W under consideration. If there is a solution for each given Wiener process, we say that the SDE has a strong solution. For the initial instant $0 \le t_0 \le T$ is arbitrary, but fixed, and $a, b : [t_0, T] \times R \to R$ are given. Most assumptions concern these coefficients

1. Measurability $a = a(t, X_t)$, $b = b(t, X_t)$ are jointly [2] (L^2-)measurable in $(t, x) \in [t_0, T] \times R$

2. Lipschitz condition There exist a constant $K > 0$, such that

$$|a(t, x) - a(t, y)| \le K|x - y|$$
$$|b(t, x) - b(t, y)| \le K|x - y|$$

   $\forall t \in [t_0, T]$ and $x, y \in R$. This condition provide the key estimates in both the proofs of uniqueness and of existence. So if the Lipschitz condition is satisfied, and, and f(x,y) is bounded, there is a solution and the solution is unique. If the Lipschitz condition is not satisfied, there is at least one other solution.

3. Linear growth bound There exist a constant $K > 0$ such that

$$|a(t, x)|^2 \le K^2(1 - |x|^2)$$
$$|b(t, x)|^2 \le K^2(1 - |x|^2)$$

   $\forall t \in [t_0, T]$ and $x, y \in R$.

4. Initial value X_{t_0} is A_{t_0}-measurable with $E(|X_{t_0}|^2) < \infty$.

---

[2] Let X be a measurable space, Y a separable metric space (or just a second countable topological space) and $f : X \times Y \to R$ a function such that f(x,y) is measurable in x and continuous in y ; then f(x,y) is jointly measurable in x and y.

Rk.: Under assumptions $A.1 - A.4$, the solution X of SDE (A.3) is a Markov process on the interval $[t_0, T]$ with transition probability $P(s, x; t, B) = P(X_T \in B | X_s = x) = P(X_t(s, x) \in B)$, $\forall t_0 \leq s \leq t \leq T$, $x \in R$ and Borel subsets[3] B of R.

In the cas of autonomous SDE:

$$dX_t = a(X_t)dt + b(X_t)dW_t$$

the solution X are homogeneous Markov process, means $P(x_1, t_1 | x_2, t_2) = P(x, 0 | x, t_2 - t_1)$. General: Solution of SDE (A.3) are diffusion process.

Theorem 3 (Diffusion process) *Assume that a and b are continuous and that $A.2 - A.4$ hold. Then, the solution X_t of (A.3) for any fixed initial value X_{t_0} is a diffusion process on $[t_0, T]$ with drift a and diffusion b.*

Theorem 4 (Pathwise unique strong solution) *Under assumptions $A.1 - A.4$ the SDE (A.3) has a pathwise unique strong solution X_t on $[t_0, T]$ with*

$$\sup_{t_0 \leq t \leq T} E(|X_t|^2) < \infty$$

We defined the strong solution and we will give a definition of the weak solution as diffusion processes. A weak solution is a solution of SDE for which the coefficients a and b of the equation, but not the Wiener process, are specified.

A.2.1 About the convergence

In the last section we spoke about the importance of the coefficients a and b, in the solution of X_t. In the following section, we will focus on the simulation of the SDE, especially their discretization scheme and then the convergence criterion.

A.2.2 Convergence criterion

Strong The goal here is to evaluate the error $\epsilon(\delta) = E(|X_T - Y_N|)$. The classical way to estimate this error is to use the Lyaponov exponents

$$\epsilon(\delta) = E(|X_T - Y_N|) \leq \sqrt{E(|X_T - Y_N|)^2}$$

---

[3]The primary example are the Borel sets on the real line (or more generally of the euclidean space), which correspond to choosing as X the space of real numbers R with the usual topology. Borel sets of the real line (or more generally of a euclidean space) are Lebesgue measurable. Conversely every Lebesgue measurable subset of the euclidean space coincides with a Borel set up to a set of measure zero.

An approximation process Y converges in the strong sense with order $\gamma \in (0, \infty]$ if there exists a finite constant K and a positive constant δ_0

$$E(|X_T - Y_N|) \leq K\delta^\gamma$$

for any time discretization with maximum step size $\delta \in (0, \delta_0)$. Usually, the theoretical error has the form Kh^p, where K is unknown, for both ODEs and SDEs. For ODEs, to obtain K, it is either possible to use a smaller step size or to use an adaptative step size routines to approximate the constant K. For SDEs, to obtain K, we can only decrease the step size but carefully the noise increments to ensure that the sample path is correctly approximated.

Theorem 5 (Strong convergence) *Suppose that*

$$E(|X_0|^2) < \infty$$
$$E(|X_0 - Y_0^\delta|^2)^{1/2} \leq K_1\delta^{1/2}$$
$$|a(t, x) - a(t, y)| + |b(t, x) - b(t, y)| \leq K_2|x - y|$$
$$|a(t, x)| + |b(t, x)| \leq K_3(1 - |x|)$$
$$|a(s, x) - a(t, x)| + |b(s, x) - b(t, x)| \leq K_4(1 - |x|)|s - t|^{1/2}$$

$\forall\ s, t \in [0, T]$ and $x, y \in R^d$, where the constants $K_1, ..., K_4$ do not depend on δ. Then for the Euler-Mayurama Y^δ the estimate

$$E(|X_t - Y^\delta(T)|) \leq K_5\delta^{1/2}$$

holds, where K_5 does not depend on δ.

This theorem establish a uniform error bound over the whole time interval $[0, T]$ rather than an error bound at just the final instant T. Furthermore, this theorem proof that the Euler-Mayurama method converges with strong order $1/2$ to the true solution.

Important remark: Euler scheme gives good numerical results when the drift and diffusion coefficients are nearly constant.

Weak   A time discrete approximation Y converges in the weak sense with order $\beta \in (0\infty]$ if for any polynomial g there exists a finite constant K and a positive constant δ_0 such that
$$|E(g(X_T))| - |E(g(Y_N))| \leq K\delta^\beta$$
for any $\delta \in (0, \delta_0)$. The Milstein scheme has a weak (convergence) order $\beta = 1$.

A.3 Random vectors on a sphere

There exist an easy way called acceptance-rejection technique made by von Neumann (1951), based on the following procedure:

1. Generate three uniform random variables ξ_i, $i \in [1, 2, 3]$ on $(0, 1)$

2. Calculate $\zeta_i = 1 - 2\xi_i$, the vector ζ is distributed uniformly in a cube of side 2 centered at the origin

3. Form the sum $\zeta^2 = \zeta_1^2 + \zeta_2^2 + \zeta_3^2$

4. For $\zeta^2 < 1$ (i.e. inside the inscribed sphere), we take $\zeta = (\zeta_1/\zeta, \zeta_2/\zeta, \zeta_3/\zeta)$ as the vector

5. For $\zeta^2 > 1$ reject the vector an return to step 1

This algorithm is still slow, then we use a slightly different one developed by Marsaglia (1972), who proposes:

1. Generate two uniform random variables ξ_i, $i \in [1, 2]$ on $(0, 1)$

2. Calculate $\zeta_i = 1 - 2\xi_i$

3. Form the sum $\zeta^2 = \zeta_1^2 + \zeta_2^2$

4. For $\zeta^2 < 1$ (i.e. inside the inscribed sphere), we take $\zeta = (2\zeta_1(1 - \zeta^2)^{1/2}, 2\zeta_2(1 - \zeta^2)^{1/2}, (1 - \zeta^2)^{1/2}$ as the vector

5. For $\zeta^2 > 1$ reject the vector an return to step 1

This method improve by a factor two the computational speed.

B Results

B.1 'Birth and death' process

The master equation for a 'birth and death' process is given by

$$\frac{dP_n}{dt} = \mu(n+1)P_{n+1} - (\lambda + \mu)nP_n + \lambda(n-1)P_{n-1}\,, \tag{A.5}$$

elementary calculations yields

$$\partial_t G(z, t) = \left[\lambda(z - 1) + \mu(\frac{1}{z} - 1)\right] G(z, t)\,. \tag{A.6}$$

A way to solve the previous Eq. (A.6) is to do a change of variable [78], $z = e^{\theta}$ and got $M(\theta, t)$. After some computations (see Appendix B.1), Eq. (A.6) reads

$$\partial_t M(\theta, t) = \left[\lambda(e^{\theta} - 1) + \mu(e^{-\theta} + 1) \right] \partial_\theta M(\theta, t) . \tag{A.7}$$

The previous equation, Eq. (A.7), is a linear partial differential equation and the solutions for

$$P \frac{\partial f}{\partial z} + Q \frac{\partial f}{\partial y} = R ,$$

is known and be rewritten as

$$\frac{dz}{P} = \frac{dy}{Q} = \frac{df}{R} .$$

Therefore $M(\theta, t)$ is a constant and

$$dt = \frac{-1}{\lambda(e^{\theta} - 1) + \mu(e^{-\theta} + 1)} d\theta$$

$$\iff dt = \frac{-e^{\theta}}{(e^{\theta} - 1)(\lambda e^{\theta} - \mu)} d\theta$$

$$\implies \int dt = t = \frac{-1}{\lambda - \mu} log(\frac{e^{\theta} - 1}{\lambda e^{\theta} - 1})$$

$$\iff 0 = (\lambda - \mu)t + log(e^{\theta} - 1) - log(\lambda e^{\theta} - \mu) \iff cst = e^{(\lambda - \mu)t} \frac{(e^{\theta} - 1)}{(\lambda e^{\theta} - \mu)} .$$

$M(\theta, t)$ can be rewritten as a linear form

$$M(\theta, t) = \psi \left(\frac{e^{(\lambda - \mu)t}(e^{\theta} - 1)}{(\lambda e^{\theta} - \mu)} \right) .$$

By a change of variable $u = \frac{e^{\theta} - 1}{\lambda e^{\theta} - \mu}$ and by elementary calculations lead to $e^{\theta} = \frac{\mu u - 1}{\lambda u - 1}$. The initial condition yields $e^{n_0 \theta} = M(\theta, t = 0) = \psi(\frac{e^{\theta} - 1}{\lambda e^{\theta} - \mu})$ and ψ is rewritten as

$$\psi(u) = e^{n_0 \theta} = \left(\frac{\mu u - 1}{\lambda u - 1} \right)^{n_0}$$

$$M(\theta, t) = \psi \left(\frac{e^{(\lambda - \mu)t}(e^{\theta} - 1)}{(\lambda e^{\theta} - \mu)} \right)$$

$$M(\theta, t) = \left(\frac{\mu \nu(\theta, t) - 1}{\lambda \nu(\theta, t) - 1} \right)^{n_0} ,$$

where $\nu(\theta, t) = \frac{e^{(\lambda - \mu)t}(e^{\theta} - 1)}{(\lambda e^{\theta} - \mu)}$. Then $G(z, t)$ reads

$$G(z, t) = \left(\frac{\mu w(z, t) - 1}{\lambda w(z, t) - 1} \right)^{n_0} , \tag{A.8}$$

where $w(z,t) = e^{(\lambda-\mu)t\frac{(z-1)}{\lambda z - \mu}}$. Moreover, in our case $n_0 = 1$, $G(z,t)$ is easily expressed in power of z^n and the solution of master equation reads

$$P_n(t) = (1-\alpha)(1-\beta)\beta^{n-1}. \tag{A.9}$$

where $\alpha = \frac{\mu(e^{(\lambda-\mu)t}-1)}{\lambda e^{(\lambda-\mu)t}-\mu}$ and $\beta = \frac{\lambda(e^{(\lambda-\mu)t}-1)}{\lambda e^{(\lambda-\mu)t}-1}$. Elementary calculations yields

$$P_n(t) = \left(\frac{e^{(\lambda-\mu)t}(1-\frac{\mu}{\lambda})}{e^{(\lambda-\mu)t}-\frac{\mu}{\lambda}}\right)\left(\frac{1-\frac{\mu}{\lambda}}{e^{(\lambda-\mu)t}-\frac{\mu}{\lambda}}\right)\left(\frac{e^{(\lambda-\mu)t}-1}{e^{(\lambda-\mu)t}-\frac{\mu}{\lambda}}\right)^{n-1}. \tag{A.10}$$

In the case of $n = 0$, $P_n(t)$ reads

$$P_0(t) = \frac{\mu(e^{(\lambda-\mu)t}-1)}{\lambda e^{(\lambda-\mu)t}-\mu}. \tag{A.11}$$

The two first moment $\langle n \rangle$ and $\langle (n-\langle n \rangle)^2 \rangle = \langle n^2 \rangle - \langle n \rangle^2$ give us access to the distribution of the process as well as the properties of the process(*e.g* diffusive or ballistic regime).

- First moment: $\langle n \rangle = \sum_n nP_n$

$$\frac{d\langle n \rangle}{dt} = \sum_n n\frac{dP_n}{dt}$$

$$= -(\lambda+\mu)\sum_n n^2 P_n + \mu\sum_n (n^2+n)P_{n+1} + \lambda\sum_n (n^2-n)P_{n-1}$$

$$= \lambda\sum_{n=1}\left[(n-1)^2 P_{n-1} + (n-1)P_{n-1}\right] + \mu\sum_{n=0}\left[(n+1)^2 P_{n+1} - (n+1)P_{n+1}\right]$$

$$- (\lambda+\mu)\sum_{n=0} n^2 P_n$$

$$\Longleftrightarrow \frac{d\langle n \rangle}{dt} = \lambda\left[\langle n^2 \rangle + \langle n \rangle\right] + \mu\left[\langle n^2 \rangle - \langle n \rangle\right] - (\lambda+\mu)\langle n^2 \rangle$$

$$\Longrightarrow \frac{d\langle n \rangle}{dt} = (\lambda-\mu)\langle n \rangle$$

$$\langle n \rangle = n(0)e^{(\lambda-\mu)t} = e^{(\lambda-\mu)t}, \ n(0) = 1. \tag{A.12}$$

- Second moment: $\langle n^2 \rangle = \sum_n n^2 P_n$

$$\frac{d\langle n^2 \rangle}{dt} = \sum_n n^2\frac{dP_n}{dt}$$

$$= -(\lambda+\mu)\sum_n n^3 P_n + \mu\sum_n (n^3+n^2)P_{n+1} + \lambda\sum_n (n^3-n^2)P_{n-1}.$$

By rewritting $(n^3 + n^2) = (n-1)^3 + 2(n-1)^2 + (n-1)$ and $(n^3 - n^2) = (n+1)^3 - 2(n+1)^2 + (n-1)$, the equation for the second moment becomes

$$\frac{d\langle n^2\rangle}{dt} = -(\lambda + \mu)\langle n^3\rangle + \mu\left[\langle n^3\rangle - 2\langle n^2\rangle + \langle n\rangle\right]$$
$$+ \lambda\left[\langle n^3\rangle + 2\langle n^2\rangle + \langle n\rangle\right]$$
$$\frac{d\langle n^2\rangle}{dt} = 2(\lambda - \mu)\langle n^2\rangle + (\lambda + \mu)\langle n\rangle . \tag{A.13}$$

In order to solve Eq. (A.13), the following method is used

$$\frac{dx}{dt} = p(t)x + q(t) \rightarrow x(t) = e^{\int p(t)dt}\left(cst + \int e^{\int p(t)dt}q(t)dt\right)$$

$$\frac{d}{dt}e^{-\int p(t)dt}x = e^{-\int p(t)dt}q(t) \rightarrow e^{-\int p(t)dt}x = \int e^{-\int p(t)dt}q(t)dt + cst .$$

In our case $p = 2(\lambda - \mu)$, $q = (\lambda + \mu)\langle n\rangle = (\lambda + \mu)e^{(\lambda+\mu)t}$ and $n_0 = 1$.

$$\langle n^2\rangle = e^{2(\lambda-\mu)t}\left[cst + \int_0^t e^{-2(\lambda-\mu)t}(\lambda + \mu)e^{(\lambda-\mu)t}dt\right]$$
$$= e^{2(\lambda-\mu)t} + \frac{(\lambda+\mu)}{(\lambda-\mu)}\left[e^{2(\lambda-\mu)t} - e^{(\lambda-\mu)t}\right]$$
$$\langle n^2\rangle = e^{2(\lambda-\mu)t} + \frac{(\lambda+\mu)}{(\lambda-\mu)}e^{(\lambda-\mu)t}\left[e^{(\lambda-\mu)t} - 1\right] , \tag{A.14}$$

and the variance reads

$$\Delta n^2 = \langle n^2\rangle - \langle n\rangle^2 = \frac{(\lambda+\mu)}{(\lambda-\mu)}e^{(\lambda-\mu)t}\left[e^{(\lambda-\mu)t} - 1\right] . \tag{A.15}$$

In the specific case when $\lambda = \mu$, Eq. (A.7) can be rewritten as

$$\partial_t M(\theta, t) = \lambda\left[e^\theta - 1 + e^{-\theta} - 1\right]\partial_\theta M(\theta, t) . \tag{A.16}$$

Same than before

$$dt = \frac{-e^\theta}{\lambda(e^\theta - 1)^2}d\theta$$
$$U = e^\theta - 1 \rightarrow du = e^\theta d\theta$$
$$dt = \frac{-e^\theta e^{-\theta}d\theta}{\lambda U^2} = -\frac{d\theta}{\lambda U^2}$$
$$t = \int dt = -\int \frac{dU}{\lambda U^2} = cst + \frac{1}{\lambda(e^\theta - 1)} \rightarrow \lambda t - \frac{1}{e^\theta - 1} = cst .$$

Hence, $M(\theta, t)$ can be put in the following form

$$M(\theta, t) = \psi \left(\lambda t - \frac{1}{e^\theta - 1} \right) . \tag{A.17}$$

$$e^{n_0 \theta} = M(\theta, t = 0) = \psi \left(-\frac{1}{\lambda(e^\theta - 1)} \right)$$

$$U = \frac{1}{e^\theta - 1} \text{ or } (e^\theta - 1)U = -1 \iff e^\theta = \frac{-1}{U} + 1$$

$$e^{n_0 \theta} = (\frac{-1}{U} + 1)^{n_0} = \psi(U) .$$

As a result, $M(\theta, t)$ reads

$$M(\theta, t) = \left(1 - \frac{1}{\lambda t - \frac{1}{e^\theta - 1}} \right)^{n_0} = \left(1 - \frac{1}{\frac{\lambda t(e^\theta - 1) - 1}{e^\theta - 1}} \right)^{n_0} = \left(\frac{\lambda t(e^\theta - 1) - 1 - (e^{\theta - 1})}{\lambda t(e^\theta - 1) - 1} \right)^{n_0}$$

$$M(\theta, t) = \left(\frac{1 - (\lambda t - 1)(e^\theta - 1)}{1 - \lambda t(e^\theta - 1)} \right)^{n_0} . \tag{A.18}$$

Then, $G(z, t)$ reads

$$G(z, t) = \left(\frac{1 - (\lambda t - 1)(z - 1)}{1 - \lambda t(z - 1)} \right)^{n_0} , \tag{A.19}$$

when $n_0 = 1$, $P_n(t)$ reads

$$P_n(t) = \frac{(\lambda t)^{n-1}}{(1 + \lambda t)^{n+1}}, \ P_0 = \frac{(\lambda t)}{(1 + \lambda t)} . \tag{A.20}$$

Equation (A.20) gives the solution of $P_n(t)$ when the coefficients λ and μ are not time dependent.

Random variable technique [78] Size of the population of individuals under consideration at time t is given by the random variable $X(t)$. At $t + \Delta t$ is $X(t + \Delta t)$ and $\Delta t X(t) = X(t + \Delta t) - X(t)$. The probability-generating function for $X(t)$ is $P(x, t)$ and for $\Delta t X(t) = X(t + \Delta t) - X(t)$ is $P(x, t + \Delta t)$. When the variable $X(t)$ and $\Delta X(t)$ are independent the nthe probability-generating function of the sum is the product of individual generating function

$$P(x, t + \Delta t) = P(x, t)\Delta P(x, t) . \tag{A.21}$$

Knowing that $P(x, t) = \mathbb{E}[x^{X(t)}]$

$$\Delta P(x, t) = \mathbb{E}[x^{\Delta X(t)}] = \sum_{x=0}^{+\infty} p(X)x^X \,,$$

where $\sum_x p(x) = 1$. In Poissonian case

- probability of having a new addition $\rightarrow \lambda \Delta t + o(\Delta t)$
- probability of having 2 or more simultaneous emission $\rightarrow o(\Delta t)$
- probability of having no change $\rightarrow 1 - \lambda \Delta t - o(\Delta t)$

These can be rewritten as

$$\lambda \Delta t + o(\Delta t) + 1 - \lambda \Delta t - o(\Delta t) = 1 - \lambda \Delta t + \lambda \Delta t$$
$$p_n(t + \Delta t) = p_{n-1}(t)\lambda \Delta t + p_n(t)(1 - \lambda \Delta t)$$
$$\Delta P(x, t) = [p_{0-1}\lambda \Delta t + p_0(1 - \lambda \Delta t)] x^0 + [p_{1-1}\lambda \Delta t + p_1(1 - \lambda \Delta t)] x^1 \,,$$

with $p_{-1} = 0$. Since if $n < 0$ the state involving precisely n events in the interval $(0, t + \Delta t)$ arises either from $n - 1$ in the interval $(0, t)$ with one new emission in Δt, or from n in $(0, t)$ with no new emission in Δt

$$\rightarrow p_1 = 0$$
$$\Delta P(x, t) = p_0(1 - \lambda \Delta t)x^0 + p_0 \lambda \Delta t x^1$$
$$= p_0 \left[1 + \lambda(x - 1)\Delta t \right] \,.$$

Moreover, $\Delta P = P(x, t + \Delta t) - P(x, t)$ and $p_0(t + \Delta t) = p_0(t)$

$$\Delta P(x, t) = 1 + \lambda(x - 1)\Delta t \,. \tag{A.22}$$

Plugging Eq. (A.22) in Eq. (A.21) yields to

$$P(x, t + \Delta t) = P(x, t)(1 - \lambda(x - 1)\Delta t)$$

Hence

$$\frac{\partial P(x, t)}{\partial t} = \lim_{\Delta t \to 0} \frac{P(x, t + \Delta t) - P(x, t)}{\Delta t}$$
$$= \lim_{\Delta t \to 0} \frac{P(x, t) \left[1 - \lambda(x - 1)\Delta t - 1 \right]}{\Delta t}$$
$$\frac{\partial P(x, t)}{\partial t} = \lambda(x - 1)P(x, t) \,.$$

The moment generating function reads

$$M(\theta, t + \Delta t) = M(\theta, t)\Delta M(\theta, t).$$

By making a change of variable $x = e^\theta$, the moment generating function reads

$$
\begin{aligned}
\Delta M(\theta, t) &= \mathbb{E}[x^{\theta \Delta X}] \\
&= (1 - \lambda \Delta t)e^0 + \lambda \Delta t e^0 \\
&= 1 + \lambda(e^0 - 1)\Delta t \\
\frac{\partial M(\theta, t)}{\partial t} &= \lim_{\Delta t \to 0} \frac{M(\theta, t + \Delta t) - M(\theta, t)}{\Delta t} \\
&= \lim_{\Delta t \to 0} \frac{M(\theta, t)\left[1 + \lambda(e^\theta - 1)\Delta t - 1\right]}{\Delta t} \\
\frac{\partial M(\theta, t)}{\partial t} &= \lambda(e^\theta - 1)M(\theta, t).
\end{aligned}
$$

The previous equations are true only if the variables are independent ! But it is not always true. Extension of the previous example approach will give a more general result. Finite number of transitions possible in the interval Δt.
Let

$$P(\Delta X(t) = j | X(t)) = f_j(X)\Delta t,\ j \neq 0 \text{ and } j = \text{possible transition},$$

where $f_j(X)$ are suitable non-negative function of $X(t)$. The index j can be positive or negative. The probability of having of no transition is given by

$$P(\Delta X(t) = 0 | X(t)) = 1 - \sum_{j \neq 0} f_j(X)\Delta t.$$

Notations

- $\underset{t}{\mathbb{E}}$ defines the expectations of some functions at time t with respect to variations in $X(t)$

- $\underset{t+\Delta t}{\mathbb{E}}$ defines the expectations of some functions at time $t + \Delta t$ for variation in $X(t + \Delta t)$

- $\underset{\Delta t | t}{\mathbb{E}}$ defines the conditional expectation at the end of the interval Δt for variations in the variable $\Delta X(t)$ given the value of $X(t)$ at time t

Moreover

$$\mathbb{E}[\mathbb{E}(X|Y)] = \mathbb{E}[X] \text{ and } \underset{\Delta t | t}{\mathbb{E}}[\Phi(X(t + \Delta t))] = \underset{t}{\mathbb{E}}[\underset{\Delta t | t}{\mathbb{E}}[\Phi(X(t) + \Delta X(t)]],$$

and $\Phi = M(\theta, t)$ can be replaced by

$$
\begin{aligned}
M(\theta, t + \Delta t) &= \mathop{\mathbb{E}}_{\Delta t|t} [e^{\theta X(t + \Delta t)}] \\
&= \mathop{\mathbb{E}}_{\Delta t|t} [e^{\theta X(t) + \theta \Delta X}] \\
&= \mathop{\mathbb{E}}_{t} [\mathop{\mathbb{E}}_{\Delta t|t} [e^{\theta X} e^{\theta \Delta X}]] \\
&\quad \text{by using } \mathbb{E}[X f(Y)|Y] = f(Y) \mathbb{E}[X|Y] \\
&= \mathop{\mathbb{E}}_{t} [e^{\theta X} \mathop{\mathbb{E}}_{\Delta t|t} [e^{\theta \Delta X}]] \,,
\end{aligned}
$$

and the the evolution equation for the moment-generating function $M(\theta, t)$ reads

$$
\begin{aligned}
\frac{\partial M(\theta, t)}{\partial t} &= \lim_{\Delta t \to 0} \frac{M(\theta, t + \Delta t) - M(\theta, t)}{\Delta t} \\
&= \lim_{\Delta t \to 0} \frac{1}{\Delta t} \left(\mathop{\mathbb{E}}_{t} [e^{\theta X} \mathop{\mathbb{E}}_{\Delta t|t} [e^{\theta \Delta X}]] - \mathop{\mathbb{E}}_{t} [e^{\theta X}] \right) \\
&\quad \text{by using } \mathop{\mathbb{E}}_{t} [e^{\theta X}] = \mathop{\mathbb{E}}_{t} [e^{\theta X} \mathop{\mathbb{E}}_{\Delta t|t} [1]] \\
&= \lim_{\Delta t \to 0} \frac{1}{\Delta t} \left(\mathop{\mathbb{E}}_{t} [e^{\theta X} \mathop{\mathbb{E}}_{\Delta t|t} [e^{\theta \Delta X} - 1]] \right) \\
&= \mathop{\mathbb{E}}_{t} [e^{\theta X} \lim_{\Delta t \to 0} \mathop{\mathbb{E}}_{\Delta t|t} [\frac{e^{\theta \Delta X} - 1}{\Delta t}]] \,,
\end{aligned}
$$

where $\mathop{\mathbb{E}}_{\Delta t|t} [\frac{e^{\theta \Delta X} - 1}{\Delta t}]]$ has a limit, $e.g.$ $\Phi(\theta, t, X)$ as $\Delta t \to 0$. The evolution equation for $M(\theta, t)$ reads

$$
\frac{\partial M(\theta, t)}{\partial t} = \mathop{\mathbb{E}}_{t} [e^{\theta X} \Phi(\theta, t, X)] = \Phi(\theta, t, \partial_\theta) M(\theta, t) \,.
$$

Then

$$
\Phi(\theta, t, X) = \lim_{\Delta t \to 0} \mathop{\mathbb{E}}_{\Delta t|t} [\frac{e^{\theta \Delta X} - 1}{\Delta t}] \,.
$$

Knowing $P(\Delta X = j|X) = f_j(X)\Delta t$, this yields to

$$P(\Delta X = 0|X) = 1 - \sum_{j \neq 0} f_j(X)\Delta t$$

$$\mathbb{E}_{\Delta t|t}[X] = \sum_x x P(\Delta X|X)$$

$$= \sum_x x(1 - \sum_{j \neq 0} f_j(X)\Delta t)$$

$$\mathbb{E}_{\Delta t|t}[\frac{e^{\theta \Delta X} - 1}{\Delta t}] = \frac{1}{\Delta t}\left\{\sum_x (e^{\theta t P(\Delta X = x|X)}) - 1\right\}$$

$$= \frac{1}{\Delta t}\left\{(1 - \sum_{j \neq 0} f_j(X)\Delta t) + \sum_{j \neq 0} f_j(X)\Delta t e^{j\theta} - 1\right\}$$

$$= \frac{1}{\Delta t}\left\{P(\Delta X = 0|X) + \sum_{x=1} x P(\Delta X = j|X)\right\}.$$

Thus, $\Phi(\theta, t, X)$ reads

$$\Phi(\theta, t, X) = \lim_{\Delta t \to 0} \frac{1}{\Delta t}\left\{(1 - \sum_{j \neq 0} f_j(X)\Delta t) + \sum_{j \neq 0} f_j(X)\Delta t e^{j\theta} - 1\right\}$$

$$= \lim_{\Delta t \to 0} \frac{1}{\Delta t}\left\{\sum_{j \neq 0}(e^{j\theta} - 1)\Delta t f_j(X)\right\}$$

$$\Phi(\theta, t, X) = \sum_{j \neq 0}(e^{j\theta} - 1)f_j(X).$$

The moment generating function reads

$$\frac{\partial M(\theta, t)}{\partial t} = \Phi(\theta, t, \partial_\theta)M(\theta, t)$$

$$\frac{\partial M(\theta, t)}{\partial t} = \sum_{j \neq 0}(e^{j\theta} - 1)f_j(\partial_\theta)M(\theta, t).$$

By doing a change of variable $e^\theta = x$ and $\partial_\theta = x\partial_x$, then the evolution of the generating function reads

$$\frac{\partial P(x, t)}{\partial x} = \sum_{j \neq 0}(x^j - 1)f_j(x\partial_x)P(x, t). \tag{A.23}$$

Rk.: often j (type of transition) can only takes the values $+1$ or -1. In the "birth" process there is only one transition $j = 1$ and the function $f_{+1}(X)$ is λX. However, in the "birth and death" process there are two transitions:

- $j = +1 \rightarrow f_{+1}(X) = \lambda X$

- $j = -1 \rightarrow f_{-1}(X) = \mu X$

In the case of the "birth and death" process, the moment generating function reads

$$\frac{\partial M(\theta, t)}{\partial t} = (e^{+\theta} - 1)\lambda \partial_\theta M(\theta, t) + (e^{-\theta} - 1)\mu \partial_\theta M(\theta, t)$$

$$\frac{\partial M(\theta, t)}{\partial t} = \left[(e^{\theta} - 1)\lambda + \mu(e^{-\theta} - 1)\right] \partial_\theta M(\theta, t).$$

Bibliography

[1] Sriram Ramaswamy. The mechanics and statistics of active matter. *Annual Review of Condensed Matter Physics*, 1(1):323–345, 2010.

[2] Étienne Fodor and M Cristina Marchetti. The statistical physics of active matter: From self-catalytic colloids to living cells. *Physica A: Statistical Mechanics and its Applications*, 504:106–120, 2018.

[3] Gandhimohan M Viswanathan, Marcos GE Da Luz, Ernesto P Raposo, and H Eugene Stanley. *The physics of foraging: an introduction to random searches and biological encounters*. Cambridge University Press, 2011.

[4] Jens Elgeti, Roland G Winkler, and Gerhard Gompper. Physics of microswimmers—single particle motion and collective behavior: a review. *Reports on Progress in Physics*, 78(5):056601, 2015.

[5] M Cristina Marchetti, Jean-François Joanny, Sriram Ramaswamy, Tanniemola B Liverpool, Jacques Prost, Madan Rao, and R Aditi Simha. Hydrodynamics of soft active matter. *Reviews of Modern Physics*, 85(3):1143, 2013.

[6] Manuele Brambilla, Eliseo Ferrante, Mauro Birattari, and Marco Dorigo. Swarm robotics: a review from the swarm engineering perspective. *Swarm Intelligence*, 7(1):1–41, 2013.

[7] Andreas Zöttl and Holger Stark. Emergent behavior in active colloids. *Journal of Physics: Condensed Matter*, 28(25):253001, 2016.

[8] Eric Lauga and Thomas R Powers. The hydrodynamics of swimming microorganisms. *Reports on Progress in Physics*, 72(9):096601, 2009.

[9] Tamás Vicsek and Anna Zafeiris. Collective motion. *Physics Reports*, 517(3-4):71–140, 2012.

[10] Pawel Romanczuk, Markus Bär, Werner Ebeling, Benjamin Lindner, and Lutz Schimansky-Geier. Active brownian particles. *The European Physical Journal Special Topics*, 202(1):1–162, 2012.

[11] Sriram Ramaswamy. Active matter. *Journal of Statistical Mechanics: Theory and Experiment*, 2017(5):054002, 2017.

[12] Karl Pearson. The problem of the random walk. *Nature*, 72(1867):342, 1905.

[13] Karl Pearson and John Blakeman. *A mathematical theory of random migration*, volume 1. Dulau and Company, 1904.

[14] Stephen J Ebbens and Jonathan R Howse. In pursuit of propulsion at the nanoscale. *Soft Matter*, 6(4):726–738, 2010.

[15] Stephen Ebbens, Richard AL Jones, Anthony J Ryan, Ramin Golestanian, and Jonathan R Howse. Self-assembled autonomous runners and tumblers. *Physical Review E*, 82(1):015304, 2010.

[16] Howard C Berg and Douglas A Brown. Chemotaxis in escherichia coli analysed by three-dimensional tracking. *Nature*, 239(5374):500, 1972.

[17] Howard C Berg. Bacterial behaviour. *Nature*, 254(5499):389, 1975.

[18] Howard C Berg. *Random walks in biology*. Princeton University Press, 1993.

[19] Howard C Berg. Symmetries in bacterial motility. *Proceedings of the National Academy of Sciences USA*, 93(25):14225–14228, 1996.

[20] Victor Sourjik and Howard C Berg. Functional interactions between receptors in bacterial chemotaxis. *Nature*, 428(6981):437, 2004.

[21] Howard C Berg. Escherichia coli in motion. *Biological, and Medical Physics Biomedical Engineering. Springer Verlag AIP: Press New York*, 2004.

[22] Hans Machemer. Ciliary activity and the origin of metachrony in paramecium: effects of increased viscosity. *Journal of Experimental Biology*, 57(1):239–259, 1972.

[23] John R Blake and Michael A Sleigh. Mechanics of ciliary locomotion. *Biological Reviews*, 49(1):85–125, 1974.

[24] JR Blake and AT Chwang. Fundamental singularities of viscous flow. *Journal of Engineering Mathematics*, 8(1):23–29, 1974.

[25] DM Woolley. Motility of spermatozoa at surfaces. *Reproduction Cambridge*, 126(2):259–270, 2003.

[26] Ingmar H Riedel, Karsten Kruse, and Jonathon Howard. A self-organized vortex array of hydrodynamically entrained sperm cells. *Science*, 309(5732):300–303, 2005.

[27] Knut Drescher, Raymond E Goldstein, Nicolas Michel, Marco Polin, and Idan Tuval. Direct measurement of the flow field around swimming microorganisms. *Physical Review Letters*, 105(16):168101, 2010.

[28] Knut Drescher, Jörn Dunkel, Luis H Cisneros, Sujoy Ganguly, and Raymond E Goldstein. Fluid dynamics and noise in bacterial cell–cell and cell–surface scattering. *Proceedings of the National Academy of Sciences USA*, 108(27):10940–10945, 2011.

[29] Knut Drescher, Kyriacos C Leptos, Idan Tuval, Takuji Ishikawa, Timothy J Pedley, and Raymond E Goldstein. Dancing volvox: hydrodynamic bound states of swimming algae. *Physical Review Letters*, 102(16):168101, 2009.

[30] Jeffrey S Guasto, Karl A Johnson, and Jerry P Gollub. Oscillatory flows induced by microorganisms swimming in two dimensions. *Physical Review Letters*, 105(16):168102, 2010.

[31] Eric Lauga and Raymond E Goldstein. Microswimmers. *Physics Today*, 65(9):30, 2012.

[32] WCK Poon. From clarkia to escherichia and janus: The physics of natural and synthetic active colloids. *Proceedings of the International School of Physics Enrico Fermi*, 184:317–386, 2013.

[33] Davod Alizadehrad, Timothy Krüger, Markus Engstler, and Holger Stark. Simulating the complex cell design of trypanosoma brucei and its motility. *PLoS computational biology*, 11(1):e1003967, 2015.

[34] Marco Polin, Idan Tuval, Knut Drescher, Jerry P Gollub, and Raymond E Goldstein. Chlamydomonas swims with two "gears" in a eukaryotic version of run-and-tumble locomotion. *Science*, 325(5939):487–490, 2009.

[35] Karin Sauer, Anne K Camper, Garth D Ehrlich, J William Costerton, and David G Davies. Pseudomonas aeruginosa displays multiple phenotypes during development as a biofilm. *Journal of Bacteriology*, 184(4):1140–1154, 2002.

[36] Bradley J Nelson, Ioannis K Kaliakatsos, and Jake J Abbott. Microrobots for minimally invasive medicine. *Annual Review of Biomedical Engineering*, 12:55–85, 2010.

[37] Joseph Wang and Wei Gao. Nano/microscale motors: biomedical opportunities and challenges. *ACS nano*, 6(7):5745–5751, 2012.

[38] Debabrata Patra, Samudra Sengupta, Wentao Duan, Hua Zhang, Ryan Pavlick, and Ayusman Sen. Intelligent, self-powered, drug delivery systems. *Nanoscale*, 5(4):1273–1283, 2013.

[39] Zhengjia Wang, Hsuan-Yi Chen, Yu-Jane Sheng, and Heng-Kwong Tsao. Diffusion, sedimentation equilibrium, and harmonic trapping of run-and-tumble nanoswimmers. *Soft Matter*, 10(18):3209–3217, 2014.

[40] Loai KEA Abdelmohsen, Fei Peng, Yingfeng Tu, and Daniela A Wilson. Micro- and nano-motors for biomedical applications. *Journal of Materials Chemistry B*, 2(17):2395–2408, 2014.

[41] Ramin Golestanian, Tanniemola B Liverpool, and Armand Ajdari. Propulsion of a molecular machine by asymmetric distribution of reaction products. *Physical Review Letters*, 94(22):220801, 2005.

[42] Jeremie Palacci, Stefano Sacanna, Asher Preska Steinberg, David J Pine, and Paul M Chaikin. Living crystals of light-activated colloidal surfers. *Science*, 339(6122):936–940, 2013.

[43] Aidan Brown and Wilson Poon. Ionic effects in self-propelled pt-coated janus swimmers. *Soft Matter*, 10(22):4016–4027, 2014.

[44] Hakan Ceylan, Immihan Ceren Yasa, Oncay Yasa, Ahmet Fatih Tabak, Joshua Giltinan, and Metin Sitti. 3d-printed biodegradable microswimmer for drug delivery and targeted cell labeling. *bioRxiv*, page 379024, 2018.

[45] Fernando Peruani, Jörn Starruß, Vladimir Jakovljevic, Lotte Søgaard-Andersen, Andreas Deutsch, and Markus Bär. Collective motion and nonequilibrium cluster formation in colonies of gliding bacteria. *Physical Review Letters*, 108(9):098102, 2012.

[46] Alexander P Petroff, Xiao-Lun Wu, and Albert Libchaber. Fast-moving bacteria self-organize into active two-dimensional crystals of rotating cells. *Physical Review Letters*, 114(15):158102, 2015.

[47] Henricus H Wensink, Jörn Dunkel, Sebastian Heidenreich, Knut Drescher, Raymond E Goldstein, Hartmut Löwen, and Julia M Yeomans. Meso-scale turbulence in living fluids. *Proceedings of the National Academy of Sciences USA*, 109(36):14308–14313, 2012.

[48] Andrey Sokolov and Igor S Aranson. Physical properties of collective motion in suspensions of bacteria. *Physical Review Letters*, 109(24):248109, 2012.

[49] Paul Stoodley, Karin Sauer, David Gwilym Davies, and J William Costerton. Biofilms as complex differentiated communities. *Annual Reviews in Microbiology*, 56(1):187–209, 2002.

[50] Julian Bialké, Thomas Speck, and Hartmut Löwen. Active colloidal suspensions: Clustering and phase behavior. *Journal of Non-Crystalline Solids*, 407:367–375, 2015.

[51] Jérémie Palacci, Cécile Cottin-Bizonne, Christophe Ybert, and Lydéric Bocquet. Sedimentation and effective temperature of active colloidal suspensions. *Physical Review Letters*, 105:088304, Aug 2010.

[52] John Toner and Yuhai Tu. Long-range order in a two-dimensional dynamical xy model: how birds fly together. *Physical Review Letters*, 75(23):4326, 1995.

[53] John Toner and Yuhai Tu. Flocks, herds, and schools: A quantitative theory of flocking. *Physical Review E*, 58(4):4828, 1998.

[54] Thomas FF Farage, P Krinninger, and Joseph M Brader. Effective interactions in active brownian suspensions. *Physical Review E*, 91(4):042310, 2015.

[55] J Tailleur and ME Cates. Statistical mechanics of interacting run-and-tumble bacteria. *Physical Review Letters*, 100(21):218103, 2008.

[56] Thomas Speck, Julian Bialké, Andreas M Menzel, and Hartmut Löwen. Effective cahn-hilliard equation for the phase separation of active brownian particles. *Physical Review Letters*, 112(21):218304, 2014.

[57] Sho C Takatori, Wen Yan, and John F Brady. Swim pressure: stress generation in active matter. *Physical Review Letters*, 113(2):028103, 2014.

[58] Michael E Cates. Diffusive transport without detailed balance in motile bacteria: does microbiology need statistical physics? *Reports on Progress in Physics*, 75(4):042601, 2012.

[59] Luanne Hall-Stoodley, J William Costerton, and Paul Stoodley. Bacterial biofilms: from the natural environment to infectious diseases. *Nature Reviews Microbiology*, 2(2):95, 2004.

[60] Jan Michels, Angela Stippkugel, Mark Lenz, Kai Wirtz, and Anja Engel. Rapid aggregation of biofilm-covered microplastics with marine biogenic particles. *Proceedings of the Royal Society B*, 285(1885):20181203, 2018.

[61] Carla CCR de Carvalho. Marine biofilms: a successful microbial strategy with economic implications. *Frontiers in Marine Science*, 5:126, 2018.

[62] Yusuf Chisti. Biodiesel from microalgae. *Biotechnology Advances*, 25(3):294–306, 2007.

[63] Andrei Andreevich Markov. Rasprostranenie zakona bol'shih chisel na velichiny, zavisyaschie drug ot druga. *Izvestiya Fiziko-Matematicheskogo Obschestva Pri Kazanskom Universitete*, 15(135-156):18, 1906.

[64] Mark Kac. *Some stochastic problems in physics and mathematics*. Socony Mobil Oil Company, Incorporated, Field Research Laboratory, 1957.

[65] Mark Kac. *Probability and related topics in physical sciences*, volume 1. American Mathematical Soc., 1959.

[66] Willliam Feller. *An introduction to probability theory and its applications*, volume 2. John Wiley & Sons, 2008.

[67] David G Kendall. Stochastic processes and population growth. *Journal of the Royal Statistical Society. Series B (Methodological)*, 11(2):230–282, 1949.

[68] JE Moyal. Stochastic processes and statistical physics. *Journal of the Royal Statistical Society. Series B (Methodological)*, 11(2):150–210, 1949.

[69] Andrey Nikolaevich Kolmogorov. On analytical methods in probability theory. *Math. Ann*, 104:415–458, 1931.

[70] William Feller. On the integro-differential equations of purely discontinuous markoff processes. In *Selected Papers I*, pages 539–566. Springer, 2015.

[71] W. Feller. On the theory of stochastic processes, with particular reference to applications. In *Proceedings of the [First] Berkeley Symposium on Mathematical Statistics and Probability*, pages 403–432, Berkeley, Calif., 1949. University of California Press.

[72] Joseph Leo Doob. *Stochastic Processes*, volume 101. New York Wiley, 1953.

[73] Mauricio Suárez. *Probabilities, causes and propensities in physics*, volume 347. Springer Science & Business Media, 2010.

[74] I. Aleksandr and Akovlevich Khinchin. *Mathematical foundations of statistical mechanics*. Courier Corporation, 1949.

[75] Yair M Guttmann. *The concept of probability in statistical physics*. Cambridge University Press, 1999.

[76] David Ruelle. *Chance and chaos*, volume 11. Princeton University Press, 1993.

[77] Petar Todorovic. *An introduction to stochastic processes and their applications*. Springer Science & Business Media, 2012.

[78] Norman TJ Bailey. *The elements of stochastic processes with applications to the natural sciences*, volume 25. John Wiley & Sons, 1990.

[79] Mircea V Soare, Petre P Teodorescu, and Ileana Toma. *Ordinary differential equations with applications to mechanics*, volume 585. Springer, 2007.

[80] David G Kendall et al. On the generalized 'birth-and-death' process. *The Annals of Mathematical Statistics*, 19(1):1–15, 1948.

[81] Niels Arley. On the theory of stochastic processes and their application to the theory of cosmic radiation. 1943.

[82] Aleksandr Yakovlevich Khinchin, DM Andrews, and Maurice Henry Quenouille. *Mathematical methods in the theory of queuing*. Courier Corporation, 2013.

[83] Robert Brown. A brief account of microscopical observations made in the months of june, july and august 1827, on the particles contained in the pollen of plants; and on the general existence of active molecules in organic and inorganic bodies. *The Philosophical Magazine*, 4(21):161–173, 1828.

[84] Jean Perrin. L'agitation moléculaire et le mouvement brownien. *Comptes rendus hebdomadaires des séances de l'académie des sciences*, 146:967–970, 1908.

[85] Paul Langevin. *On the theory of Brownian motion*. 1908.

[86] Norbert Wiener and P Masani. Collected works-vol. 1, 1976.

[87] Peter E Kloeden and Eckhard Platen. *Numerical solution of stochastic differential equations*, volume 23. Springer Science & Business Media, 2013.

[88] Kiyosi Itô. *Stochastic processes: lectures given at Aarhus University*. Springer Science & Business Media, 2013.

[89] William T Coffey and Yuri P Kalmykov. *The Langevin equation: with applications to stochastic problems in physics, chemistry and electrical engineering*, volume 27. World Scientific, 2012.

[90] Mark J Schnitzer. Theory of continuum random walks and application to chemotaxis. *Physical Review E*, 48(4):2553, 1993.

[91] Howard C Berg and Edward M Purcell. Physics of chemoreception. *Biophysical Journal*, 20(2):193–219, 1977.

[92] Lutz Schimansky-Geier, Michaela Mieth, Helge Rosé, and Horst Malchow. Structure formation by active brownian particles. *Physics Letters A*, 207(3-4):140–146, 1995.

[93] Étienne Fodor, Cesare Nardini, Michael E Cates, Julien Tailleur, Paolo Visco, and Frédéric van Wijland. How far from equilibrium is active matter? *Physical Review Letters*, 117(3):038103, 2016.

[94] Michael E Cates and Julien Tailleur. When are active brownian particles and run-and-tumble particles equivalent? consequences for motility-induced phase separation. *EPL (Europhysics Letters)*, 101(2):20010, 2013.

[95] Claudio Maggi, Umberto Marini Bettolo Marconi, Nicoletta Gnan, and Roberto Di Leonardo. Multidimensional stationary probability distribution for interacting active particles. *Scientific Reports*, 5:10742, 2015.

[96] H. Risken. *The Fokker-Planck Equation*. Springer-Verlag Berlin Heidelberg, 1984.

[97] Valery I. Klyatskin. *Stochastic Equations: Theory and Applications in Acoustics, Hydrodynamics, Magnetohydrodynamics, and Radiophysics, Volume 1*. Springer International Publishing Switzerland, 2015.

[98] V. V. Konotop and L. Vasquez. *Nonlinear Random Waves*. Worl Scientific, Singapore, 1994.

[99] T. D. Frank. Delay fokker-planck equations, perturbation theory, and data analysis for nonlinear stochastic systems with time delays. *Physical Review E*, 71:031106, Mar 2005.

[100] E. A. Novikov. Functionals and the random-force method in turbulence theory. *Journal of Experimental and Theoretical Physics*, 20(5), 1964.

[101] Jean Zinn-Justin. *Quantum field theory and critical phenomena*. Clarendon Press, 2002.

[102] Francisco J. Sevilla and Luis A. Gómez Nava. Theory of diffusion of active particles that move at constant speed in two dimensions. *Physical Review E*, 90:022130, Aug 2014.

[103] Francisco J. Sevilla and Mario Sandoval. Smoluchowski diffusion equation for active brownian swimmers. *Physical Review E*, 91:052150, May 2015.

[104] Francisco J. Sevilla. Diffusion of active chiral particles. *Physical Review E*, 94:062120, Dec 2016.

[105] Jérémy Vachier and Marco G Mazza. Dynamics of sedimenting active brownian particles. *The European Physical Journal E*, 42(1):11, 2019.

[106] Arnold Sommerfeld. *Partial differential equations in physics*, volume 1. Academic press, 1949.

[107] Aleksandr Danilovich Aleksandrov, Mikhail Alekseevich Lavrent'ev, et al. *Mathematics: its content, methods and meaning*. Courier Corporation, 1999.

[108] David Roxbee Cox. *The theory of stochastic processes*. Routledge, 2017.

[109] Subrahmanyan Chandrasekhar. Stochastic problems in physics and astronomy. *Reviews of Modern Physics*, 15(1):1, 1943.

[110] Timothy Sauer. Numerical solution of stochastic differential equations in finance. In *Handbook of computational finance*, pages 529–550. Springer, 2012.

[111] John D. Weeks, David Chandler, and Hans C. Andersen. Role of Repulsive Forces in Determining the Equilibrium Structure of Simple Liquids. *Journal of Chemical Physics*, 54(12):5237–5247, 1971.

[112] Jaroslav M Ilnytskyi and Mark R Wilson. A domain decomposition molecular dynamics program for the simulation of flexible molecules of spherically-symmetrical and nonspherical sites. ii. extension to nvt and npt ensembles. *Computer Physics Communications*, 148(1):43–58, 2002.

[113] Pulak K Ghosh, Vyacheslav R Misko, Fabio Marchesoni, and Franco Nori. Self-propelled janus particles in a ratchet: Numerical simulations. *Physical Review Letters*, 110(26):268301, 2013.

[114] Vasily Kantsler, Jörn Dunkel, Marco Polin, and Raymond E Goldstein. Ciliary contact interactions dominate surface scattering of swimming eukaryotes. *Proceedings of the National Academy of Sciences USA*, 110(4):1187–1192, 2013.

[115] A. Pototsky and H. Stark. Active brownian particles in two-dimensional traps. *EPL (Europhysics Letters)*, 98(5):50004, 2012.

[116] Caleb G Wagner, Michael F Hagan, and Aparna Baskaran. Steady-state distributions of ideal active brownian particles under confinement and forcing. *Journal of Statistical Mechanics: Theory and Experiment*, 2017(4):043203, 2017.

[117] Sophie Hermann and Matthias Schmidt. Active ideal sedimentation: exact two-dimensional steady states. *Soft Matter*, 14:1614–1621, 2018.

[118] Katrin Wolff, Aljoscha M. Hahn, and Holger Stark. Sedimentation and polar order of active bottom-heavy particles. *The European Physical Journal E*, 36(4):43, Apr 2013.

[119] J. Tailleur and M. E. Cates. Sedimentation, trapping, and rectification of dilute bacteria. *EPL (Europhysics Letters)*, 86(6):60002, 2009.

[120] Mihaela Enculescu and Holger Stark. Active colloidal suspensions exhibit polar order under gravity. *Physical Review Letters*, 107:058301, Jul 2011.

[121] Christina Kurzthaler, Sebastian Leitmann, and Thomas Franosch. Intermediate scattering function of an anisotropic active brownian particle. *Scientific Reports*, 6:36702, 2016.

[122] R. W. Nash, R. Adhikari, J. Tailleur, and M. E. Cates. Run-and-tumble particles with hydrodynamics: Sedimentation, trapping, and upstream swimming. *Physical Review Letters*, 104:258101, Jun 2010.

[123] Ambarish Ghosh and Peer Fischer. Controlled propulsion of artificial magnetic nanostructured propellers. *Nano Letters*, 9(6):2243–2245, 2009.

[124] Sangwon Kim, Famin Qiu, Samhwan Kim, Ali Ghanbari, Cheil Moon, Li Zhang, Bradley J Nelson, and Hongsoo Choi. Fabrication and characterization of magnetic microrobots for three-dimensional cell culture and targeted transportation. *Advanced Materials*, 25(41):5863–5868, 2013.

[125] Corinna C Maass, Carsten Krüger, Stephan Herminghaus, and Christian Bahr. Swimming droplets. *Annual Review of Condensed Matter Physic*, 7:171–193, 2016.

[126] Carsten Krüger, Gunnar Klös, Christian Bahr, and Corinna C. Maass. Curling liquid crystal microswimmers: A cascade of spontaneous symmetry breaking. *Physical Review Letters*, 117:048003, Jul 2016.

[127] Chenyu Jin, Carsten Krüger, and Corinna C Maass. Chemotaxis and autochemotaxis of self-propelling droplet swimmers. *Proceedings of the National Academy of Sciences USA*, 114(20):5089–5094, 2017.

[128] Edward M Purcell. Life at low reynolds number. *American Journal of Physics*, 45(1):3–11, 1977.

[129] Ramin Golestanian. Anomalous diffusion of symmetric and asymmetric active colloids. *Physical Review Letters*, 102:188305, May 2009.

[130] Borge Ten Hagen, Felix Kümmel, Raphael Wittkowski, Daisuke Takagi, Hartmut Löwen, and Clemens Bechinger. Gravitaxis of asymmetric self-propelled colloidal particles. *Nature Communication*, 5:4829, 2014.

[131] Andrew I. Campbell, Raphael Wittkowski, Borge ten Hagen, Hartmut Löwen, and Stephen J. Ebbens. Helical paths, gravitaxis, and separation phenomena for mass-anisotropic self-propelling colloids: Experiment versus theory. *Journal of Chemical Physics*, 147(8):084905, 2017.

[132] Félix Ginot, Isaac Theurkauff, Demian Levis, Christophe Ybert, Lydéric Bocquet, Ludovic Berthier, and Cécile Cottin-Bizonne. Nonequilibrium equation of state in suspensions of active colloids. *Physical Review X*, 5:011004, Jan 2015.

[133] Felix Ginot, Alexandre Solon, Yariv Kafri, Christophe Ybert, Julien Tailleur, and Cecile Cottin-Bizonne. Sedimentation of self-propelled janus colloids: polarization and pressure. *New Journal of Physics*, 20(11):115001, 2018.

[134] N.G. Van Kampen. *Stochastic Processes in Physics and Chemistry*. North Holland; 3 edition, 23 April 2007.

[135] C.W. Gardiner. *Handbook of Stochastic Methods.* Springer-Verlag Berlin Heidelberg, 1983.

[136] Till Daniel Frank. *Nonlinear Fokker-Planck Equations.* Springer-Verlag Berlin Heidelberg, 2005.

[137] Grigorios A. Pavliotis. *Stochastic Processes and Applications Diffusion Processes, the Fokker-Planck and Langevin Equations.* Springer-Verlag New York, 2014.

[138] Valery Ilyin, Itamar Procaccia, and Anatoly Zagorodny. Fokker-planck equation with memory: the crossover from ballistic to diffusive processes in many-particle systems and incompressible media. *Condensed Matter Physics*, 16:13004, 2013.

[139] Holger Stark. Swimming in external fields. *The European Physical Journal Special Topics*, 225(11-12):2369–2387, 2016.

[140] Sidney Redner. *A guide to first-passage processes.* Cambridge University Press, 2001.

[141] Sambeeta Das, Astha Garg, Andrew I Campbell, Jonathan Howse, Ayusman Sen, Darrell Velegol, Ramin Golestanian, and Stephen J Ebbens. Boundaries can steer active janus spheres. *Nature Communications*, 6:8999, 2015.

[142] G K Batchelor. Sedimentation in a dilute dispersion of spheres. *Journal of Fluid Mechanics*, 52(2):245–268, 1972.

[143] P. N. Segrè, E. Herbolzheimer, and P. M. Chaikin. Long-range correlations in sedimentation. *Physical Review Letters*, 79:2574–2577, Sep 1997.

[144] Roberto Piazza. Settled and unsettled issues in particle settling. *Reports on Progress in Physics*, 77(5):056602, 2014.

[145] Aparna Baskaran and M Cristina Marchetti. Statistical mechanics and hydrodynamics of bacterial suspensions. *Proceedings of the National Academy of Sciences USA*, 106(37):15567–15572, 2009.

[146] Cristóbal López. Self-propelled nonlinearly diffusing particles: Aggregation and continuum description. *Physical Review E*, 72(6):061109, 2005.

[147] Ramin Golestanian. Bose-einstein-like condensation in scalar active matter with diffusivity edge. *Physical Review E*, 100:010601, 2019.

[148] Shibananda Das, Gerhard Gompper, and Roland G Winkler. Confined active brownian particles: theoretical description of propulsion-induced accumulation. *New Journal of Physics*, 20(1):015001, 2018.

[149] Giacomo Frangipane, Dario Dell'Arciprete, Serena Petracchini, Claudio Maggi, Filippo Saglimbeni, Silvio Bianchi, Gaszton Vizsnyiczai, Maria Lina Bernardini, and Roberto Di Leonardo. Dynamic density shaping of photokinetic e. coli. *Elife*, 7:e36608, 2018.

[150] Cristóbal López. Macroscopic description of particle systems with nonlocal density-dependent diffusivity. *Physical Review E*, 74(1):012102, 2006.

[151] Robert Grossmann, Lutz Schimansky-Geier, and Pawel Romanczuk. Active brownian particles with velocity-alignment and active fluctuations. *New Journal of Physics*, 14(7):073033, 2012.

[152] Pawel Romanczuk, Markus Bär, Werner Ebeling, Benjamin Lindner, and Lutz Schimansky-Geier. Active brownian particles. *The European Physical Journal Special Topics*, 202(1):1–162, 2012.

[153] Michael E Cates and Julien Tailleur. Motility-induced phase separation. *Annual Review of Condensed Matter Physics*, 6(1):219–244, 2015.

[154] Pasquale Digregorio, Demian Levis, Antonio Suma, Leticia F Cugliandolo, Giuseppe Gonnella, and Ignacio Pagonabarraga. Full phase diagram of active brownian disks: From melting to motility-induced phase separation. *Physical Review Letters*, 121(9):098003, 2018.

[155] Pradeep K Singh, Amy L Schaefer, Matthew R Parsek, Thomas O Moninger, Michael J Welsh, and EP Greenberg. Quorum-sensing signals indicate that cystic fibrosis lungs are infected with bacterial biofilms. *Nature*, 407(6805):762, 2000.

[156] Julie S Biteen, Paul C Blainey, Zoe G Cardon, Miyoung Chun, George M Church, Pieter C Dorrestein, Scott E Fraser, Jack A Gilbert, Janet K Jansson, Rob Knight, et al. Tools for the microbiome: nano and beyond, 2015.

[157] George A O'Toole and Gerard CL Wong. Sensational biofilms: surface sensing in bacteria. *Current Opinion in Microbiology*, 30:139–146, 2016.

[158] Catherine R Armbruster, Calvin K Lee, Jessica Parker-Gilham, Jaime de Anda, Aiguo Xia, Kun Zhao, Keiji Murakami, Boo Shan Tseng, Lucas R Hoffman, Fan Jin, et al. Heterogeneity in surface sensing suggests a division of labor in pseudomonas aeruginosa populations. *eLife*, 8:e45084, 2019.

[159] Yasuhiko Irie, Bradley R Borlee, Jennifer R O'Connor, Preston J Hill, Caroline S Harwood, Daniel J Wozniak, and Matthew R Parsek. Self-produced exopolysaccharide is a signal that stimulates biofilm formation in pseudomonas aeruginosa. *Proceedings of the National Academy of Sciences USA*, 109(50):20632–20636, 2012.

[160] Kun Zhao, Boo Shan Tseng, Bernard Beckerman, Fan Jin, Maxsim L Gibiansky, Joe J Harrison, Erik Luijten, Matthew R Parsek, and Gerard CL Wong. Psl trails guide exploration and microcolony formation in pseudomonas aeruginosa biofilms. *Nature*, 497(7449):388, 2013.

[161] Yun Luo, Kun Zhao, Amy E Baker, Sherry L Kuchma, Kimberly A Coggan, Matthew C Wolfgang, Gerard CL Wong, and George A O'Toole. A hierarchical cascade of second messengers regulates pseudomonas aeruginosa surface behaviors. *MBio*, 6(1):e02456–14, 2015.

[162] Kelly M Colvin, Vernita D Gordon, Keiji Murakami, Bradley R Borlee, Daniel J Wozniak, Gerard CL Wong, and Matthew R Parsek. The pel polysaccharide can serve a structural and protective role in the biofilm matrix of pseudomonas aeruginosa. *PLoS Pathogens*, 7(1):e1001264, 2011.

[163] Sophie Hermann and Matthias Schmidt. Active ideal sedimentation: exact two-dimensional steady states. *Soft Matter*, 14(9):1614–1621, 2018.

[164] Stefano Bo and Ralf Eichhorn. Driven anisotropic diffusion at boundaries: noise rectification and particle sorting. *Physical Review Letters*, 119(6):060603, 2017.

[165] Anatoly Malevanets and Raymond Kapral. Mesoscopic model for solvent dynamics. *The Journal of Chemical Physics*, 110(17):8605–8613, 1999.

[166] Calvin K Lee, Jaime de Anda, Amy E Baker, Rachel R Bennett, Yun Luo, Ernest Y Lee, Joshua A Keefe, Joshua S Helali, Jie Ma, Kun Zhao, et al. Multigenerational memory and adaptive adhesion in early bacterial biofilm communities. *Proceedings of the National Academy of Sciences USA*, 115(17):4471–4476, 2018.

[167] Udo Seifert. Fluctuation theorem for birth–death or chemical master equations with time-dependent rates. *Journal of Physics A: Mathematical and General*, 37(42):L517, 2004.

[168] Lennart Dabelow, Stefano Bo, and Ralf Eichhorn. Irreversibility in active matter systems: Fluctuation theorem and mutual information. *Physical Review X*, 9(2):021009, 2019.

[169] Rick Durrett. *Probability: theory and examples*, volume 49. Cambridge University Press, 2019.

[170] Jean Jacod and Philip Protter. *Probability essentials*. Springer Science & Business Media, 2012.

[171] Nils Berglund. Processus aléatoires et applications. *arXiv preprint arXiv:1312.7796*, 2013.

[172] Dmytro Gusak, Alexander Kukush, Alexey Kulik, Yuliya Mishura, and Andrey Pilipenko. *Theory of stochastic processes*. Springer, 2012.

Jérémy Vachier

Education

2016 – 2020	**PhD in theoretical physics**, *Göttingen University - Germany*. Title: «Collective behavior of active particles»
2015 – 2016	**Master 2 level international P3TMA degree in theoretical physics - "Academy of Excellence"**, *Aix-Marseille University - Luminy Campus*. Condensed matter theoretical physics as a major
2014 – 2015	**Master (1st year) degree in physics**, *Aix-Marseille University - St-Charles Campus*. Fundamental physics as a major
2011 – 2014	**Bachelor degree in physics and chemistry**, *Aix-Marseille University - Luminy Campus*. Physics as a major
2010 – 2011	**General baccalaureate**, *Secondary school at Joliot-Curie - Aubagne*. Scientific series specialty Engineering Sciences

Work experiences

October 2016 – March 2020	**PhD in theoretical physics**, *Max Planck Institute for Dynamics and Self-organization - Germany*. Title: «Collective behavior of active particles»
March 2016 to June 2016	**Master thesis | Ecole Normal Supérieur Lyon - Laboratory C.B.P**. Title: «Stochastic Modeling of Epigenetic.»
April 2015 to June 2015	**Internship | Laboratory C.P.T**. Title: «Complex networks and systems with long range interactions.»
June 2014 to July 2014	**Internship | Laboratory C.I.N.A.M**. Title: «The morphological evolution of a single crystal surface.»
June 2013 to July 2013	**Internship | Laboratory C.P.T**. Title: «Permutations in mathematics - Study of Groups theory.»
June 2012 to July 2012	**Internship | Laboratory C.I.M.L**. Title: «Study of the random walk properties by means of simulations.»